Universidad Autónoma de Madrid

Departamento de Física Teórica

THE MAKER AND THE MASK:

COSMIC WEB AND DUST EFFECTS IN THE FORMATION AND EMISSION OF GALAXIES

Memoria de tesis doctoral presentada por

Aura Obreja

para optar al título de doctor en Ciencias Físicas

Supervisado por

Directora de Tesis: Prof. Dr. Rosa Domínguez-Tenreiro

Codirector: Dr. Christopher Brook

Departamento de Física Teórica, UAM

3 de Marzo de 2015

Contents

Chapter 1

General introduction

The first observations of galaxies date back to the 18th century (Messier's nebulae), but the field of galaxy formation only started its exponential development in the 1920' with the Hubble law. At that time, the focus was on the then–recent theory of General Relativity, and the linear scaling between galaxy redshifts and distances made a strong argument for an expanding Universe. As more sensitive detectors started to be available and more observations were made, it became obvious that galaxies come in a variety of flavors, from large dispersion supported ellipticals to rotation dominated spirals, to small strongly disturbed irregulars. The drive to explain the morphology and observed properties of these objects made galaxy formation a research topic in its own right.

Almost a century later, we have observations of millions of galaxies (e.g. Sloan Digital Sky Survey, `http://www.sdss.org/`), intricate analytical models (e.g. Cole et al. 2000; Benson 2012) and high-resolution cosmological simulations worth millions of CPU hours (e.g. Illustris Project `http://www.illustris-project.org/`). However, the galaxy formation process(es) is(are) still far from having the last nail. On one hand, the nature of most of the matter in the Universe is unknown. However, we do have the ΛCDM model (Blumenthal et al. 1984) that succeeds at reproducing a variety of observations, from galaxy rotation curves to galaxy clustering. On the other hand, the non-linear processes driving galaxy formation, their coupling to each other and their combined effects on a huge dynamical range are still beyond our analytical models as well as our numerical ones.

This thesis has two main parts. The first one is concerned with the origin of the different components of disk galaxies (stellar halo, bulge and disk), as they emerge from the Cosmic Web. The focus of this part is on the effect of the Cosmic Web dynamics in the formation of the stellar

halo, bulge and disk, while trying to explain how these processes can be interpreted as an extension of the two–phase formation model for Elliptical galaxies, previously developed in the group.

In Chapter 3 we study bulge formation in cosmological simulations, finding compelling evidence for a two–mode process that results in simulated bulges being a combination of a metal poor, α–enriched, mainly velocity dispersion supported old classical one and a younger bulge having opposite characteristics. The prevalence of one or the other is linked to the merger history and the subgrid implementations in the simulations codes. In Chapter 4 we analyze the differences in the assembly histories between stellar disks and spheroids, looking at the regions of the Cosmic Web they sample, the acquisition and loss of angular momentum and the evolution of their progenitor gas general properties. In the last chapter of this first part, Chapter 5, we further separate the simulated disks into thin and thick ones studying the differences in their properties and comparing at all steps with recent observations of the solar neighborhood. The results in Chapters 3 and 4 have already been published in Obreja et al. (2013) and Domínguez-Tenreiro et al. (2015), while those in Chapter 5 are part of work in progress.

The second part of this thesis is concerned with the methods employed when comparing simulations and observations, namely radiative transfer in post-processing of simulated galaxies. With this aim, our group in close collaboration with Prof. G.L. Granato and L. Silva at Osservatorio Astronomico di Trieste, Italy, has developed a new spectrophotometric code, GRASIL-3D (Domínguez-Tenreiro et al. 2014), for which I have made the imaging module and the post-processing pipeline. This code has various strong points. It solves the radiative transfer using ray tracing and not the more commonly applied Monte Carlo method, and does that by treating separately the cold dusty gas, associated with regions of recent star formation, and the diffuse gas. The detailed implementation of dust effects allows for in–depth comparison with observational data in mid–infrared where the distinguishable signs of polycyclic aromatic hydrocarbons appear. The code has been tested by comparisons with a wide range of observational data from far–ultraviolet to far–infrared. In Chapter 6 we give a description of the code and the its first applications to simulated galaxies. The additional information with respect to the published article concerns the post-processing pipeline and the finalized/ongoing projects in which it is employed. The very first project in which the code was used is described in Chapter 7, the results being published in Obreja et al. (2014). In this last chapter, we applied GRASIL-3D to a sample of high resolution simulated galaxies in a cosmological context and studied their evolution in the stellar mass – star formation rate – Oxygen abundance space, finding good agreement with observational data, and implicitly with mass and

star formation rate tracers based on broad band fluxes.

Each chapter has its own introduction, methods, results and references. The results in chapters 3, 4, 6 and 7 have already been published (the intro notes at the beginning of each one give the complete references to the published articles). Additional information is given in their corresponding appendices. In chapter 5 we show results of an ongoing-project, while in chapter 2 we give a brief theoretical background, as well as a description of the codes we use and of some important analysis methods. In chapter 8 we summarize our results and present our conclusions.

References

Benson, A. 2012, New Astronomy, 17, 175

Blumenthal, G. R., Faber, S. M., Primack, J. R., & Rees, M. J. 1984, Nature, 311, 517

Cole, S., Lacey, C. G., Baugh, C. M., & Frenk, C. S. 2000, MNRAS, 319, 168

Domínguez-Tenreiro, R., Obreja, A., Brook, C. B., Martínez-Serrano, F. J., Stinson, G., & Serna, A. 2015, ApJ, 800, L30

Domínguez-Tenreiro, R., Obreja, A., Granato, G. L., et al. 2014, MNRAS, 439, 3868

Obreja, A., Brook, C. B., Stinson, G., Domínguez-Tenreiro, R., Gibson, B. K., Silva, L., & Granato, G. L. 2014, MNRAS, 442, 1794

Obreja, A., Domínguez-Tenreiro, R., Brook, C., et al. 2013, ApJ, 763, 26

Chapter 2

Physical framework and methods

In this chapter, we give a brief overview of the theoretical background on structure formation. We also give details on the simulations codes we use and on the methods we employ to analyze the simulations.

2.1 The Cosmic Web

Analyses of the current large scale distribution of galaxies and mass show that both are hierarchically organized into a highly interconnected network, displaying a wealth of structures and substructures over a huge range of densities and scales, the so-called cosmic web (Bond et al. 1996), made of filaments, walls, nodes which surround vast empty regions, the voids (Zel'dovich 1970; Shandarin & Zeldovich 1989).

This web can be understood as the main feature of the anisotropic nature of gravitational collapse (Peebles 1980), as well as of its intrinsic hierarchical character, and in fact it is the main dynamical engine responsible for structure formation in the Universe (Sheth & Tormen 2004; Sheth & van de Weygaert 2004; Shen et al. 2006), including at galaxy scales (Domínguez-Tenreiro et al. 2011).

According to the standard model of cosmology, large-scale structures observed in the Universe today are seeded by infinitesimal primordial density and velocity perturbations. The physical processes underlying their dynamical development until the cosmic web emergence can be explained by theories and models on the gravitational instability. Indeed, the advanced non-linear stages of gravitational instability are described by the Adhesion Model (see Gurbatov & Saichev 1984, Gurbatov et al. 1989, Shandarin & Zeldovich 1989, Vergassola et al. 1994 and Gurbatov et al. 2012,

for a recent review), an extension of the popular non-linear Zeldovich Approximation (Zel'dovich 1970). These models are now corroborated by a profusion of cosmological simulations, the first of them purely N-body simulations (see e.g. Yepes et al. 1992; Pogosyan et al. 1998; Jenkins et al. 1998; Colberg et al. 2005; Springel et al. 2005; Dolag et al. 2006), while recent ones include baryons and stellar physics too (see e.g. Domínguez-Tenreiro et al. 2011; Metuki et al. 2015).

2.1.1 Growth of perturbations in an expanding Universe: Linear Theory

The Cosmic Web forms from the small perturbations in the matter density field at matter-radiation decoupling (Cosmic Microwave Background, z$\sim$ 1100). The density contrast at this epoch is of the order of 10^{-5}, which means that the Universe can be approximated as being homogeneous, and the evolution of the matter content can be studied using linear perturbation theory.

This means solving the equation describing the growth of perturbation contrast, $\delta(t,\vec{r})$, linearized in the Newtonian limit:

$$\ddot{\delta} + 2H\dot{\delta} - v^2 a^{-2}\nabla^2\delta = 4\pi G\rho_b\delta, \tag{2.1}$$

where H is the Hubble constant ($H = \dot{a}/a$) with a the expansion factor, G is the gravitational constant, ρ_b is the background density and the overdots stand for time derivative $\partial/\partial t$.

The solutions indicate that a growing mode always exists, so that $\delta(t,\vec{r})$ can always be expressed as $\delta(t,\vec{x}) = A(\vec{x})D_+(t)$.

In the current concordance cosmological model, $D_+(t)$ has different behavior depending on the cosmological epoch. At high redshift, when the Universe dynamics is well described by the Einstein – de Sitter model, $D_+(t) = (3/5)(t/t_i)^{2/3}$, where t_i is the initial time. At low redshift ($z \lesssim 0.6$), when the cosmological constant starts to dominate, we have:

$$D_+(a(t)) \propto \mathfrak{B}_x(5/6, 2/3)\left(\frac{\Omega_0}{\Omega_\Lambda}\right)^{1/3}\left[1 + \frac{\Omega_M}{a^3\Omega_\Lambda}\right]^{1/2}, \tag{2.2}$$

where $\mathfrak{B}_x$ is the incomplete β function, and

$$x \equiv \frac{a^3\Omega_\Lambda}{\Omega_0 + a^3\Omega_\Lambda}, \tag{2.3}$$

describing a frozen perturbation in the limit of $t \to \infty$.

2.1.2 The Zeldovich Approximation

Once the density contrast approaches unity, linear perturbation theory is no longer a valid approximation. To fill this gap, Zeldovich proposed a model in which, instead of following the evolution of the density contrast, one follows the particle trajectories (Zel'dovich 1970) and he extended its validity up to the advanced non-linear stages of gravitational instability (i.e., the so-called Zeldovich Approximation).

In comoving coordinates, Zeldovich's approximation is given by the *Lagrangian map*:

$$\vec{x}(\vec{q},t) = \vec{q} + D_+ s(\vec{q}) \tag{2.4}$$

where q and x are comoving Lagrangian and Eulerian coordinates of fluid elements, $D_+(t)$ is the growing density mode from the linear gravitational instability theory, and s is proportional to $\nabla\phi$, with ϕ the gravitational potential.

Mass conservation together with Equation 2.4 results in the following expression for the density field in physical coordinates, $\vec{r} = a(t)\vec{x}$:

$$\rho(\vec{r},t) = \frac{\rho_b(t)}{[1 - D_+(t)\lambda_1(\vec{q})][1 - D_+(t)\lambda_2(\vec{q})][1 - D_+(t)\lambda_3(\vec{q})]}, \tag{2.5}$$

where $\rho_b(t)$ is the background density and $\lambda_1(\vec{q}) > \lambda_2(\vec{q}) > \lambda_3(\vec{q})$ are the eigenvalues of the local deformation matrix $\partial^2\phi/\partial q_i \partial q_j$.

Equation 2.5 describes formation of caustics (singularities in the *Lagrangian map*) in the Zeldovich Approximation. A positive eigenvalue means collapse along the direction of the corresponding eigenvector, while a negative one means expansion. According to this model, the collapse of a patch of matter will proceed sequentially, first along the direction of the larger eigenvalue, when $D_+(t)\lambda_1(\vec{q}) = 1$, then along the second largest ($D_+(t)\lambda_2(\vec{q}) = 1$), and last along the smallest ($D_+(t)\lambda_3(\vec{q}) = 1$), supposing all three eigenvalues are positive. In three dimensional space caustics can be walls, filaments and nodes, equivalent of surfaces, curves and points in the Eulerian $\vec{x}$ space.

This collapse model explains nicely the structuring of matter observed in N-body simulations, where walls first form, then filaments and then nodes (i.e., the Cosmic Web elements, see Bond et al. 1996).

2.1.3 The Adhesion Model

The problem of the Zeldovich approximation is that it predicts pancakes and filaments to blur due to multistreaming soon after they form. However, in cosmological simulations this thickening of structures is not observed. To fix this problem, Gurbatov et al. (1989) and Kofman et al. (1990) added a viscous term, ν, in Zeldovich's momentum equation, that is effectively zero anywhere but at the caustics. Considering this term which is effective only in the regions with large velocity variations, the so-called "Adhesion Model" is capable of reproducing the structuring observed in numerical studies (Cautun et al. 2014). A review of physically motivated derivations of the "Adhesion Model" was presented by Buchert & Domínguez (2005).

As in the Zeldovich Approximation, the initial velocity field can be written in terms of the gradient of the potential, $\phi(\vec{q})$, characterizing the perturbation field. The solutions for the equation of the velocity field in the limit $\nu \to 0$ behave similar to the analytical solutions of Burgers' equation (Burgers 1974). These analytical solutions are discontinuous, which implies that singularities must develop. These singularities are the caustics in the Zeldovich Approximation, walls forming first and filaments later on.

These model predicts that, at a given scale, walls surrounding voids, filaments and nodes successively emerge in multi-streaming regions. This structuring, at a given scale, vanishes sequentially, as mass flows from voids to walls, from walls to filaments, and finally from filaments to nodes, where mass pills up and virializes, after the web-like mass configuration, at the scale considered, turns around and collapses (see e.g. Domínguez-Tenreiro et al. 2011). At the same time this organization occurs at larger and larger scales.

The "cold flow" scenario (Kereš et al. 2005) emerges naturally as a consequence of the "Adhesion Model".

2.1.4 Gas in the Cosmic Web

At the singular regions of the web, energy transfer from ordered to disordered motions takes place. For the gas, this means that kinetic energy transforms to internal energy. Since gas can cool, it will do so and sink further into the potential wells, making then even denser. At any scales, however, the dense and diffuse gas phases are mixed. This means that the less dense gas also gets heated at singularities, and hence pressurized. Part of this hot gas can have extremely long cooling time, which will ensure that some might stay hot all the way to $z = 0$. The evolution of this

multiphase gas in the cosmic web structure can not be described analytically. Instead cosmological hydrodynamical simulations allow us to follow these interlaced processes.

2.2 Spherical collapse

The growth of the initial density field perturbations occurs in an expanding universe. This means that overdensities will initially expand until the collapse induced by the self gravity overtakes the expansion. At this point, also known as time of maximum expansion, the overdense region decouples from the background expansion, turns around and collapses onto itself.

In order to have an estimation of the times of turn-around and collapse, one can use the evolution of a spherical shell enclosing a fixed mass, and assume that shells do not cross each other during their expansion and collapse.

If we consider a collapsing spherical shell of constant mass, we can derive the maximum radius it can attain, r_{turn}, and the time of maximum expansion / turn-around, z_{turn} (Padmanabhan 1993):

$$r_{turn} = r_i(1 + \frac{1}{\delta_i}) \tag{2.6}$$

$$\delta_{turn} = \frac{9\pi^2}{16} - 1 \approx 4.6 \tag{2.7}$$

$$1 + z_{turn} \simeq 0.57(1 + z_i)\delta_i \tag{2.8}$$

where δ_i is the average value of the shell density contrast an the initial redshift, z_i. After a perturbation attains its maximum extension, the contraction phase begins, which will end up with all the mass concentrated in one point, if we extrapolate the equations derived so far.

However, this approximation breaks down long before this happens. Apart from the fact that the real collapse is not spherical, when the density gets high the random velocities of the particles also increase. In this regime, the dark matter fluid suffers the so-called "violent relaxation" process, and as a consequence reaches a stage of equilibrium (virializes). This process is caused by the rapidly fluctuating potential during the collapse, on timescales of the order of the free-fall time, $t_{freefall} \sim (8GM/\pi^2R^3)^{-1/2}$, which implies that particles no longer follow constant energy orbits, but instead have wide energy distributions. When the system reaches virial equilibrium, its potential energy is two times the kinetic energy. Taking into account that at the time of maximum expansion all energy is in potential form, the radius (r_{vir}) and redshift ($z_{collapse}$) at equilibrium can be written in terms of the corresponding values at turn-around:

$$r_{vir} = r_{turn}/2 \tag{2.9}$$

$$1 + z_{collapse} = 0.63(1 + z_{turn}) \tag{2.10}$$

2.3 The origin of angular momentum

One aspect of crucial importance for galaxy evolution is angular momentum. The galaxies that we observe in the Local Universe can be roughly classified into two groups: systems supported by velocity dispersions (e.g. Ellipticals) and supported by rotation (e.g. Spirals). The difference in the rotational support of these two types of systems is directly determined by the manner in which they gain and/or lose angular momentum.

2.3.1 Tidal Torque Theory

Angular momentum of a collapsing patch of matter (or overdensity peak) is thought to originate from the torques induced by the collapse of the neighboring overdensities. The theoretical framework explaining it is called the Tidal Torque Theory (Peebles 1969; Doroshkevich 1970; White 1984), and we shall give a brief overview here. It has been derived using the Zeldovich Approximation in the quasi-linear regime of perturbation growth.

Each collapsing overdensity can be described in terms of its inertia tensor, **I**, and deformation tensor, **T**, defined as:

$$I_{ij} = \rho(a)a \int_{\Gamma} x_i x_j d^3x, \tag{2.11}$$

and

$$T_{ij} = -\frac{\partial^2 \phi}{\partial x_i \partial x_j} \tag{2.12}$$

where **x** gives the comoving coordinate (**r**=a**x**), Γ is the Lagrangian volume of the overdensity, ρ is the mean density of the universe, and ϕ is the gravitational potential. The traceless part of **T** is called the "tidal" tensor, and the traceless part of **I** is the quadrupolar inertia tensor. According to the Tidal Torque Theory, the angular momentum vector, **J** is given by the antisymmetric tensor product of the inertia and tidal tensors:

$$J_i \propto \epsilon_{ijk} T_{jl} I_{lk} \tag{2.13}$$

This model predicts that in the linear regime of perturbation growth, angular momentum increases linearly with time ($J_i \propto t$). Once the Lagrangian volume reaches its maximum size and decouples from the background expansion, the tidal torques are no longer efficient and the system collapses, roughly conserving its angular momentum. Given that initially baryons follow the evolution of dark matter, the same mechanism for angular momentum acquisition applies. However, baryons and dark matter show important differences. For example, the spin of dark matter halos, λ_{DM}, has been found to have a lognormal distribution with maximum at 0.035 (Bullock et al. 2001), while disk galaxies have typical spins of 0.4–0.5. Therefore, there has to be additional processes that explain the difference of ∼90% between the angular momentum baryons acquire through tidal torques and their final **J**. Gas, as opposed to dark matter, can cool and collapse further into the halo, increasing its binding energy while conserving its angular momentum. The spin of the gas will thus increase since it scales with the square root of the energy.

2.3.2 The role of filaments

After the decoupling from the background expansion, the angular momentum of the Lagrangian volume, j_{patch} is roughly conserved, but redistributed (Pichon et al. 2011). Filaments form from the collapse of matter flows coming from opposite directions. These flows coherently wind up (Codis et al. 2012) into whirls with their spin s directions roughly aligned with the filament. At the same time, matter elements also acquire a net transverse motion (i.e., an orbital j relative to the patch center), due to the asymmetric forces acting on filaments from the voids they divide.

Once the filaments form, they collimate matter, either clumpy or diffuse, towards the growing central mass accumulation, coherently transporting j. The j content of in falling matter grows with its distance to the patch center (lever effect). The implications this ordering has on j acquisition by *gas* at the scales of *galaxy halos* has been analyzed by Sales et al. (2012) for Milky-Way-sized galaxies. In their simulations, disk galaxies form via two channels: from in falling gas with highly coherent angular momentum and/or through gas that gets accreted at late times from spinning hot coronae. They conclude that "cold flows" most likely favor the formation of slowly rotating spheroids than disks. On the other hand, Stewart et al. (2013) get the opposite results studying also Milky-Way-sized simulated SPH galaxies. Cold-mode gas accretes onto the halo through the cosmic filaments and carry more angular momentum (a reformulation of the lever effect previously

described) than hot-mode gas which is accreted isotropically. They find that cold gas accreted at later times, j-rich, forms extended "cold-flow disks" which rotate in the same direction as the galaxy, and hence cause disk growth. The scenario proposed by Stewart et al. (2013) has been confirmed in adaptive mesh simulations by Danovich et al. (2014), albeit at high redshift (z > 1.5).

2.3.3 Torques at the circumgalactic region

To analyze the changes in angular momentum near the inner, early settled disk, Danovich et al. (2014) introduced a simple, analytic toy model. Let us consider the gravitational potential generated by a uniform axisymetric disk with radius R and mass M, placed at the $x--y$ plane around the origin. At point (r, θ), the monopole and quadrupole terms, sufficient to describe the potential far enough from the disk, read:

$$\Phi(r,\theta) = -\frac{GM}{r} + \frac{\alpha G M R^2}{r^3} P_2(\cos\theta) + O(\frac{R^4}{r^5}) \tag{2.14}$$

where θ is the spherical polar angle measured from the z axis, α is a numerical factor, and P_2 is the second order Legendre polynomial. The resulting torque is:

$$\tau_\varphi = -\frac{\partial\Phi}{\partial\theta} \propto \frac{\alpha G M R^2}{r^3} \cos\theta \sin\theta. \tag{2.15}$$

The torque in the Cartesian x direction in the disk plane is:

$$\tau_x = -\tau_\varphi \sin\varphi \propto \frac{\alpha G M R^2}{r^3} \cos\theta \sin\theta \sin\varphi. \tag{2.16}$$

This simple model indicates that torques due to an axisymmetric disk do not affect the j component parallel to the disk axis of symmetry, but tend to add j in a direction perpendicular to it, inducing rotation in a plane normal to the disk. This implies moving mass towards the disk plane.

For a particle moving around the disk with angular momentum tilted with respect to the disk axis, the disk induces torques normal the particle angular momentum, causing its precession. For an extended set of such particles, if they are gas, the differential precession will cause dissipation. Therefore, such particles will tend to gradually align themselves with the inner disk, making it grow. If the particles are not gas, they cannot suffer from energy loses and therefore, they will not be placed at the energy minimum of the axisymetric potential (circular orbits in the disk plane). This explains why gas disks are thinner than stellar ones.

For not aligned particles, either collisional or collisionless, torques can also reduce the j amplitude, therefore, inducing them to spiral in.

2.4 Simulation codes

Hydrodynamical simulations in a cosmological context are a helpful tool to address the above questions. In order to make a robust characterization of spheroids and disks, precise differences in morphology, kinematic and composition need to be measured. For these reasons, some particular aspects of the codes are very important. In first place, the codes should accurately conserve angular momentum. Also, they should include the effects of stellar feedback on the surrounding gas, and characterize realistically the gas by implementing detailed chemical evolution. Since we are looking for effects coming from a generic and fundamental level of physical description, we will be comparing results based on simulations run with different codes, `P-DEVA` and `GASOLINE`.

`P-DEVA` (Serna et al. 2003) is an entropy conserving AP3M-SPH code where the main concern in its design was that the conservation laws hold as accurately as possible. To this end, a double loop has been implemented in the neighbor search algorithm to ensure that if the i particle is in the neighbor list of j, then j is in that of i. In this way, the second Newton's law holds with high accuracy at the expenses of rapidity. The code incorporates a scheme of delayed gas restitution from stars by means of a probabilistic approach designed to reduce the statistical noise and, hence, to allow for the study of the inner chemical structure of objects with moderately high numbers of particles. The chemical enrichment is based on Talbot & Arnett (1973), implementing the full dependence of metal production on the detailed chemical composition of stellar particles by using, for the first time in SPH codes, the Qij matrix formalism that relates each nucleosynthetic product to its sources, improving the [α/Fe] determination in galaxies. The code involves 11 elements and it includes chemical feedback both by SNe Ia and SNe II, as well as mass loss from intermediate mass stars, (Martínez-Serrano et al. 2008). Radiative cooling takes into consideration the full element distribution at each point and time through a particular implementation of the Dimension Reduction regression (Weisberg 2002), while a SPH metal diffusion term mimics turbulent effects (Monaghan 2005). The simulations run with `P-DEVA` assume that supernova feedback works on subgrid scales and results in a low star formation efficiency, which is thus used as an input parameter that implicitly mimics the energetic feedback (Agertz et al. 2011). A Salpeter IMF (Salpeter 1955) is used to compute the stellar yields.

GASOLINE (Wadsley et al. 2004) is a parallel SPH tree-code, which includes metal line cooling (Shen et al. 2010), the effect of a ultraviolet ionizing background, supernova and early stellar feedback (Stinson et al. 2006, 2013). The blastwave formalism (Stinson et al. 2006) is used to implement supernova feedback, at the end of massive stars ($8\,M_\odot$) lifetime, 10^{51} erg of energy being deposited into the surrounding medium. Prior to their explosion as SNe, massive stars inject energy into the surrounding gas. This feedback mechanism has also been included (Stinson et al. 2013) as pure thermal energy feedback in order to mimic the weak coupling to the surrounding gas (Freyer et al. 2006). Thermal energy feedback is highly inefficient in these types of simulations (Katz 1992; Kay et al. 2002), 90% of the injected energy being rapidly radiated away. A Chabrier IMF (Chabrier 2003) is used to compute the ejected mass and metals, which are distributed among the nearest neighbor gas particles according to the smoothing kernel (Stinson et al. 2006). Metal abundances are based on the SNII yields of Woosley & Weaver (1995) and SNIa yields of Nomoto et al. (1997). The turbulent metal mixing is mimicked using a shear-dependent diffusion term (Shen et al. 2010). Cooling rates are computed by taking into account the diffused metals.

2.5 The kinematic decomposition

The k–means method has been used by Doménech-Moral et al. (2012) to disentangle the fine structure of simulated late type galaxies. This is an unsupervised clustering algorithm (Schölkopf et al. 1998; Karatzoglou et al. 2004; Dhillon et al. 2004) looking for clusters in a 3-dimensional space of stellar particles kinematic variables. This algorithm separates a sample in a given number, n, of equal variance groups by minimizing the sum of within–cluster distances squared, where the metric need not be Euclidean. This criteria, also referred to as "inertia" is a measure of a cluster's internal coherence. It scales well with the number of elements in the sample and it will always converge, although it might need many iterations to do so and the convergence can be to a local minimum. Two of the underlying assumptions of the method are that clusters are convex and isotropic, which means that clusters will tend to be spherical (in the corresponding multi-dimensional space) and to have comparable number of members.

Specifically, for each stellar particle, i, in a given galaxy, its total binding energy, $E_{\rm i}$, $\epsilon_{\rm J,i} \equiv j_{\rm z,i}/J_{\rm C,i}(E_{\rm i})$ and $j_{\rm p,i}/J_{\rm C,i}(E_{\rm i})$ have been used as variables, where $j_{\rm z,i}(j_{\rm p,i})$ are the particle angular momentum projections on the disk axis (plane) and $J_{\rm C,i}(E_{\rm i})$ is the angular momentum of a circular orbit with energy $E_{\rm i}$. By applying this method, with no priors assumed apart from the number of

clusters, the fine structure of galaxies emerges naturally (see Figure 7 in Doménech-Moral et al. 2012, where more details can be found). Once classified, the systematics of spheroid, thick disk and thin disk star observational properties is recovered, as well as their mutual correlations (Doménech-Moral et al. 2012; Obreja et al. 2013). The same is true for `GASOLINE` galaxies, although using a different classification scheme (Brook et al. 2012a). To do the classification we have used *scikit–learn* (Pedregosa et al. 2011).

References

Agertz, O., Teyssier, R., & Moore, B. 2011, MNRAS, 410, 1391

Binney, J. 1977, ApJ, 215, 492

Bond, J. R., Kofman, L., & Pogosyan, D. 1996, Nature, 380, 603

Brook, C. B., Stinson, G., Gibson, B. K., Wadsley, J., & Quinn, T. 2012a, MNRAS, 424, 1275

Brook, C. B., Stinson, G. S., Gibson, B. K., et al. 2012b, MNRAS, 426, 690

Brooks, A. M., Governato, F., Quinn, T., Brook, C. B., & Wadsley, J. 2009, ApJ, 694, 396

Bullock, J. S., Dekel, A., Kolatt, T. S., Kravtsov, A. V., Klypin, A. A., Porciani, C., & Primack, J. R. 2001, ApJ, 555, 240

Buchert, T., & Domínguez, A. 2005, A&A, 438, 443

Burgers, J. M. 1974, The nonlinear diffusion equation : asymptotic solutions and statistical problems, ISBN 90-277-0494-5, Dordrecht-Holland, Boston

Cautun, M., van de Weygaert, R., Jones, B. J. T., & Frenk, C. S. 2014, ArXiv e-prints

Chabrier, G. 2003, ApJ, 586, L133

Codis, S., Pichon, C., Devriendt, J., et al. 2012, MNRAS, 427, 3320

Colberg, J. M., Krughoff, K. S., & Connolly, A. J. 2005, MNRAS, 359, 272

Danovich, M., Dekel, A., Hahn, O., Ceverino, D., & Primack, J. 2014, ArXiv e-prints

Dhillon, I., Guan, Y., & Kulis, B. 2004, A unified view of kernel k-means, spectral clustering and graph cuts, Tech. Rep. TR-04-25, University of Texas at Austin, Department of Computer Sciences

Dolag, K., Meneghetti, M., Moscardini, L., Rasia, E., & Bonaldi, A. 2006, MNRAS, 370, 656

Doménech-Moral, M., Martínez-Serrano, F. J., Domínguez-Tenreiro, R., & Serna, A. 2012, MNRAS, 421, 2510

Domínguez-Tenreiro, R., Oñorbe, J., Martínez-Serrano, F., & Serna, A. 2011, MNRAS, 413, 3022

Domínguez-Tenreiro, R., Obreja, A., Granato, G. L., et al. 2014, MNRAS, 439, 3868

Domínguez-Tenreiro, R., Obreja, A., Brook, C. B., Martínez-Serrano, F. J., Stinson, G., & Serna, A. 2015, ApJ, 800, L30

Doroshkevich, A. G. 1970, Astrophysics, 6, 320

Freyer, T., Hensler, G., & Yorke, H. W. 2006, ApJ, 638, 262

Gilmore, G., Wyse, R. F. G., & Kuijken, K. 1989, ARA&A, 27, 555

Gurbatov, S. N., & Saichev, A. I. 1984, Radiofizika, 27, 456

Gurbatov, S. N., Saichev, A. I., & Shandarin, S. F. 1989, MNRAS, 236, 385

Gurbatov, S. N., Saichev, A. I., & Shandarin, S. F. 2012, Physics Uspekhi, 55, 223

Hoffman, Y., Metuki, O., Yepes, G., et al. 2012, MNRAS, 425, 2049

Ivezić, Ž., Beers, T. C., & Jurić, M. 2012, ARA&A, 50, 251

Jenkins, A. & et. al 1998, ApJ, 499, 20

Karatzoglou, A., Smola, A., & Hornik, K. 2004, Journal of Statistical Software, 1

Katz, N. 1992, ApJ, 391, 502

Kay, S. T., Pearce, F. R., Frenk, C. S., & Jenkins, A. 2002, MNRAS, 330, 113

Kereš, D., Katz, N., Fardal, M., Davé, R., & Weinberg, D. H. 2009, MNRAS, 395, 160

Kereš, D., Katz, N., Weinberg, D. H., & Davé, R. 2005, MNRAS, 363, 2

Kofman, L., Pogosian, D., & Shandarin, S. 1990, MNRAS, 242, 200

Martínez-Serrano, F. J., Serna, A., Domínguez-Tenreiro, R., & Mollá, M. 2008, MNRAS, 388, 39

Metuki, O., Libeskind, N. I., Hoffman, Y., Crain, R. A., & Theuns, T. 2015, MNRAS, 446, 1458

Monaghan, J. J. 2005, Reports on Progress in Physics, 68, 1703

Mould, J. R. 1982, ARA&A, 20, 91

Nomoto, K., Hashimoto, M., Tsujimoto, T., et al. 1997, Nuclear Physics A, 616, 79

Obreja, A., Brook, C. B., Stinson, G., et al. 2014, MNRAS, 442, 1794

Obreja, A., Domínguez-Tenreiro, R., Brook, C., et al. 2013, ApJ, 763, 26

Ocvirk, P., Pichon, C., & Teyssier, R. 2008, MNRAS, 390, 1326

Padmanabhan, T. 1993, Structure Formation in the Universe, ISBN 0521424860, Cambridge University Press

Pedregosa, et al. 2011, JMLR, 12, pp. 2825-2830

Peebles, P. J. E. 1969, ApJ, 155, 393

Peebles, P. J. E. 1980, The large-scale structure of the universe, Research supported by the National Science Foundation. Princeton, N.J., Princeton University Press

Pichon, C., Pogosyan, D., Kimm, T., et al. 2011, MNRAS, 418, 2493

Pogosyan, D., Bond, J. R., & Kofman, L. 1998, JRASC, 92, 313

Sales, L. V., Navarro, J. F., Theuns, T., et al. 2012, MNRAS, 423, 1544

Salpeter, E. E. 1955, ApJ, 121, 161

Schölkopf, B., Smola, A., & Müller, K.-R. 1998, Neural Comput., 10, 1299

Serna, A., Domínguez-Tenreiro, R., & Sáiz, A. 2003, ApJ, 597, 878

Shandarin, S. F., & Zeldovich, Y. B. 1989, RvMP, 61, 185

Shen, J., Abel, T., Mo, H. J., & Sheth, R. K. 2006, ApJ, 645, 783

Shen, S., Wadsley, J., & Stinson, G. 2010, MNRAS, 407, 1581

Sheth, R. K., & Tormen, G. 2004, MNRAS, 350, 1385

Sheth, R. K., & van de Weygaert, R. 2004, MNRAS, 350, 517

Springel, V. & et. al 2005, Nature, 435, 629

Stewart, K. R., Brooks, A. M., Bullock, J. S., et al. 2013, ApJ, 769, 74

Stinson, G., Seth, A., Katz, N., et al. 2006, MNRAS, 373, 1074

Stinson, G., Brook, C., Macciò, A. V., et al. 2013, MNRAS, 428, 129

Talbot, Jr., R. J., & Arnett, W. D. 1973, ApJ, 186, 51

Tillson, H., Devriendt, J., Slyz, A., Miller, L., & Pichon, C. 2012, ArXiv e-prints

Vergassola, M., Dubrulle, B., Frisch, U., & Noullez, A. 1994, A&A, 289, 325

van de Voort, F., Schaye, J., Booth, C. M., Haas, M. R., & Dalla Vecchia, C. 2011, MNRAS, 414, 2458

Wadsley, J. W., Stadel, J., & Quinn, T. 2004, New Astronomy, 9, 137

Weisberg, S. 2002, Journal of Statistical Software, 7

White, S. D. M. 1984, ApJ, 286, 38

White, S. D. M., & Rees, M. J. 1978, MNRAS, 183, 341

Woosley, S. E., & Weaver, T. A. 1995, ApJS, 101, 181

Yepes, G., & Dominguez-Tenreiro, R., & Couchman, H. M. P. 1992, ApJ, 401, 40

Zel'dovich, Y. B. 1970, A&A, 5, 84

Chapter 3

A two-phase scenario for bulge assembly in ΛCDM cosmologies

This chapter is a copy of

"A Two-phase Scenario for Bulge Assembly in ΛCDM Cosmologies"

by Obreja, Domínguez-Tenreiro, Brook, Martínez-Serrano, Doménech-Moral, Serna, Mollá & Stinson,

published in ApJ 763, 26, 15, 2013

Supplementary information is presented in the Appendix.

3.1 Introduction

Understanding how bulges form and evolve is important within the theories and models of galaxy formation and evolution. Bulges are the component responsible for the central light in excess of the exponential disk (Freeman 1970), and account for more than 25% of the starlight emitted in the local Universe. There are three main classes of observed bulge: classical, pseudo-, and boxy or peanut-shaped bulges, see Kormendy & Kennicutt (2004) and Athanassoula (2005) for a detailed discussion on bulge classification. The distinction is important in that different classes cloud have formed and evolved in different ways.

The Milky Way Bulge is the only case in which individual stars are resolved, and thus provides unique information about bulge properties. The Milky Way is considered to have a boxy bulge, yet increased evidence for an old, α-enriched stellar population formed on a short time-scale has resulted in a two-component model (e.g. Tsujimoto & Bekki 2012) of the Bulge. It had been shown that two

stellar populations coexist in the Bulge, separated in age and metallicity (McWilliam & Rich 1994; Feltzing & Gilmore 2000; Barbuy et al. 1999; van Loon et al. 2003; Groenewegen & Blommaert 2005; Zoccali et al. 2006; Fulbright et al. 2007; Zoccali et al. 2008) and that the separation somewhat extends to kinematics (Zhao et al. 1994; Soto et al. 2007), even if age determinations through color-magnitude diagrams showed that most bulge stars in the Galaxy are older than 10 Gyrs (Ortolani et al. 1995; Feltzing & Gilmore 2000; Zoccali et al. 2006; Clarkson et al. 2008).

Recently Bensby & et al. (2011) reported a 2-13 Gyrs age span among microlensed turn-off Bulge stars. These latest data from high resolution spectrography, have put increased emphasis on the picture of a two-component Bulge. Indeed, analyses of giant stars confirmed the presence of two distinct populations: a metal-poor enriched in [α/Fe] one with kinematics consistent with an old spheroid, and a metal-rich one with roughly solar [α/Fe] and with bar-like kinematics (Babusiaux et al. 2010; Hill et al. 2011; Gonzalez et al. 2011; De Propris et al. 2011; Johnson et al. 2011; Robin et al. 2012; Soto et al. 2012; Ness & Freeman 2012; Ness et al. 2012). Comparing metallicities and compositions at different galactic latitudes, it has been found that while the [α/Fe] remains roughly constant and metal-poor stars show a remarkable homogeneity (Lecureur et al. 2007; Johnson et al. 2011; Gonzalez et al. 2011), the most metal-rich stars near the galactic plane disappear at higher latitudes (see Zoccali et al. 2008; Lecureur et al. 2007; Babusiaux et al. 2010, among others). Further, the younger population is associated with the bar (Babusiaux et al. 2010, and references therein). These differences could be an indication that younger, more metal-rich stars in the Bulge define a smaller region than metal-poor ones (see also Robin et al. 2012). Otherwise, Johnson et al. (2012) explored the link between Bulge and thick disk formation and found diverging behaviors in the cases of [Na/Fe] and [La/Fe], which results in the Bulge resembling more the spheroid.

In the bulges of external galaxies, similar conclusions have been reached. Stellar population studies suggest that in many cases a secondary stellar population is superimposed on an older one (Ellis et al. 2001; Thomas & Davies 2006; Carollo et al. 2007), and that the two populations are kinematically distinguishable, with the old population having spheroid-like kinematics, while this secondary population is more disk-like, see for example Prugniel et al. (2001), and the results from the SAURON project (Peletier et al. 2007; Erwin 2008). Bulge stellar masses are generally dominated by the old populations, with the young ones contributing less than a 25% in most cases (MacArthur et al. 2009), although Kormendy et al. (2010) points out that significant numbers of local massive spiral galaxies appear to have dominant pseudo-bulges.

Jablonka et al. (2007) conclude that most external bulges in their observed sample are more

metal rich and have lower [α/Fe] enhancement in their central regions than in their outer parts, a result consistent with Moorthy & Holtzman (2006), and with Milky Way Bulge results. MacArthur et al. (2009) find a wide range of gradients, both positive and negative, allowing for different bulge formation mechanisms. A complementary piece of information are age gradients, where most authors find that the central regions of external bulges are younger than the outer ones, (e.g. Moorthy & Holtzman 2006; Jablonka et al. 2007; MacArthur et al. 2009; Sánchez-Blázquez et al. 2011). The last authors, however, have also found some cases with negative age gradients.

It would appear that bulge formation and evolution in a cosmological context has to account for a duality in stellar populations, and for the coexistence of spheroid-like features with disk-like ones, whilst some particularities may be related to minor merger events (see ussion in Combes 2009). Theoretical models focusing on the physical processes responsible for bulge properties have a long history, a sample of which is presented below. Generally, the classical type is thought to originate from fast gas collapse at high redshift, or from gas clumps in a proto-disk that are driven to the central regions by dynamical friction. Whilst instabilities of the disk, perhaps associated with bars, are believed to result in the formation of pseudo- and/or boxy bulges.

Metal enrichment in bulges was first analytically studied through pure chemical evolution models. Matteucci & Brocato (1990) first predicted an [α/Fe] enhancement at bulges as a consequence of the different SNe I and II nucleosynthetic time-scales, observationally confirmed by McWilliam & Rich (1994). Mollá et al. (2000) used a multiphase multi-zone chemical evolution model and provided solutions to bulge chemical abundances and spectral indices. Ferreras et al. (2003) found that very short infall time-scales are required for bulges. These models provided the basis of later developments to be implemented in hydrodynamical simulations, and, at the same time, gave clear insights into some of the physical processes involved.

On the other hand, purely collisionless numerical studies of bulge formation have focused on morphology and dynamics by analyzing disk evolution in pre-prepared simulations. Such studies showed that spheroidal-like bulges cannot be formed through bar-buckling instabilities (Debattista et al. 2004), while disk-like and boxy/peanut bulges are different in their nature, although both classes are associated with the presence of a bar (Athanassoula 2005). On the other hand, Eliche-Moral et al. (2011) analyze the effect of minor mergers on the inner part of disk galaxies, finding this process to be efficient in forming rotationally supported stellar inner components, i.e. disks, rings or spiral patterns. Hopkins et al. (2010) use a different approach, by constructing semi empirical models, based on observationally motivated halo occupation numbers from the Millenium

simulation, aiming to quantify the relative effect of galaxy mergers on bulge formation. They find major mergers to be the dominant mechanism for L_* bulge and spheroid formation and assembly, while minor mergers contribute relatively more in lower mass systems.

The first numerical studies of bulge formation using dissipative collapse by Samland & Gerhard (2003) model the formation of a large disk inside a spinning ($\lambda = 0.05$), growing dark matter (DM) halo, with an added accretion history taken from the large-scale simulations of the GIF-VIRGO consortium (Kauffmann et al. 1999). Chemical evolution is followed through two fiducial elements tracing the fraction of heavy elements produced by type Ia or type II SNe. The resulting bulge consists of at least two stellar sub-populations, an early collapse population and another one that formed later in the bar. Nakasato & Nomoto (2003) presented results of the evolution of a spherical 3σ top-hat over-dense region of 1.4 Mpc co-moving radius in rigid rotation evolved with a gravohydrodynamical code. Again the nucleosynthetic yields of type Ia or type II SNe are used, tracing the chemical enrichment in metallicity, O and Fe. Their results suggest that bulges consist of two chemically different components; one that has formed quickly through a sub-galactic merger in the proto-galaxy, and another one that formed gradually in the inner disk. Kobayashi & Nakasato (2011) further developed this latter chemical evolution implementation, and used it to simulate a Milky Way-like galaxy. Their kinematic and chemical results follow closely the observed properties of the Galaxy halo, bulge and thick disk. These simulations, however, do not take into account the cosmological gas infall.

Few studies on bulge formation have been made within a fully cosmological context. Tissera & Dominguez-Tenreiro (1998) and Governato et al. (2009) have studied the effects of mergers on classical bulge stellar populations. Guedes et al. (2011) have run the highest resolution up-to-now simulation of Milky Way like disk formation, and got realistic disk and bulge properties but their focus on the details of bulge formation is relatively minor. Okamoto (2012) finds that pseudo bulges form, in his simulated Milky Way galaxies, by rapid gas supply at high-redshift, with their progenitors observable as high-redshift disks, and that this occurs prior to formation of the final disk. Brook et al. (2012a) obtained a lower mass late-type disk galaxy which has a bulge that grows from $z = 1$ mainly through purely secular processes. Other authors have put more emphasis on metal enrichment. For example, Rahimi et al. (2010) run a fully cosmological simulation with the `GCD+` code (Kawata & Gibson 2003), which incorporates chemical enrichment both by SNe Ia (Iwamoto et al. 1999; Kobayashi et al. 2000) and SNe II (Woosley & Weaver 1995), as well as mass loss from intermediate mass stars. The code does not include a mechanism to diffuse

metals between gas particles, resulting in an artificially high spread in the metallicity distributions, but robust averages. Their results underline the importance of mergers in bulge formation and their possible kinematic implications, the dependence of metal content on age, and the existence of accreted stars within the bulge.

Thus it would appear that a variety of conclusions are being drawn from different groups using different codes and different physical models for their galaxy formation simulations. By analyzing in a unified manner (measuring the relevant properties with the same pipeline) simulated disk galaxies that are run with different codes and different physical prescriptions and merger histories, we hope to shed light on what processes of bulge formation, and subsequent bulge properties, are common within such simulations. Specifically, we analyze the bulges of three of the more massive galaxies presented in Doménech-Moral et al. (2012), run with the `P-DEVA` (Serna et al. 2003; Martínez-Serrano et al. 2008) code, and those of two `GASOLINE` galaxies described in Brook et al. (2012a) and Stinson et al. (2012), with the aim of deciphering the patterns of bulge formation by focusing in the properties of their stellar populations.

Doménech-Moral et al. (2012) analyze disk formation in a cosmological context by running zoom simulations with `P-DEVA`. This code (Martínez-Serrano et al. 2008) incorporates a statistical implementation of chemical enrichment based on Talbot & Arnett (1973), including chemical feedback both by SNe Ia and SNe II, as well as mass loss from intermediate mass stars, involving 11 elements. Radiative cooling takes into consideration the full element distribution at each point and time through a particular implementation of the Dimension Reduction regression (Weisberg 2002), while a SPH metal diffusion term mimics turbulent effects (Monaghan 2005). They have produced disk systems whose different components (thin and thick disk, halo, bulge) have properties nicely consistent with observations, for example, they have g-band B/T ratios between 0.13 and 0.36. In particular, bulge metallicity and [α/Fe] distributions show bimodal patterns, that they interpret as resulting from fast and slow modes of star formation. The simulations run with `P-DEVA` assume that supernova feedback works on sub-grid scales and results in a low star formation efficiency, which is thus used as an input parameter (see discussion in Agertz et al. 2011) that implicitly mimics the energetic feedback.

On the other hand, the simulations run with the `GASOLINE` code have explicit feedback from massive stars which drives large scale outflows. The two particular `GASOLINE` simulations were chosen for this study because (i) G-1578411 was shown to have a bulge which is mostly formed after the merger epoch. It is the late type simulated disk galaxy from Brook et al. (2012a). A

secular bulge grows between $z = 1$ and $z = 0$, driven at least partly by a bar. The final bulge to total light ratio is B/T=0.21. (ii) G-1536 is the simulated L* galaxy run by our MaGICC program that matches the widest range of observed galaxy properties (see Stinson et al. (2012) and SG5LR in Brook et al. (2012b)). It has a B/T ratio of 0.35.

We use this suite of 5 inhomogeneous simulated disk galaxies to analyze the mass-weighted three-dimensional shape, size and kinematics of the bulges, as well as their mass-weighted age, metallicity and chemical composition. More specifically, we first show that the simulated bulges consist of roughly two stellar populations (old and young) whose properties are correlated with their shape, kinematics, metallicity and composition, in line with the observational results we have previously described. In view of this agreement with observations, we investigate the physical processes underlying bulge formation and particularly, their relation with the dynamics of the cosmic-web at high redshift, and of their host galaxies at low zs.

An interesting aspect of this work is to clarify to what extent the formation mechanisms proposed for massive ellipticals also apply to the formation of bulges, as suggested by similarities in observed properties (e.g. Franx 1993; Peletier et al. 1999; Carollo et al. 2001; Bureau 2002; Peletier 2008). In ellipticals the characteristics of mass assembly and star formation rate histories can be interpreted in terms of dark halo dynamics and its consequences. Analytical models as well as N-body simulations show that two different phases can be distinguished along the *halo* mass assembly process (Wechsler et al. 2002; Zhao et al. 2003): i) first a violent fast phase with high mass aggregation rates, resulting from collapse-like and merger events, and ii) later on a slow phase with much lower mass aggregation rates. Small box hydrodynamical simulations (Domínguez-Tenreiro et al. 2006) as well as larger box ones (Oser et al. 2010; Domínguez-Tenreiro et al. 2011) confirmed this scenario as well as its implications on elliptical properties at low z (Cook et al. 2009). This scenario nicely explains apparently paradoxical observational data of elliptical galaxies.

3.2 The simulations

The main properties and resolution of our five simulated galaxies are shown in Table 3.1. All galaxies have previously appeared in the literature, where more details can be garnered. Here we outline the main features of the codes and simulations.

3.2.1 P-DEVA

We use the OpenMP parallel version of the `DEVA` code (Serna et al. 2003), which includes the chemical feedback and cooling methods described in Martínez-Serrano et al. (2008), and in which the conservation laws (e.g. momentum, energy, angular momentum and entropy) hold accurately (Serna et al. 2003). Full details of the recipes used are found in Doménech-Moral et al. (2012) where the simulations are first presented. The star formation recipe follows a Kennincutt – Schmidt-like law with a given density threshold, ρ_*, and star formation efficiency c_*. In line with Agertz et al. (2011), we implement inefficient SF parameters (see Table 3.1), which implicitly account for the regulation of star formation by feedback energy processes by mimicking their effects, which are assumed to work on sub-grid scales.

The chemical evolution implementation (Martínez-Serrano et al. 2008) accounts for the dependence of radiative cooling on the detailed metal composition of the gas, by means of a fast algorithm based on a metallicity parameter, $\zeta(T)$. The code also tracks the full dependence of metal production on the detailed chemical composition of stellar particles (Talbot & Arnett 1973), through a Q_{ij} formalism implementation of the stellar yields, for the first time in SPH. The delayed gas restitution from stars has been implemented through a probabilistic approach, that reduces statistical noise when compared with previous approaches, and therefore allows for a fair description of element enrichment at a lower computational cost. Moreover, the metals are diffused in such a way as to mimic the turbulent mixing in the interstellar medium.

The simulations use the cosmological "zoom-in" technique, with high-resolution gas and dark matter in the region of the main object. The cosmological parameters of a ΛCDM model were assumed ($\Omega_\Lambda = 0.723$, $\Omega_m = 0.277$, $\Omega_b = 0.04$, and $h = 0.7$), in a 10 Mpc per side periodic box. Stellar masses are distributed according to the Salpeter initial mass function (IMF) (Salpeter 1955), with a mass range of $[M_l,M_u]=[0.1,100]M_\odot$.

3.2.2 GASOLINE

The `GASOLINE` galaxies are cosmological zoom simulations derived from the McMaster Unbiased Galaxy Simulations (MUGS, Stinson et al. 2010). In G-1578411, the initial conditions (ICs) are scaled down, so that rather than residing in a 68 h^{-1} Mpc cube, it is inside a cube with 34 h^{-1} Mpc sides, while G-1536 uses the same ICs as in the MUGS runs.

When gas becomes cool ($T < 15000$ K) and dense ($n_{th} > 9.3$ cm^{-3}), it is converted to stars

Object	δM_{bar} $10^5 M_\odot$	h_{soft} h^{-1}kpc	ρ_* cm^{-3}	c_* %	IMF	r_{bulge} kpc	M_* $10^{10} M_\odot$	M_{gas} $10^8 M_\odot$	L_{box} Mpc
G-1578411	0.2	0.15	9.4	1.7	Kroupa93	1.30	0.83	1.64	34
G-1536	1.9	0.15	9.4	3.3	Chab03	2.10	0.96	5.92	68
HD-5004A	3.94	0.2	6	1.0	Salp55	1.00	1.50	3.67	10
HD-5004B	3.94	0.2	10	0.8	Salp55	1.55	1.60	5.33	10
HD-5103B	3.78	0.2	12	0.8	Salp55	1.73	1.47	4.61	10

Table 3.1: The initial mass of gas particles (δM_{bar}), minimum SPH smoothing length (h_{soft}), density threshold (ρ_*), star formation efficiency (c_*), initial mass function (IMF), bulge radius (r_{bulge}), stellar (M_*) and gas (M_{gas}) mass of the simulated bulges (at $z = 0$), and periodic box length (L_{box}). The mass values correspond to the position selection. The `P-DEVA` runs use a fixed mass for the baryonic particles, equal to δM_{bar}. For the two GASOLINE galaxies, G-1578411 and G-1536, a value of 10^{51}erg was assumed for the SN feedback (E_{SN}). The face–on and edge-on projections of both stellar and gas mass densities for all five galaxies are given in Figure 3.11 of the Appendix 3.9.

according to a Kennincutt – Schmidt-like law with the star formation rate $\propto \rho^{1.5}$. Effective star formation rates are determined by the combination and interplay of $c_\star$ and feedback, $c_\star$ is ultimately the free parameter that sets the balance of the baryon cycle off cooling gas, star formation, and gas heating. Stars feed energy back into surrounding gas. Supernova feedback is implemented using the blastwave formalism (Stinson et al. 2006) and deposits 10^{51} erg of energy into the surrounding medium at the end of the stellar lifetime of every star more massive than $8\,M_\odot$. Energy feedback from massive stars prior to their explosion as supernovae has also been included. Without the ability to resolve the details, we employ a relatively crude thermal implementation of radiation feedback from massive stars, with the aim being to mimic their most important effects on scales that we resolve, i.e. to regulate star formation, enhance inhomogeneity, and to allow the expansion of the SNe driven super-bubbles which drive outflows. To mimic the weak coupling of this energy to the surrounding gas (Freyer et al. 2006), we inject pure thermal energy feedback, which is highly inefficient in these types of simulations (Katz 1992; Kay et al. 2002). We inject 10% of the available energy during this early stage of massive star evolution, but 90% is rapidly radiated away, making an effective coupling of the order of 1%.

The two simulations have different initial mass functions, with G-1536 having a factor of ~ 2

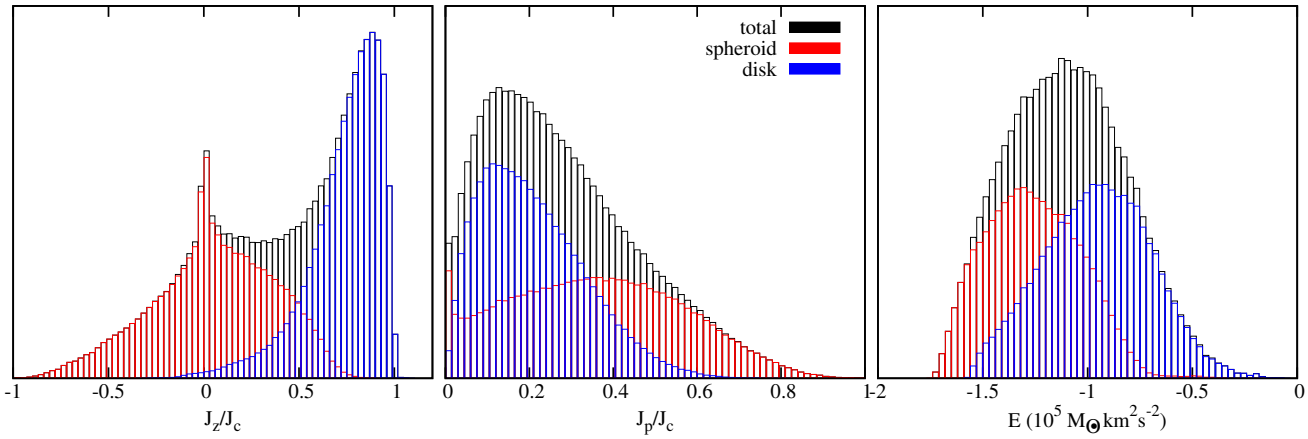

Figure 3.1: The J_z/J_c (left), J_p/J_c (center) and E (right) histograms for the galaxy G-1536. The spheroid and disk contributions, as derived with the clustering algorithm are given in red and blue, respectively. The histograms considering all the galaxy stellar particles are given in black.

more massive stars (Chabrier 2003) than G-1578411 (Kroupa et al. 1993), meaning that G-1536 is less efficient at turning baryons into stars.

Ejected mass and metals are distributed to the nearest neighbor gas particles using the smoothing kernel (Stinson et al. 2006). Literature yields for SNII (Woosley & Weaver 1995) and SNIa (Nomoto et al. 1997) are used. Metal are diffused by treating unresolved turbulent mixing as a shear-dependent diffusion term (Shen et al. 2010), allowing proximate gas particles to mix their metals. Metal cooling is calculated based on the diffused metals.

3.3 Bulge selection criteria

The classical method of separating the contribution of the inner region from the disk rests on fitting the light radial profile of the spiral galaxy with two (or more) components (e.g. exponential disk + a Sérsic profile). However, this method does not provide any way in which individual stellar particles can be assigned to the inferred galaxy components. Therefore we make a kinematic separation of bulge and disk stars using clustering algorithms. For each star particle we computed J_p, the angular momentum in the plane of the disk, J_z, the angular momentum perpendicular to the disk, and J_c, the angular momentum of a particle with the same binding energy (E), moving in a circular orbit at the same radius. Each stellar particle within the virial radius is then dynamically defined by three variables: J_z/J_c , J_p/J_c, and binding energy (E). These variables are normalized to [0,1] in order to

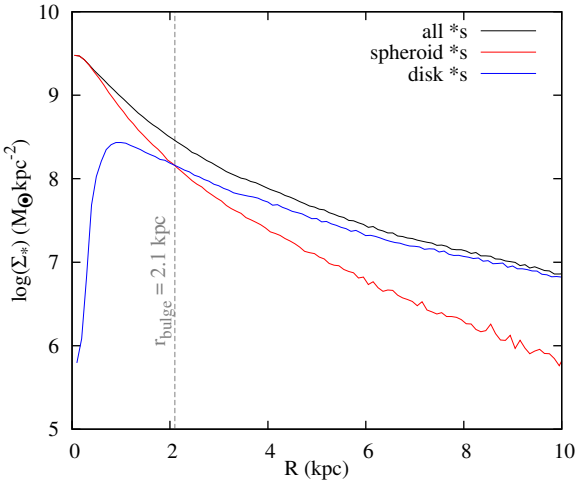

Figure 3.2: The projected stellar mass density for the kinematic disk (blue curve) and spheroid (red curve), and all stellar particles (black curve) of galaxy G-1536. The grey dashed line gives the position of the radial cut used to define the bulge region.

give equal weight to all variables, and then fed to the clustering algorithm, which requires as prior only the number of clusters (we chose *n=2* for bulge + disk). The normalization assumes a linear mapping between [X_{min},X_{max}] and [0,1] (with J_z/J_c, J_p/J_c and E as X), which is appropriate if the histogram of X does not have extremely extended tails. We considered the distance in the phase space to be the Euclidean one. The algorithm, starting from an initial random partitioning into n clusters, iteratively searches for the partitioning which would minimize the intracluster distance. In Figure 3.1 we show the output of the clustering algorithm in the form of the histograms of J_z/J_c, J_p/J_c and E for disk, spheroid and galaxy stars in the case of G-1536. As expected, the spheroid stars peak at $J_z/J_c = 0$ in accordance with a system sustained by velocity dispersion, while the disk ones peak closer to $J_z/J_c = 1$. In the J_p/J_c histrograms the disk shows a peak at ~ 0.1, characteristic of a system whose particles move little perpendicular to the disk plane, although some of them can have an important vertical motion which shows up as the tail extending to $J_p/J_c \sim 0.6$. In Figure 3.13 in the appendix to this chapter we show the results of the clustering for the same galaxy in form of 2D histograms.

Once the dynamical decomposition has been done, the projected stellar mass density profiles of the disk (thin plus thick) and spheroid naturally provide us with the radial cut necessary to delimit the bulge, in the form of the radius, r_{bulge}, where the two intersect. Within this cut the mass contribution of the disk stars is much smaller than the spheroid, therefore minimizing

the contamination from disk stars when determining the bulge global properties. An example of projected stellar mass density for the disk, spheroid and galaxy stellar particles is given in Figure 3.2 for G-1536, as well as the position of the radial cut we use to define the bulge region.

Although a dynamical separation of galaxy components is of great help in analysis of galaxy structure formation, from an observational point of view the different dynamical components of the central galactic regions are usually hard to disentangle. For this reason, we also use an observationally based selection for the bulge stars, in the form of a simple radial cut at r_{bulge}.

Summing up, we use two bulge selection criteria: i) the stars within an sphere of radius r_{bulge}, hereafter position selection, and ii) the stars within an sphere of radius r_{bulge} that at the same time belong to the galaxy spheroid according to the kinematic-decomposition, hereafter kinematic selection. In Table 3.1 we give r_{bulge}, the total stellar and gas mass of each bulge at $z = 0$, as well as the mass resolution for each simulation.

3.4 Bulge populations

To analyze the bulge stellar populations and their link with dynamical processes, we constructed Figure 3.3, in which both the star formation rate (SFR) histories of the bulge and the galaxy mass aggregation tracks (MATs) have been drawn. The MATs each give the evolution of mass inside a fix radius (right axis in each panel). Virial radii have been calculated based upon the Bryan & Norman (1998) fitting function to determine the over-density threshold. For the baryonic component, radii are binned in equally spaced steps in a logarithmic scale. On the right (left) panels the colored curves show the stellar (stellar plus cold gas) masses within the respective radii as a function of the Universe age (t_U is the Universe age at $z = 0$) and redshift. MATs corresponding to radii within r_{bulge} are drawn with different colors, while those at larger radii are given in cyan.

Major mergers ($M_{secondary}/M_{main} > 0.25$), minor mergers and slow accretion processes in the dark matter or baryonic component can be clearly identified as big or small mass jumps in the MATs, or as continuous mass increments, respectively (note the different mass scales on the right axes for the `P-DEVA` and `GASOLINE` galaxies). Two different phases are reflected in the noticeable knee-like shape of the MATs in all objects shown in Figure 3.3: an initial phase where the mass assembly rate is high, and then a much slower phase, when mass is more slowly acquired.

Superimposed on the same figure are the bulge SFR histories (left axis in each panel), for both position and kinematic selected bulge populations. All objects present starbursts at large redshifts,

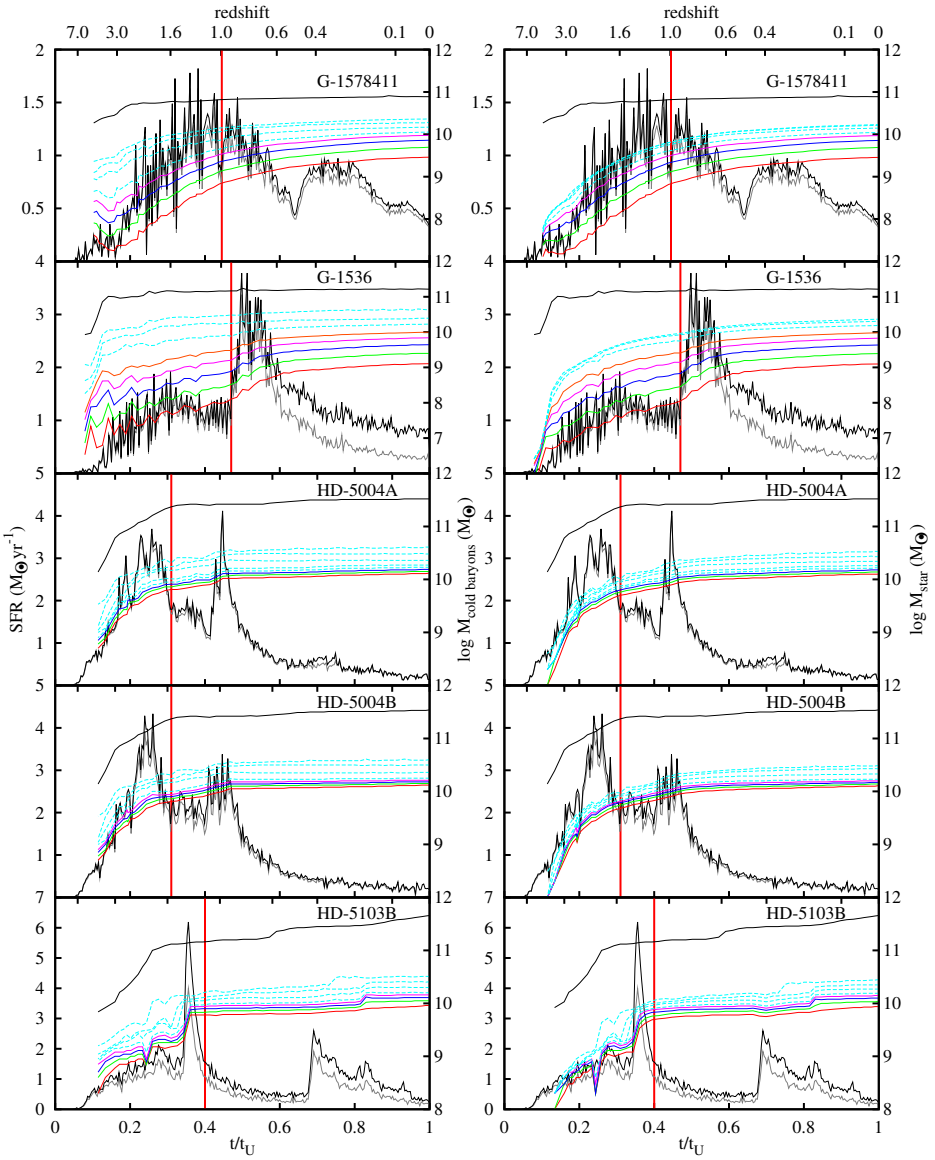

Figure 3.3: Bulge star formation rate comparisons for kinematic (solid gray) and position (solid black) selected bulge stars with sizes given by r_{bulge}. The position of the thick red vertical (values in Table 3.2) indicate the separation between the old and young stellar populations. The colored lines represent the mass aggregation tracks (MATs) of cold baryons (left) and stars (right) along the main branch of the merger tree for each object, the masses being computed inside fixed radii of 0.50, 0.72, 1.03, 1.47, 2.10, 4.30, 8.80 and 25.80 kpc from bottom to top. The upper solid black line is the total mass inside the virial radius (virial mass), the solid curves in red, green, blue, magenta and orange correspond to radii roughly within the bulge, while the dashed cyan ones correspond to radii exceeding r_{bulge} (see Table 3.1).

peaking between $z = 3$ and $z = 1$, where significant *substructure* is also apparent in many cases. These early star formation peaks are expected when the primordial gas suffers a violent collapse and are correlated with the knee-like feature visible in their corresponding MATs. The high redshift SF peak is a direct consequence of the first phase of mass assembly. The simulations also show later peaks in star formation that are related to merger/accretion events.

At lower redshifts a variety of processes appear imprinted in the SFR histories: during quiescent periods, the SFR decays to an approximately constant tail at the same time as the MATs get flattened. The low tails present in all SFR histories correspond to periods of mass assembly where only minor mergers or gas accretion at slow rates show up in the MATs. All simulation also show secondary jumps in SFRs, associated with later merger events. These vary in time, and in size relative to the initial starbursts, for example HD-5103B has a relatively late (t/t_U) accretion event that shows up in the total mass MAT (black line) as well as the build up of bulge mass and the star formation rate.

Some qualitative differences are apparent in the two `GASOLINE` runs compared to the `P-DEVA` ones. The initial starbursts associated with the fast phase of mass accretion are less peaked in the former, due to the affects of feedback. In G-1578411, which has the lower mass but also lower feedback of the two `GASOLINE` simulations, the initial starburst has a longer duration than the other simulations, while in G-1536 the initial starburst in the bulge region is more suppressed relative to the overall star formation within the bulge, due to the more efficient feedback in this simulation. Also, due to energetic feedback, the MATs of G-1578411 and G-1536 show delayed baryon mass assembly relative to their halos collapse at high zs. As a result, these objects have low central baryonic mass density, the effect being more marked at high-z.

Regardless of these specific differences, the correlations between MATs and SFR histories suggest that a meaningful stellar age classification can be based upon the two phases showing up in the MATs. Therefore we classify as old bulge stellar population the stars formed as a direct consequence of the fast phase (with formation times smaller than the temporal cut drawn in thick red in Figure 3.3), while the stars formed later on we globally denote by young bulge stellar populations. In a quantitative sense, the temporal cuts correspond to the time from which the second derivative of the MAT(r_{bulge}) becomes flat, reflecting a transition from a fast clumpy mass assembly to a slow smooth regime, without considering the MAT variations induced by low redshift mergers, like in the case of HD-5103B. Further information on how the cut–off was defined is given Section 3.9, where we also show the MAT and its derivatives for the galaxy G-157811 (see Figure 3.14). The

Object	t_{cut}/t_U	z_{cut}	M_{old*}/M_*	n_{old}	n_{young}	n_{total}
G-1578411	0.45	0.98	0.39	1.17	1.07	1.22
G-1536	0.47	0.90	0.31	1.19	1.59	1.39
HD-5004A	0.31	1.54	0.43	2.95	2.09	2.57
HD-5004B	0.31	1.54	0.42	3.96	3.38	3.23
HD-5103B	0.40	1.12	0.50	3.49	3.27	3.68

Table 3.2: The temporal separation between the distinct star formation episodes for the simulated bulges,the corresponding mass percentage of old and young stars in the position-selection, and the Sérsic indices derived from fitting the projected stellar mass density of old and young (according to the bulge temporal cut), and of all galaxy stellar particles.

values of the temporal cuts, t_{cut}, for all bulges are given in Table 3.2, together with the mass weight of the old population.

3.5 3D shapes, sizes and kinematics

To quantify the shape of the bulges, as well that of the old and young bulges as defined above, we show the correlations between the axis ratios of each ellipsoid of inertia in Figure 3.4. The inertia tensor was computed following González-García & van Albada (2005), and subsequently diagonalized. Next, the eigenvalues ($\lambda_1 > \lambda_2 > \lambda_3$) were used to compute the length of the principal axis a $\geqslant$ b $\geqslant$ c. Red and blue represent the old and young bulge, while black gives the average over the whole object. Filled and empty symbols correspond to the objects in the position and kinematic selection, respectively.

The objects situated on the dashed black line in Figure 3.4 have $b = c$, while the dashed-dotted gray curves denoted by $T = 0.3$ and $T = 0.7$, respectively, separate the oblate objects from the triaxial and the prolate ones according to the T parameter introduced by de Zeeuw & Franx (1991) with the definition $T = (1 - (b/a)^2)/(1 - (c/a)^2)$. The oblate objects correspond to $c/a < 0.9$ and $T < 0.3$, the prolate to $c/a < 0.9$ and $T > 0.7$, and the rest to triaxial ones. In this perspective, we observe that both complete bulges as well as their distinct components are all oblate with the exception of the secular bulge of G-1578411 which is triaxial regardless of the selection criteria. Old and young populations are clearly segregated, either in the position or in the kinematic selections, and more separated in c/a than in b/a. Old populations are more spheroid-like, while the young

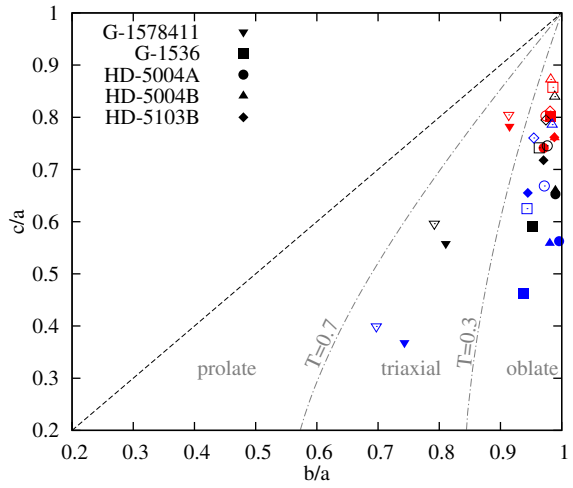

Figure 3.4: The axis ratios of the five spheroids. Red and blue represent the old and young bulge, while black gives the average over the whole object. Filled and empty symbols correspond to the objects in the position and kinematic selection, respectively. The dashed-dotted gray curves separate prolate, triaxial and oblate morphologies.

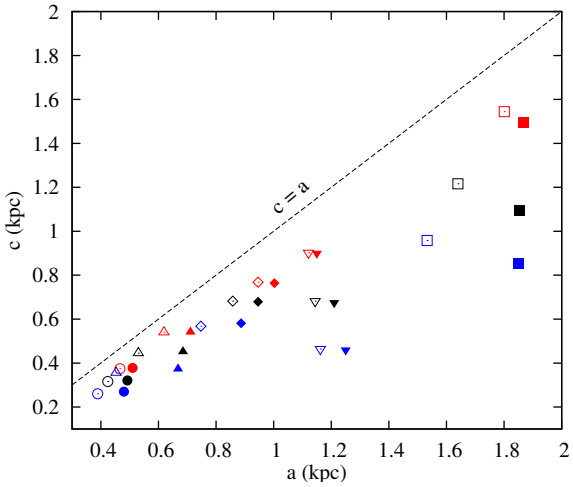

Figure 3.5: Minor vs major semi axis for the five spheroids. Red and blue represent the old and young bulge, while black gives the average over the whole object. Filled and empty symbols correspond to the objects in the position and kinematic selection, respectively. The dashed line is where c=a. Young bulge populations are smaller than old ones, with the exception of G-1578411.

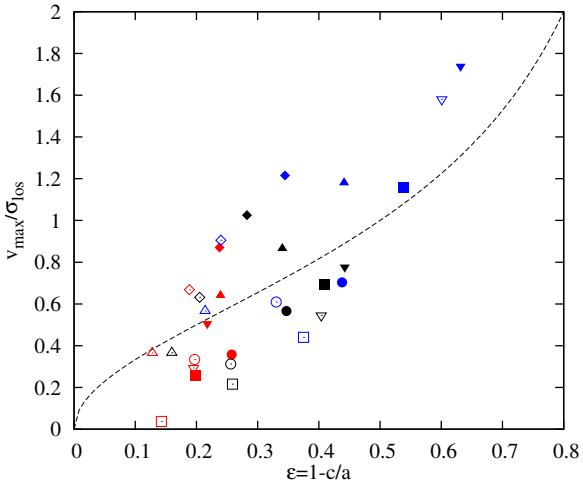

Figure 3.6: Rotational support versus ellipticity. Red and blue represent the old and young bulge, while black gives the average over the whole object. Filled and empty symbols correspond to the objects in the position and kinematic selection, respectively. Young bulges are more rotationally supported and less spherical than the old populations, even when kinematically selected to exclude the disk.

are more oblate, consistent with observations.

Figure 3.5 gives an idea of the sizes of the five bulges by plotting c vs a. In all but one case (the a value of G-1578411), the old bulges have larger sizes (as given by a and even more by c) than the young ones, sustaining the idea that younger stellar populations ocupy a smaller volume than their corresponding old counterparts. In this respect the following inequality holds, irrespective of the selection criteria used: $\sqrt[3]{a_y b_y c_y} < \sqrt[3]{a_t b_t c_t} < \sqrt[3]{a_o b_o c_o}$, where y, t and o stand for young, total and old, respectively. This graph shows a clear sequence, the size increasing from the younger to the older, with the total population in between. Also, as it was proven by the previous graph, the older bulge components are closer to be perfect spheroids (they appear closer to the dashed line for which $c = a$).

The difference between the results obtained using the two selection criteria are only qualitative. Indeed, the trends in shapes and sizes are the same for both selections. The kinematic-selection leads, on average, to bulge components closer to being spherically symmetric than the position selection does. This is an expected result since position selection implies the exclusion of precisely some of the particles encountered in ordered rotation which would otherwise lead to ellipsoids of inertia characteristic of more disk-like objects.

Also, the shape and size trends with stellar age are the same for the `P-DEVA` and `GASOLINE`

bulges. The only difference is that GASOLINE bulges have lower mass concentrations and therefore larger values for a and c, due to energetic feedback.

Let us now turn to the bulges kinematical analysis, including some of their classical or pseudo-bulge properties, therefore using line-of-sight (los) velocities. In order to analyze the rotational support, we align the galaxies with the z-axis perpendicular to the disk. Since the rotational velocity can be best observationally measured in edge-on projection, we consider two lines of sight (along the x- and y-axes), and compute the radial profiles of the velocities – $v_{\rm los=x}(R = y, z)$ and $v_{\rm los=y}(R = x, z)$, respectively – along the two. The dependence of the profiles on the altitude z above the galactic plane is important both when studying whether the bulge or its components are in cylindrical rotation, as well as from the point of view of comparison with observations. In the latter case, data are normally taken, due to the extinction effect in the disk plane, with long-slit or IFUs at altitudes higher than the vertical scale height of the thin disk. Considering all these observational limitations, we constructed the velocity profiles using a z-binning of 0.2 kpc, averaging the curves in the two hemispheres in order to minimize the statistical noise in the slits at higher latitudes where the number of particles is smaller. Complementary to the profiles of rotational velocity, we also constructed the los velocity dispersion radial profiles, $\sigma_{\rm los}(R, z)$, which are approximately flat. Given the flatness of these profiles, we considered the $\sigma_{\rm los}(z)$ as the average of $\sigma_{\rm los=x|y}(R = y \mid x, z)$ over all lines of sight $R = y \mid x$[1], and weighted with the number of particles in each bin n_R. Once the rotational velocity profiles were constructed, we took as $v_{max}(z)$ the weighted average of the profile extremes. Finally, we averaged $v_{max}(z)$ and $\sigma_{\rm los}(z)$ over the two lines of sight, los=x and los=y.

In order to choose a representative z-bin for all bulges, we considered both the disk vertical scale heights as well as the bulge radial extensions. Therefore, we selected the bin with $0.4 <\mid z \mid < 0.6$ kpc. Given this choice, within the current section, v_{max} and $\sigma_{\rm los}$ will refer to this specific slit.

Figure 3.6 plots rotational support, defined as the maximal rotational velocity (v_{max}) divided by the bulge los velocity dispersion ($\sigma_{\rm los}$), as a function of the intrinsic ellipticity $\varepsilon = 1 - c/a$. The dashed black curve in the graph represents oblate-spheroid systems with isotropic velocity dispersion flattened only by rotation (Binney 1978), and is approximately described by $\sqrt{\varepsilon/(1-\varepsilon)}$ (Kormendy 1982).

The results show a clear trend of higher eccentricities and rotational support for the younger populations (blue symbols) as compared to the older ones (red symbols), while the whole bulges, in

[1] $y \mid x$ stands for y or x

black, occupy intermediate positions. It is important to note that these patterns hold irrespective of the code used to run the simulations or the bulge selection criteria, as well as of the slit positioning. Note however that increasing (decreasing) the z slit positioning lowers (increases) the specific values of $v_{max}/\sigma_{\rm los}$ for all the five bulges as well as in their distinct stellar components. Therefore, the bulges appear more classical as we move away from the galactic plane, but always they show same trends with stellar age, with the younger component being more rotationally supported. In all cases, a weighting by light rather than mass will provide increased prominence to the younger pseudo-bulge-like populations. In two cases (HD-5004A and HD-5103B in the dynamical selection), the bulge as a whole has a slightly lower value of $v_{max}/\sigma_{\rm los}$ even than the old population. In these cases, the bulges have velocity dispersions approximately equal to the old components, but have slightly smaller v_{max}. This difference in v_{max} can be explained through misalignments and/or kinematical peculiarities.

Another parameter describing the bulge shape is the Sérsic index (n). Thus, we fitted the projected stellar mass density profiles of our five galaxies with a Sérsic + an exponential disk. The data and the fits are depicted in Figure 3.7, while the Sérsic indices are given in Table 3.2. With the aim of checking whether n varies if considering only the old or only the young stars, we also fitted the two stellar subpopulation of the galaxies, using for the temporal cut the limit defined with respect to the bulge region. It is important to stress, that n values are to a large extent dependent on the amount of feedback. In the case of `GASOLINE` galaxies, the incresed feedback leads to a flattening of the projected stellar mass curves at small radii. For this reason, the Sérsic indices of G-1578411 an G-1536 are < 2 irrespective of considering all galaxy stars or only the corresponding components, while those of HD-5004A, HD-5004B and HD-5103B (simulated without explicit energetic feedback) are > 2. In any case, the difference between n_{old} and n_{young} is small in any of the simulated galaxies, with a slight tendency for the old stars to have larger n than the younger ones, with the exception of G-1536, which was simulated with a considerable amount of feedback. From an observational point of view, no define trend with the band has been detected either, see for example Fisher & Drory (2008), or more recently McDonald et al. (2011). The Sérsic index has been used, together with other parameters like rotational support, to classify bulges. For example, Kormendy & Kennicutt (2004) consider pseudo bulges to have < 2, while classical ones have > 2. In this respect, the three `P-DEVA` galaxies have classical bulges, the old bulges being more classical than the young ones ($n_{old} > n_{young}$). On the other hand, the two `GASOLINE` ones have pseudo bulges according to this classification, and show no definite trend with age. In the

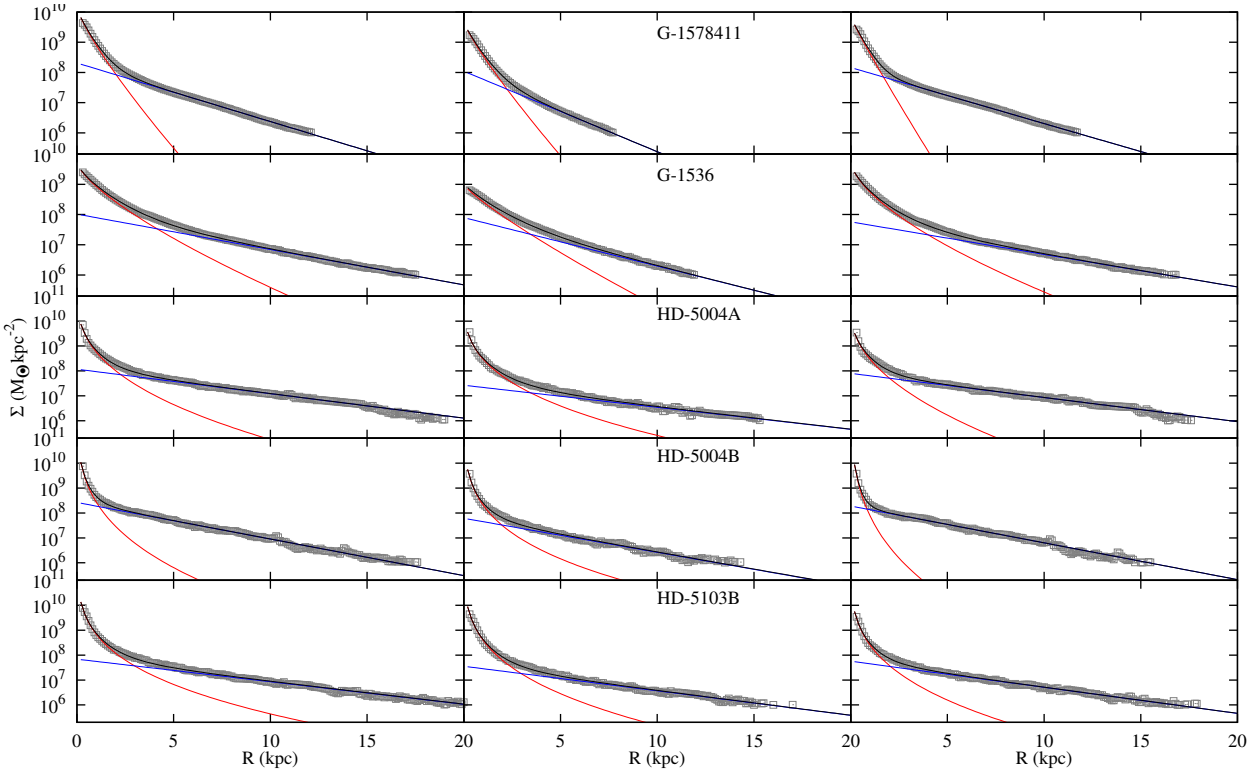

Figure 3.7: The Sérsic + exponential disk fits of the projected mass density of galaxy stars (left panels), and of the corresponding old (central panels) and young (right panels) stellar sub-populations, separated according to the bulge temporal cut in Table 3.2. The color code is: grey open squares for the data, red and blue lines for the Sérsic and exponential disk contributions, and black lines for the total fit.

same perspective, the pseudo bulges of Okamoto (2012), formed at high redshift, roughly during what we define as the fast phase of mass assembly, have < 2. However, his simulations also use energetic feedback which is at least partially responsible for the low values of n. Therefore, we think that further studies are needed in order to disentangle to what extent the n values depend on the particular modes of mass assembly and to what extent on the amount and implementation of the feedback effects. In this respect, our results show that v/σ separates more reliably the young from the old bulge than n, which tends to be similar for old and young stellar populations.

3.6 Ages and abundances

This section concerns the ages and metallicities of the old and young bulge stars at $z = 0$.

Although details differ slightly, in both the `P-DEVA` and `GASOLINE` simulations trace the production and enrichment of chemical elements in broadly the same way. Newly produced elements, as by-products of stellar evolution and death, are released to the surrounding interstellar medium as increments in the metal content of nearby gas particles. Metal diffusion is implemented among gas particles with a diffusion constant, allowing for elements to mix in a given environment, mimicking what happens in a turbulent interstellar medium. Both codes consider the evolution of the following elements: H, He, C, N, O, Ne, Mg, Si, S, Ca and Fe. As we are looking at broad trends here, the relatively small differences in the implementation chemistry between the codes are not critical. As a measure of metallicity we used either [Fe/H] or the average values of these elements; also, we used [Mg/Fe] to follow α-element properties and checked that using [O/Fe] does not change substantially our results. The reference values for the solar metallicities were taken from Grevesse & Sauval (1998).

We analyze the distributions of metallicity and α-element abundances in the different bulge populations. They are plotted in Figure 3.8 (central and right panels), where it can be seen that the abundance distributions of young and old bulge populations are segregated (the old stars have a lower metallicity and a higher [Mg/Fe]), giving in most cases overall two-peak [Fe/H] and [Mg/Fe] distributions. The slightly cleaner separation of two populations in [Mg/Fe] space in the `P-DEVA` simulations as compared to the `GASOLINE` ones might partially be an effect of the energetic feedback in the latter, which delays the SF relatively to dynamical processes (see Figure 3.3 and the corresponding comments in Section 3.4) and enhances the mixing, although the differences in the details of implementation of metal enrichment could also play a role, as well as in the wider

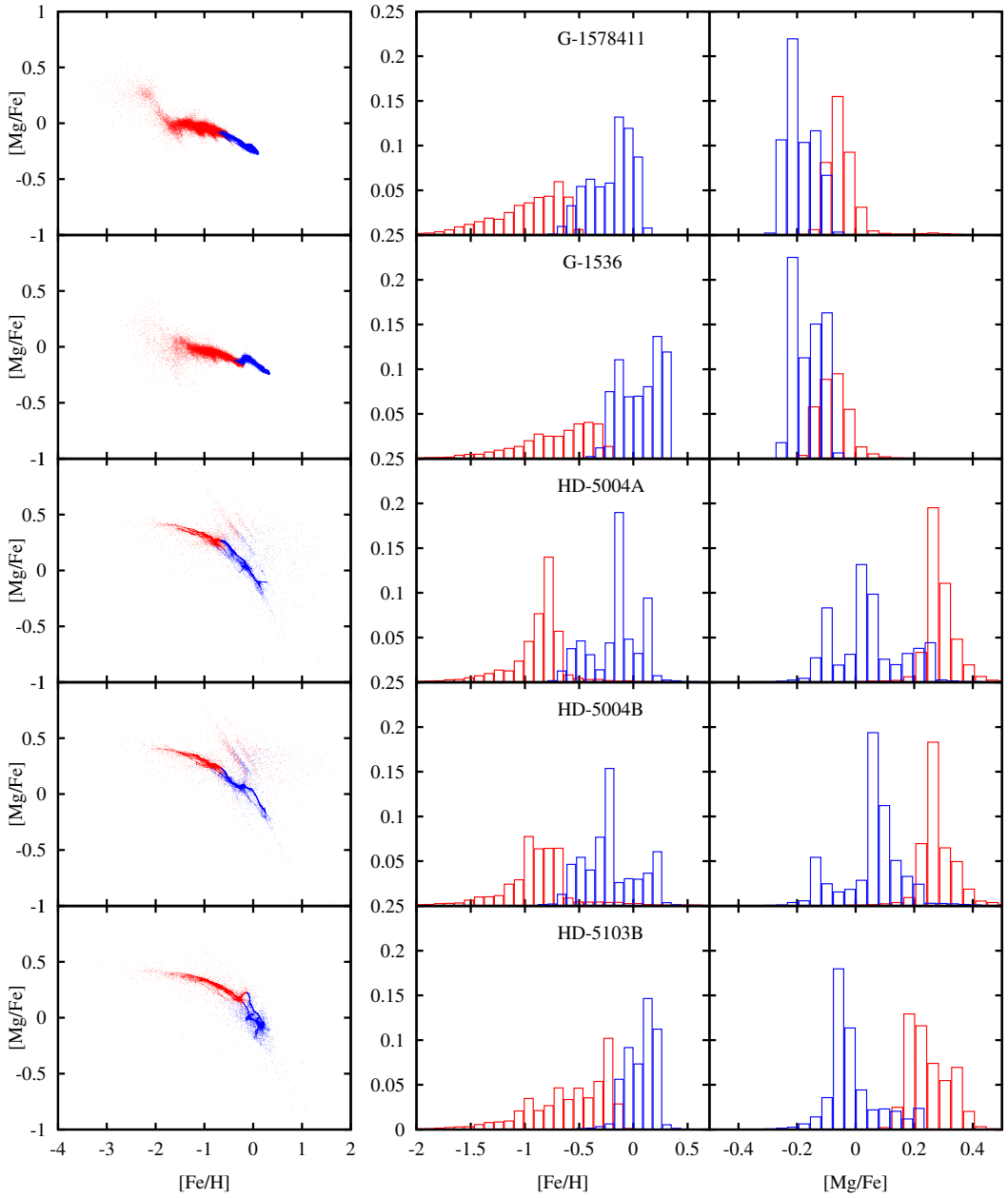

Figure 3.8: [Mg/Fe] vs [Fe/H] (left), and the [Fe/H] (center) and [Mg/Fe] (right) histograms for the simulated bulges. The bin widths for [Fe/H] and [Mg/Fe] are 0.07 and 0.04 dex, respectively. Red and blue represent the old and young bulges.

ranges of [Mg/Fe] of the P-DEVA runs. However, the important point here is that both codes result in broadly the same relative trends in metal abundances and enrichments of their old and young populations.

In this respect, we also plot [Mg/Fe] as a function of [Fe/H] (left panel). Again the young and old populations show up at different loci. A feature to be noted in the graphs [Mg/Fe] versus [Fe/H] are the slopes of the two stellar population types in the sense that the old one has a milder slope, while the young population shows a steeper one. Again, these trends are apparent in all simulations, and what is interesting is that the age selection we have used invariably separate at the "knees" of the abundance trends. This feature has to do with the different nucleosynthetic origin of α and Fe elements, a clean knee-like pattern being expected in stellar populations where the SFR is concentrated in an episode with a very short time-scale followed by an epoch of more quiet star formation. The plateau corresponds to the early stages when SNe II dominate the metal enrichment, followed by a downturn to lower [Mg/Fe] when enough time has elapsed since the high redshift starburst that SNe Ia come into play (see Wyse 1999, and references therein).

These results on the chemical composition of bulge populations agree with recent observations of the Milky Way Bulge, like those of Babusiaux et al. (2010), who found two distinct populations in Baade's Window, one old, metal-poor component with kinematics of a spheroid and a younger, metal-rich one displaying kinematic characteristics similar to a bar. Otherwise, Ness et al. (2012) extended this work by enlarging the number of windows, finding consistent results (see Section 3.1 for more details).

Figure 3.9 gives the averaged metallicities and ages of the distinct stellar populations as functions of the los velocity dispersion. In this case, $\sigma_{\rm los}$ was computed in the same way as in Section 3.5, the only difference being that no z-binning was used. First of all a clear population segregation stands out in both panels, irrespective of the code or the selection criteria employed. In the upper panel, the metallicity appears to be increasing with the velocity dispersion, when considering all five bulges. However, if discarding the G-1578411 bulge (bottom-up triangles), $\langle Z \rangle$ seems to be almost constant with $\sigma_{\rm los}$. On the other hand, if considering only the `P-DEVA` bulges, $\langle Z \rangle$ decreases with $\sigma_{\rm los}$. These trends should be considered with caution, given the inhomogeneity of our sample. In the age – $\sigma_{\rm los}$ plot, the slope is positive, in accordance with the findings of MacArthur et al. (2009). Taking $\sigma_{\rm los}$ as a measure of the objects mass (Binney & Tremaine 1987) (see Table 3.1 for the bulge stellar masses), it can be noted that the more massive objects also have the older average overall populations.

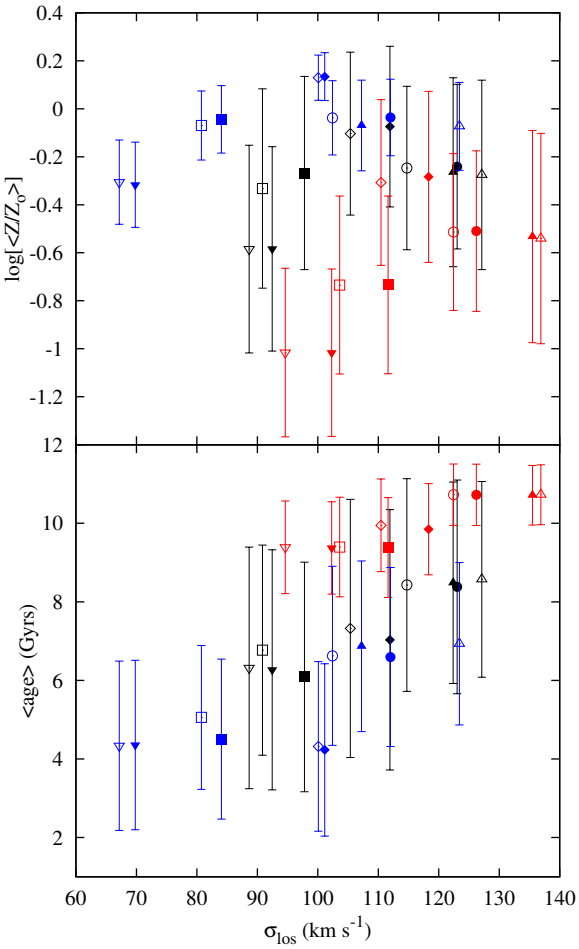

Figure 3.9: Average metallicity (top) and age (bottom) of the distinct bulge components versus los velocity dispersion. Red and blue represent the old and young bulge, while black gives the average over the whole object. Filled and empty symbols correspond to the objects in the position and kinematic selection, respectively.

3.7 Bulges within the Cosmic Web

We trace the evolution of particles in the bulge at low $z_{low} = 0$ to their origins at $z_{in} = 10$, following them at 60 different redshifts in between. In Figure 3.10 we plot the evolution of the baryons that form the bulge stars of HD-5004A at $z = 0$ (left and central graphs) at four zs (top to bottom) representing relevant consecutive events in this bulge formation, as well as the object's surroundings (right graphs) at each redshift[2]. In the other simulations this sequence of evolution is similar enough that we can use this as a representative example. The left sequence aims at illustrating the differences in the space configurations that old $z = 0$ bulge-to-be stars (red points) form along their evolution as compared to those of young $z = 0$ bulge-to-be stars (blue). The emphasis here is on the two population types, irrespective whether they are gas or stars at the Universe age corresponding to the plot. The central sequence takes into consideration the bulge-to-be stellar particle properties at the zs plotted, namely points are green for cold gaseous particles ($T(z) < 10^6 K$), black for hot ones ($T(z) > 10^6 K$), and red and blue for stellar particles, depending on their time of birth according to Table 3.2. Its aim is to illustrate the differences in the birthplaces of the two bulge stellar populations relative either to the cosmic-web (at high zs) or to the protogalaxy components (at lower zs), as well as their evolution towards their final configuration at $z = 0$. Finally, in the right panels all the particles in the same volumes are shown, and with the same color code as in the central one, in order to compare the dynamical processes of the bulge-to-be stellar particles with those of the surroundings mass elements causing them.

We first analyze the sequence of bulge formation events in terms of the cosmic-web element dynamics (central panels). Before $z = 3.5$ mass piles up in caustics [3], where already some nodes show up. At this redshift, star formation is already triggered in the densest of these nodes at *separated places*. Comparing the two upper snapshots in any of the vertical sequences, we see that an overall collapse-like event acts in between onto a structured net of cells as a contractive deformation. It somehow erases the cell structure, joining together clumps mainly along filaments, and therefore only very low relative angular momentum is involved at these zs. The collapse-

[2] As Figure 3.3 shows, the first snapshot at $t/t_U = 0.13$ gives us the configuration of the bulge-to-be stars at the very beginning of the collapse-like event; the second one at $t/t_U = 0.28$ roughly corresponds at the end of the fast phase; the third one at $t/t_U = 0.38$ is just before the beginning of the major merger causing the strong stellar burst in the slow phase, and finally the fourth one at $t/t_U = 0.59$ corresponds to the end of this burst.

[3] Caustics are the elements of the cellular structure where dense mass elements show up at high zs. They are classified into walls, filaments and nodes, and, at a given scale, these represent a temporal sequence of mass piling up. See Shandarin & Zeldovich (1989) and Domínguez-Tenreiro et al. (2011) for more details.

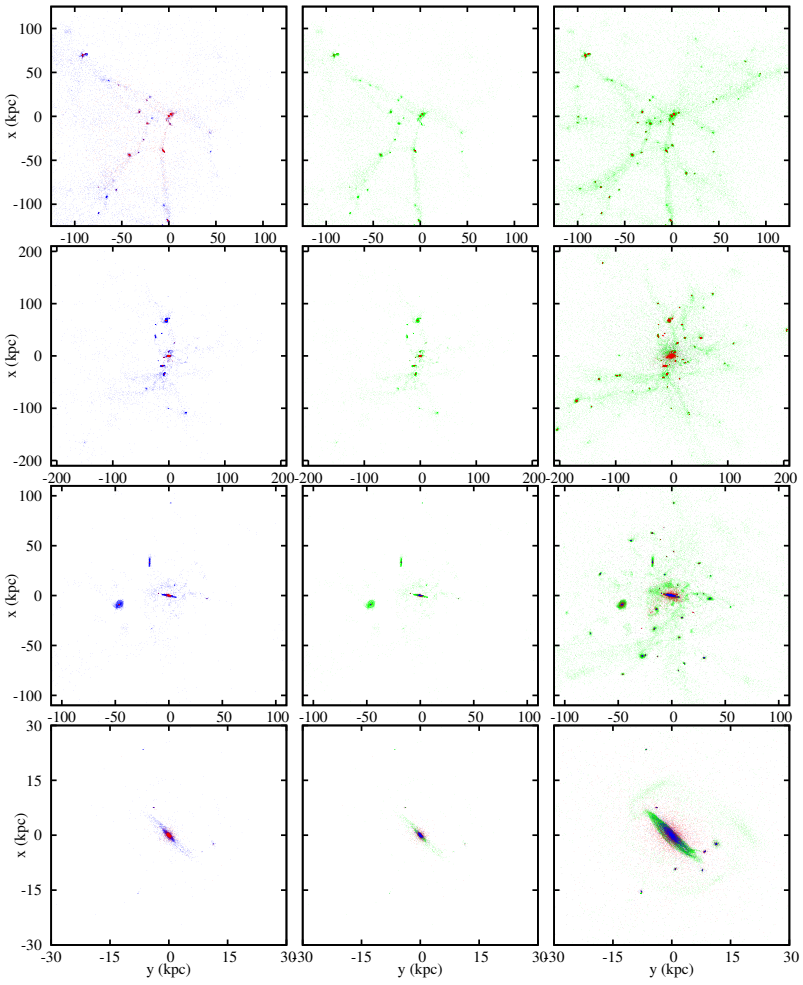

Figure 3.10: The different components of the bulge HD-5004A (left and central panels) and its surroundings (right panels) at redshifts 3.50, 1.75, 1.21 & 0.58 (t/t_U of 0.13, 0.28, 0.38 & 0.59), from top to bottom. The left panels give the positions of the bulge stellar particles identified at $z = 0$ when traced back to each of the four zs. Red corresponds to baryon particles (either gas or stars) whose transformation into stars occurs along the fast phase of bulge formation (i.e., at $t_{\rm form}/t_U < 0.31$, or equivalently, $z > 1.54$ in this particular case), and blue to bulge baryon particles that become stars at later times. The same traced back positions are given in the central panels, but in this case with a color code representing particles properties *at the zs plotted*, namely green for cold gaseous particles ($T < 10^6$K), black for the hot ones, and red and blue for the stellar particles according to their time of birth (older and respectively younger than $z = 1.54$). The right panels show the positions of all baryonic particles within a limiting radius of the galaxy's progenitor center using the same colors as in the central graphs.

like event shrinks the volume visualized at $z = 3.5$ into that at $z = 1.75$, where a central mass concentration fed by filaments stands out. Gas keeps on flowing through filaments towards the central regions between snapshots two and three. A diffuse component (i.e., outside caustics) is also evident at high z. This diffuse component tends to flow into caustics, therefore vanishing as evolution proceeds. Otherwise, by $z = 1.21$ the filaments have practically been removed in favor of clumps and some cold gas in irregular structures. Moreover, two small gaseous disk-like structures and a third central disk with a stellar component, seen edge-on, have formed in the interval between the second and third snapshots. At $z = 1.21$, the stars are at the center of these disks, or at the center of other smaller gaseous structures. The young-to-be bulge stars begin to show up (blue points). Finally, after a major merger occurring between the third and fourth snapshots, by $z = 0.58$ practically all the baryonic particles that are to form the HD-5004A bulge stars at $z = 0$ come to be bound in a unique system (except for some small clumps). Most of the particles that have transformed into stars (red and blue at the central sequence) are at the center, while those that are still gaseous (in green) show up in a rebuilt disk-like configuration. This configuration disappears later on, and by $z = 0.35$ (not shown in Figure 3.10) practically all the bulge particles are at their place within a sphere of radius r_{bulge}.

It is very useful to compare these evolutionary processes with the mass distribution of their surroundings visualized in the right graphs of Figure 3.10. This comparison makes it even clearer that bulge material has been involved in caustic formation at high z although part of it remains as diffuse gas quite a while. Interestingly, a fraction of it has formed transient gaseous disks or has been a part of the former disk of the HD-5004A object.

We now analyze the differences in the assembly patterns of the young and old bulge stellar populations relative to the cosmic-web dynamics (left graphs in Figure 3.10). Most mass elements identified at $z = 0$ as old stellar particles (red points) are already concentrated in caustics by $z = 3.5$. These are the densest regions at this time. In contrast, an important fraction of the mass elements identified at $z = 0$ as young stellar particles (blue points) are not yet involved in caustics. The difference increases as evolution proceeds. In fact, the strong contractive deformation acting between the first and second snapshots involves preferentially the old-stellar-to-be particles, in such a way that by $z = 1.75$ the old component has a very small volume, while the young component still spans a scale of ~ 200 kpc and has an important diffuse gas fraction (with some nodes formed at local contractions as well). In the third snapshot we see that a fraction of the mass elements that are to form young stars now shows disk-like patterns, while old stars are at the centers of

these small disks. These disk-like configurations provide a key to explain the different kinematic properties of young bulge populations as compared to old ones, because of the angular momentum content of the former. As said above, the disks seen in the third snapshots merge. This causes their central old stars to form a unique bulge-like structure. At the same time, new stars – belonging to the young bulge – form and appear within it. On its turn, the young component, partially still as diffuse gas, forms structures (i.e. a disk in the case of HD-5004A as it can be seen in Figure 3.10) around the old stars spheroid. Some of the small nodes remain as satellites, carrying a small bit of old population at their centers. Finally, by $z = 0.35$ (not shown in Figure 3.10), both the old and young bulge populations (or the gaseous particles to form the latter) are bound to their respective central spheroids, where they remain until $z = 0$.

This evolutionary track shows similarities with massive ellipticals Domínguez-Tenreiro et al. (2011). In this case, stellar particles at $z = 0$ exhibit a gaseous web-like morphology at $z \sim 3.5 \div 6$, with scales of ~ 1 physical Mpc. The densest mass elements of this gaseous web, dynamically organized as attraction basins for mass flows, have already turned into stars by $z \sim 6$. At high z these basins undergo fast contractive deformations which violently shrinks them in quasi-radial directions, therefore involving very low angular momentum. They can be described as collapse events with very complex geometries, causing high rates of dissipation and stellar formation out of the available gas, most of if it being transformed into stars at the end of this process. Afterwards, during the second phase, the mass assembly rate is much lower and is characterized by mergers involving significantly larger amounts of angular momentum.

To sum up, the old and young populations of the bulge HD-5004A are not only segregated in their z=0 properties, but also show quite different assembly patterns in terms of the cosmic-web dynamics. Overall, this scenario also holds for the other four bulges. Indeed, most of the old stars formed at disjoint places within attraction basins during the early fast processes, and undergo an important assembly episode later on, through multiclump collapse-like events shrinking these basins in quasi-radial directions. This assembly phase results in a relative low angular momentum of the merging clumps.

The ancestors of young bulge stars, on their turn, in many cases have been part of disk structures before arriving to the galaxy central regions. Different destabilizing processes can be responsible for this inward material transport, such as mergers or secular processes in the disks. Young bulge stars keep partial dynamical memory of their angular momentum content. These differences in the assembly patterns relative to the angular momentum involved, would be a key piece in explaining

the segregated properties of the two bulge components. Although our sample is small, the mass weight of the old component varies between 31 and 50%. An even more important variation of this weight, together with the different inward mass transport mechanisms in the second assembly phase, could explain the important dispersion in bulge properties.

3.8 Summary and conclusions

We have analyzed the bulges of an inhomogeneous suite of five spiral galaxies emerging from high resolution hydrodynamical simulations in a cosmological context. Our aim is to decipher the underlying physical processes in bulge assembly that could be responsible for their observed properties, focusing on relevant structural, kinematical and chemical properties of their stellar populations and paying particular attention to their observationally suggested segregation by age.

Concerning the problem of bulge formation, the main particularity of this work is that we analyze simulated disk galaxies that are run with different codes (including different sub-grid physical prescriptions) where the chemical evolution has been carefully implemented, by using a common pipeline to measure the relevant stellar population properties. The simulations have been run with `P-DEVA` and `GASOLINE`. Feedback from massive stars is implemented explicitly in the two `GASOLINE` simulations through the blast-wave formulation (Stinson et al. 2006), while in `P-DEVA` simulations the effects of discrete energy injection are assumed to be on subgrid scales, resulting in the low star formation efficiency which is assumed to mimic them (see discussion in Agertz et al. 2011).

Although details differ slightly, both `P-DEVA` and `GASOLINE` simulations trace the production and enrichment of chemical elements in broadly the same way. The newly formed elements, as by-products of stellar evolution and death, are released to the surrounding interstellar medium as increments in the metal content of nearby gas particles. The metals are diffused among gas particles, allowing the elements to get mixed and therefore, mimicking the turbulent interstellar medium. Both codes consider the evolution of 11 elements. As we are looking for broad trends here, the relatively small differences in the implementation chemistry between the codes is not critical.

We have studied in detail the mass-averaged three-dimensional sizes, shapes and kinematics, as well as stellar ages and element compositions of these five bulges. This is an intrinsic approach as opposed to looking for quantities closer to observations (i.e., light-averaged). We keep as this level because our aim is to find out the patterns of bulge mass assembly by focusing on their stellar population properties.

We have found a satisfactory qualitative agreement with the latest observational data for the Milky Way as well as for other external bulges (see Section 3.1). Our results indicate that bulges in our sample have an old stellar population, formed at high z at disjoint places within attraction basins, and joined together through their rapid quasi-radial multiclump collapse, where the relative angular momentum of the collapsing/merging clumps is low. A second phase follows, with lower mass assembly and star formation rates, but with higher angular momenta. This phase shows a variety of assembly patterns: i) only minor mergers without further significant SF bursts but a SF tail, ii) major mergers with secondary SF bursts, as the galaxy HD-5004A shows in Figures 3.3 and 3.10, and/or iii) secular evolution of the galactic disk, as is the case for G-1578411, which was shown in an earlier study to form its young bulge through secular processes after $z = 1$, at least partially driven by a bar (Brook et al. 2012a).

The sizes, shapes, kinematics, stellar ages and metal contents of the stellar populations formed in these distinct phases, can be nicely distinguished in simulated bulges. Indeed, we have found that the young component tends to occupy a smaller volume, to have disk-like morphology (note that G-1578411 is rather triaxial), to be more rotationally supported, to have roughly solar metallicities and sub-solar α-element enhancements. The old population, by contrast, is more spheroid-like, has sub-solar metallicities and larger α-element enhancements. On the other hand, no clear trend with age shows up in the Sérsic indices, a result in agreement with observations. The stellar metal content as well as the [Mg/Fe] ratios of these bulges have segregated distributions and, in some cases, show two clearly distinguishably peaks corresponding to the old and young populations. These stellar populations are also clearly segregated by their loci in the [Mg/Fe] vs [Fe/H] plots, where the old population has only a mild slope, while the slope of the young population appears steeper, with the two populations meeting at the knee. This kind of behavior is expected given the different nucleosynthetic origin of α and Fe-group elements.

These trends have been shown to be robust against the different codes used, which have differences in their gravitational and hydrodynamical force integrators, in mass and spatial resolutions, simulation box sizes, star formation parameterizations, chemical feedback and evolution, and energetic feedback implementations. Also, changing the bulge identification criteria from a simple radial cut to a kinematic based one, did not affect the age tendencies described above. The temporal cut-offs used to separate the two stellar populations have been chosen based on the shapes of the galaxy mass aggregation tracks and on the behavior of the SFRs at the bulge scale. Varying slightly these cut-offs does not affect these tendencies, either.

If we associate the old populations formed during the rapid phase with classical bulges, and the young ones formed during the slow phase with pseudo bulges, all the simulations in this paper show both classical and pseudo bulge components, but with varying relative masses. Therefore, the classical vs pseudo-bulge characteristics would be a question of degree, rather than nature. Otherwise, in all cases, measuring the light will result in higher relative contributions of the slow phase of bulge formation, i.e., pseudo bulges. In this respect, the feedback in G-1536 is particular effective at quenching star formation in the early phase, resulting in a relatively less significant (in mass) classical bulge population (see Table 3.2). This may be pointing toward the solution to the issue raised in Kormendy et al. (2010), who point out that a significant number of local, massive spiral galaxies have pseudo bulges rather than classical bulges.

These assembly patterns are reminiscent of the two phases found in hydrodynamical simulations by Domínguez-Tenreiro et al. (2006); Oser et al. (2010); Domínguez-Tenreiro et al. (2011) for more massive early type galaxies. The main difference lies in the percentage of gas transformed into stars at early epochs. In the case of massive ellipticals most of the available gas at the attraction basins for mass flows is transformed into stars during its "collapse" along the first phase. On the contrary, no such exhaustive gas consumption occurs for the less massive galaxies, where gas remains available along the slow phase, first as a diffuse component, and later on being part of different structures (the host galaxy disk itself, other small disk-like satellites and/or small clumps) before it is incorporated to the bulge.

If indeed real bulges follow a similar formation pattern as simulated ones, their observational features discussed in Section 3.1 can be nicely explained. More so, this approach provides a possible explanation for some apparently paradoxical observational results. For example, metal gradients could result from the different space distributions of the old and young populations, with the latter being more concentrated at the center due to dissipation. Also, bulge rejuvenation can be easily explained within this scenario.

We conclude that bulges can follow different assembly patterns, which can be summarized as two-phase processes (as in ellipticals) where non exhaustive gas transformation into stars occurs in the fast phase (unlike in ellipticals), with the additional effects, along the slow phase, of major and minor mergers, as well as of disk secular instabilities, in some cases. These different patterns and their combinations in different epochs as well as in different proportions, might explain the important dispersion in bulge properties observationally found.

The assembly of bulges is driven to a large extent by dynamical processes at larger scales. This

is particularly true concerning bulge-forming starbursts. As our simulations show, the bulge mass aggregation is a delayed consequence of its host galaxy mergers in the slow phase, and the result of collapse-like events in the fast one. We have shown that galaxy mass and feedback can affect the relative contributions of these two phases, although it is certain that specific basin deformation/collapse processes, as well as merger histories will also play a role. A set of statistical samples of simulation runs with various physical parameters is needed in order to break the degeneracy with the merging history and provide further insights into the importance of the two phases of bulge formation.

3.9 Appendix

In this section we present some additional information for the five simulated galaxies. First we show in Figure 3.11 the face-on and edge-on projected mass maps, for both stars and gas at $z = 0$. The box size for the two GASOLINE galaxies is two times bigger than for the P–DEVA ones. All five galaxies have relatively thin stellar disks (second column) and extended gaseous ones (forth column). They all show a central stellar concentration. The two GASOLINE disks are thicker than the P-DEVA ones because of the explicit supernova feedback that drives outflows in the case of the former.

For clarity, we also show in Figure 3.12 the stellar mass densities profiles for the five bulges. The P-DEVA bulges have steep profiles in the very inner region (see Table 3.2) and there is no clear distinction between the old and young stellar populations trends, except for HD-5103B which has a higher (smaller) contribution of the young bulge in the innermost (outer) region. This galaxy is a product of multiple major mergers. These steep profiles are not however recovered in the corresponding surface brightness. Doménech-Moral et al. (2012) gives B/T ratios of 0.30, 0.23 and 0.42 in the r-band for HD-5004A, HD-5004B and HD-5103B, respectively. The GASOLINE galaxies, on the other hand, have milder inner slopes (see Table 3.2). If we look at these two galaxies in surface brightness, G-1536 has a B/T of 0.26 in the r-band, while G-1578411 is basically bulgeless. This behavior is directly linked with the SNe feedback which effectively removes low angular momentum material (Brook et al. 2011), hence preferentially gas from the very inner region, and thus flattens the profiles.

In order to give a clearer picture of the dynamical classification we employ, we show in Figure 3.13 the 2D maps for Jz/Jc vs. Jp/Jc, Jz/Jc vs. E, and Jp/Jc vs. E for the same galaxy given

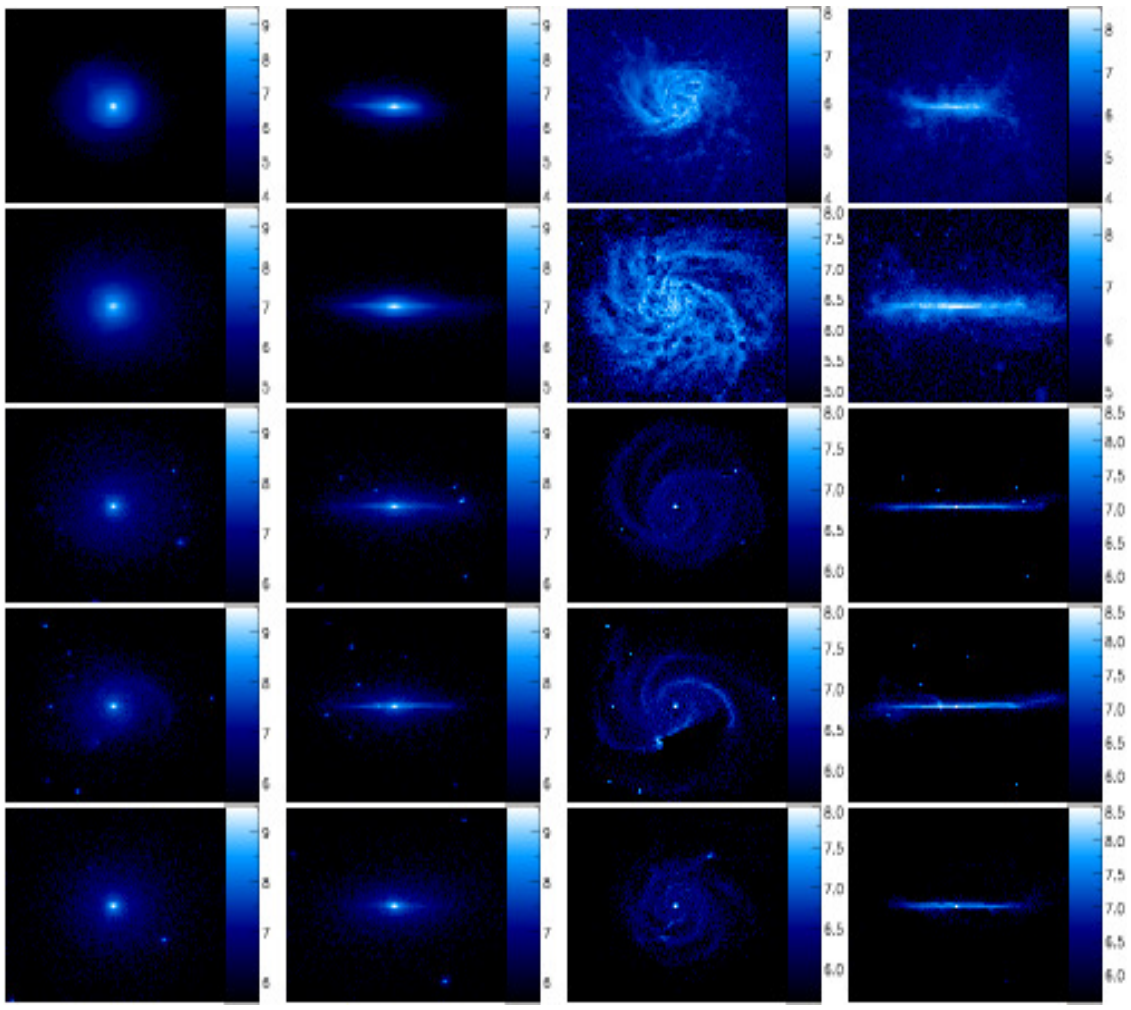

Figure 3.11: Projected images of the stellar (first and second columns) and gas (third and fourth columns) mass in all five galaxies (G-1578411, G-1536, HD-5004A, HD-5004B and HD-5103B from top to bottom). The first two rows have a box of 80 kpc per side, while the last three of 40 kpc per side. The saturation limits for the face-on and edge-on, stellar and gas masses have been forced to the same values in all 5 galaxies.

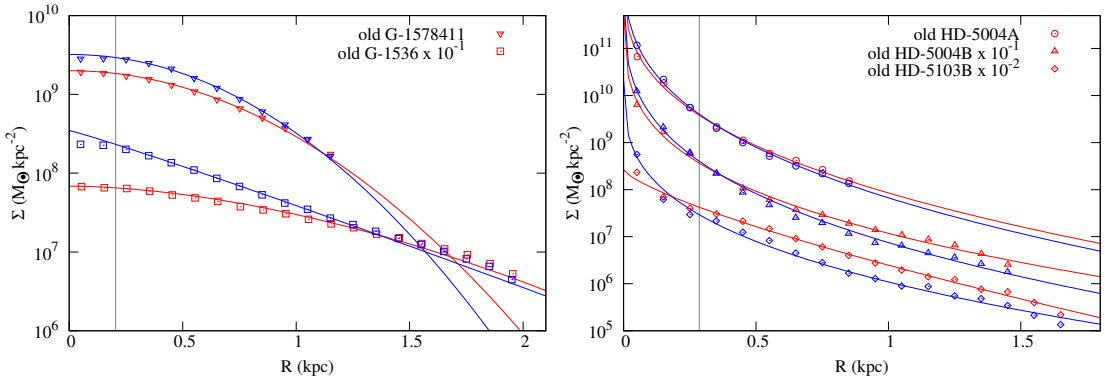

Figure 3.12: Surface mass densities profiles for the old (red) and young (blue) stellar populations in the bulges of the GASOLINE (left) and P–DEVA galaxies (right).

in Figure 3.1, namely G-1536, and their separation in spheroid and disk components, where we can see the two components occupying different regions of the parameter space. This figure is similar to Figure 7 in Doménech-Moral et al. (2012).

One import aspect of this study is the manner in which we define old and young bulge stellar populations. As explained in Section 3.4, we choose the temporal cut–off to separate old from young bulge stellar populations based on the transition we can observe in the mass assembly tracks. In Figure 3.14 we show the mass accretion track corresponding to r_{bulge} and its first and second derivatives for the galaxy G-1578411. As explained earlier, we defined the temporal cut t_{cut} as the time where the second derivative of the bulge mass accretion track becomes zero and keeps flat, moment which marks the transition from a fast clumpy mass assembly to a slow smooth regime (vertical red line in the figure). This is the reason why the temporal cut for G-1578411 appears just after the peak of the early starburst.

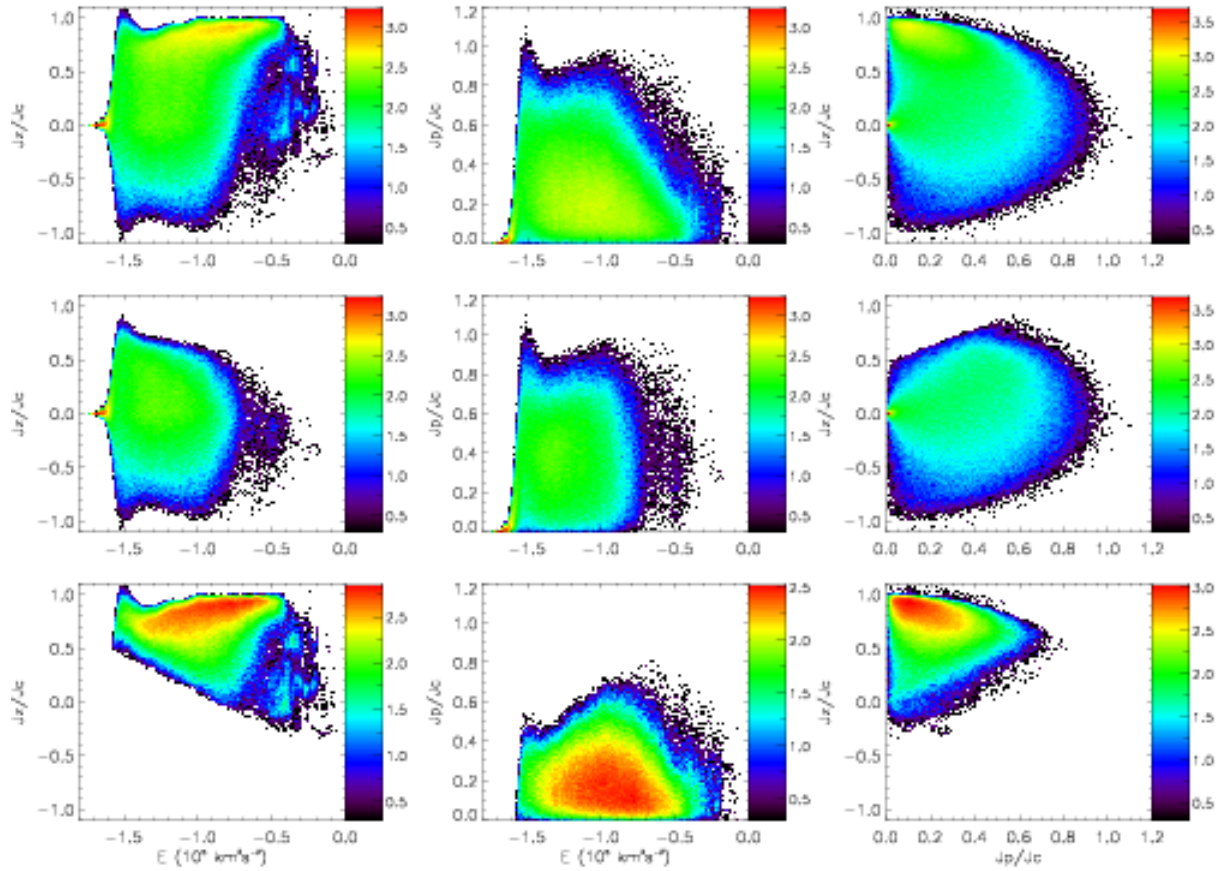

Figure 3.13: The clustering result for the galaxy G-1536. On the top row we give the J_z/J_c vs E (left panel), J_p/J_c vs E (central panel) and J_z/J_c vs J_p/J_c (right panel) distributions for all galaxy stars. The central row gives the same distributions for the stars classified as belonging to the spheroid, while the bottom one shows the distributions for the disk stars. The number of stellar particles, in a logarithmic scale, is quantified by the color code.

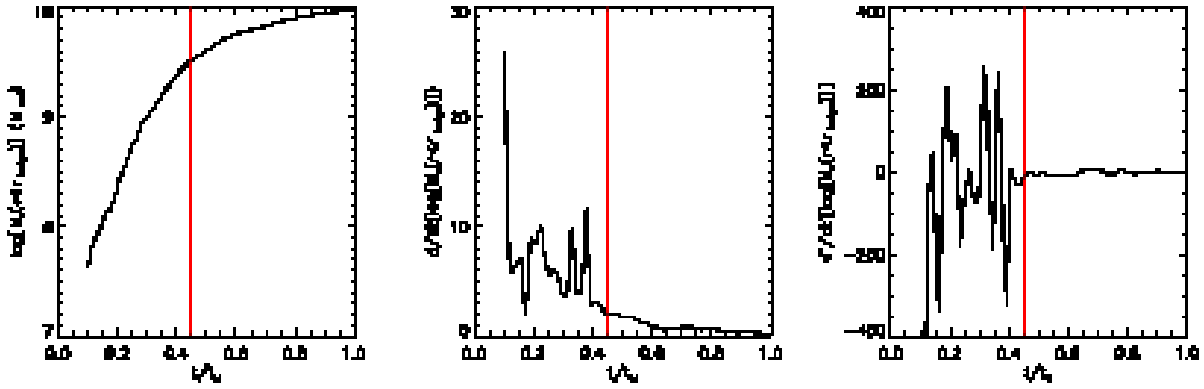

Figure 3.14: The MAT corresponding to the bulge radius for the galaxy G-1578411 (left), and its first (center) and second (right) derivatives. The vertical red line gives the temporal cut used to separate the old and young bulges (it corresponds to the value given in Tabel 3.2). It can be clearly seen that the temporal cut corresponds to the point where the second derivative of the mass curve becomes approximately constant and equal to zero.

References

Agertz, O., Teyssier, R., & Moore, B. 2011, MNRAS, 410, 1391

Athanassoula, E. 2005, MNRAS, 358, 1477

Babusiaux, C., Gómez, A., Hill, V., et al. 2010, A&A, 519, A77+

Barbuy, B., Ortolani, S., Bica, E., & Desidera, S. 1999, A&A, 348, 783

Bensby, T., & et al. 2011, A&A, 533, A134

Binney, J. 1978, MNRAS, 183, 501

Binney, J., & Tremaine, S. 1987, Galactic dynamics (Princeton, NJ, Princeton University Press)

Brook, C. B., Governato, F., Roškar, R., et al. 2011, MNRAS, 415, 1051

Brook, C. B., Stinson, G., Gibson, B. K., et al. 2012a, MNRAS, 419, 771

Brook, C. B., Stinson, G., Gibson, B. K., Wadsley, J., & Quinn, T. 2012b, MNRAS, 3222

Bryan, G. L., & Norman, M. L. 1998, ApJ, 495, 80

Bureau, M. 2002, in Astronomical Society of the Pacific Conference Series, Vol. 275, Disks of Galaxies: Kinematics, Dynamics and Peturbations, ed. E. Athanassoula, A. Bosma, & R. Mujica,

71–82

Carollo, C. M., Scarlata, C., Stiavelli, M., Wyse, R. F. G., & Mayer, L. 2007, ApJ, 658, 960

Carollo, C. M., Stiavelli, M., de Zeeuw, P. T., Seigar, M., & Dejonghe, H. 2001, ApJ, 546, 216

Chabrier, G. 2003, ApJ, 586, L133

Clarkson, W., Sahu, K., Anderson, J., et al. 2008, ApJ, 684, 1110

Combes, F. 2009, in Astronomical Society of the Pacific Conference Series, Vol. 419, Galaxy Evolution: Emerging Insights and Future Challenges, ed. S. Jogee, I. Marinova, L. Hao, & G. A. Blanc, 31–+

Cook, M., Lapi, A., & Granato, G. L. 2009, MNRAS, 397, 534

De Propris, R., Rich, R. M., Kunder, A., et al. 2011, ApJ, 732, L36+

de Zeeuw, T., & Franx, M. 1991, ARA&A, 29, 239

Debattista, V. P., Carollo, C. M., Mayer, L., & Moore, B. 2004, ApJ, 604, L93

Doménech-Moral, M., Martínez-Serrano, F. J., Domínguez-Tenreiro, R., & Serna, A. 2012, MNRAS, 2503

Domínguez-Tenreiro, R., Oñorbe, J., Martínez-Serrano, F., & Serna, A. 2011, MNRAS, 413, 3022

Domínguez-Tenreiro, R., Oñorbe, J., Sáiz, A., Artal, H., & Serna, A. 2006, ApJ, 636, L77

Eliche-Moral, M. C., González-García, A. C., Balcells, M., et al. 2011, ArXiv e-prints

Ellis, R. S., Abraham, R. G., & Dickinson, M. 2001, ApJ, 551, 111

Erwin, P. 2008, in IAU Symposium, Vol. 245, IAU Symposium, ed. M. Bureau, E. Athanassoula, & B. Barbuy, 113–116

Feltzing, S., & Gilmore, G. 2000, A&A, 355, 949

Ferreras, I., Wyse, R. F. G., & Silk, J. 2003, MNRAS, 345, 1381

Fisher, D. B., & Drory, N. 2008, AJ, 136, 773

Franx, M. 1993, in IAU Symposium, Vol. 153, Galactic Bulges, ed. H. Dejonghe & H. J. Habing, 243–+

Freeman, K. C. 1970, ApJ, 160, 811

Freyer, T., Hensler, G., & Yorke, H. W. 2006, ApJ, 638, 262

Fulbright, J. P., McWilliam, A., & Rich, R. M. 2007, ApJ, 661, 1152

Gonzalez, O. A., Rejkuba, M., Zoccali, M., et al. 2011, A&A, 530, A54

González-García, A. C., & van Albada, T. S. 2005, MNRAS, 361, 1030

Governato, F., Brook, C. B., Brooks, A. M., et al. 2009, MNRAS, 398, 312

Grevesse, N., & Sauval, A. J. 1998, SSRv, 85, 161

Groenewegen, M. A. T., & Blommaert, J. A. D. L. 2005, A&A, 443, 143

Guedes, J., Callegari, S., Madau, P., & Mayer, L. 2011, ArXiv e-prints

Hill, V., Lecureur, A., Gomez, A., et al. 2011, ArXiv e-prints

Hopkins, P. F., Bundy, K., Croton, D., et al. 2010, ApJ, 715, 202

Iwamoto, K., Brachwitz, F., Nomoto, K., et al. 1999, ApJS, 125, 439

Jablonka, P., Gorgas, J., & Goudfrooij, P. 2007, A&A, 474, 763

Johnson, C. I., Rich, R. M., Fulbright, J. P., Valenti, E., & McWilliam, A. 2011, ApJ, 732, 108

Johnson, C. I., Rich, R. M., Kobayashi, C., & Fulbright, J. P. 2012, ArXiv e-prints

Katz, N. 1992, ApJ, 391, 502

Kauffmann, G., Colberg, J. M., Diaferio, A., & White, S. D. M. 1999, MNRAS, 303, 188

Kawata, D., & Gibson, B. K. 2003, MNRAS, 340, 908

Kay, S. T., Pearce, F. R., Frenk, C. S., & Jenkins, A. 2002, MNRAS, 330, 113

Kobayashi, C., & Nakasato, N. 2011, ApJ, 729, 16

Kobayashi, C., Tsujimoto, T., & Nomoto, K. 2000, ApJ, 539, 26

Kormendy, J. 1982, in Saas-Fee Advanced Course 12: Morphology and Dynamics of Galaxies, ed. L. Martinet & M. Mayor, 113–288

Kormendy, J., Drory, N., Bender, R., & Cornell, M. E. 2010, ApJ, 723, 54

Kormendy, J., & Kennicutt, Jr., R. C. 2004, ARA&A, 42, 603

Kroupa, P., Tout, C. A., & Gilmore, G. 1993, MNRAS, 262, 545

Lecureur, A., Hill, V., Zoccali, M., et al. 2007, A&A, 465, 799

MacArthur, L. A., González, J. J., & Courteau, S. 2009, MNRAS, 395, 28

Martínez-Serrano, F. J., Serna, A., Domínguez-Tenreiro, R., & Mollá, M. 2008, MNRAS, 388, 39

Matteucci, F., & Brocato, E. 1990, ApJ, 365, 539

McDonald, M., Courteau, S., Tully, R. B., & Roediger, J. 2011, MNRAS, 414, 2055

McWilliam, A., & Rich, R. M. 1994, ApJS, 91, 749

Mollá, M., Ferrini, F., & Gozzi, G. 2000, MNRAS, 316, 345

Monaghan, J. J. 2005, Reports on Progress in Physics, 68, 1703

Moorthy, B. K., & Holtzman, J. A. 2006, MNRAS, 371, 583

Nakasato, N., & Nomoto, K. 2003, ApJ, 588, 842

Ness, M., & Freeman, K. 2012, in European Physical Journal Web of Conferences, Vol. 19, European Physical Journal Web of Conferences, 6003

Ness, M., Freeman, K., Athanassoula, E., et al. 2012, ArXiv e-prints

Nomoto, K., Hashimoto, M., Tsujimoto, T., et al. 1997, Nuclear Physics A, 616, 79

Okamoto, T. 2012, ArXiv e-prints

Ortolani, S., Renzini, A., Gilmozzi, R., et al. 1995, Nature, 377, 701

Oser, L., Ostriker, J. P., Naab, T., Johansson, P. H., & Burkert, A. 2010, ApJ, 725, 2312

Peletier, R. F. 2008, in Astronomical Society of the Pacific Conference Series, Vol. 390, Pathways Through an Eclectic Universe, ed. J. H. Knapen, T. J. Mahoney, & A. Vazdekis, 232–+

Peletier, R. F., Balcells, M., Davies, R. L., et al. 1999, MNRAS, 310, 703

Peletier, R. F., Falcón-Barroso, J., Bacon, R., et al. 2007, MNRAS, 379, 445

Prugniel, P., Maubon, G., & Simien, F. 2001, A&A, 366, 68

Rahimi, A., Kawata, D., Brook, C. B., & Gibson, B. K. 2010, MNRAS, 401, 1826

Robin, A. C., Marshall, D. J., Schultheis, M., & Reylé, C. 2012, A&A, 538, A106

Salpeter, E. E. 1955, ApJ, 121, 161

Samland, M., & Gerhard, O. E. 2003, A&A, 399, 961

Sánchez-Blázquez, P., Ocvirk, P., Gibson, B. K., Pérez, I., & Peletier, R. F. 2011, MNRAS, 415, 709

Serna, A., Domínguez-Tenreiro, R., & Sáiz, A. 2003, ApJ, 597, 878

Shandarin, S. F., & Zeldovich, Y. B. 1989, Reviews of Modern Physics, 61, 185

Shen, S., Wadsley, J., & Stinson, G. 2010, MNRAS, 407, 1581

Soto, M., Kuijken, K., & Rich, R. M. 2012, ArXiv e-prints

Soto, M., Rich, R. M., & Kuijken, K. 2007, ApJ, 665, L31

Stinson, G., Seth, A., Katz, N., et al. 2006, MNRAS, 373, 1074

Stinson, G. S., Bailin, J., Couchman, H., et al. 2010, MNRAS, 408, 812

Stinson, G. S., Brook, C., Prochaska, J. X., et al. 2012, MNRAS, 425, 1270

Talbot, Jr., R. J., & Arnett, W. D. 1973, ApJ, 186, 51

Thomas, D., & Davies, R. L. 2006, MNRAS, 366, 510

Tissera, P. B., & Dominguez-Tenreiro, R. 1998, MNRAS, 297, 177

Tsujimoto, T., & Bekki, K. 2012, ApJ, 747, 125

van Loon, J. T., Gilmore, G. F., Omont, A., et al. 2003, MNRAS, 338, 857

Wechsler, R. H., Bullock, J. S., Primack, J. R., Kravtsov, A. V., & Dekel, A. 2002, ApJ, 568, 52

Weisberg, S. 2002, Journal of Statistical Software, 7

Woosley, S. E., & Weaver, T. A. 1995, ApJS, 101, 181

Wyse, R. F. G. 1999, Ap&SS, 267, 145

Zhao, D. H., Mo, H. J., Jing, Y. P., & Börner, G. 2003, MNRAS, 339, 12

Zhao, H., Spergel, D. N., & Rich, R. M. 1994, AJ, 108, 2154

Zoccali, M., Hill, V., Lecureur, A., et al. 2008, A&A, 486, 177

Zoccali, M., Lecureur, A., Barbuy, B., et al. 2006, A&A, 457, L1

Chapter 4

The stellar spheroid, the disk and the dynamics of the Cosmic Web

This chapter is a copy of
"The stellar spheroid, the disk and the dynamics of the Cosmic Web"
by Domínguez-Tenreiro, Obreja, Brook, Martínez-Serrano, Stinson & Serna,
published in ApJL 800, L30, 2015.
Supplementary information is presented in the Appendix.

4.1 Introduction

The idea that galaxies get most of their gas through cold, dense streams (i.e., the so-called "cold mode" for galaxy mass assembly) was first formulated by Binney (1977) and (re)discovered in the last decade (Birnboim & Dekel 2003; Kereš et al. 2005; Ocvirk et al. 2008; Brooks et al. 2009; van de Voort et al. 2011). This scenario has received a lot of attention in the last few years because it helps to explain DM halo and galaxy angular momentum acquisition through filaments (see Pichon et al. 2011; Kimm et al. 2011; Codis et al. 2012; Tillson et al. 2012; Danovich et al. 2012; Stewart et al. 2013; Dubois et al. 2014; Welker et al. 2014; Danovich et al. 2014), and, in addition, for its possible implications in the star formation history of galaxies (Kereš et al. 2009; Brooks et al. 2009; Obreja et al. 2013).

In the context of the theories for the advanced stages of gravitational instability, cold streams feeding clumps is a general prediction of the Zeldovich Approximation (Zel'dovich 1970) extended to the Adhesion Model (see e.g. Gurbatov et al. 1989; Kofman et al. 1990; Gurbatov et al. 2012),

predictions now confirmed in detail by numerical simulations (Cautun et al. 2014). Indeed, the Adhesion Model predicts that, at a given scale, walls surrounding voids, filaments and nodes (i.e., the Cosmic Web, CW, elements, see Bond et al. 1996) successively emerge in multi-streaming regions. Then they vanish as mass elements flow through the voids towards the walls, through the walls towards the filaments, and finally from filaments to nodes, where mass elements pill up and virialize after the web-like mass configuration, at the scale considered, turns around and collapses (see e.g., Domínguez-Tenreiro et al. 2011). Meanwhile, the same CW elements emerge at larger and larger scales, disappearing later on in favour of voids and nodes.

These considerations strongly suggest that the stellar populations of current galaxies displayed a web-like structure as part of the CW at high z, later on removed due to the CW evolution. The question arises if the CW dynamics might also explain the origin of the fine structure of late-type galaxies (hereafter, LTGs). Indeed, stellar populations of LTGs come in three different categories, those forming the spheroid (i.e., the bulge and stellar halo), the thick disk and the thin disk (see Mould 1982; Gilmore et al. 1989; Ivezić et al. 2012, for reviews), whose different properties are thought to be driven by their different specific angular momentum j content. We see that its acquisition by galaxies is a key piece of the debate.

For a typical disk galaxy the total j[1] enclosed within the Lagrangian patch associated with its halo, j_{patch}, grows as predicted by the Tidal Torque Theory (based on the Zeldovich Approximation, see Peebles 1969; Doroshkevich 1970; White 1984) prior to patch maximum expansion. Later on, j_{patch} is roughly conserved, but redistributed (Pichon et al. 2011). Indeed, as filaments form from the collapse of matter flows coming from opposite directions, the flows coherently wind up (Codis et al. 2012) into whirls with their spin s directions roughly aligned with the filament. At the same time, matter elements also acquire a net transverse motion (i.e., an orbital j relative to the patch center), due to the asymmetric forces acting on filaments from the voids they divide.

Once the filaments form, they collimate longitudinal motions towards the growing central mass accumulation, coherently transporting j either as clumpy or diffuse material. Pichon et al. (2011) show that, at a given time, the j content of infalling matter grows with its distance to the patch center (lever effect). The implications this ordering has on j acquisition by *gas* at the scales of *galaxy halos* has been analyzed by Sales et al. (2012) for Milky-Way-sized galaxies, and by Stewart et al. (2013) who pointed out the importance of *fresh gaseous accretion* to increase the j content in the inner halo as time progresses (a reformulation of the lever effect previously described). Recently

[1] relative to the patch center where the galaxy is to be assembled

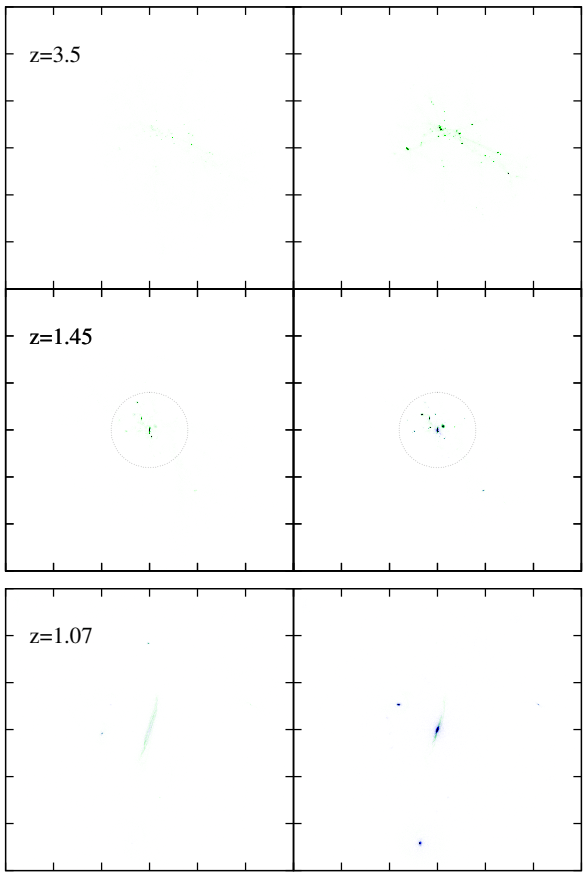

Figure 4.1: For the HD-5004A galaxy, a projection of the positions of its stellar particles identified at $z = 0$ when traced back to $z_{\rm high} = 3.5$, 1.45 and 1.07. Left: (thin) disk-to-be particles. Right: spheroid-to-be particles. Green (blue): gaseous (stellar) particles at the respective $z_{\rm high}$s. From top to bottom the box sides are 600, 600 and 60 kpc, respectively. Circles stand for the projection of the virial sphere.

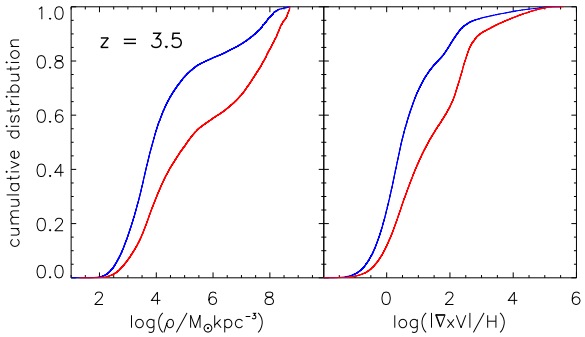

Figure 4.2: Cumulative PDFs for $\log(\rho_i)$ and $\log(w_i)$ for the HD-5004A galaxy at $z_{\rm high} = 3.5$. Red (blue) lines stand for gaseous spheroid (disk) precursors.

Danovich et al. (2014) have confirmed these ideas, and have shown that gravitational torques from the early settled disk cause gas and, to a lesser extent, star alignments at the circumgalactic region.

We see that new ideas have recently emerged to explain j adquisition by gas. One of the still unaswered questions is why do some late type galaxies have a spheroid at all. More specifically, did these spheroid stellar populations lose most of their j they have acquired at high z, as discussed above, or they have always been j-poor? What are the differences between the progenitors of spheroid and disk stellar populations? The specific purpose of this study is to contribute to answer these questions in the context of CW dynamics.

4.2 Methods and results

Hydrodynamical simulations in a cosmological context are a helpful tool to address the above questions. For a proper spheroid and disk characterization, one needs to measure precise differences in morphology, kinematic and composition. Therefore accurate conservation of angular momentum and a detailed implementation of chemical evolution are two fundamental issues. Moreover, we also need to consider the effects of discrete energy injection by stellar physics. Comparisons among the results of different codes are advisable, because we are looking for effects coming from a generic and fundamental level of physical description.

In view of these considerations, we present results of simulations run with two different SPH codes. `P-DEVA` (Serna et al. 2003; Martínez-Serrano et al. 2008) is an entropy conserving AP3M code where the main concern in its design was j conservation. Chemical evolution makes use of the Q_{ij} formalism (Talbot & Arnett 1973). Stellar feedback is implicitely implemented through (inefficient)

SF parameters, as discussed in Agertz et al. (2011). We also use the code GASOLINE (Wadsley et al. 2004), in which SNe feedback is implemented using the blastwave-formalism (Stinson et al. 2006, 2013).

To run the simulations, a zoom-in technique has been used with baryon particle masses of $m_B = 3.79 - 3.74 \times 10^5 M_\odot$ and initial gaseous mass of $m_{\rm gas} = 0.25 - 2.0 \times 10^5 M_\odot$, gravitational softening of $\epsilon_g = 400/{\rm h}$ pc and $\epsilon_g = 315.5 - 156.2$ pc in P-DEVA and GASOLINE, respectively. We base our analysis on a P-DEVA set of 4 galaxies (LD-5101A, LD-5003A, HD-5103B and HD-5004A) and a GASOLINE set of 2 galaxies (g1536 and g21647), with $z = 0$ stellar masses in the ranges of $M_* = 1.29 - 3.26$ (P-DEVA) and 2.26 - 2.32 $\times 10^{10} M_\odot$ (GASOLINE). The total numbers of stellar particles (including the stellar halo) are in the range $N_{\rm star} = 34000 - 83000$ (P-DEVA), and 583000 and 650000, for the two GASOLINE galaxies. The main results are discussed in terms of one of the P-DEVA galaxies (HD-5004A) and a GASOLINE one (g1536). P-DEVA galaxies have been studied by Doménech-Moral et al. (2012) at $z = 0$, who analyzed some aspects of their fine structure, g1536 by Brook et al. (2012b) and Obreja et al. (2014). In addition, Obreja et al. (2013) who addressed bulge formation, and Domínguez-Tenreiro et al. (2014) who analyzed their HI and H2 content, SEDs and colors, included galaxies run using both codes. In all these cases, we found satisfactory consistency with observational data.

The *kk*-means method has been used by Doménech-Moral et al. (2012) to disentangle the fine structure of simulated LTGs. This is an unsupervised clustering algorithm (Schölkopf et al. 1998; Karatzoglou et al. 2004; Dhillon et al. 2004) looking for clusters in a 3-dimensional space of LTG stellar particles kinematic variables. Specifically, for each stellar particle, i, in a given galaxy, its total binding energy, $E_{\rm i}$, $\epsilon_{\rm J,i} \equiv j_{\rm z,i}/J_{\rm C,i}(E_{\rm i})$ and $j_{\rm p,i}/J_{\rm C,i}(E_{\rm i})$ have been used as variables, where $j_{\rm z,i}(j_{\rm p,i})$ are the particle angular momentum projections on the disk axis (plane) and $J_{\rm C,i}(E_{\rm i})$ is the angular momentum of a circular orbit with energy $E_{\rm i}$. By applying this method, with no priors assumed appart from the number of clusters to look for, the fine structure of galaxies emerges naturally (see Figure 7 in Doménech-Moral et al. 2012, where more details can be found). Once classified, the systematics of spheroid, thick disk and thin disk star observational properties is recovered, as well as their mutual correlations (Doménech-Moral et al. 2012; Obreja et al. 2013, Obreja et al. in preparation). The same is true for GASOLINE galaxies, although using a different classification scheme (Brook et al. 2012a).

To decipher the imprints left by the CW dynamics onto current stellar populations, we have traced back these populations to their progenitors at high z. Specifically, for each simulated galaxy

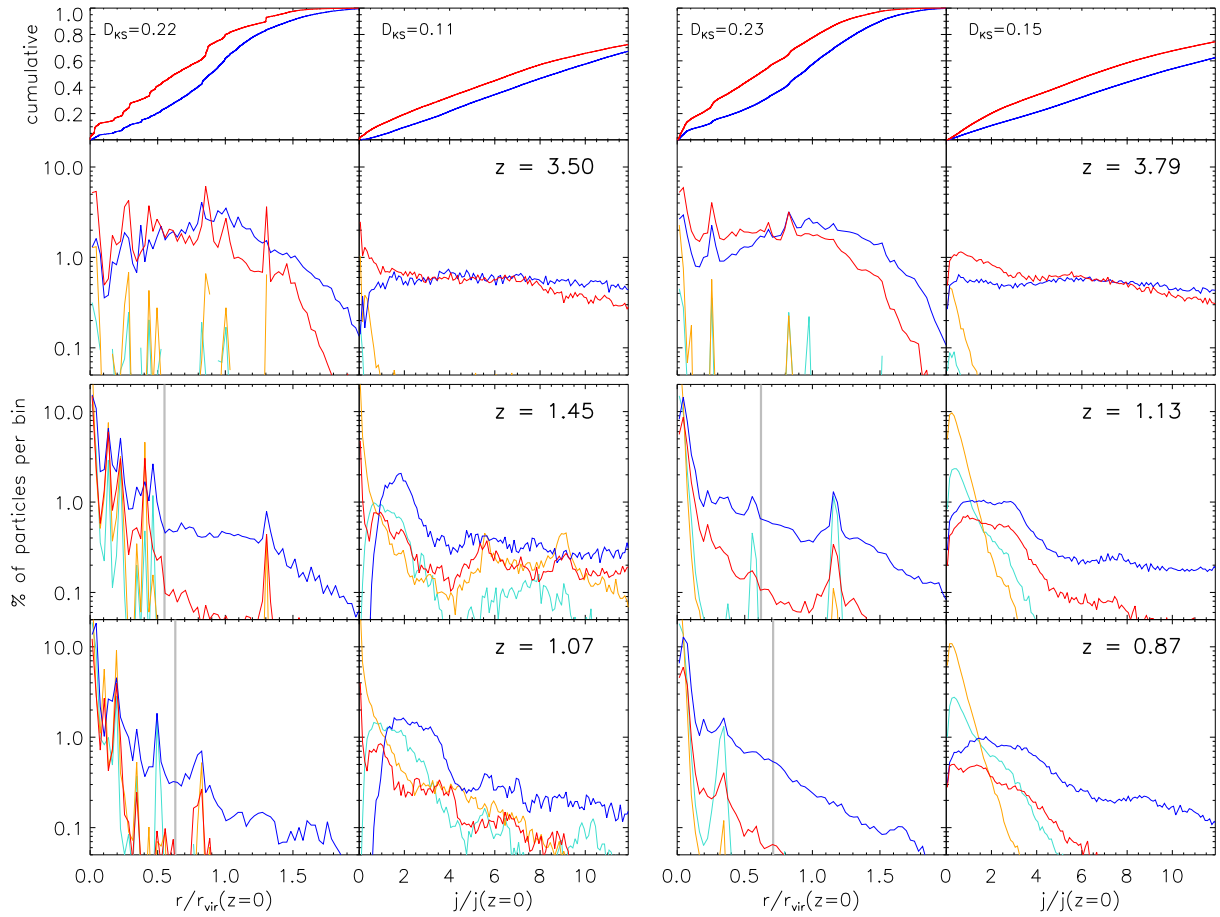

Figure 4.3: PDFs for r_i and j_i measured on HD-5004A and g1536 galaxies -to-be particles at different $z_{\rm high}$ values, with cumulative ones at the highest zs in the first row. Red (blue) lines stand for gaseous spheroid (disk) precursors, while orange (cyan) lines refer to spheroid (disk) precursors particles that are already stellar at the respective $z_{\rm high}$s. The vertical normalization has been separately taken for the two kinds of precusors, including in any case both the gas and the stars. Distance units are the virial radii at $z = 0$ (138 and 167 kpc, respectively), while j_i is given in units of the total baryonic (spheroid + disk) specific angular momenta at $z = 0$. The thick grey lines correspond to the virial radii at these zs.

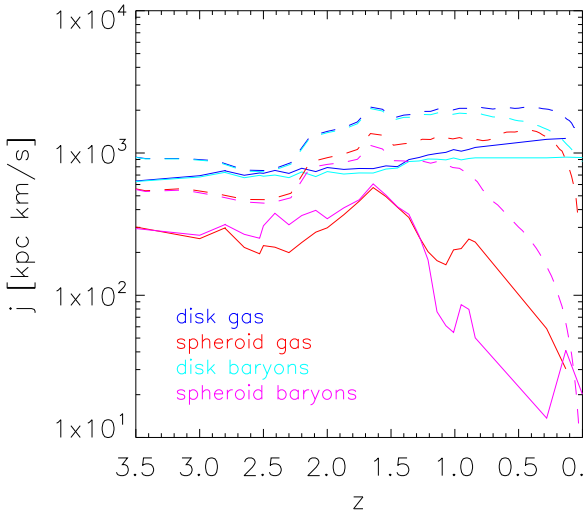

Figure 4.4: The total specific angular momentum content of HD-5004A (full lines) and g1536 (dashed lines) galaxies -to-be particles as a function of z. Red (blue) lines stand for gaseous spheroid (disk) precursors, while magenta (cyan) lines refer to spheroid (disk) precursors particles that are either stellar or gaseous at the respective zs.

we have identified all the stellar particles belonging to each component at $z = 0$ and traced these particles back to different high redshifts $z_{\rm high}$. By plotting the positions of all the progenitors together, we confirm that indeed they display a clear CW-like structure before collapse, whose evolution follows the Adhesion Model. A main filament can be identified in this structure (Dubois et al. 2014; Danovich et al. 2014), with the disk initially normal to this filament (Figure 4.1, lower panel), as expected. Moreover, the systematics of j acquisition by disks at the halo scale is recovered (see §4.1).

If we separately plot the positions of the progenitors of each component, we still find CW-like configurations, but with different characteristics. In Figure 4.1 we plot, for a galaxy in the `P-DEVA` set, the projections on a given plane of the progenitor positions at $z_{\rm high} = 3.5$ and 1.45 (roughly at proto-object collapse). The left panel corresponds to the (thin) disk progenitors, while the right panel corresponds to the spheroid progenitors. The visual impression is that spheroid progenitors have been involved in multistreaming events from earlier on than disk progenitors, in such a way that at given z, they form a CW-like structure whose dynamical state is more advanced than the CW corresponding to the thin disk. This more advanced stage of gravitational instability can be characterized mainly through the distributions of density and vorticity of gas elements, that are biased towards higher values than less advanced ones, see below. In addition, it implies i), the

tendency for spheroid-to-be particles to be closer to the system center of mass (c.o.m.) than disk progenitors, and ii), more stars formed within the (disconnected) densest nodes before collapse, from low spin s material (s-rich gas particles within these clumps form small disks around the stellar centers, see lower panel). The Figure also indicates that by $z_{\rm coll}$ (middle panel) most spheroid-to-be particles are within the halo and roughly half of them have turned into stars, while part of the disk predecessors are still being assembled as diffuse gas into a gaseous disk, where disk stars will eventually form. Indeed, the age distributions of different simulated disk galaxies can be found in Doménech-Moral et al. (2012), where this age segregation among the different components is confirmed (see their Figure 10). Concerning baryon mass assembly of the spheroid population, it mostly occurs at $z > z_{\rm coll}$ through collapse-induced merging, that is, along the so-called *fast phase* of galaxy evolution, as Obreja et al. (2013) have found[2]. In this case, as we will see in more detail below, it is the proximity to the patch center that segregates those particles that will be involved in the collapse and suffer from severe j loses from those that will not.

In the lower panel we plot the progenitors at $z = 1.07$, when the system has decoupled from expansion and filaments at the virial scale are significantly weaker than at earlier times. At this point, when the the proto-disk is settled, gravitational torques appear at the disk scale that tend to redistribute j, and to gradually align gaseous particles (either diffuse or in satellites) with the main disk (Danovich et al. 2014) as they dissipate energy due to their j precession. Collisionless mass elements cannot dissipate their energy, therefore they are not prone to being aligned. The important point here is that while well aligned material (either originally or as a consequence of gravitational torques) is incorporated to the disk, the rest of the material is not. An example of such behaviour shows up in the lower panel, where we see that a disk originally aligned with the main progenitor is almost entirely incorporated to the thin disk (right panel), however for two disks that are not parallel to the main at $z = 1.07$ only a fraction or their gaseous component goes to the thin disk, while the rest goes to thick disk (not shown) or to the spheroid (right panel). In these cases, the CW evolution has provided different initial conditions for the torques to act upon.

The visual differences in Figure 4.1 have been quantified by means of a V-Web-inspired method (Hoffman et al. 2012). For a given simulated galaxy and different $z_{\rm high}$s, the SPH density ρ_i and vorticity w_i (measuring the spin of resolution scale whirls) of each gaseous particle, and the distances r_i and angular momenta j_i, relative to the system c.o.m, for gaseous and stellar particles at the $z_{\rm high}$s have been calculated, as well as their respective probability distribution functions (PDFs).

[2]These authors found that classical bulges have also a kinematical disky stellar component formed after collapse.

The results confirm the visual impression that the spheroid-to-be gas particles are the first to be involved in shell-crossing events.

To illustrate these results, in Figure 4.1 we plot the $\log(\rho_i)$ and $\log(w_i)$ cumulative PDFs at $z_{\rm high} = 3.5$, for the same galaxy as in Figure 4.1. The PDFs show that, at given times, the spheroid-to-be gas particles have the highest densities and vorticities, maping out the CW element locations. In Figure 4.3, the r_i distributions (first column) confirm that the spheroid-to-be particles (in red) are, *at any z*, closer to the system c.o.m. than the disk progenitors (blue), having therefore a lower probability of being j-rich (i.e., lever effect, second column). This is true also at high zs as the first row, giving the corresponding cumulative PDFs of r_i and j_i for gaseous precursors, illustrates. The relative differences in the r_i PDFs are particularly important at the inner region. A K-S test confirms that the red and blue distributions differ at a confidence level higher than a 99.8%. We also see in the third row panels that, remarkably, the spheroid-to-be particles are involved in the system collapse by $z \sim 1.5$, so that most of the spheroid-to-be gas particles are within the virial radius (80 kpc) at $z < 1.5$, having suffered from severe j_i losses at collapse (middle and bottom panels).

By contrast, proto-disk particles are further away, and therefore not significantly affected by collapse. Many proto-disk particles enter the halo as j-rich gas particles later on, where they fall to the central regions as they lose j in a more gradual manner (narrow low j_i component at the left). The j content of the gas of the disk component is increased as time goes by, because delayed particles have a higher j_i at larger distances (lever effect, see §4.1).

On the right hand side of Figure 4.3 we show a similar plot for a galaxy in the `GASOLINE set`. The results are similar to those of the `P-DEVA` set concerning the r_i and j_i distribution patterns and their evolution for the two components[3]. The similarity in the patterns of j evolution are even clearer from Figure 4.4, where we present the total $j(z) \equiv \mid \vec{j}(z) \mid$ for the disk-to-be ($j_{\rm disk}(z)$, blue and cyan) and for the spheroid-to-be ($j_{\rm sph}(z)$, red and magenta) components. We see that $j_{\rm sph}(z)$ is lower than $j_{\rm disk}(z)$ for any z. We also see that after a gain period, there are severe $j_{\rm sph}$ losses beginning at $z_{\rm coll} \sim 1.5$ (1.0) i.e., collapse for HD-5004A (g1536) repectively, affecting the gas (in red) and later on the stars (in magenta). On the contrary, $j_{\rm disk,gas}(z)$ is roughly constant (g1536) or increases after collapse all the way to $z = 0$ (HD-5004A), while $j_{\rm disk,star}(z)$ slightly decreases or keeps constant, showing differences with the gaseous component at $z < 0.2$.

[3]Some differences exist, however, likely due to the blast wave energy injected in the configuration in the `GASOLINE` case, preventing high gas densities to develop.

4.3 Summary and discussion

In summary, the baryons forming current spheroid stellar populations come from gas particles that differ from the proto-disk particles. Firstly, prior to collapse, the spheroid progenitors have a higher probability of i), sampling the shell-crossing regions, thereby forming stars from earlier on, and, ii), being closer to the system c.o.m. with a lower j content. Secondly, because of this proximity, they are involved in the collapse event and lose most of their j. Thirdly, once the main disk is settled, spheroid progenitors at the circumgalactic region have not succeeded at aligning their j with it, either because they are more likely to be stars rather than gas, or because of their orbital configuration.

The results, obtained with two codes that are different in their design and subgrid modelling (see §4.2), strongly suggest that indeed the different properties of stellar populations in the spheroid and disk express information imprinted at high z (prior to collapse) while they displayed a CW configuration, and that this information comes from a fundamental level of physical description, as encapsulated within the Zeldovich Approximation and the Adhesion Model, see §4.1.

Gas j content changes take place at collapse, and later on within the circumgalactic region (e.g., disk-induced alignments, among many other processes), changes that can remove the imprints of CW dynamics left at these smaller scales. In this respect, our results show that the spheroid and disk stellar populations of local galaxies (i.e., at disk scale) keep memory of the CW dynamics at high z. This strongly suggest that, in the long run, the ordering imprinted on the cosmic inflow (that provides with segregated initial conditions for lower z processes) overcomes the complex astrophysical processes occurring in the circumgalactic environment of forming disks.

4.4 Appendix

4.4.1 Some data on the galaxy sample and their SFR histories

We analyze six cosmological zoom simulations: two from the the MaGICC project (Brook et al. 2012a; Stinson et al. 2013), run with `GASOLINE` (g1536 and g21647), and four run with `P-DEVA` (LD-5003A, HD-5004A, LD-5101A and HD-5103B), (Doménech-Moral et al. 2012). `P-DEVA` galaxies have been studied by Doménech-Moral et al. (2012) at $z = 0$, who analyzed some aspects of their fine structure, g1536 by Brook et al. (2012b), Stinson et al. (2013) and Obreja et al. (2014). In addition, Obreja et al. (2013) who addressed bulge formation, and Domínguez-Tenreiro et al. (2014)

who analyzed their HI and H2 content, SEDs and colors, included galaxies run using both codes. In all these cases, we found satisfactory consistency with observational data.

P-DEVA galaxies and some GASOLINE ones show broken luminosity profiles. They have been analyzed by Martínez-Serrano et al. (2008) and Sánchez-Blázquez et al. (2009), respectively, in terms of radial migration. Radial migration causes also specific patterns in element abundance gradients. A detailed report on this subject as well as on comparisons to observational data and to other simulations, can be found in Miranda et al., 2015 submitted.

Edge-on projections of the disk (left, blue) and spheroid (center, red) stars of the four (two) P-DEVA (GASOLINE) galaxies at $z = 0$ are given in Figures 4.5 (Figures 4.6). The classification is kinematic (k-means, see Chapter 2).

The corresponding star formation histories for disks and spheroids are given in the same Figures (right), tracing merger events as maxima in the star formation rates. We see that, in general, spheroids form their stars earlier on, this distinction being clearer for the P-DEVA set (see Doménech-Moral et al. 2012, for more details). One thing in common for the P-DEVA galaxies is that the disk star formation rate stays at relatively low and almost constant values throughout the galaxy lifespan, while most of the spheroid star formation occurs at high redshift.

The star formation rate of both spheroid and disk for the two GASOLINE galaxies, on the other hand, is delayed in comparison with the P-DEVA runs due to the particular implementation of the early stellar feedback (Stinson et al. 2013). In any case, for these two galaxies also, the spheroids form their stars earlier than the disks, and in shorter times (the later is not valid for g21647, however). In the case of the g1536 galaxy, two important starbursts can be observed in the star formation rate (upper right of Figure 4.6) of the spheroid (red curves) at $\sim$4 and $\sim$7 Gyrs, which correspond to merger events in the corresponding black curve of Figure 4.7 (see next section). The first one is a major merger, while the later is a sequence of minor mergers. The disk star formation rate (blue curve) also shows an increase at the later merger, but not as big as the spheroid one.

Two galaxies show some major particularities in their SFR history. HD-5103B has multiple major mergers at various times in its evolution ($\sim$ 4, 8, 10 Gyr and one at the very end). The major merger at $\sim$ 4 Gyr, in particular, triggers a very powerful burst of star formation in the spheroid gas (red curve in the bottom right panel of Figure 4.5). An important point to note here is that in spite of having such an entertaining history, this galaxy still has a relatively extended thin disk at $z = 0$ (up to $\sim$10 kpc).

The other particular case is g21647. This galaxy suffers a recent (less than 2 Gyr ago) major

Simulation	g1536	g21647	LD-5003A	HD-5004A	LD-5101A	HD-5103B
M_{min} ($10^4 M_\odot$)	5.70	5.70	38.22	39.45	37.93	37.80
h_{soft} (pc)	156.2	156.2	571	571	571	571
M_{vir} ($10^{11} M_\odot$)	7.06	8.24	1.70	2.97	1.09	3.62
r_{vir} (kpc)	257	269	114	138	99	147
M_* ($10^{10} M_\odot$)	2.36	2.51	1.77	3.69	1.48	3.26
f_{gas}	0.74	0.74	0.25	0.20	0.23	0.20
f_{*disk}	0.52	0.50	0.34	0.38	0.43	0.36
j_* (kpc km/s)	450	198	212	357	203	410
j_{*disk} (kpc km/s)	841	407	592	929	515	946
$j_{*spheroid}$ (kpc km/s)	24	11	18	20	50	116
z_{turn}	1.6	0.7	0.8	2.4	2.0	undefined
z_{coll}	0.85	0.25	0.8	1.5	1.1	undefined

Table 4.1: Properties of the simulated galaxies at $z = 0$. M_{min} and h_{soft} are the minimum gas particle mass and the gravitational softening length. M_{vir}, r_{rvir}, M_* and f_{gas} are the virial mass and radius, stellar mass and gas mass fraction (computed as the total gas mass divided by the total baryon mass in the halo). f_{*disk} is the fraction of stellar mass in the disk according to the k-means criteria. j_*, j_{*disk} and $j_{*spheroid}$ are the specific angular momenta of all galaxy stars, and of those that belong to the disk and spheroid, respectively. z_{turn} is the redshift of maximum expansion (see definition in Section 4.4.2). z_{coll} is an estimation of the collapse redshift.

merger associated with increased star formation rates, both in the spheroid and in the disk (see below for details).

The values of the stellar masses and the stellar mass fraction in the k–means selected disk for the six galaxies are given in Table 4.1, as M_* and f_{*disk}, respectively, together with some of their important properties at $z = 0$.

4.4.2 Events and milestones in disk galaxy mass assembly

In Chapter 3 we showed that two different phases can be distinguished in the mass assembly of classical bulges, as an extension of those of elliptical galaxies.

Concerning disks, and more particularly thin disks, as seen in the previous sections of this

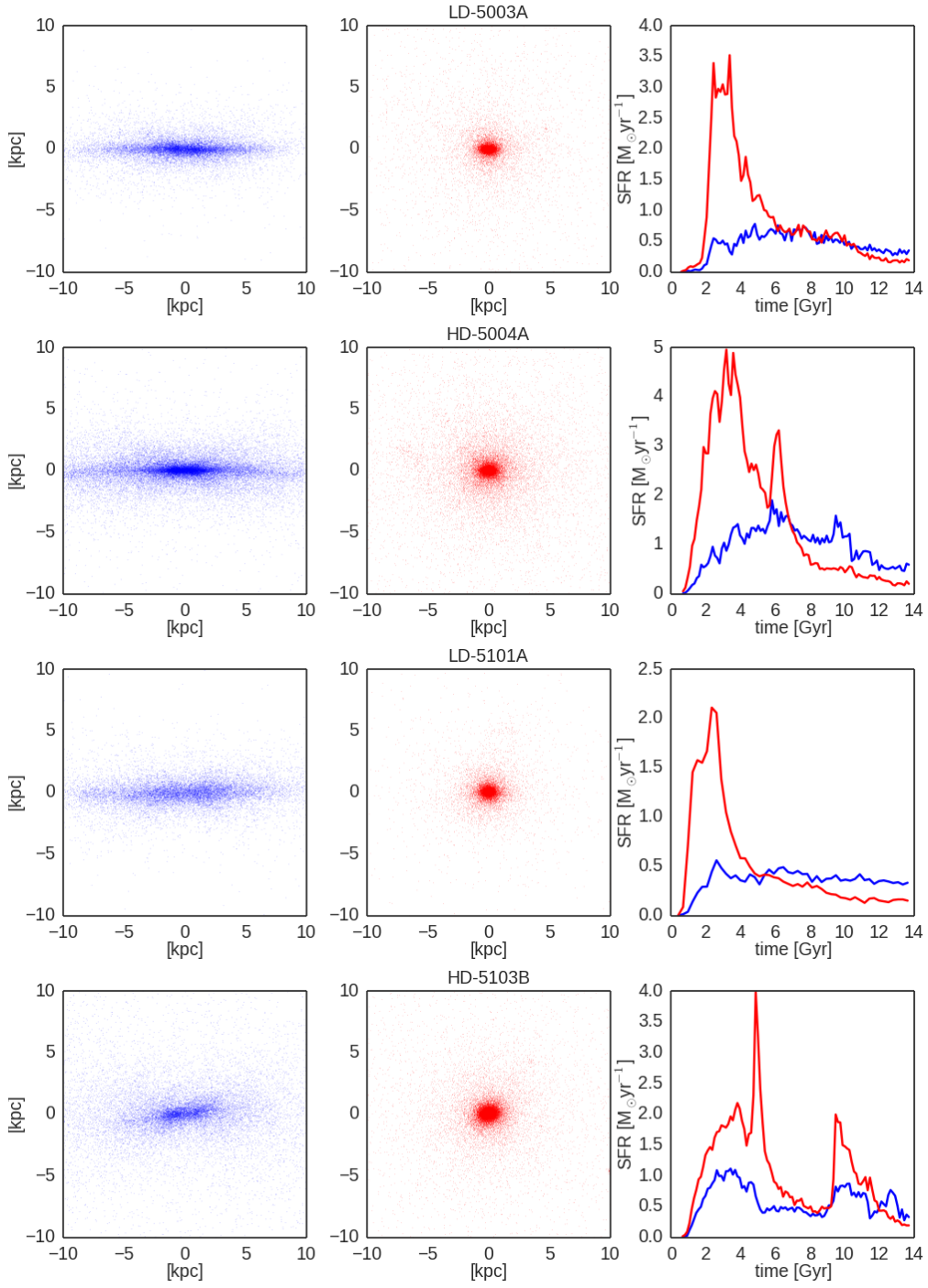

Figure 4.5: Edge-on projections of the disk (left, blue) and spheroid (center, red) stars of the four P-DEVA galaxies at $z = 0$ according to the kinematic classification, and their corresponding star formation histories (right).

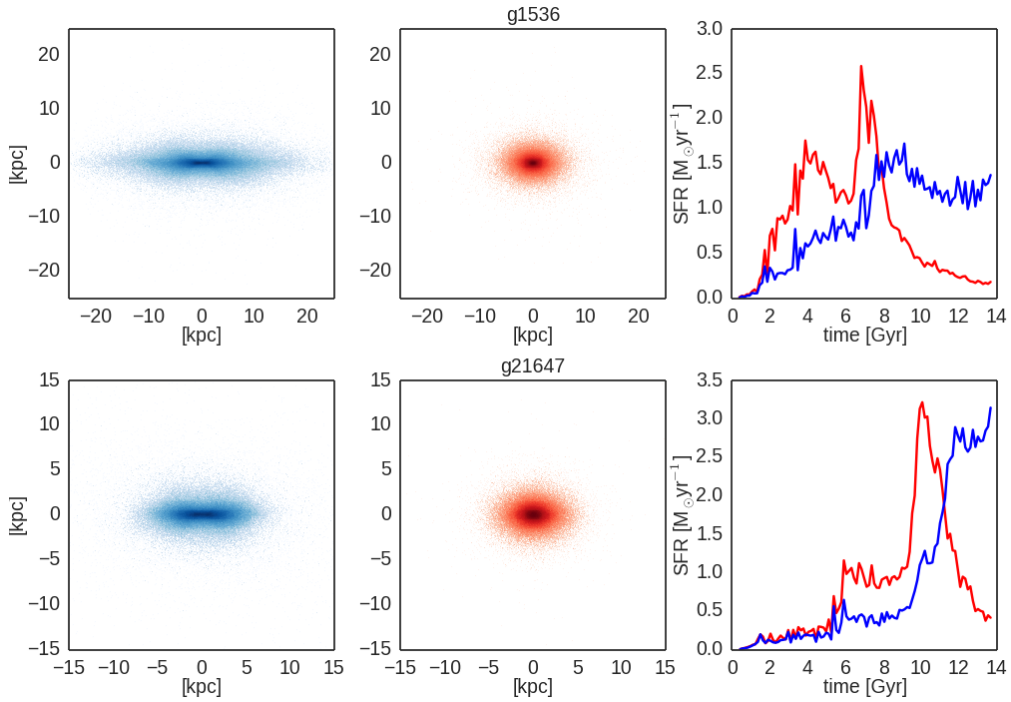

Figure 4.6: Edge-on projections of the disk (left, blue) and spheroid (center, red) stars of the two GASOLINE galaxies at $z = 0$ according to the kinematic classification, and their corresponding star formation histories (right). The projections are shown as logarithmic 2D histograms due to the large number of particles.

Chapter, an important fraction of their stellar-to-be particles are not inside the virial radii at collapse. In this case, important milestones are determined by angular momentum acquisition, too.

Following the previous sections, we see that chronologically ordered, important events/milestones are the following:

- **tidal torques in the Cosmic Web, up to turn-around at** z_{turn}.
- j **redistribution within the CW**: filaments get charged of j, and collimate it towards nodes where galaxies are to be formed.
- **collapse event at** z_{coll}, when most of the spheroid mass enters the virial radii, and filaments get blurred or removed.
- **old disk formation**, in general with its plane normal to the thicker filament.
- **torques at the circumgalactic region**, that add mass at the disk plane, and make the disk grow from circumgalactic material.

The physical basis for these processes has been introduced in Chapter 2. In the following subsections we develop the concepts by applying them to the mass assembly and angular momentum acquisition of our simulated set of galaxies.

Identifying the time of turn-around and collapse

As explained in Chapter 2, the spherical collapse theory predicts that an overdensity in an expanding universe grows faster than average until a given threshold, then it turns around, decoupling from the cosmic expansion, collapses and virializes. Collapse is not spherical, as the Zeldovich Approximation and the Adhesion model predict, and as numerical simulations confirm. However, the spherical collapse theory is successful at catching the more relevant patterns of halo formation, and, as such, it is very useful as a guide.

Therefore, the redshifts when turn-around and collapse events take place in the assembly history of our simulated galaxies (z_{turn} and z_{coll}, respectively) have been looked for. As we will see, in some cases their determination is clean; however, in other cases, mergers along the simulated galaxy assembly history make the determinations more complex.

Indeed, as we say, in practice the overdensities that grow to be the $z = 0$ halos with their embedded galaxies are not spherical, and as such we can not apply the formulas valid for the

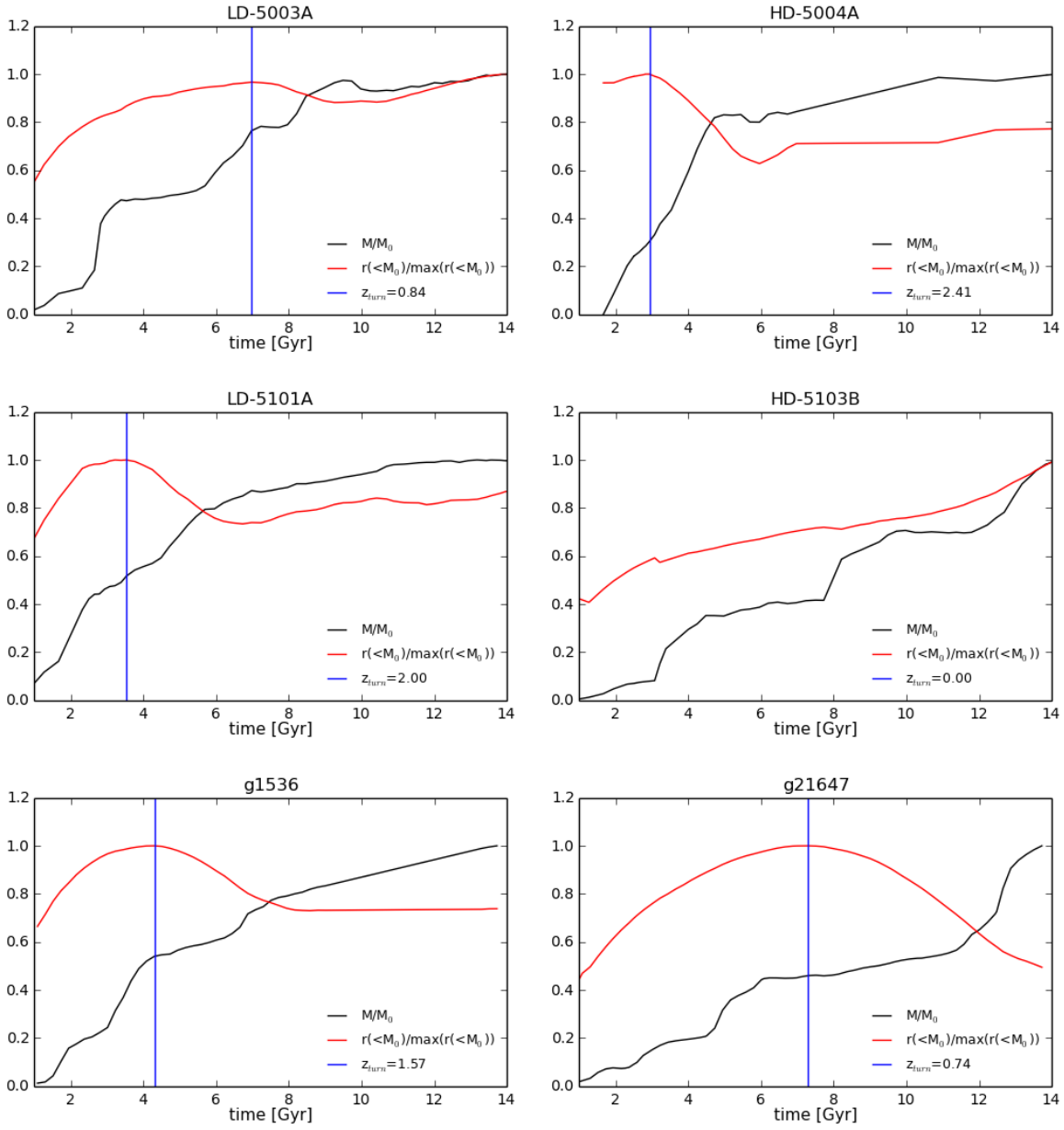

Figure 4.7: Evolution of the virial mass normalized to the $z = 0$ value (black curves) and of the radius enclosing the $z = 0$ halo mass normalized to its maximum value (red curves), for the six simulated galaxies. The redshift of turn-around or maximum expansion, z_{turn}, has been identified (when possible) as that corresponding to the maximum of the radius enclosing the $z = 0$ halo mass, and is shown as the blue line.

spherical collapse (equations 2.6, 2.7 and 2.8). We can, however, identify the moment of maximum expansion by looking at the evolution of the radius enclosing a fixed mass. Thus, we use the dark matter halo mass at $z = 0$, and going backwards in time we center our simulations on the halo progenitor and compute the radius that encloses this mass at each timestep.

The results of this exercise are shown in Figure 4.7, where the above mention radius, $r(< M_0)$, normalized to its maximum value is given in red. In five of the six simulated galaxies (LD-5003A, HD-5004A, LD-5101A, g1536 and g21647), a clear maximum is visible in these plots. For the galaxy HD-5103B, which suffers multiple major mergers, the radius enclosing fixed mass grows monotonically with time. These maxima give the times of the halos maximum expansion and can be identified as the turn-around redshifts, z_{turn}. In the same figure, we also show the evolutions of the virial mass normalized to the $z = 0$ value in solid black. These curves are very useful at identifying the mergers each halo experiences during their assembly.

This figure gives some important insights into the causes which determine the final appearance of our simulated galaxies (see Figures 4.5 and 4.6). The galaxy having the most extended disk (up to ∼25 kpc at $z = 0$), g1536 (bottom left panel in Figure 4.7), shows in particular a very clear evolutionary trend. The matter around the traced-back halo center expands until $z = 1.57$ and then contracts until $z \sim 0.6$. At this moment the system reaches virial equilibrium which is conserved until the present epoch, hence for almost 6 Gyr. Another notable aspect is that the merger epoch also reaches its end at about the same time, the subsequent growth in the virial mass being smooth (black curve in the same panel).

The two cases at the other extreme are g21647 and HD-5103. g21647 reaches maximum expansion at $z = 0.74$, but then the contraction phase extends all the way to the present epoch. As shown in the halo mass track in Figure 4.7, this galaxy suffered a recent (less than 2 Gyr ago) major merger which drives the particular final equilibrium state it reaches at $z = 0$. The merger is also associated with increased star formation rates. The spheroid shows a strong starbust previous to the two galaxies actually merging, which decays rapidly. The disk, on the other hand, increases its star formation rate more than two times, after the two galaxies form a bound object. Therefore, in this case we see pre-merger induced starburst in the spheroid and post-merger in the disk.

For the four galaxies (LD-5003A, LD-5101A, g1536 and HD-5004A) that show a clear sign of expansion at high-z and/or contraction later on, with a nicely stabilized radius enclosing a fix mass at later times (red curves in Figure 4.7), most of the star formation in the spheroid occurs prior to the time of virialization, when the radius enclosing a fixed mass either keeps constant or grows

slowly and smoothly.

The values of the turn-around redshifts for the six galaxies are given in Table 4.1, as z_{turn}.

As for z_{coll}, this moment can be identified in the panels of Figure 4.7 as the time when the radius enclosing the $z = 0$ halo mass stabilizes. Or, almost equivalently, as the time when time derivative of the virial mass (black curve in Figure 4.7) changes abruptly, indicating the end of the fast phase of mass assembly.

The values of the collapse redshifts for the six galaxies are given in Table 4.1, as z_{coll}.

4.4.3 Where did the gas forming the disk and spheroid come from?

In order to look for possible imprints left by Cosmic Web dynamics in the current stellar populations of late type galaxies, we have traced back these populations to their progenitors at high z. By plotting the positions of all the progenitors together, we confirm that they display a clear Cosmic Web-like structure before collapse, whose evolution follows the Adhesion Model. If we separately plot the positions of the progenitors of each component, we also find Cosmic Web-like configurations, but with different characteristics.

In Figures 4.8, 4.9, 4.10, 4.11, 4.12 and 4.13 we show projections of the disk and spheroid progenitors for the six galaxies at various redshifts. The two `GASOLINE` galaxies, g1536 and g21647, are shown in boxes of 600 kpc/side and in zoom of 180 kpc/side. The `P-DEVA` galaxies, LD-5003A, HD-5004A, LD-5101A and HD-5103B, are shown in boxes of 600 kpc/side and in zoom of 60 kpc/side.

In the case of g1536 shown in Figure 4.8, the progenitor gas of the disk (blue) and spheroid (red) trace very similar web–like structures at high-z (3.42). As the evolution proceeds, the spheroid progenitor gas shrinks on shorter timescales, such that by $z = 1.88$ the distinction is already clear, with the disk material still traces the remains of the high z–web. The visual difference between the two increases as time goes by, and so by $z = 0.82$, slightly after z_{coll} for this object, all spheroid material is within the virial radius, and has already been transformed into stars. This galaxy forms most of its extended disk from $z = 1$ onwards. In the last timestep shown ($z = 0.82$) we still can see the disk progenitor gas spanning a wide region, while, as said, most of the spheroid is concentrated.

A messier behavior can be observed in Figure 4.9, where we show g21647 at $z = 3.42$, 2.00, 1.07 and 0.20. In this case, there is less distinction between the spheroid and disk projections, both showing very similar high-z webs. For this galaxy, as previously explained, the collapse continues all the way from $z_{turn} = 0.74$ to the present epoch, most of the stars of both spheroid and disk

forming after this time (red curve in the bottom right panel of Figure 4.7). The major merger seen in the $z = 1.07$ panel is the trigger for the very strong starburst seen in the spheroid progenitor gas (red curve in th bottom right panel of Figure 4.6).

We turn now to the `P-DEVA` galaxies shown in similar projections plots in Figures 4.10 to 4.13. These galaxies have a ten times lower resolution and, for that reason, appear more washed out. For all four galaxies, we see the same web-like filamentary structure at high z, which disappears as evolution proceeds, first for the spheroid progenitors and later for the disk. A noticeable difference between these four galaxies and the previous two is given by the larger number of satellites in the former with respect to the later. This is a direct consequence of the differences in the star formation implementations in the two codes. `P-DEVA` uses a low efficiency for star formation in order to account for the unresolved stellar feedback related processes. Following dark matter, gas in filaments tends to fragment in nodes, where spheroid-to-be stars form (see the corresponding star formation rate histories in Figure 4.5), with small gaseous disks around them. In this case, it is j conservation combined with a low SF efficiency, that prevents gas from being completely transformed into stars.

Gas fragmentation happens to a much lesser extent in the `GASOLINE` runs because the explicit feedback partially prevents gas from cooling and hence from collapsing, delaying star formation, see Figure 4.5.

We will look in more detail at HD-5004A (see Figure 4.11), that has been thoroughly discussed in Domínguez-Tenreiro et al. (2015). Here we expand what was said in this paper. As said there, the visual impression is that spheroid progenitors have been involved in multistreaming events from earlier on than disk progenitors, in such a way that at given z, they form a web-like structure whose dynamical state is more advanced than corresponding to the disk. This more advanced stage of gravitational instability can be characterized mainly through the distributions of density and vorticity of gas elements (the vorticity closely follows the density), that are biased towards higher values than less advanced ones. In addition, spheroid-to-be particles have a tendency to be closer to the system center of mass than disk progenitors. Also the first form more stars within the (disconnected) densest nodes before collapse, from low spin material. The rich spin gas particles within these clumps form small disks around the stellar centers, which are clearly visible in the 60 kpc/side zoom in the bottom panels of the same figure.

This figure also indicates that by the time of collapse $z_{coll} \backsimeq 1.45$ (third column from left to right) most spheroid-to-be particles are within the halo and roughly half of them have already

turned into stars, while part of the disk predecessors are still being assembled as diffuse gas into a gaseous disk. This moment can also be roughly identified in the upper right panel of Figure 4.7 as the time when the radius enclosing the $z = 0$ halo mass stabilizes. In the Figure 4.5 we can see that the star formation in the spheroid gas reaches its maximum at about the time of maximum expansion ($z_{turn} = 2.41$). The baryon mass assembly of the spheroid population occurs mostly at $z > z_{coll}$ through collapse-induced merging, that is, along the so-called *fast phase* of galaxy evolution (e.g. Obreja et al. 2013). In this case it is the proximity to the patch center that segregates those particles that will be involved in the collapse, and suffer from severe j loses from those that will not.

In the right most panels we plot the disk and spheroid progenitors of HD-5004A at $z = 1.07$, when the system has decoupled from expansion and filaments at the virial scale are significantly weaker than at earlier times. At this point, when the the proto-disk is settled, it causes gravitational torques at the disk scale that tend to change j (see Chapter 2). One of the effects of these torques is to gradually align gaseous particles (either diffuse or in satellites) with the main disk (Danovich et al. 2014) through j-precession driven energy dissipation (see the physical reasons at Chapter 2), placing them in the configuration of minimum energy in an axisymmetric potential (see Binney's book), i.e., circular orbits in a plane normal to the potential axis, in this case a thin disk in the outskirts of the old disk plane. Summing up, we see that once a proto-disk is settled, it ideally attracts gas particles that self align to grow this disk. Collisionless mass elements cannot dissipate their energy, therefore they are not prone to reach the configuration of minimum energy in a thin plane normal to the disk axis. The important point here is that while well aligned material (either originally or as a consequence of gravitational torques) is incorporated to the (thin) disk, the rest of the material is not.

Note that in these cases, the Cosmic Web evolution has provided different initial conditions for the torques to act upon.

A very similar behavior is shown up in Figures 4.8 and 4.12. Also, a similar behavior, once we take into account the effects of mergers occurred along their lifespan, can be found in Figures 4.9, 4.10, and 4.13. Particularly remarkable is the fact that these galaxies have grown disks after major mergers.

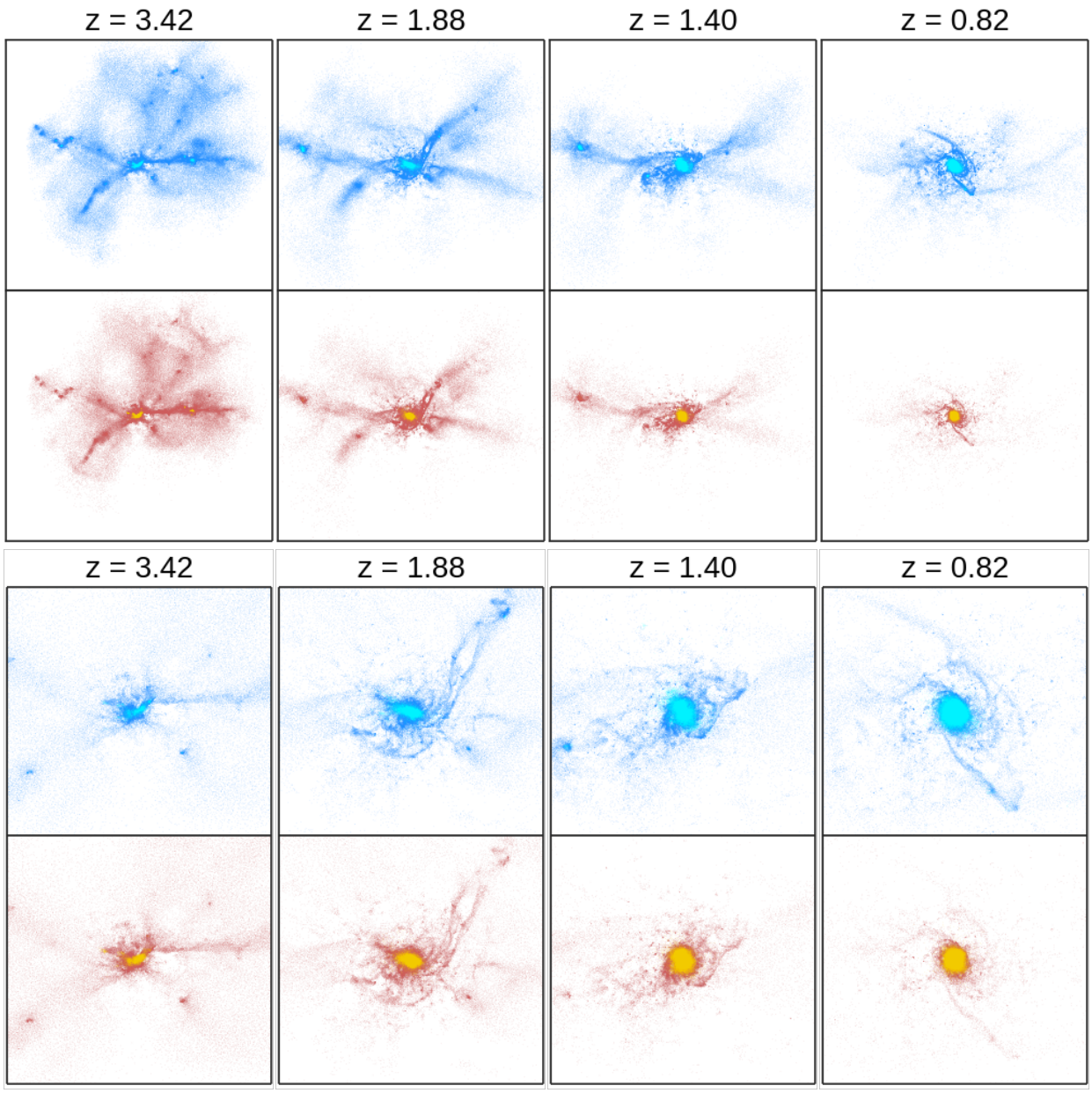

Figure 4.8: One projection of the progenitor baryons of the disk and spheroid of g1536 at four different zs. Upper two rows show 600 kpc/side panels, while the bottom two show the corresponding zoom in 180 kpc/side. Blue (cyan) stands for progenitor disk gas (stars), while red (yellow) for progenitor spheroid gas (stars).

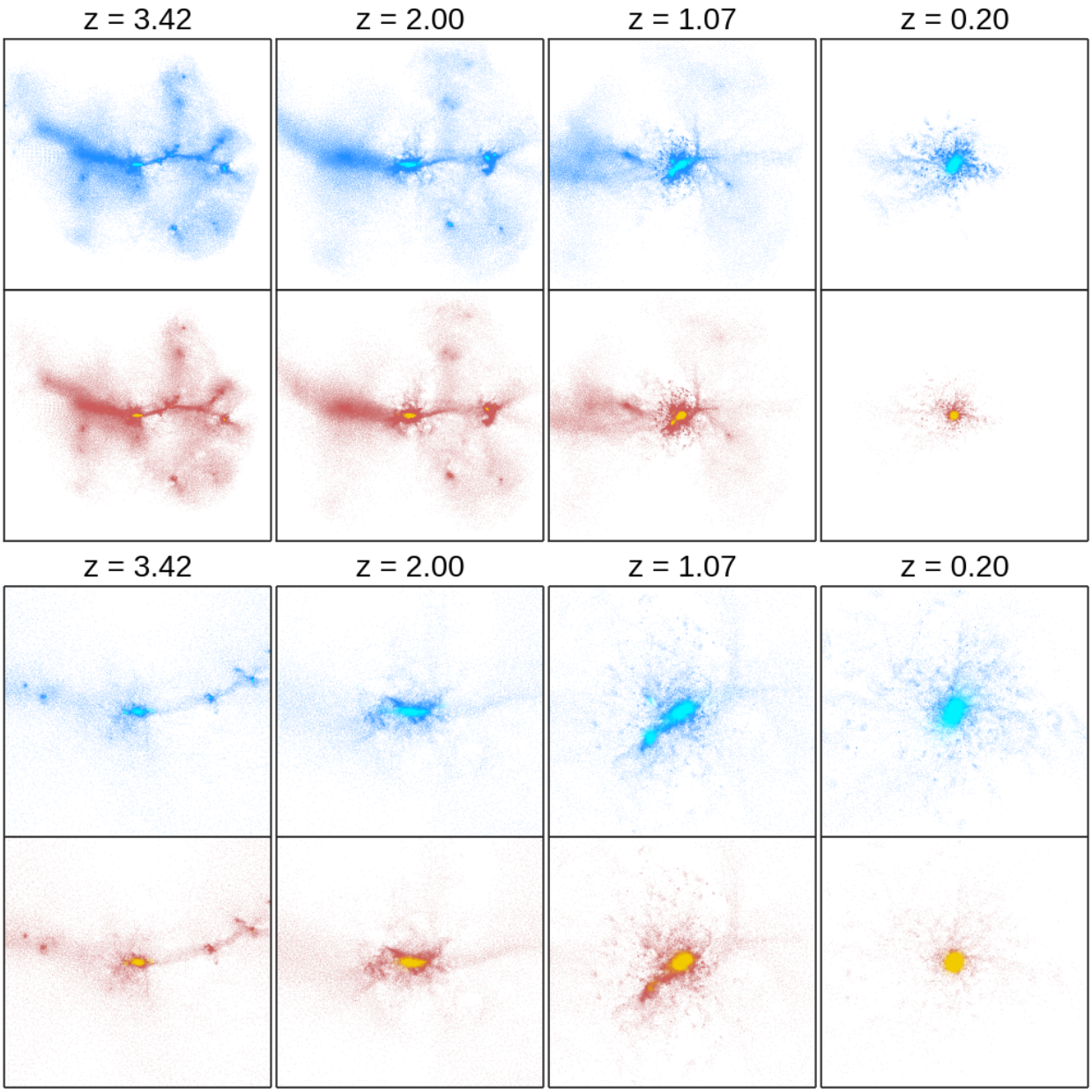

Figure 4.9: One projection of the progenitor baryons of the disk and spheroid of g21647 at four different zs. The panel sizes and colors are the same as in Figure 4.8.

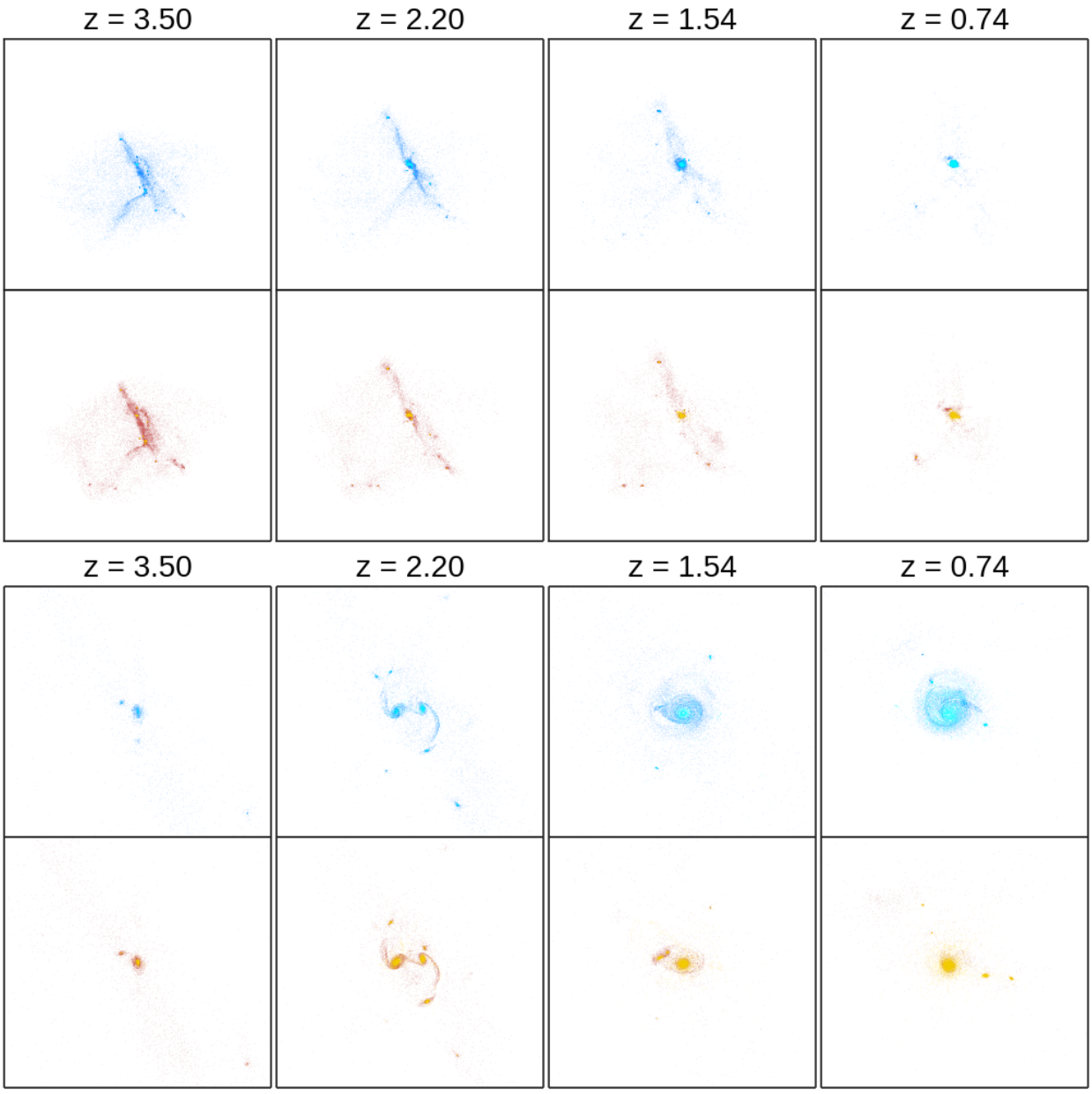

Figure 4.10: One projection of the progenitor baryons of the disk and spheroid of LD-5003A at four different zs. The colors are the same as in Figure 4.8. The panel sizes are 600 kpc/side and 60 kpc/side for the upper and lower two rows, respectively.

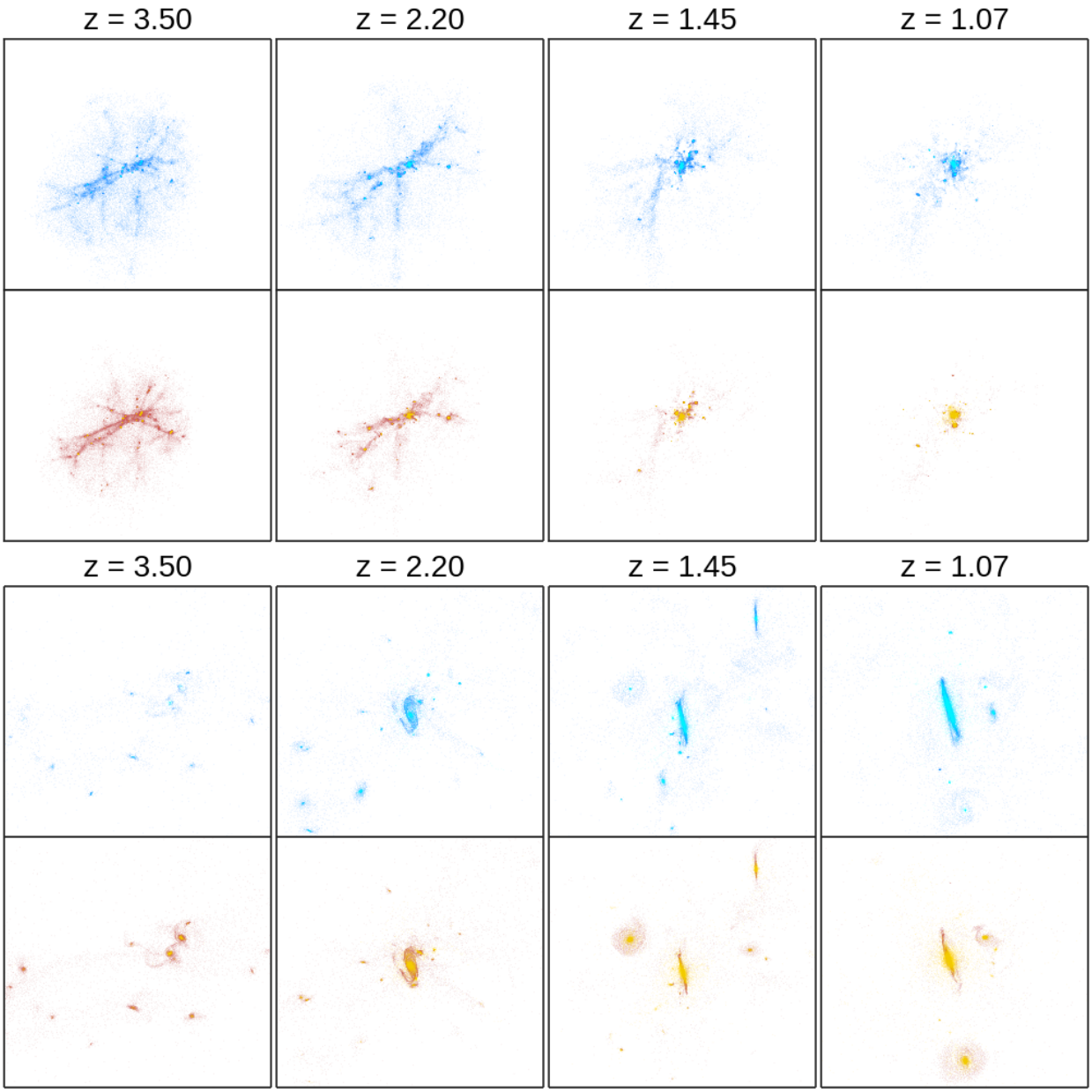

Figure 4.11: One projection of the progenitor baryons of the disk and spheroid of HD-5004A at four different zs. The panel sizes and colors are the same as in Figure 4.10.

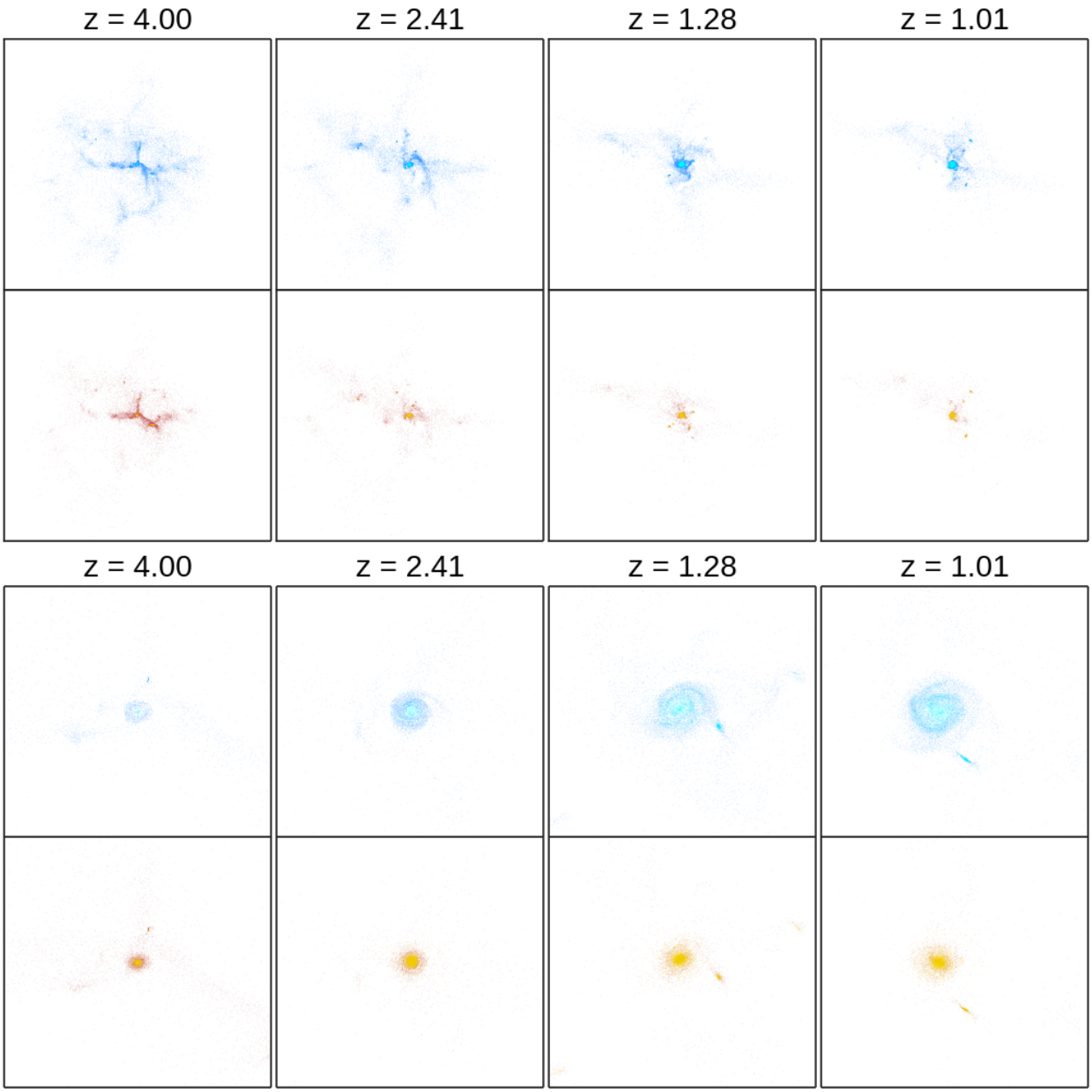

Figure 4.12: One projection of the progenitor baryons of the disk and spheroid of LD-5101A at four different zs. The panel sizes and colors are the same as in Figure 4.10.

Figure 4.13: One projection of the progenitor baryons of the disk and spheroid of HD-5103B at four different zs. The panel sizes and colors are the same as in Figure 4.10.

4.4.4 Distributions of positions, angular momenta and densities

In this section we expand the results presented on this subject by Domínguez-Tenreiro et al. (2015) to the whole sample of simulated galaxies, and we give some more details on the corresponding physical aspects discussed therein.

The visual differences in Figures 4.8 to 4.13 have been quantified by means of a V-Web-inspired method (Hoffman et al. 2012). For a given simulated galaxy and different zs, the SPH density ρ, distances r and angular momenta j, relative to the system c.o.m, for gaseous and stellar particles at the corresponding zs have been calculated, as well as their respective probability distribution functions (PDFs). The results confirm the visual impression that the spheroid-to-be gas particles are the first to be involved in shell-crossing events.

Therefore, we show show in Figures 4.14, 4.15 and 4.16 the PDFs of the distances and specific angular momenta for the disk and spheroid progenitors, normalized to the total number of baryon mass (i.e., gas and stellar mass) in each component (spheroid and disk), so that the relative numbers of gas (red and blue lines) and stellar masses (yellow and cyan) are meaningful. We also plot, on the right panels, the CDFs of the corresponding gas density, for the whole sample, at the same zs as in the previous projection plots. The vorticity closely follows the density, and as such we do not show it in these figures. In this figures, we see disk gas having more extended tails towards larger distances than the spheroid gas, as expected also from the visual impression in the projection plots discussed earlier.

The CDFs on the right show that the spheroid-to-be gas particles are the first to reach the highest densities, mapping out the Cosmic Web element locations, after, in some cases (when mergers are important) a less marked difference at the highest zs plotted in these Figures. Indeed, the distinction between the two curves is somewhat blurred in the cases where important merging activity occurs (e.g. HD-5103 shown in the right panels of Figure 4.16).

In addition, these figures confirm that the spheroid-to-be particles (red) are, *at any* z, closer to the system c.o.m. than the disk (blue) progenitors (first column), and therefore have a lower probability of being j-rich (i.e., lever effect, second column). The relative differences in the distance PDFs are particularly important at the inner region.

By contrast, proto-disk particles are further away, and therefore not significantly affected by the collapse. Many proto-disk particles enter the halo as j-rich gas particles later on, where they fall to the central regions as they lose j in a more gradual manner (narrow low j component at the

left). The j content of the gas of the disk component is increased as time goes by, because delayed particles have a higher j since they come from further away (lever effect, see Section 2.3).

The corresponding specific angular momentum PDFs (same figures) show the same behavior as the distance ones, having larger tail at high j for the disk progenitors than for the spheroid ones (see the discussion on the lever effect in Chapter 2). For the `P-DEVA` galaxies in Figures 4.15 and 4.16, at low values of j, the stars tracks the corresponding gas distribution, either for the disk or the spheroid, and show an excess at the lowest j. This peak is a consequence of star formation preferentially occurring in the lowest angular momentum gas. For the `GASOLINE` galaxies in Figure 4.14 the situation is a bit different, with gas having a wider distribution than the corresponding stars.

4.4.5 Evolution of specific angular momentum

Another important aspect in the evolution of our simulated galaxies is the global gain and loss of angular momentum. To study this aspect we have computed the global specific angular momentum for all the baryons progenitors of the $z = 0$ stellar populations of the galaxies, as well as that of the spheroid and disk progenitors separately. Therefore, we show in Figure 4.17 the evolution of specific angular momenta for the traced-back stellar populations at $z = 0$. We distinguish on one hand between disk and spheroid progenitors, and on the other, within the first classification between stars and gas.

If we first look at the full traced-back stellar population (thick grey curves) we see cases in which it stays constant (HD-5004A), grows all the way to $z = 0$ (LD-5101A) or grows initially and then decays (LD-5003A, HD-5103B, g1536, g21647). LD-5003A has a more peculiar behavior showing a late phase of j-increase. The disk stars–to–be at $z = 0$ (solid blue curves), for the cases in which the total j decreases at later times, show the same behavior but less marked. However, the spheroid stars–to–be at $z = 0$ suffer severe loss of angular momentum at collapse (solid red curves), the difference between their maximum j and the final one being at least an order of magnitude. The marked peaks in all three tracks (thick grey and solid blue and red curves) are caused by major mergers (see Figures 4.13 and 4.9 for the assembly patterns of the disk and spheroid of HD-5103B and g21647, respectively).

In all six simulated galaxies, we see that the angular momentum of the spheroid progenitors is lower than that of the disk ones. This is an expected results since we know that disk progenitors have a larger spatial extent, therefore are further away from the center of mass, and as a consequence have higher-j than spheroid ones. Both have similar increases at high-z, as predicted by the Tidal

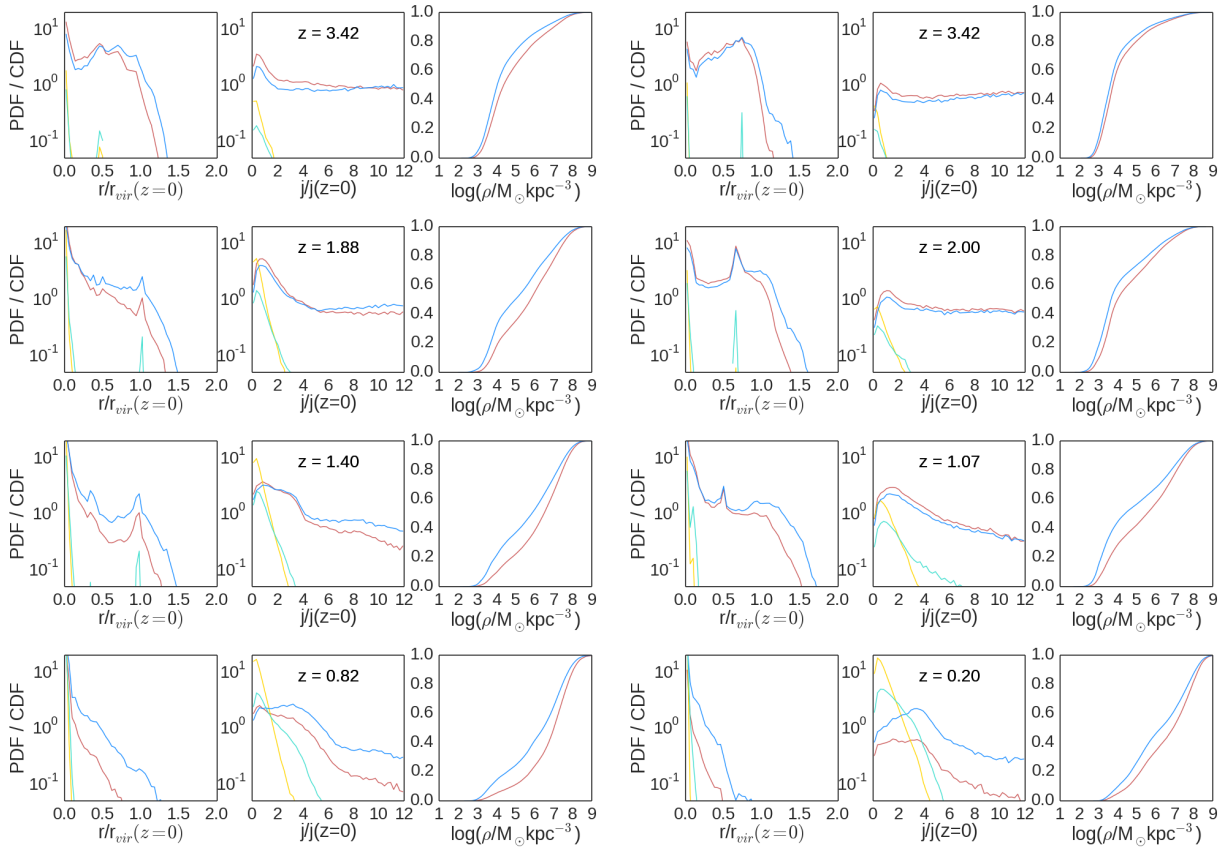

Figure 4.14: PDFs for r and j, and CDF for ρ measured on g1536 (left) and g21647 (right) galaxies-to-be particles at different zs values. Red (blue) lines stand for gaseous spheroid (disk) precursors, while orange (cyan) lines refer to spheroid (disk) precursors particles that are already stellar at the respective zs. The vertical normalization has been separately taken for the two kinds of precursors, including in any case both the gas and the stars. Distance units are the virial radii at $z = 0$, while j is given in units of the total baryonic (spheroid + disk) specific angular momenta at $z = 0$ (see Table 4.1).

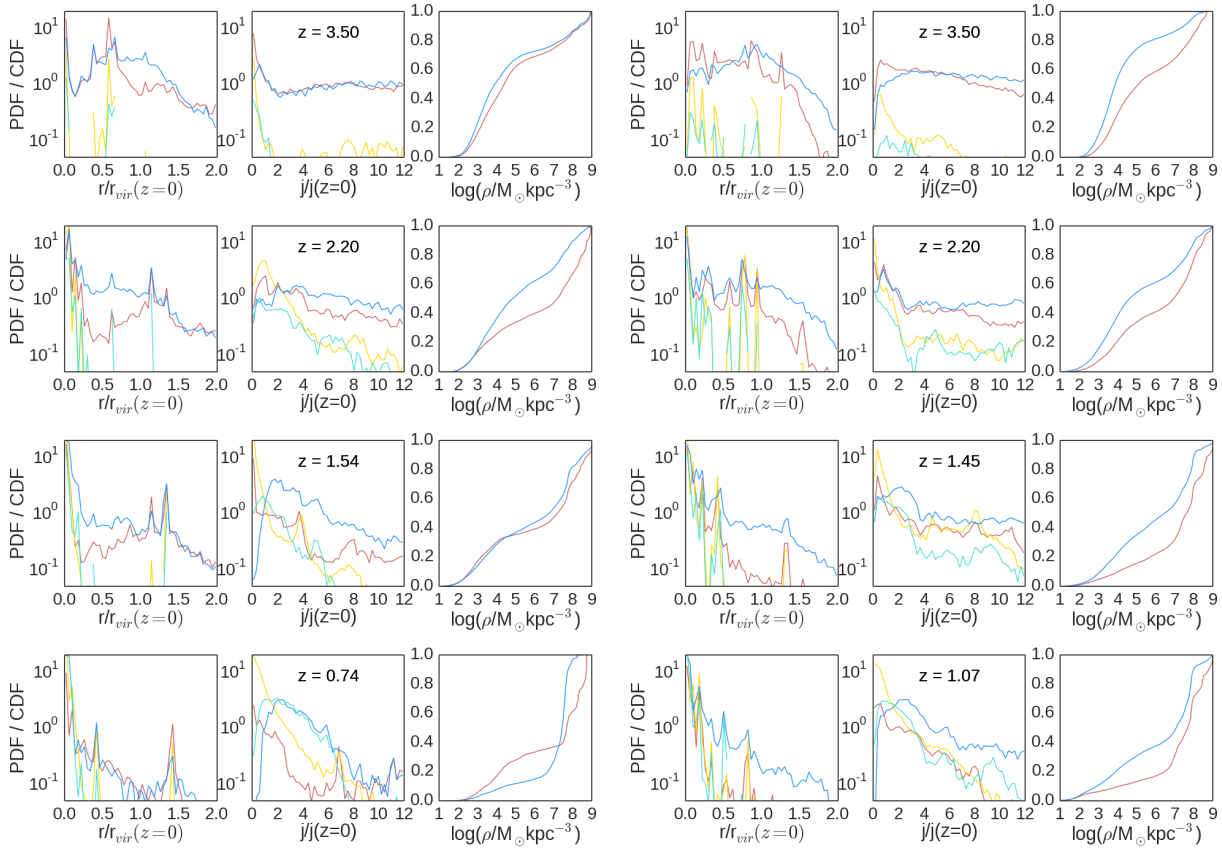

Figure 4.15: Same as Figure 4.14 for galaxies LD-5003A (left) and HD-5004 (right).

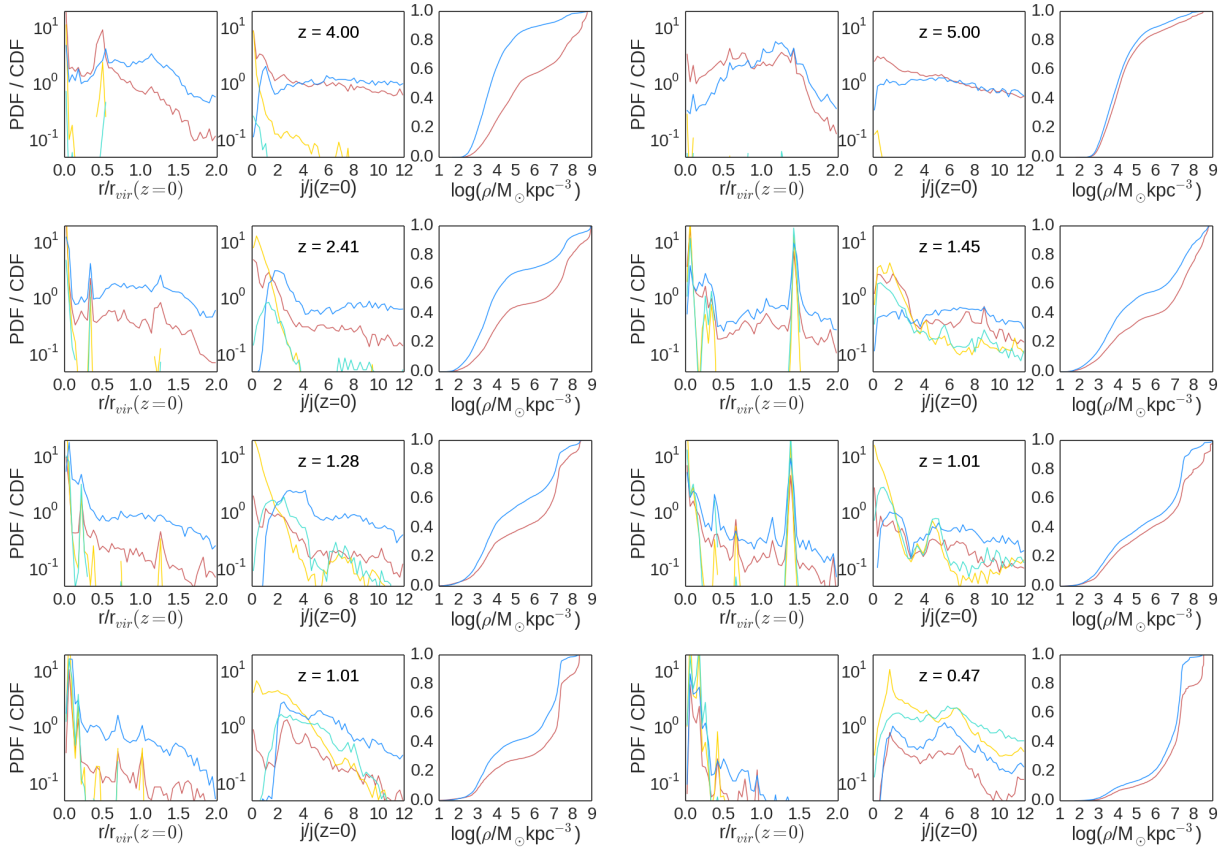

Figure 4.16: Same as Figure 4.14 for galaxies LD-5101A (left) and HD-5103 (right).

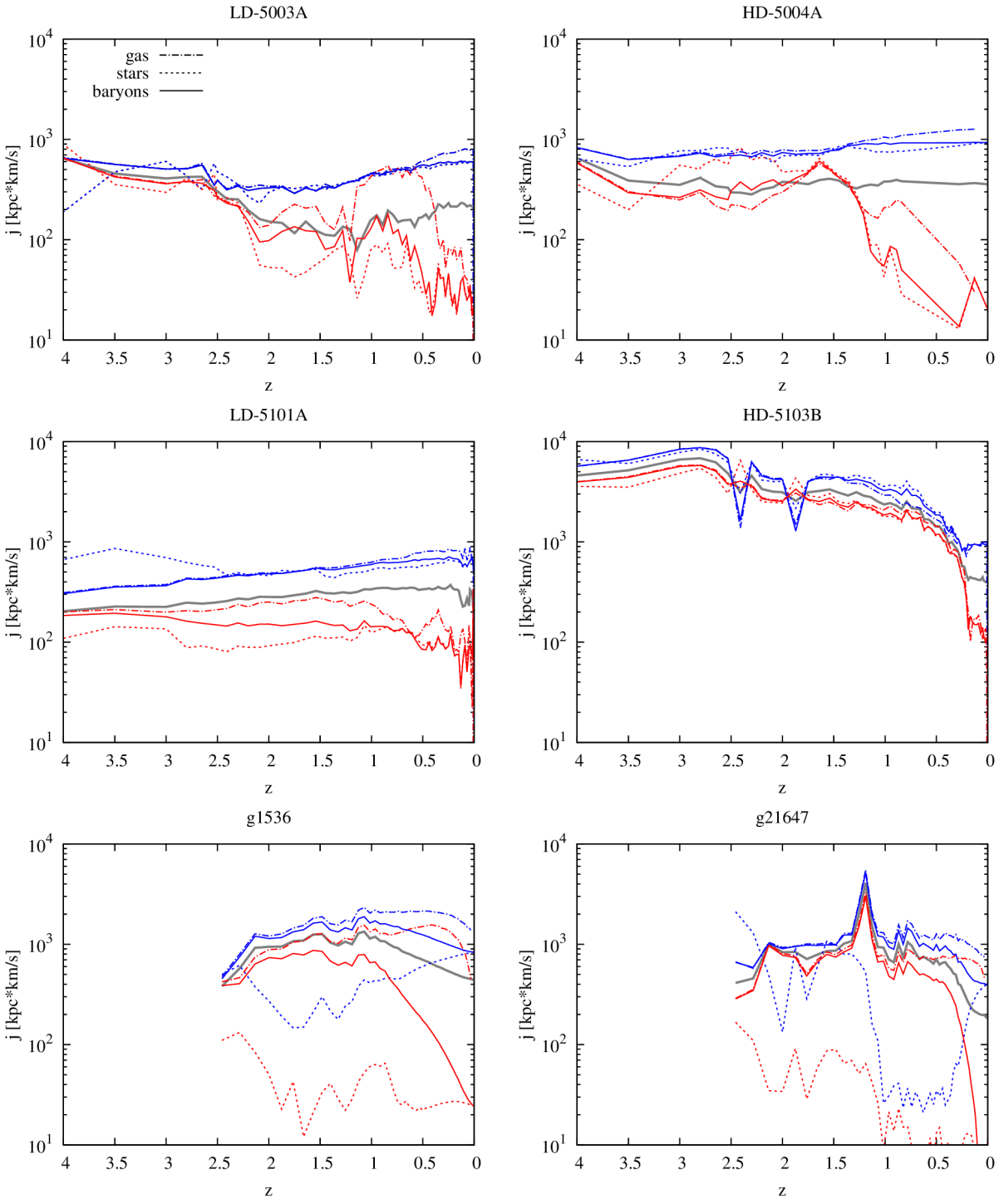

Figure 4.17: Specific angular momentum evolution of the disk (blue) and spheroid (red) for the six simulated galaxies. The thick grey line gives the specific angular momentum of all traced back baryons.

Torque Theory (see Chapter 2), however, spheroid progenitors lose most of the angular momentum they gain up to the time of maximum expansion in their subsequent fast collapse, while the disk-to-be-stars keep most of their initial angular momentum.

The fact that in some of the cases, the total specific angular momentum of the traced-back populations (grey curves) decreases at later times could be due to late merging activity, certainly present in HD-5103B and g12647. Note, however, and this is the relevant point, that by $z = 0$ the specific angular momentum of the stellar disk component is, in all but the g21647 galaxy, around $j = 10^3$ kpc $\times$ km/s.

4.4.6 Summary and conclusions

We have studied the assembly patterns of a sample of six late type simulated galaxies with the aim of understanding the connection between the formation of galactic scale components (spheroids vs disks) and the dynamics of the Cosmic Web. The first question we wanted to answer is whether the Cosmic Web influences/drives the formation of the rotational and non-rotational supported galactic structures, and if so to what extent and by what processes.

For these purposes, we have used a sample of six simulated galaxies in a cosmological context, run with two different SPH codes. The main difference between the two codes is the star formation implementation. `P-DEVA` takes into account the stellar feedback implicitly by assuming a low star formation efficiency, while `GASOLINE` uses an explicit feedback scheme by injecting supernova energy as thermal energy in the surrounding gas.

These galaxies have kinematically distinguishable disks and spheroids, which have been classified as such using stellar kinematic variables with a clustering algorithm (k-means).

Tracing back the progenitors of the disks and spheroids, we have found that both display web like structures at high-z, albeit with different spatial extensions. The collapse of the spheroid web comes first than that of the disk one. This happens at any scale, i.e., not only at the halo scale. In fact, spheroid to be particles form very early nodes within filaments where stars form, while disk progenitors delay their incorporation into filaments, and when they do so, they do not collapse into nodes, and they do not form stars that early. Another interesting finding is that spheroid-to-be particles tend to be closer the the system's center of mass and therefore have lower angular momentum than disk progenitors.

The build up of angular momentum in the high-z universe proceeds similar for the disk and spheroid progenitors, as described by the Tidal Torque Theory. The difference in the final equi-

librium stage of the system comes from the evolution of the matter patches between the time of maximum expansion, when they decouple from the background, and the time when the first disk settles. Between these times, spheroid progenitors undergo a fast collapse at halo scale, losing most of their angular momentum and form stars in relatively short times, an important fraction prior to halo collapse event. Disk progenitors, on the other hand, accrete onto the halos at slower pace, over more extended times and conserve a large fraction of their initial angular momentum. The disk star formation occurs at lower rates than the spheroid one and over longer times, in most cases already in the disk.

Gaseous disk progenitors elements are prone to be aligned with the first settled proto-disk into thin disk configurations, due to their energy loses as a consequence of differential j precession at the circumgalactic regions as a consequence of disk induced torques. As a consequence, they can access the minimum energy configuration in an axisymmetric potential. In contrast, stellar particles are not likely to be incorporated into this plane configuration because they can not lose energy.

These results suggest that the spheroid and disk stellar populations of local galaxies keep partial memory of the Cosmic Web dynamics at high z.

References

Agertz, O., Teyssier, R., & Moore, B. 2011, MNRAS, 410, 1391

Binney, J. 1977, ApJ, 215, 492

Birnboim, Y., & Dekel, A. 2003, MNRAS, 345, 349

Bond, J. R., Kofman, L., & Pogosyan, D. 1996, Nature, 380, 603

Brook, C. B., Stinson, G., Gibson, B. K., Wadsley, J., & Quinn, T. 2012a, MNRAS, 424, 1275

Brook, C. B., Stinson, G. S., Gibson, B. K., et al. 2012b, MNRAS, 426, 690

Brooks, A. M., Governato, F., Quinn, T., Brook, C. B., & Wadsley, J. 2009, ApJ, 694, 396

Cautun, M., van de Weygaert, R., Jones, B. J. T., & Frenk, C. S. 2014, ArXiv e-prints

Codis, S., Pichon, C., Devriendt, J., et al. 2012, MNRAS, 427, 3320

Danovich, M., Dekel, A., Hahn, O., Ceverino, D., & Primack, J. 2014, ArXiv e-prints

Danovich, M., Dekel, A., Hahn, O., & Teyssier, R. 2012, MNRAS, 422, 1732

Dhillon, I., Guan, Y., & Kulis, B. 2004, A unified view of kernel k-means, spectral clustering and graph cuts, Tech. Rep. TR-04-25, University of Texas at Austin, Department of Computer Sciences

Doménech-Moral, M., Martínez-Serrano, F. J., Domínguez-Tenreiro, R., & Serna, A. 2012, MNRAS, 421, 2510

Domínguez-Tenreiro, R., Oñorbe, J., Martínez-Serrano, F., & Serna, A. 2011, MNRAS, 413, 3022

Domínguez-Tenreiro, R., Obreja, A., Granato, G. L., et al. 2014, MNRAS, 439, 3868

Domínguez-Tenreiro, R., Obreja, A., Brook, C. B., Martínez-Serrano, F. J., Stinson, G., & Serna, A. 2015, ApJ, 800, L30

Doroshkevich, A. G. 1970, Astrophysics, 6, 320

Dubois, Y., Pichon, C., Welker, C., Le Borgne, D., & et al. 2014, MNRAS, 444, 1453

Gilmore, G., Wyse, R. F. G., & Kuijken, K. 1989, ARA&A, 27, 555

Gurbatov, S. N., Saichev, A. I., & Shandarin, S. F. 1989, MNRAS, 236, 385

—. 2012, Physics Uspekhi, 55, 223

Hoffman, Y., Metuki, O., Yepes, G., et al. 2012, MNRAS, 425, 2049

Ivezić, Ž., Beers, T. C., & Jurić, M. 2012, ARA&A, 50, 251

Karatzoglou, A., Smola, A., & Hornik, K. 2004, Journal of Statistical Software, 1

Kereš, D., Katz, N., Fardal, M., Davé, R., & Weinberg, D. H. 2009, MNRAS, 395, 160

Kereš, D., Katz, N., Weinberg, D. H., & Davé, R. 2005, MNRAS, 363, 2

Kimm, T., Devriendt, J., Slyz, A., et al. 2011, ArXiv e-prints

Kofman, L., Pogosian, D., & Shandarin, S. 1990, MNRAS, 242, 200

Martínez-Serrano, F. J., Serna, A., Domínguez-Tenreiro, R., & Mollá, M. 2008, MNRAS, 388, 39

Mould, J. R. 1982, ARA&A, 20, 91

Obreja, A., Brook, C. B., Stinson, G., et al. 2014, MNRAS, 442, 1794

Obreja, A., Domínguez-Tenreiro, R., Brook, C., et al. 2013, ApJ, 763, 26

Ocvirk, P., Pichon, C., & Teyssier, R. 2008, MNRAS, 390, 1326

Peebles, P. J. E. 1969, ApJ, 155, 393

Pichon, C., Pogosyan, D., Kimm, T., et al. 2011, MNRAS, 418, 2493

Sales, L. V., Navarro, J. F., Theuns, T., et al. 2012, MNRAS, 423, 1544

Sánchez-Blázquez, P., Courty, S., Gibson, B. K., & Brook, C. B. 2009, MNRAS, 398, 591

Schölkopf, B., Smola, A., & Müller, K.-R. 1998, Neural Comput., 10, 1299

Serna, A., Domínguez-Tenreiro, R., & Sáiz, A. 2003, ApJ, 597, 878

Stewart, K. R., Brooks, A. M., Bullock, J. S., et al. 2013, ApJ, 769, 74

Stinson, G., Seth, A., Katz, N., et al. 2006, MNRAS, 373, 1074

Stinson, G., Brook, C., Macciò, A. V., et al. 2013, MNRAS, 428, 129

Talbot, Jr., R. J., & Arnett, W. D. 1973, ApJ, 186, 51

Tillson, H., Devriendt, J., Slyz, A., Miller, L., & Pichon, C. 2012, ArXiv e-prints

van de Voort, F., Schaye, J., Booth, C. M., Haas, M. R., & Dalla Vecchia, C. 2011, MNRAS, 414, 2458

Wadsley, J. W., Stadel, J., & Quinn, T. 2004, New Astronomy, 9, 137

Welker, C., Devriendt, J., Dubois, Y., Pichon, C., & Peirani, S. 2014, ArXiv e-prints

White, S. D. M. 1984, ApJ, 286, 38

Zel'dovich, Y. B. 1970, A&A, 5, 84

Chapter 5

Thick versus thin disks

5.1 Introduction

As mentioned in a previous chapters, the stellar populations in the disk of galaxies can be split into two distinct groups: the thin and the thick disk. It has been pointed out by different authors that other subcomponents can also be considered: metal-poor thin disk, metal-rich thick disk (see, for example, Adibekyan et al. 2012, and references therein), but in this work we focus on the simpler classification of the disk stellar populations into thin and thick components.

The standard view from observational data (Mould 1982; Gilmore et al. 1989, 1995; Fuhrmann 1998; Bensby et al. 2003; Soubiran et al. 2003; Reddy et al. 2006; Ivezić et al. 2012) is that the differences among these two components involve: i) shape: the vertical scale-length is smaller for the thin disk component than for the thick one, ii) kinematic aspects: the thin disk is colder than the thick disk, no matter the velocity component; it is more rotationally supported than the thick disk, iii) the age of the stellar populations: thick disk stars are older on average, iv) metallicity: the thin disk populations are metal richer than thick disk ones, and v) α-element enrichment.

While authors agree on the statements above, different methods to quantify the differences and to accurately assign a given star to the thin or thick populations, can be found in literature. Additional difficulties come from the current limitations to the stellar age determinations, as well as to the metallicity and α-element enrichment. These difficulties and the possibility that there is not a clean cut in the differences imply that there is no simple way to unambiguously classify stellar populations.

Some authors' classification rests on the chemical properties (i.e., the [α/Fe] vs [Fe/H] or other similar plots (see, for example, Bovy et al. (2012) or Adibekyan et al. (2012) and references therein)

as a reflection of the stellar age. Other authors use directly the stellar age, as a characterization of the different physical conditions prevailing at the thick or thin disk formation epoch, i.e., the different properties of the gas the two populations of stars formed from (Haywood et al. 2013).

A physical sound classification scheme is the kinematic one, as explained in Chapter 4. This kind of scheme has mostly been used in hydrodynamical simulations (e.g. Abadi et al. 2003; Doménech-Moral et al. 2012), but also in observations (Soubiran et al. 2003; Bensby et al. 2003).

In this Chapter we analyze the origin of the thin disk relative to the thick disk, using two of the galaxies presented in the previous chapters, namely HD-5004A and g1536 (see Section 4.2 for a description of the simulations and Table 4.1 for some relevant parameters).

The first task in this respect is to make sure that we do have thin and thick disks in our simulated galaxies, with properties similar to those found in observational data. A detailed analysis of different correlations shown by these two components in a sample of `P-DEVA` galaxies can be found in Doménech-Moral et al. (2012). In what follows we go deeper into these relations, focusing on their comparison to recent observational data.

Best quality data come from stars in the solar neighborhood. Haywood et al. (2013) have analyzed a sample of solar neighborhood stars with high-quality abundance data (Adibekyan et al. 2012, and references therein). They have determined the age of a subsample of 363 FGK stars for which kinematic data and maximum vertical height from the disk plane, z_{max}, are available. They have made a careful study of the thin and thick disk populations involving all these variables and their correlations. Therefore, we take it as a first basis of our comparison to observational data, using it to analyze the possible correlations between shape, kinematics, age, and chemical abundances.

Two classification schemes have been used by these authors: i) a chemical one, based on the [α/Fe] vs [Fe/H] plot for this sample, and ii) a stellar-age one, based on the [α/Fe] vs age behavior, where the age separation comes from a clear knee at age 8 Gyears in this plot. The analysis of the sample based on the one or the other classification schemes does not result in relevant differences.

Our simulated galaxies show a well-defined knee-like [α/Fe] vs age plot, allowing us to clearly determine the age separation for each of them. However, the patterns found in the [α/Fe] vs [Fe/H] plot for the solar vicinity do not unambiguously show up in the plots corresponding to the different simulated galaxies, so that we will not make use of this chemical classification method.

5.2 Comparing simulations with observational data

5.2.1 The [α/Fe] vs age relation

We have used as starting point for our analysis all the stellar particles forming the galaxy at $z = 0$, as Haywood et al. (2013) paid no attention to the possible contamination by halo stars in their solar neighborhood stellar sample.

In order to refine the analysis, the spheroid component has been excluded. In this case, the stellar particles classified as spheroid by the kinematic k–means method have been removed. (see Sections 3.3 and 2.5 for the k–means method).

After that, the thin and thick disks have been defined as those stars younger and older, respectively, than t_{knee}, with t_{knee} the age where the knee appears in the [α/Fe] vs age plot, see Figure 5.1 for an illustration. Finally, these disks have been split into cylindrical, 2 kpc wide shells, and only those with $R > 4kpc$ have been considered.

An additional comment is in order regarding the [α/Fe] vs age plot. The knee structure is expected from the different time scales for α and Fe elements formation and injection into the ISM, related to they having SN type II and SN type Ia, respectively, as the main nucleosynthetic formation paths.

5.2.2 The age-metallicity relation

In Figures 5.2 and 5.3 we plot [Fe/H] vs age for the two galaxies, in three shells with radii between 4 and 6 (top), 6 and 8 (center), and 8 and 10 kpc (bottom). If we look at the old stars (thick disk, stars older than 6.5 and 6.0 Gyr for HD-5004A and g1536, respectively), we see a tight correlation between age and metallicity with a steep slope linked to an important decrease in the iron production. The young stars (or the thin disk), on the other hand show almost no correlation between age and [Fe/H].

In the right side of the two figures we show the same number density 2D-histograms as in the left panels, now with the scatter plot color coded by α-enhancement superposed. In this panels it can be seen that stars with [Mg/Fe]$>\sim$0.1 dex and $>\sim$-0.1 dex for HD-5004A and g1536, respectively, mostly belong to the thin disk, as expected from Figure 5.1.

When we compare these two figures with Figure 9 of Haywood et al. (2013), it is clear that simulations follow the same patterns as the solar vicinity observations. We should recall that the temporal separation in the simulation is 6.5 and 6.0 Gyr for g1536 and HD-5004A, respectively,

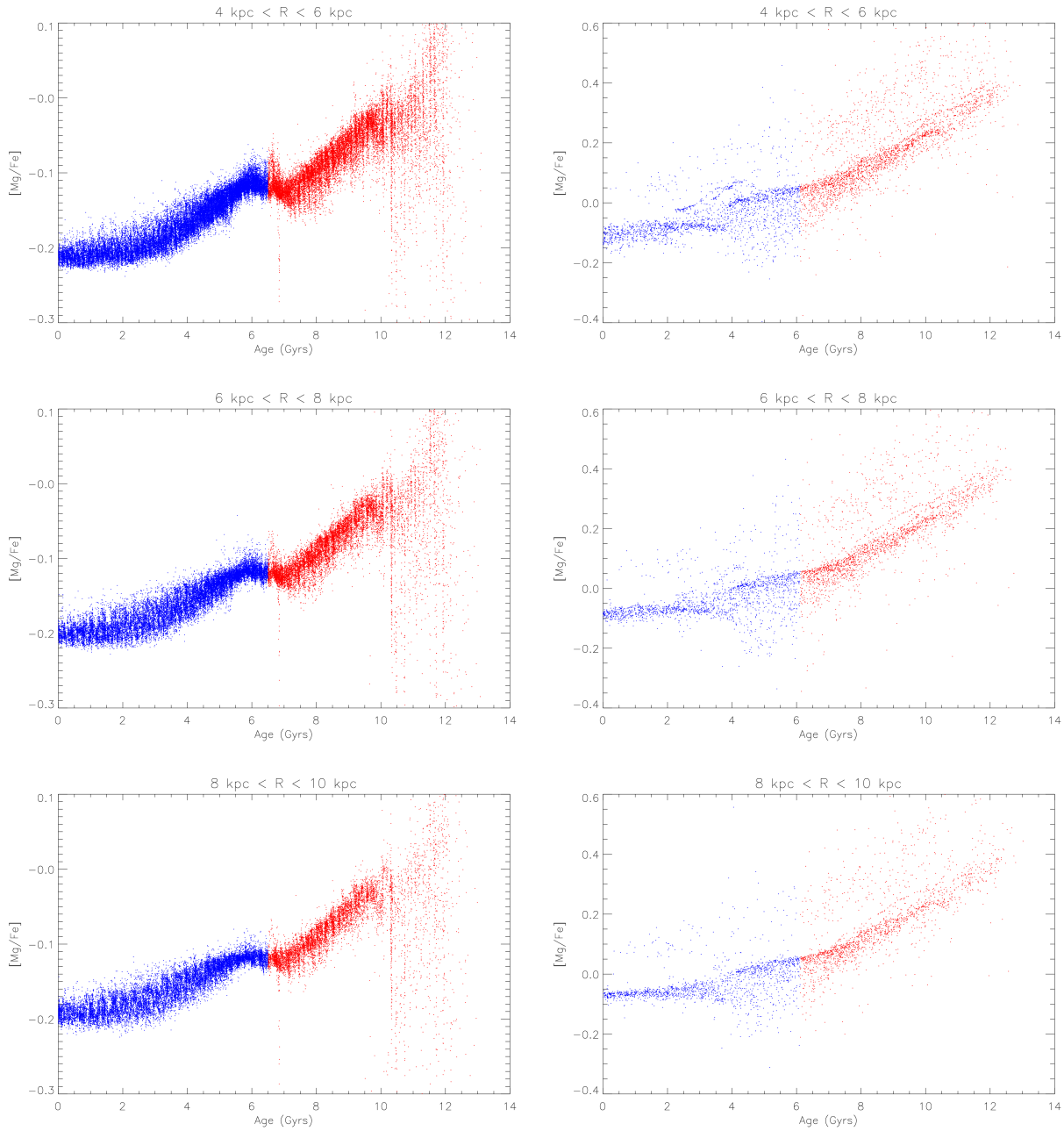

Figure 5.1: α–enhancement as a function of age for the stars in three shells for the galaxies g1536 (left) and HD-5004A (right). The two obvious branches in this plots define an age cut–off that will be used to separate the thin disk (blue) from the thick one (red). The cut–off values are 6.5 and 6.0 Gyr for g1536 and HD–5004A, respectively.

while the one in the observational data set is ∼8 Gyr. Also, the [Mg/Fe] cut–off corresponding to the age separation is more similar to the observational data in the case of HD-5004A than g1536 which is systematically less α-enhanced than the Milky Way.

5.2.3 The [α/Fe] vs [Fe/H] distribution: a temporal sequence?

Once the metallicity vs age and α-element vs age relations have been examined, we turn to the [α/Fe] vs [Fe/H] distribution, and to the possible age stratification in this diagram.

The [α/Fe] vs [Fe/H] distributions are drawn in Figures 5.4 and 5.5 (left) for the same two galaxies. In addition, we show on the right panels the same distributions with the scatter plot color coded by stellar age superposed. A clear tendency for stratification according to stellar age shows up in the thick disks. Older stars are metal poorer and more α enhanced than the younger ones. This indicates that thick disks have formed as [Fe/H] poor, [α/Fe] enriched systems, gradually evolving into more metal abundant and less [α/Fe] enhanced populations. This trend continues when the thin disk starts to form its stars.

However, within the thin disk the age sequence becomes less clear, except maybe at the outer shell. From these figures, mixing of young and middle age stars is apparent around [Fe/H] $\simeq$ 0.1 dex. However, there is still a tendency for thin disk stellar populations to be more metal rich and less α enhanced with decreasing age. The metallicity dispersion is always large in the populated regions of the plot and increases from low to high [α/Fe] due to radial mixing induced by dynamical effects. In both simulated galaxies, the youngest stars show a tight [α/Fe] – [Fe/H] correlation, that flattens as we go from the inner to the outer shells.

Similar tendencies have been found in the solar neighborhood by Haywood et al. (2013).

5.2.4 Vertical distributions

An analysis of the vertical profiles for `P-DEVA` galaxies, based on RGB stellar counts, has been presented by Doménech-Moral et al. (2012). The vertical scale heights differ for the thin and thick disk components, as expected, with ratios of the thick to the thin vertical scales of around 4, with a large spread (see their Table 3), as usual found for external spirals (see, e.g, Yoachim et al. 2006). The MaGICC galaxy, g1536, has been studied in this respect by Stinson et al. (2013), who found a smooth variation in both scaleheights and scalelengths when dividing stars into mono abundance populations. Their results is that more metal–rich and less α–enhanced populations have the shortest scalelengths and the larger scaleheights.

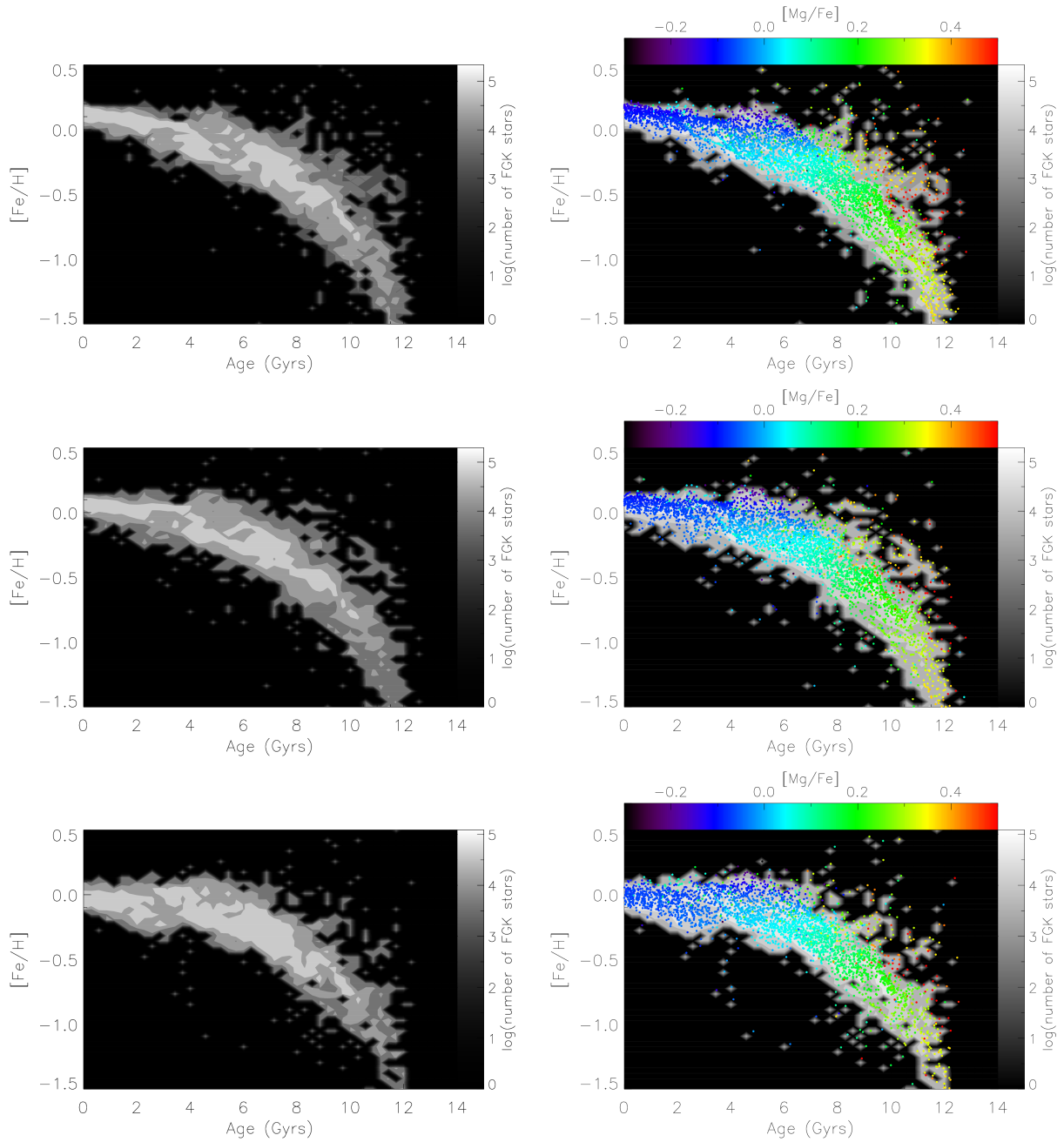

Figure 5.2: The 2D histogram of [Fe/H] as a function of age for the stars in three shells: 4 kpc <R< 6 kpc (top), 6 kpc <R< 8 kpc (center) and 8 kpc <R< 10 kpc (bottom), for the galaxy HD-5004A, with the scattered distribution colored by α–enhancement (right).

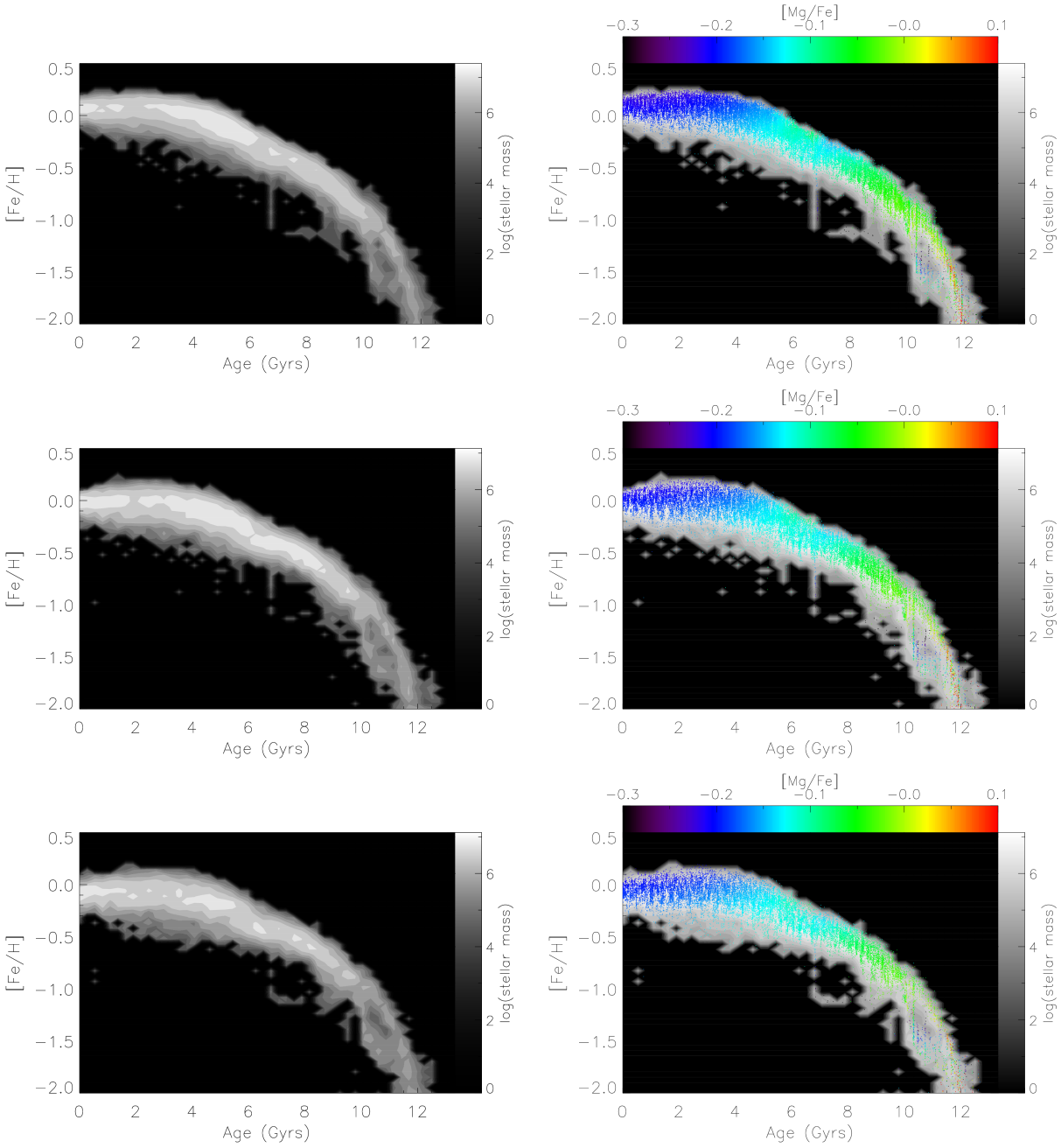

Figure 5.3: Same as Figure 5.2 for the galaxy g1536.

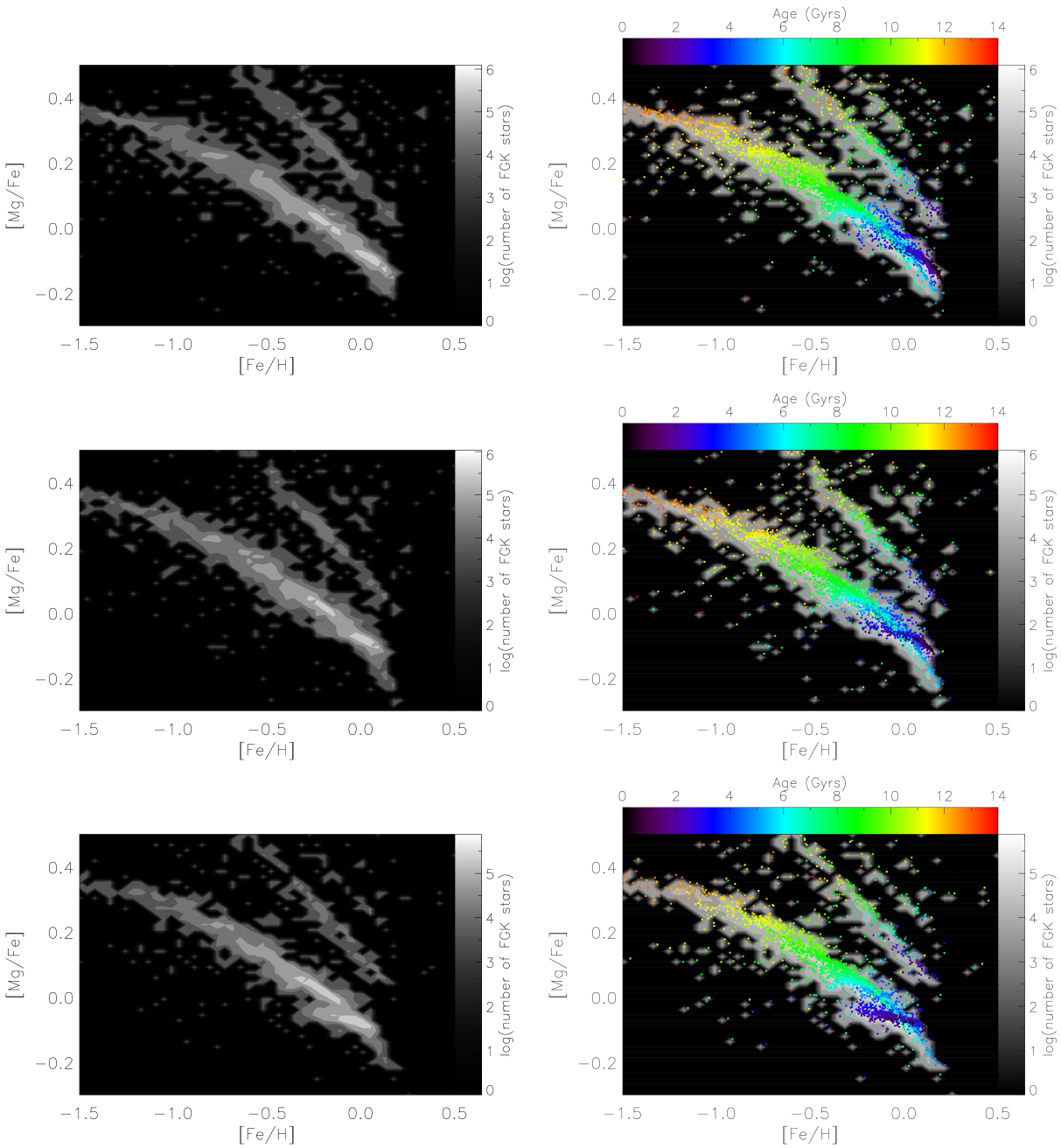

Figure 5.4: The 2D histogram of α–enhancement as a function of [Fe/H] for the stars in three shells: 4 kpc <R< 6 kpc (top), 6 kpc <R< 8 kpc (center) and 8 kpc <R< 10 kpc (bottom), for the galaxy HD-5004A, with the scattered distribution colored by stellar age (right).

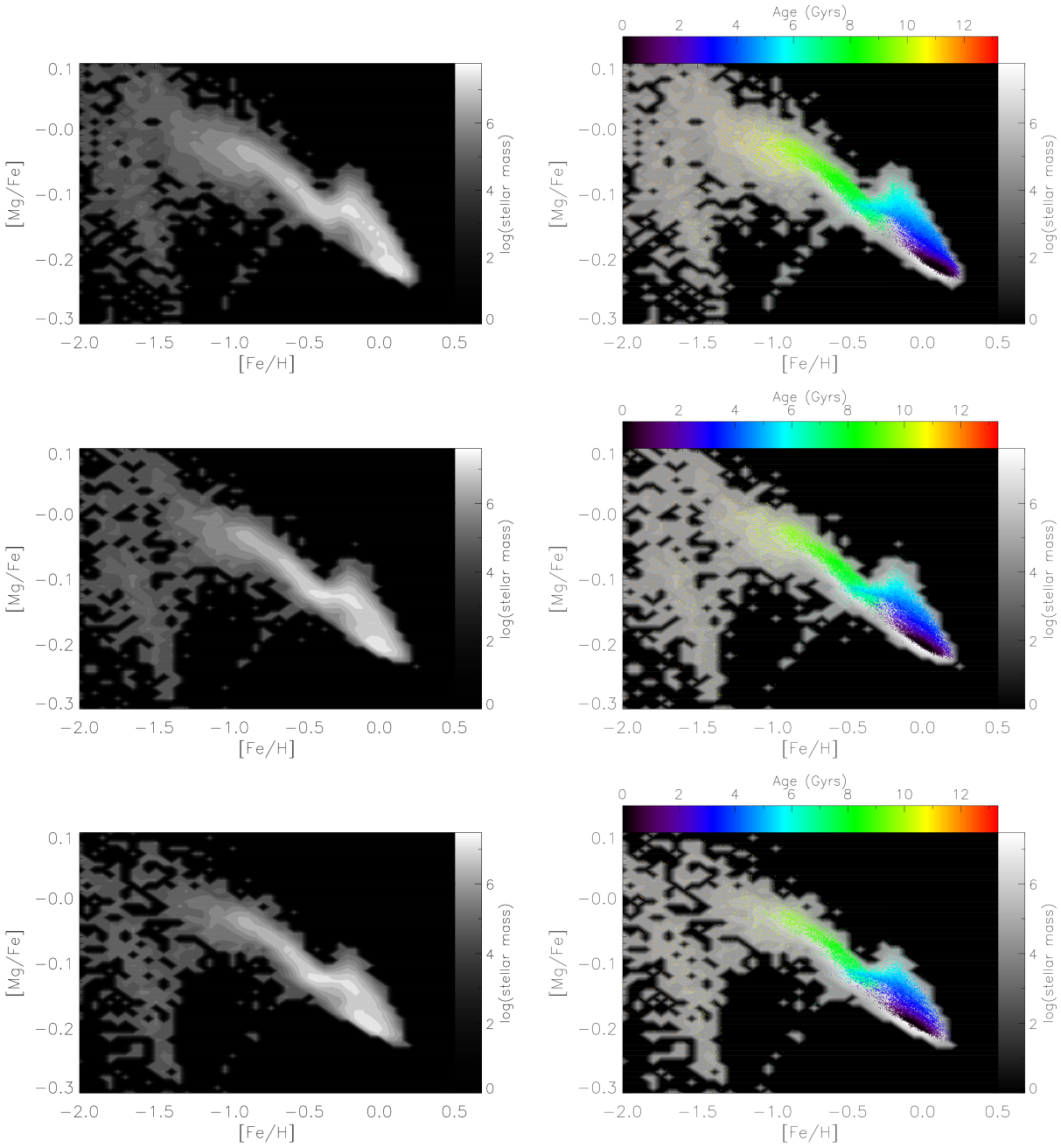

Figure 5.5: Same as Figure 5.4 for the galaxy g1536.

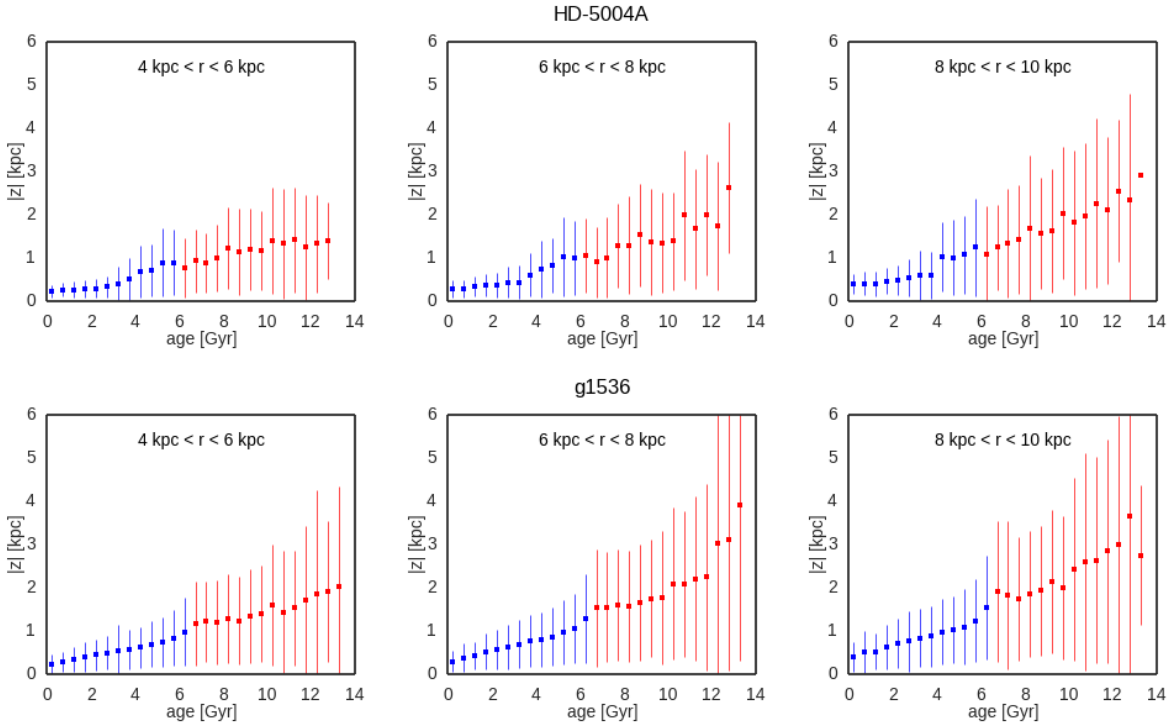

Figure 5.6: The height as a function of age for the thin (blue) and thick (red) disks of the galaxies HD-5004A (top) and g1536 (bottom), in three shells (left to right).

In Figure 5.6 we show the average height above the plane with its corresponding dispersion for the stars of the thin and thick disks, selected in three radial shells. This is consistent with Figure 12 of Haywood et al. (2013) where we see the stars of the thick disk reaching higher maximum distance from the galactic plane than those of the thin one.

5.2.5 Kinematics

The particle velocity field is usually expressed in cylindrical coordinates (the symbols V, W, and U will hereafter be used for the tangential, vertical, and radial velocities, respectively; and σ_V, σ_W, and σ_U for their corresponding dispersions). The velocities are calculated relative to the galaxy center of mass, and the z axis is taken to be parallel to the angular momentum of the gaseous disk at $z = 0$.

Figure 5.7 is an illustration of the radial behavior of V, W, and U and their dispersions for the thin and thick disk stellar populations. We see that, as expected, the thin disk appears to be more rotationally supported than the thick one, while the later has higher velocity dispersions. The interesting aspect to note here is that HD-5004A has decreasing rotational velocities for both thin and thick disk (upper left), while g1546 shows a constant rotational velocity in the thin disk and a decreasing one in the thick (lower left). Other important difference can be seen in the radial velocities (right), the dispersion for the thick disk of g1536 being almost double that of the HD-5004A. Both galaxies satisfy the Tully-Fisher relation (Doménech-Moral et al. 2012; Brook et al. 2012).

We should remember that the innermost regions are generally classified as belonging to the bulge (see Chapter 3), and as such we only show the radial profiles starting from 2 kpc. We will now consider in more detail some relations involving velocities, ages and abundances.

Relations involving the vertical velocity dispersions

Figure 5.8 illustrates the correlation between W and age for g1536 (left) and HD-5004A (right). The black lines are the corresponding σ_W vertical velocity dispersions, and have been separately calculated for the thin (blue) and thick (red) disk populations. A clear trend is clear from this figure, σ_W increasing with age. Figure 5.9 gives the correlation between W and [Mg/Fe] for g1536 (left) and HD-5004A (right). The black lines are the corresponding σ_W vertical velocity dispersions, and have been separately calculated for the thin (blue) and thick (red) disk populations. They show that σ_W increasing with α-enhancement.

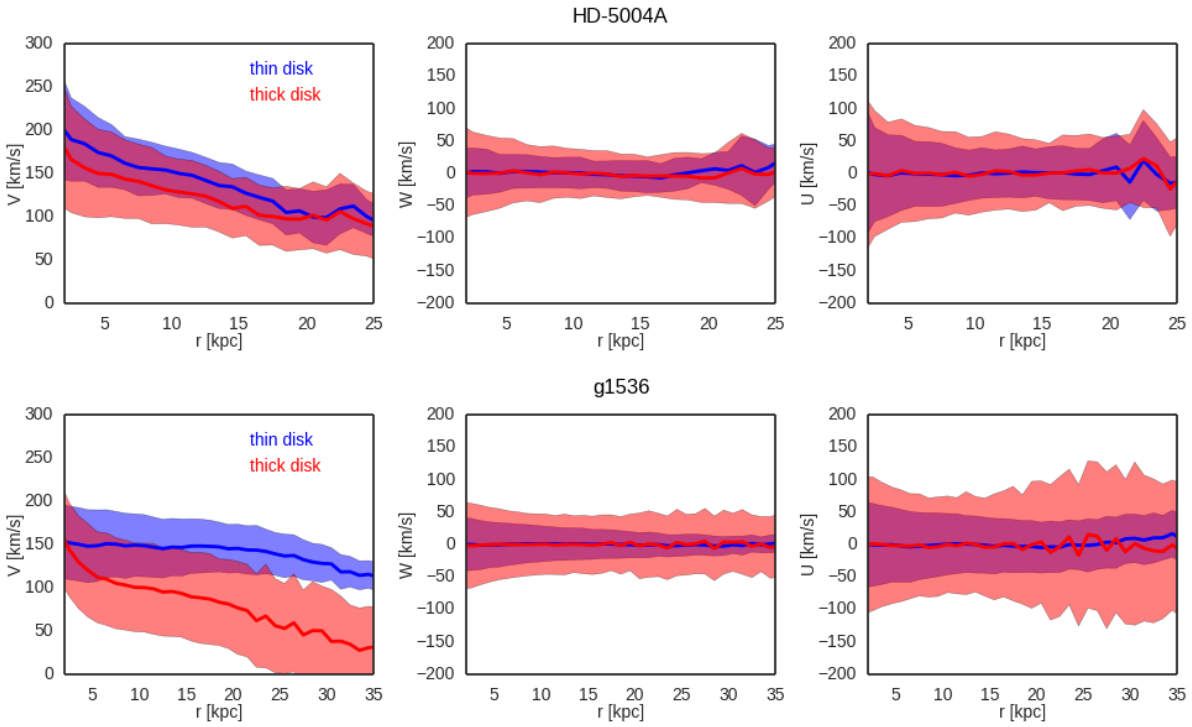

Figure 5.7: The rotational (left), vertical (center) and radial (left) velocities, for the thin (blue) and thick (red) disks, with their corresponding dispersions as shaded regions, of the galaxies HD-5004A (top) and g1536 (bottom).

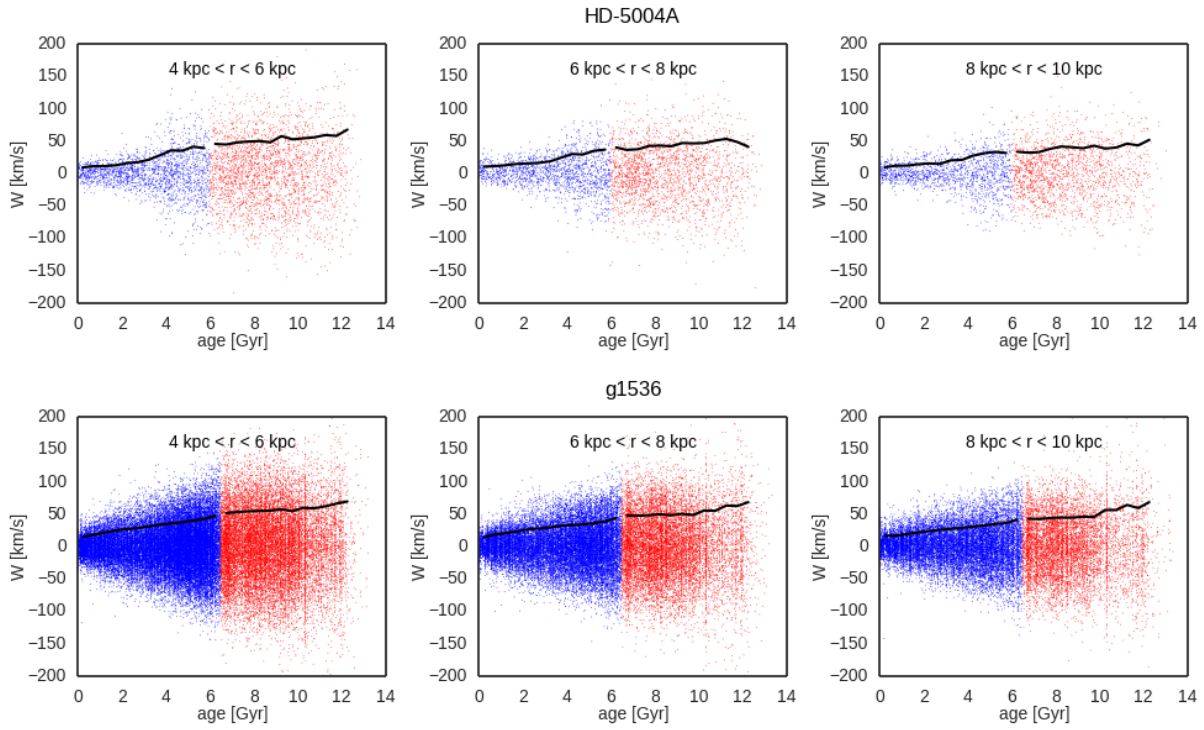

Figure 5.8: The vertical velocity, W, as a function of age for the thin (blue) and thick disk (red), in three shells (left to right), for the galaxies HD-5004A (top) and g1536 (bottom). The thick black lines give the vertical velocity dispersion, σ_W.

These results are very similar to solar neighborhood data (see Figure 11, right of Haywood et al. 2013), including the ranges of σ_W values, the higher σ_W for the metal poor thin disk sequence, the higher σ_W for the older stars when compared with thin disk stars having similar [α/Fe], and the lack of an abrupt transition between the thin and the thick disks.

Simulated galaxies allow us to add that σ_W-age and σ_W-[α/Fe] relations flatten in the outer shells. Moreover, the curves are very similar for the two outer shells, result which is in agreement with the constant vertical dispersion at large radii, as shown in Figure 5.7, similar to the observational results of Herrmann et al. (2009).

Relations involving rotational velocities

With the aim of understanding the Galactic disk evolution, a lot of effort has been dedicated to the analysis of the Milky Way disk stars rotation in correlation with their abundance properties. However, still no agreement has been reached, one reason for it being the discrepancy regarding

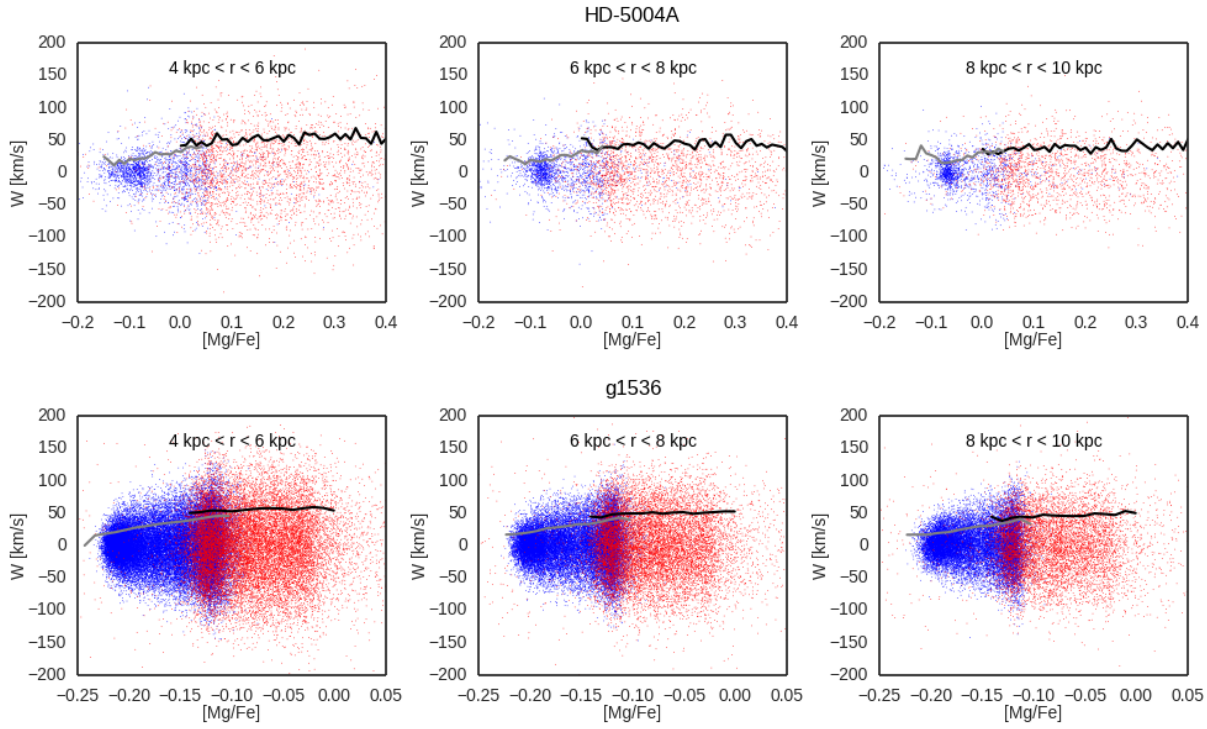

Figure 5.9: The vertical velocity, W, as a function of [Mg/Fe] for the thin (blue) and thick disk (red), in three shells (left to right), for the galaxies HD-5004A (top) and g1536 (bottom). The thick black (grey) lines give the vertical velocity dispersion, σ_W for the thick (thin) disks.

how samples are defined by various authors, which affects the classification of disk stars into thin or thick. For example, Loebman et al. (2011), Navarro et al. (2003) have not found a V - [Fe/H] correlation in neither old nor thin disk stars. However, Spagna et al. (2010) and Lee et al. (2011) report on such correlation in the thick disk. Simulated galaxies offer us a good opportunity to try clarify this issue.

Rotation - metallicity relation

In Figure 5.10 we show the V-$[Fe/H]$ relation for the same two galaxies. In each case, thick and thin disk stars are shown together in three different shells (increasing radius from left to right). It should be noted the big dispersion in rotational velocities, in both simulations and observations data sets (see upper panel in Figure 14 of Haywood et al. (2013)).

We see that, in general, thick disk populations (older than 6.0 and 6.5 Gyr for HD-5004A and g1536, respectively) have a lower V at lower $[Fe/H]$, while the thin ones show almost flat relations.

It is worth noting that these results are sensitive to the sample definition. For example, as a result of the different sign of the slopes in the linear correlation analysis, by taking a different age as separator in the population classification, we would be led to different results. This explains the different results obtained by different authors using different sample definitions.

Our results for the solar shell compare adequately well with Haywood's ones, who use the same sample definition, where the following patterns show up (Figure 14, upper left panel; note that the metal poor thin disk populations is in fact a thick disk population, according to our classification scheme).

Rotation - [α/Fe] relation

In the observational data of Haywood et al. (2013) (see their Figure 15, upper panel), the thin disk population shows basically no correlation of rotational velocity with $[Mg/Fe]$. The normalized velocities for this population are less than $\sim$ 100 km/s in absolute value, and most of the stars have α-enhancements up to $\sim$0.20 dex, just a few showing up at higher values (<0.30dex). The thick disk in their data shows similar velocities with the thin for $[\alpha/Fe]$ in the range (0.0, 0.20), but with the velocity mean centered in negative values, not zero. The thick disk has also a more α-enhanced population ($[\alpha/Fe] > 0.20$), with a high dispersion in velocities, which reach all the

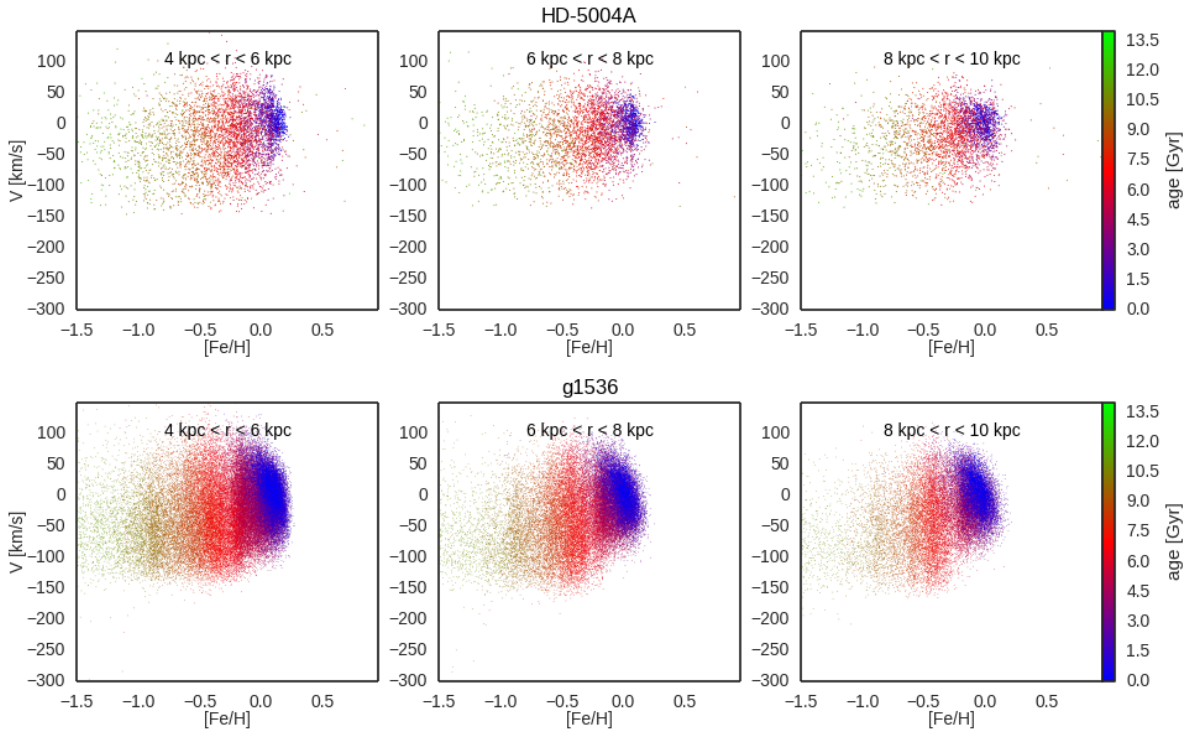

Figure 5.10: The rotational velocity, V, as a function of [Fe/H] for the thin and thick disk together, in three shells (left to right), for the galaxies HD-5004A (top) and g1536 (bottom). The colors represent the ages of the particles.

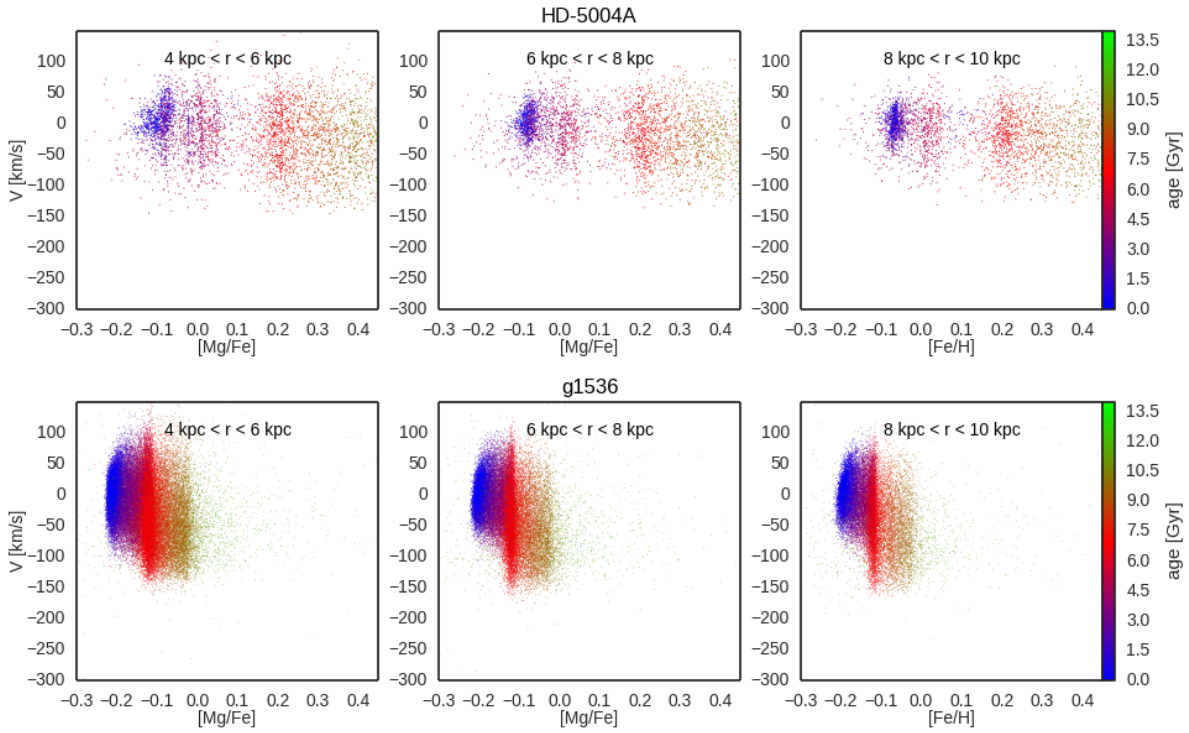

Figure 5.11: The rotational velocity, V, as a function of [Mg/Fe] for the thin and thick disk together in three shells (left to right), for the galaxies HD-5004A (top) and g1536 (bottom). The colors represent the ages of the particles.

way to -250 km/s.

In Figure 5.11 we show the rotational velocities for the thin and thick disks together, with points color coded by the age of the stellar particles. Both galaxies show behaviors similar to the observations. The thin disks, selected according to their age (younger than 6.0 and 6.5 Gyr for HD-5004A and g1536, respectively), with $[Mg/Fe] \lesssim 0.10$ and -0.15 dex for HD-5004A and g1536 show considerably less dispersion in their velocities than their corresponding thick disks, which appear to be lagging behind the thins (lower rotational velocities on average than the thin disk).

Rotation - age relation

Figure 5.12 show that the rotational velocity is only slightly anticorrelated with age, for both thin and thick disk stars, similar to the results of Haywood et al. (2013).

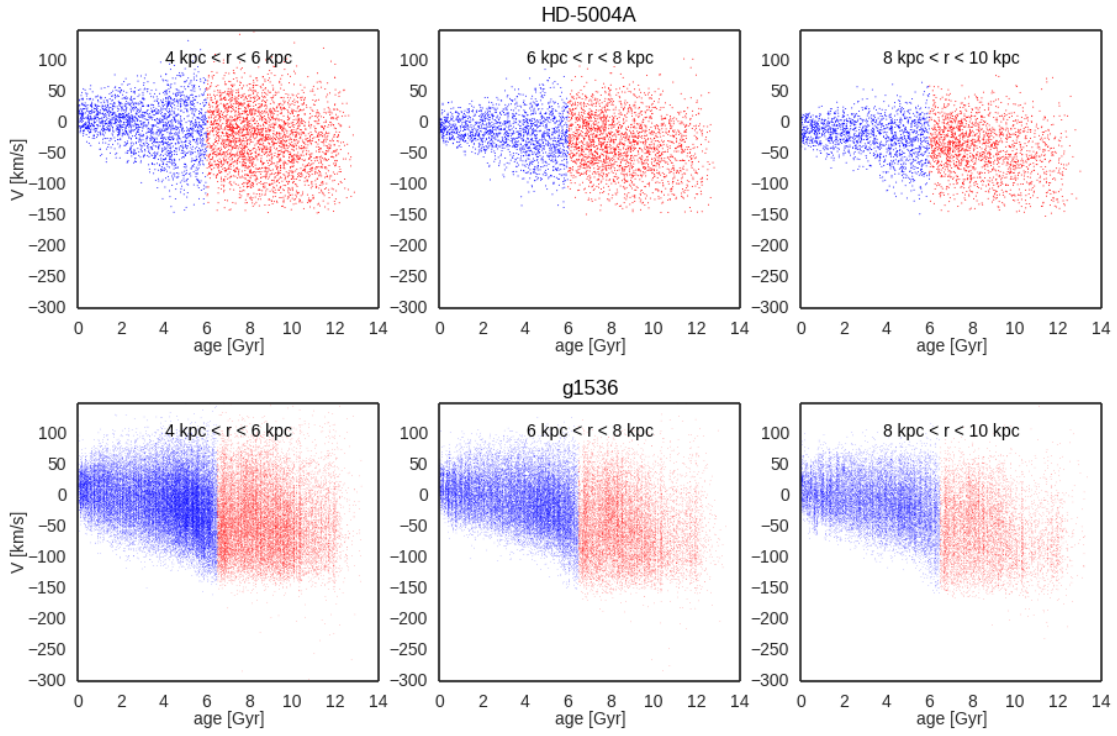

Figure 5.12: The rotational velocity, V, as a function of age for the thin (blue) and thick (red) disks, in three shells (left to right), for the galaxies HD-5004A (top) and g1536 (bottom).

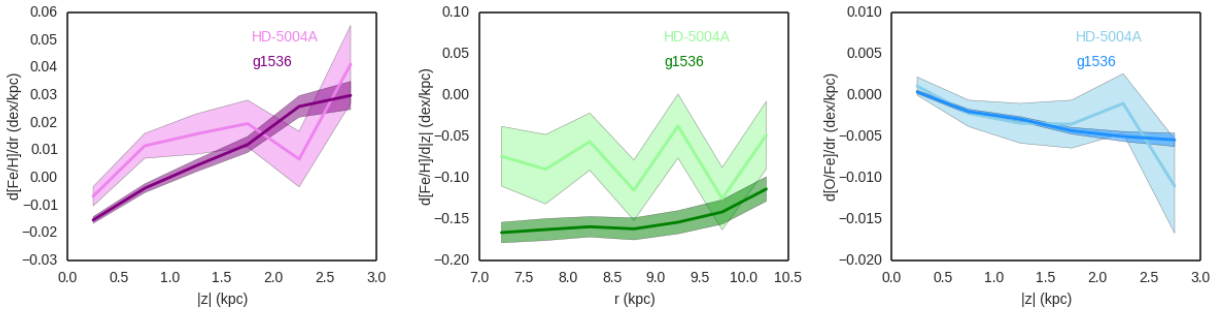

Figure 5.13: Radial (left) and vertical (center) [Fe/H] gradients, and radial [O/Fe] gradient (right) for HD-5004A (violet, light green and light blue) and g1536 (purple, green and blue). The thin and thick disks have been taken together.

5.2.6 Abundance gradients

In Figure 5.13 we draw the radial (left) and vertical metallicity gradients for for the two galaxies. We see that the radial disk gradients are always positive, that is, the [Fe/H] abundances grow at larger galactocentric cylindrical distances. However, the gradients are flat or even negative on the galactic plane. To calculate these gradients we have used a R range of $5kpc < R < 10kpc$. The vertical metallicity gradients are always negative and bigger, in absolute value, than the radial ones (see right panel in the same figure). They have been drawn for the external disk, where data are available. A range $1kpc <\mid z \mid< 3kpc$ has been used to make the fits, corresponding more likely to thick disk stars. These abundance gradients compare adequately well with observational data, as well as with results of the MaGICC-g15784 `GASOLINE` galaxy and 109-CH from Ramses simulations. A detailed report on comparisons to observational data, to other simulations, and the interpretation of the results in terms of radial migration (Martínez-Serrano et al. 2008; Sánchez-Blázquez et al. 2009) can be found in Miranda et al., 2015 submitted.

5.2.7 Summary of results

Simulation properties well matched to observations

- In the [α/Fe] vs age relation a clear bend in the correlation can be identified, and that time has been used to classify the disk stellar populations into thin and thick disks.
- The [α/Fe] and [Fe/H] vs age diagrams show two distinct phases in their evolution. For the old stars classified as belonging to the thick disk, [α/Fe] decreases much faster and [Fe/H] grows much faster than the corresponding trends for the young stars which belong to the thin disk.
- The [α/Fe] vs [Fe/H] relation for thick disk stars is stratified according to stellar age. A similar age sequence is less clear for the thin disk.
- Stars of the thick disks reach higher heights above the galaxy plane than those of the thin. The vertical structure of both thin and thick disks can be described by exponentials (see Doménech-Moral et al. 2012, for `P-DEVA` galaxy set). Ratios of thick to thin vertical scales of $\sim$4, with a large spread, have been found by these authors for `P-DEVA` galaxies.
- The vertical dispersion grows with age and [α/Fe], hence thick disk stars have higher vertical velocity dispersions than thin disk ones.
- There is not a discontinuity in the V - metallicity relation as we go from thick to thin disk stars; however, the former have a slightly lower rotational velocity than the later with the same [Fe/H].
- Results in the V - [Fe/H] are very dependent on the way the how samples are defined.
- α-enriched, old stars tend to rotate slower than α-poor, young stars.
- Vertical and radial metallicity gradients for HD-5004A.

These pattern of correlations found in the simulated galaxies agree to a great extent with those in the local star sample analyzed by Haywood et al. (2013).

5.3 The thin versus thick disk formation

Once we have tested the properties of the thin and thick components of our simulated galaxies, and have found that in general they compare satisfactorily well with observational data, we are in position to try unveil the physical processes underlying their mass assembly.

We will follow the same scheme as in previous chapters, when analyzing the spheroid versus disk formation. We note, however, that this is a work in progress, therefore we will not go that deeper into the details as in the previous chapter.

5.3.1 Going backwards in time

We will look at projections of the thin– and thick– disk–to–be–stars at $z = 0$ in a similar way to what we did in Chapter 4.

In Figures 5.14 and 5.15 we show a high and respectively, low, redshift sequence for the disk of HD-5004A. From this figure, we see that both thick (up) and thin (bottom) disk progenitors display a web–like structure at high z, and that the collapse of the later is delayed with respect to the former. From this perspective, the evolution of the thick disk resembles more the spheroid than the thin disk (see Figure 4.11). In the lower redshift sequence in Figure 5.15 we see how the stellar content of infalling satellites is incorporated to the thick disk, while the gas goes to the thin one.

Similar projection sequences are shown in Figures 5.16 and 5.17 for g1536. In this case, at high z, the differences between the thick (Figure 5.16 up) and thin (Figure 5.16 bottom) disks are less marked than for HD-5004A, but still clearly visible by $z = 2.00$. At the densest nodes of the thick disk web we can observe how stars start to form, leading to an important merger at $z \sim 2.00$. In the lower z figure, 5.17, we can see a marked difference between the structure (web-like) of the thin disk material, still in gaseous form at $z = 1.40$ and the compactness of the thick disk, mostly as stars by this time. Another interesting point to note in the lowest z thick disk panel is the disruption of the infalling satellite (visible in the $z = 0.96$ panel slightly upwards and left of the main object) stellar component.

From these projections in correspondence with the results shown in the previous chapter, we can conclude that simulations with both `P-DEVA` and `GASOLINE` show a temporal sequence with the formation of the spheroid at early times, followed by that of the thick disk, and ended with the assembly of the thin disk. The progenitor gas particles of the three components display web-like

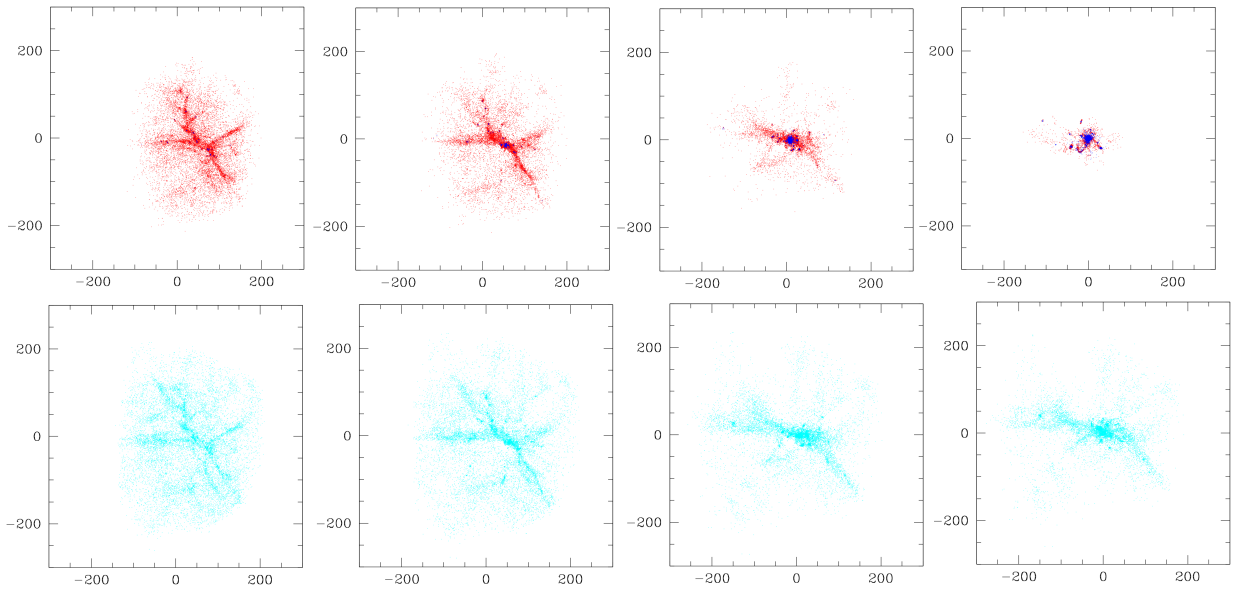

Figure 5.14: One projection of the thick (top) and thin (bottom) disks of the galaxy HD-5004A, at high redshifts, 4.0, 3.0, 2.0 and 1.28 from left to right. The box size is 600 kpc. The gas of the thick (thin) disk is shown in red (cyan). The stars of the thick (thin) disk are shown in blue (red).

structures at high z, which sequentially collapse.

5.3.2 Angular momentum of thin and thick disks

It is also instructive to look at the global angular momentum acquisition and loss. Therefore, in Figure 5.18 we show the evolution of the specific angular momentum of the three galactic components: thin disk, thick disk and spheroid. The curves in this figure correspond to the baryon progenitors of star–to–be at $z = 0$. As expected from Figure 4.17, we see the disk component only slightly decreasing for g1536 and staying basically constant for HD-5004A, after the epoch of angular momentum acquisition at high redshift. On the other hand, the $\mathrm{j}_{spheroid}$ drops two order of magnitudes between the time of maximum angular momentum gain and $z = 0$ for both galaxies.

If we concentrate on the distinction between the thin and the thick disk in this figure, we can notice that the thick disk is very stable and has slightly lower specific angular momentum than the thin disk. Basically, after all the thick disk is in place as stars, its angular momentum stays constant, as expected since stars are not effective in redistributing it. On the other hand, the thin disk loses some amount of its initial angular momentum due to circumgalactic gas redistribution, as discussed in Chapter 4.

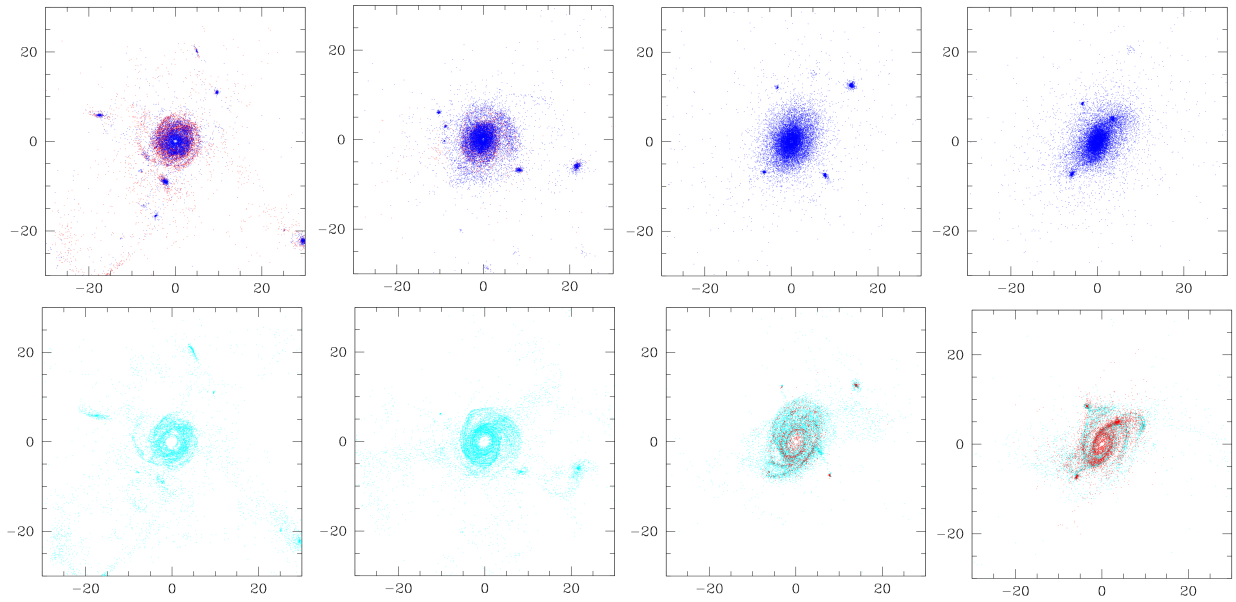

Figure 5.15: Same projection of HD-5004A as in Figure 5.14, but at low redshifts (1.28, 0.89, 0.58 and 0.41, from left to right) and in a 60 kpc/side box.

5.4 Conclusions

In this study, we divided the kinematically selected disks of one `P-DEVA` and one `GASOLINE` galaxies into thin and thick ones based on their behavior in the age–α-enhancement plane. Similar to the solar neighborhood observational data of Haywood et al. (2013), two different tracks can be clearly identified in this relation, allowing us to separate thin from thick disk stellar populations. We found very good agreement with the Haywood et al. (2013) data for both simulated thin and thick disk, in metallicities, ages, velocities and velocity dispersion trends. There is less agreement in the range of α-enhancement in g1536 galaxy, as well as in its gradients. While observationally thin and thick disk samples can also be selected from the [Fe/H]–[α/H] plane, there is no clear transition gap in our simulations. It has to be remembered, however, the limited coverage of the observations. We followed the assembly patterns of the selected thin and thick disks, finding web-like structures at high z for both components. This structuring first disappears for the thick disk, and later for the thin. In relation with Chapter 4, we find that spheroids, thick and thin disks display a web–like structure at high z, which sequentially disappear first for the spheroids, then for the thick disks, and in the end for the thin ones.

All three galaxy components gain angular momentum at early epochs as predicted by the Tidal Torque Theory. Their final appearance, however, depends on the time and timespan of the collapse.

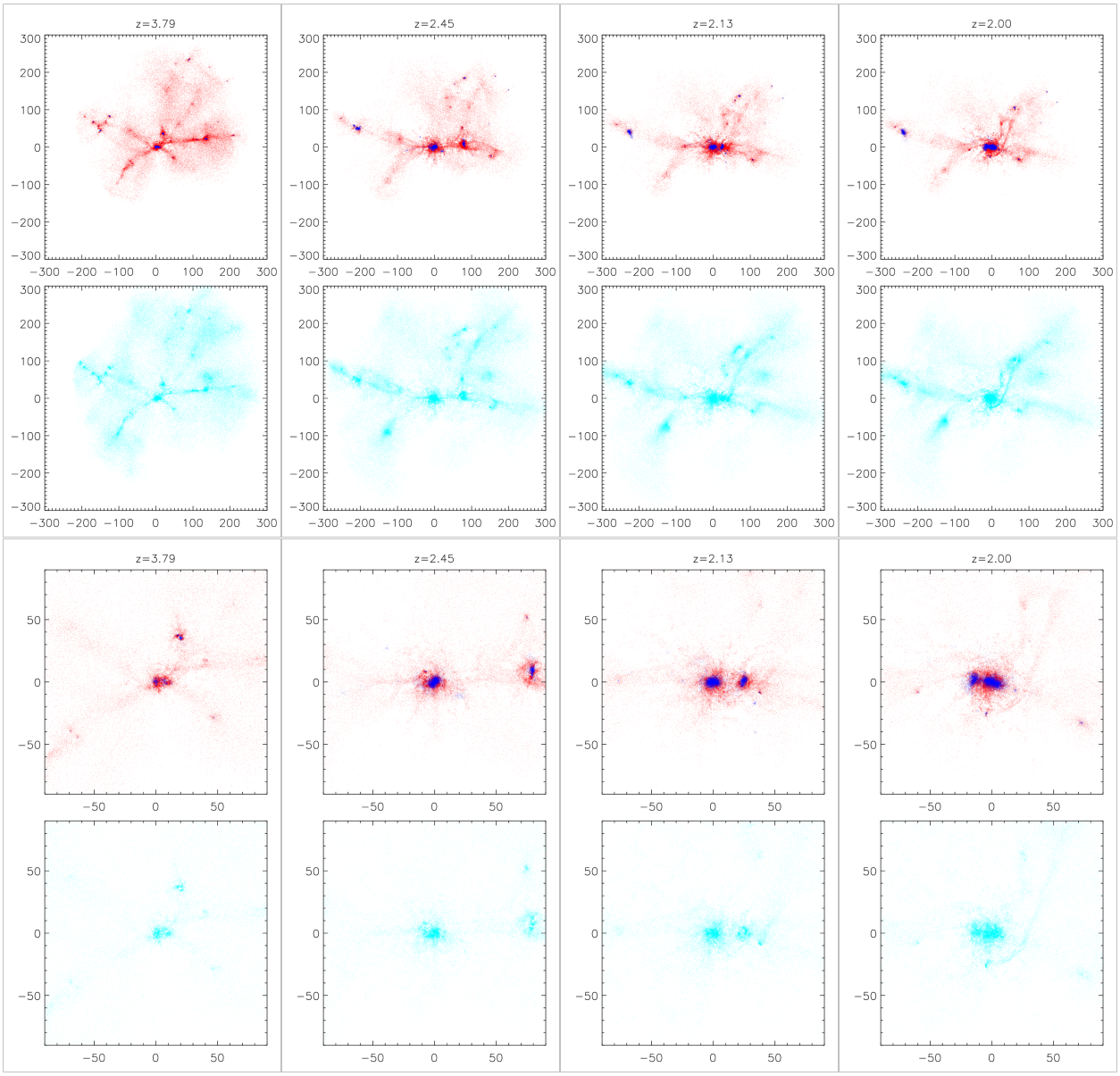

Figure 5.16: One projection of the thick (first and third rows from top) and thin (second and forth rows from top) disks of the galaxy g1536 at four high redshifts shown in each panel (left to right). The bottom two rows are zoom–ins of the top two. The color code is the same as in Figure 5.14.

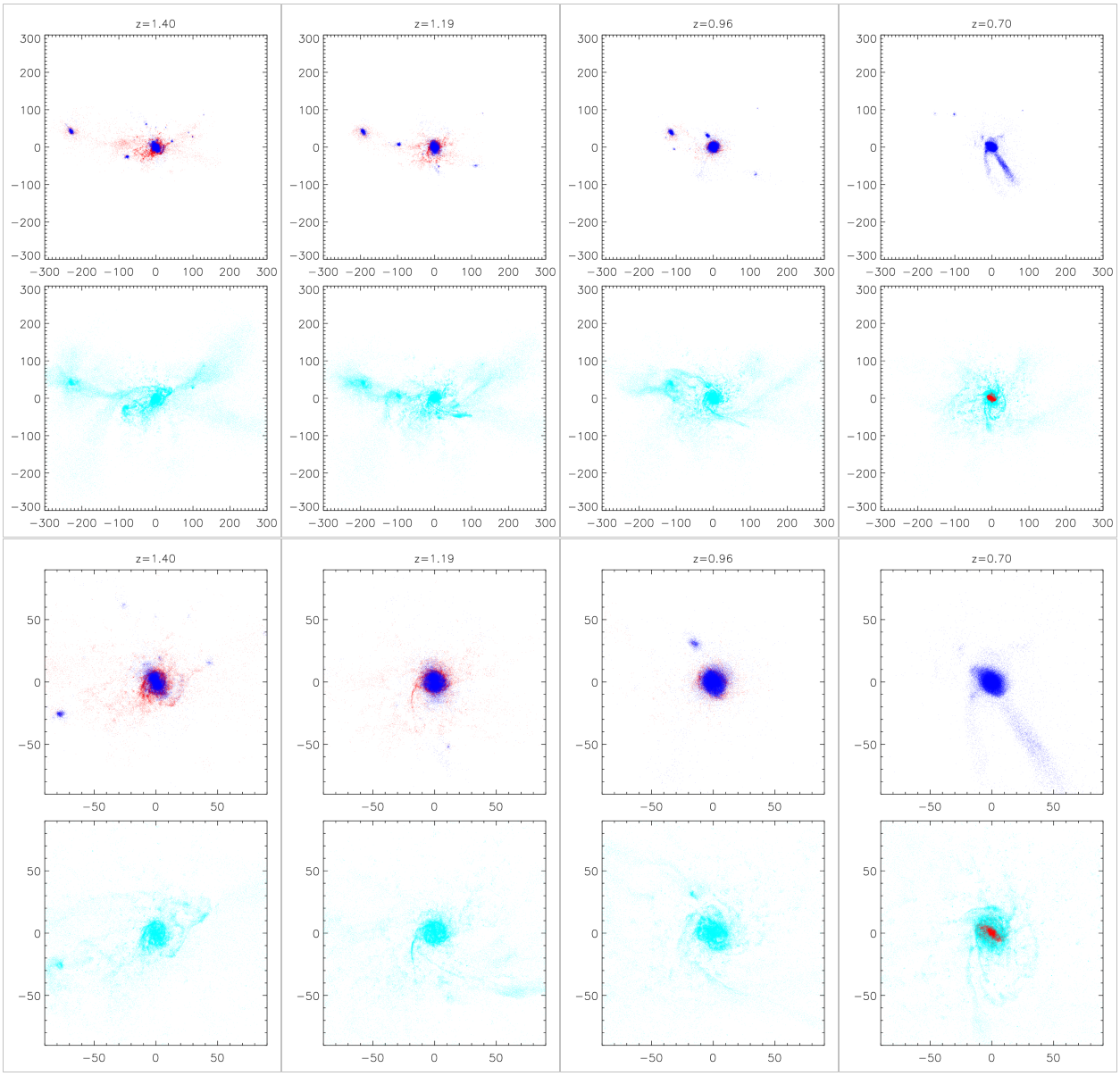

Figure 5.17: One projection of the thick (first and third rows from top) and thin (second and forth rows from top) disks of the galaxy g1536 at four low redshifts shown in each panel (left to right). The bottom two rows are zoom–ins of the top two. The color code is the same as in Figure 5.14.

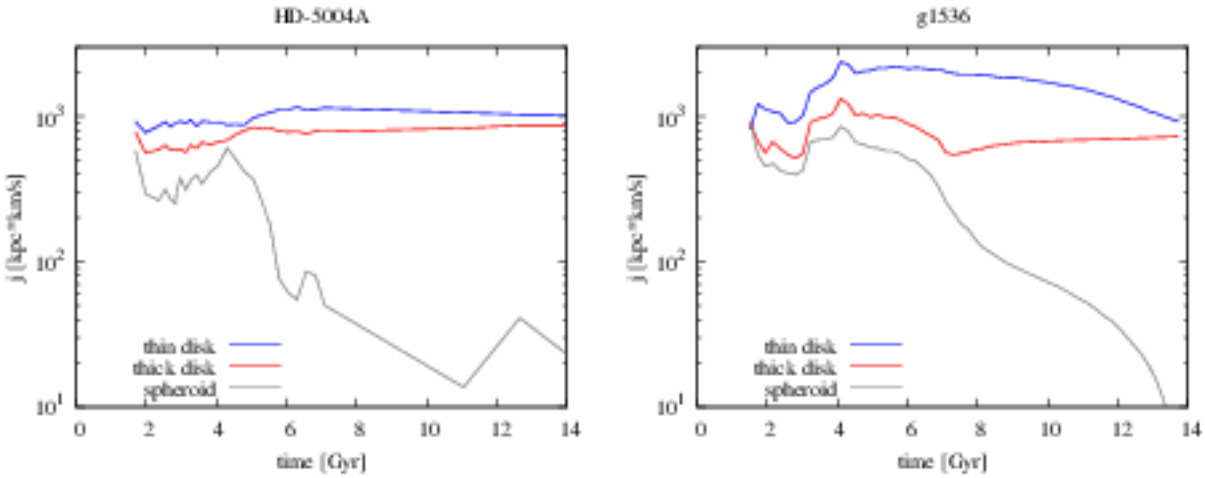

Figure 5.18: Specific angular momentum evolution of the thin disk (blue), thick disk (red) and spheroid (grey) for the two simulated galaxies.

In this sense, progenitor gas of spheroids is the first to collapse on short timescales, losing much of its angular momentum. Later on the thick, and then thin disk material get assembled, but more gradually than in the spheroid case. They also lose some of their initial angular momentum, in this case due to redistribution at the circumgalactic regions, but to a much lesser degree.

The thick disk behaves closer to the spheroid as far as the link with the Cosmic Web and the collapse are concerned. However, concerning the low-z angular momentum conservation, the thick disk is more similar to the thin disk than the spheroid. The spheroid undergoes early collapse and angular momentum loses, mainly at this event. Its progenitors do not succeed at being aligned with the proto-disk. The thick disk is comprised of those baryon particles that do not lose angular momentum at collapse. The part that gets incorporated as stars to the disk has angular momenta only partially aligned. The thin disk particles enter the halo post-collapse mostly in the form of gas, and as a consequence get aligned and assembled as a very flat, thin disk. The final outcome is a sequence of later assembly times, increasing angular momenta, higher metallicities and younger ages as we go from thin to thick disks to spheroids.

References

Abadi, M. G., Navarro, J. F., Steinmetz, M., & Eke, V. R. 2003, ApJ, 597, 21

Adibekyan, V. Z., Sousa, S. G., Santos, N. C., Delgado Mena, E., González Hernández, J. I., Israelian, G., Mayor, M., & Khachatryan, G. 2012, A&A, 545, A32

Bensby, T., Feltzing, S., & Lundström, I. 2003, A&A, 410, 527

Bovy, J., Rix, H.-W., Liu, C., Hogg, D. W., Beers, T. C., & Lee, Y. S. 2003, ApJ, 753, 148

Brook, C. B., Stinson, G., Gibson, B. K., Wadsley, J., & Quinn, T. 2012a, MNRAS, 424, 1275

Doménech-Moral, M., Martínez-Serrano, F. J., Domínguez-Tenreiro, R., & Serna, A. 2012, MNRAS, 2503

Fuhrmann, K. 1998, A&A, 338, 161

Gilmore, G., Wyse, R. F. G., & Jones, J. B. 1995, AJ, 109, 1095

Gilmore, G., Wyse, R. F. G., & Kuijken, K. 1989, ARA&A, 27, 555

Haywood, M., Di Matteo, P., Lehnert, M. D., Katz, D., & Gómez, A. 2013, A&A, 560, A109

Herrmann, K. A., Ciardullo, R., & Sigurdsson, S. 2009, ApJ, 693, L19

Ivezić, Ž., Beers, T. C., & Jurić, M. 2012, ARA&A, 50, 251

Lee, Y. S., Beers, T. C., An, D., Ivezić, Ž., Just, A., Rockosi, C. M., Morrison, H. L., Johnson, J. A., Schönrich, R., Bird, J., Yanny, B., Harding, P., & Rocha-Pinto, H. J. 2011, ApJ, 738, 187

Loebman, S. R., Roškar, R., Debattista, V. P., Ivezić, Ž., Quinn, T. R., & Wadsley, J. 2011, ApJ, 737, 8

Martínez-Serrano, F. J., Serna, A., Domínguez-Tenreiro, R., & Mollá, M. 2008, MNRAS, 388, 39

Mould, J. R. 1982, ARA&A, 20, 91

Navarro, J. F., Abadi, M. G., Venn, K. A., Freeman, K. C., & Anguiano, B. 2011, MNRAS, 412, 1203

Reddy, B. E., Lambert, D. L., & Allende Prieto, C. 2006, MNRAS, 367, 1329

Sánchez-Blázquez, P., Courty, S., Gibson, B. K., & Brook, C. B. 2009, MNRAS, 398, 591

Soubiran, T., Bienaymé, S., & Siebert, I. 2003, A&A, 398, 141

Spagna, A., Lattanzi, M. G., Re Fiorentin, P., & Smart, R. L. 2010, A&A, 510, L4

Stinson, G. S., Bovy, J., Rix, H.-W., Brook, C., Roškar, R., Dalcanton, J. J., Macciò, A. V., Wadsley, J., Couchman, H. M. P., & Quinn, T. R. 2013, MNRAS, 436, 625

Yoachim, P., & Dalcanton, J. 2006, AJ, 131, 226

Chapter 6

GRASIL-3D

This chapter is a copy of
"GRASIL-3D: an implementation of dust effects in the SEDs of simulated galaxies",
by Domínguez-Tenreiro, Obreja, Granato, Schurer, Alpresa, Silva, Brook & Serna
published in MNRAS 439, 3868, 2014
Supplementary information is presented in the Appendix.

6.1 Introduction

The investigation of the process of galaxy formation and evolution by means of hydrodynamical simulations, though not yet producing a well defined and unique picture (see for instance Scannapieco et al. 2012), has nevertheless already provided fundamental insights. A basic limitation is that most of the processes driving the evolution of luminous matter, which has also some back-reaction on dark matter (DM), occurs many orders of magnitude below the resolution of any feasible cosmological simulation. They are implemented in the simulation by means of approximate and uncertain prescriptions, containing several adjustable parameters. In any case, when compared to the alternative approach followed in the literature to understand the origin of galaxy populations, namely the so called Semi Analytic Models (SAMs), simulations provide, at least in principle, information on the 6D phase space as a function of time, i.e. a detailed dynamical information. They also provide, for each particle or volume element depending on the implementation, ages of the stellar component and temperature of the gaseous one, and, when metal enrichment is implemented, chemical composition of both.

However, to compare this rich information with the huge data sets available nowadays, the quite

delicate and complex step of predicting the multi-wavelength Spectral Energy Distributions (SED) of mock objects is required. Indeed, while simulations by themselves only trace the evolution of mass, observations trace light. The huge amount of multi-wavelength data collected in the last decades have evidenced a fundamental complication and uncertainty of this step, namely the significant reprocessing of light emitted by primary sources (stars or active galactic nuclei) by means of the dusty Inter Stellar Medium (ISM). Due to this effect, which tends to be increasingly important in galaxies characterized by higher specific star formation rates, the predicted SED has a strong dependence on the relative geometry of stars and dust, as well as on the optical properties of dust grains. Both on theoretical as well as on empirical ground the latter are expected to vary from galaxy to galaxy, and are difficult to predict (e.g. Calura et al. 2008; Schurer et al. 2009; Rocca-Volmerange et al. 2013).

Therefore to test the simulations against observations, it is essential to interface their outputs with tools that can predict a multi-wavelength SED, including a careful treatment of the radiation transfer through the dust. A few tools already exist for this purpose, for example: SUNRISE (Jonsson 2004, 2006; Jonsson et al. 2010); RADISHE (Chakrabarti et al. 2008; Chakrabarti & Whitney 2009); Art^2 (Li et al. 2007, 2008; Yajima et al. 2012), all using Monte Carlo techniques to follow the radiation of photons through the diffuse ISM and to calculate a global radiation field, and hence the dust re-emission. In addition SUNRISE includes the treatment of star-forming regions using the dust and photo-ionization code MAPPINGSIII (Groves et al. 2008).

RADISHE is a self-consistent three-dimensional code to solve radiative transfer under the assumption of radiative equilibrium, using a Monte Carlo code based on the Lucy (1999) algorithm. Dust is assumed to be in thermal equilibrium with the radiation field, and the energy it absorbs is re-emitted as thermal emission. Therefore, the effects of the stochastically heated small grains on the SEDs are not considered.

ART^2 also uses a Monte Carlo technique to solve the radiative transfer in dusty media under the assumption of radiative equilibrium, adding two modules that couple the continuum and Lyα line emissions, and take into account the effects of ionization and dust absorption in the propagation and scattering of photons. The Continuum module of ART^2 was developed by Li et al. (2008), who adopted the radiative equilibrium algorithm by Bjorkman & Wood (2001). The new ART^2 version includes the treatment of Lyα radiative transfer in dusty and ionized ISM as its particular improvements.

In a somewhat different context, the dust radiative-transfer model GRASIL (Silva et al. 1998;

Silva 1999) has been used highly successfully for many years in two main ways. On one hand, it has been used in combination with simple chemical evolution model, `CHE_EVO`, to calculate SEDs, which, at their turn have been used to study individual galaxies, inferring galaxies properties such as star-formation histories and dust masses (e.g. Panuzzo et al. 2007; Calura et al. 2008; Iglesias-Páramo et al. 2007; Vega et al. 2008; Lo Faro et al. 2013). On the other hand, GRASIL in combination with more sophisticated galaxy evolution models, particularly SAMs of galaxy formation (e.g. Granato et al. 2000, 2004; Baugh et al. 2005; Lacey et al. 2008; Cook et al. 2009; Fontanot et al. 2009; Silva et al. 2012), was used to predict SEDs which can then be compared to observed ones, thereby testing the proposed galaxy formation scenarios. The code has been used successfully with the GALFORM (Cole et al. 2000; Granato et al. 2000; Baugh et al. 2005; Lacey et al. 2008), the MORGANA (Monaco et al. 2007; Fontanot et al. 2008, 2009) and the ABC (Granato et al. 2004; Silva et al. 2005; Lapi et al. 2006; Cook et al. 2009) models. It has been the first model to take into account the age-dependent dust reprocessing of stellar populations, arising from the fact that younger stars are associated with denser ISM environments. GRASIL can use the outputs from SAMs, in particular star formation and chemical enrichment histories, as well as the limited geometric information they provide, in order to produce self-consistent SEDs of mock galaxies relatively quickly. Moreover, a substantially faster version of the code was presented recently (Silva et al. 2011, 2012), exploiting artificial neural networks. However, despite its many strengths, it assumes equatorial and axial symmetry for the galaxy. While this is highly suitable for SAMs, the use of GRASIL with galaxies produced by hydrodynamical simulations would imply the loss of a large quantity of useful information.

We present here a new model, GRASIL-3D, based on the GRASIL formulism, but designed to be applied to any hydrodynamic simulation. The many strengths of GRASIL coupled with the need for properly comparing hydrodynamic simulations with observations provided the motivation for this work.

GRASIL solves the radiative-transfer equation under the condition of thermal equilibrium for dust grains bigger than a given size $a \geq a_{flu}$ (usually taken to be 250 Å), with a size-dependent temperature. However, for smaller grains a single gray body spectrum has been found not to work correctly. Indeed, as first noted by Greenberg (1968), small grains can be stochastically heated to temperatures much higher than the temperature that they would be expected to reach if they were in temperature equilibrium. Thus a more detailed calculation for smaller grains is required, as in the Guhathakurta & Draine (1989) method incorporated in GRASIL. This allows for a proper

treatment of small grains and of polycyclic aromatic hydrocarbons (PAHs) which show distinctive features in mid-infrared (MIR).

6.2 Calculating the SEDs of simulated galaxies

To develop the GRASIL-3D code, we have followed the main characteristics and scheme of GRASIL, which we briefly recall here. The gas is subdivided in a dense phase (fraction f_{mc} of the total mass of gas) associated with young stars (star-forming molecular clouds, MCs) and a diffuse phase (*cirrus*) where more evolved (*free*) stars and MCs are placed. The young stars leave the parent clouds in the time-scale t_0. The MCs are represented as spherical clouds with optical depth $\tau \propto \delta\, m_{mc}/r_{mc}^2$ (where δ is the dust to gas mass ratio, m_{mc} is the mass of MCs, and r_{mc} is their radius), with a central source, whose radiative transfer trough the MCs is computed. The radiative transfer of the radiation emerging from MCs and that from free stars is then computed through the cirrus dust (for more details see Silva et al. (1998) and Silva (1999)).

The aim of GRASIL-3D is to calculate multi-wavelength SEDs and images of simulated galaxies identified in simulations run with either Lagrangian or Eulerian codes. We recall that the former follow the evolution of particles, while the latter describe the relevant dynamical evolution through functions of position and time. In the case of Lagrangian codes, the particles are classified into dark, gaseous or stellar. Each galaxy-like-object produced in the simulations is sampled by particles of these three kinds. However, dark matter plays no role in the determination of the galaxy SEDs.

The main quantities that determine the SED are the star formation history, the mass of gas and the metallicity of stars and gas. In simple models these quantities are relatively simple functions of time, and the information on their spatial distributions, if present, is limited to the scale radii of stars and gas for an analytical and symmetrical density profile. In the case of simulated galaxies, the outputs provide detailed information on the spatial distribution of stars and gas, possibly their metallicity, and the age distribution of stars. All these quantities are then output at different times (snapshots).

6.2.1 Simulation code outputs

Smoothing procedures on direct outputs, or direct outputs themselves in the case of Eulerian codes, provide, among other functions, the following spatial mass distributions necessary for the SEDs:

1. Stellar matter distribution, $\rho_{x*}(\vec{r}, t)$, x here specifies particular properties of the stellar pop-

ulations, for example $x = y$ (young) or f (free).

2. Gaseous matter distribution, $\rho_x(\vec{r}, t)$, x here specifies particular properties of the gas particles (e.g. "mc" for the dense phase, or "c" for the cirrus)

3. Codes where metal enrichment is implemented, provide the stellar or gaseous metallicity $Z_x(\vec{r}, t)$, where again x specifies particular properties of the gaseous or stellar particles, for example, "cold gas" or "young stellar population".

In this work we focus on how to work with the outputs of Lagragian codes using particles, the adaptations needed to work with Eulerian codes being straighforward.

To smooth out the functions above, GRASIL-3D uses a cartesian grid whose cell size is set by the smoothing length used in the simulation code. The smoothed functions provide the geometry of the different simulated galaxy components, their position dependence $\vec{r}$ indicating that they are expected to miss any symmetry.

Given these outputs, we need to specify in detail how to implement in GRASIL-3D the space distributions $\rho_{mc}(\vec{r}, t)$ (see §6.2.2), and $\rho_c(\vec{r}, t)$ for the diffuse ISM (see §6.2.3), including a dust model and a scheme for the radiative transfer within these two components (see §6.2.5 and §6.2.5).

6.2.2 Implementation of the space distribution of the MC component

For the star forming molecular clouds, we follow the main characteristics of their modeling in GRASIL, but taking advantage of the new possibilities provided by the detailed outputs of the simulations. In GRASIL the mass in the MC component in a given object at time t_G, M_{mc}, is set by the parameter $f_{mc} = M_{mc}/M_{gas}$, where M_{gas} is the model gas mass at t_G. This is a free global parameter.

Here we *derive* f_{mc} under the assumption that MCs are defined by a threshold, $\rho_{mc,thres}$, and by a probability distribution function (PDF) in the gas density pattern the simulation returns. With these quantities, we get the total amount M_{mc} of gas in the dense phase, and correspondingly the amount and density field of the diffuse gas. In principle, also the density field for the dense phase of the ISM could be defined in this way, but here we make the assumption that all the MCs are active, i.e., they are associated with star formation, as in GRASIL. Therefore, after defining M_{mc}, we distribute it following $\rho_{y*}(\vec{r}, t)$ (the density of young stars, see 6.2.2). This prescription is in a sense equivalent to smoothing out the subresolution MC field, given by the PDF, to the scale of the young stellar field, that is, to the scale of the simulation resolution. In this way, the free and

young stellar field, as well as the MC field, are resolved as given by the simulation, while the diffuse gaseous field (cirrus) is described at subresolution scales by the PDF [1].

The probability distribution function

The PDF is a model for the gas distribution at sub-resolution scales characterized by two parameters ρ_0 and σ.

Simulations at $\sim$ 1 kpc scales indicate that either $f_{pd}(\rho)d\rho$ (i.e., the number of cells with densities in the range $[\rho, \rho + d\rho]$) or $f_{pd,M}(\rho)d\rho$ (i.e., the mass fraction in cells whose density is in the range $[\rho, \rho + d\rho]$) can be fit by log-normal functions, characterized by a dispersion σ (the same for both of them) and a density parameter, ρ_0 and $\rho_{0,M} = \rho_0 e^{\sigma^2}$, respectively. The expression for $f_{pd}(\rho)d\rho$ is:

$$f_{pd}(\rho)d\rho = \frac{1}{\sqrt{2\pi}\sigma} \exp[-\frac{\ln(\rho/\rho_0)^2}{2\sigma^2}]d\ln\rho \tag{6.1}$$

The volume-averaged density $< \rho >_V$, and mass-averaged density $< \rho >_M$ are given, respectively, by (see, for example, Elmegreen 2002, and Wada & Norman 2007):

$$< \rho >_V = \rho_0 e^{\sigma^2/2}; < \rho >_M = \rho_0 e^{2\sigma^2} \tag{6.2}$$

providing a relationship between the ρ_0 and σ parameters.

Calculating M_{mc}

The fraction of gas in molecular clouds $f_{mc}(\vec{r}, t)$ can be calculated from a theoretical PDF, assuming that cold gas with density $> \rho_{mc,thres}$ is in the form of MCs. More specifically, the calculation of $f_{mc}(\vec{r}, t)$ has been made as follows:

1. Choose a PDF for the cold gas, $f_{pd}(ln\rho; ln\rho_0; \sigma)$, see Section 6.2.2.

2. Choose a density threshold for MC formation $\rho_{mc,thres}$.

[1] A second possibility with only active MCs, as in GRASIL, would be to distribute the light from young stars according to the density field of MCs, assigning to each cell a luminous energy proportional to its MC mass content. We tested this prescription for simulated galaxy SEDs, and found insignificant differences with the prescriptions adopted in the text.

3. To determine the fraction of MC mass in the i-th particle at position $\vec{r}_i$[2] relative to cold gas, we calculate:

$$f_{mc}(\vec{r}_i; \rho_{mc,thres}, \rho_0, \sigma) = \frac{I(\rho_{mc,thres}, \rho_0, \sigma))}{I(0; \rho_0, \sigma)} \tag{6.3}$$

where

$$I(\rho_{min}, \rho_0, \sigma) = \int_{\ln \rho_{min}}^{\infty} \rho f_{pd}(\ln \rho; \ln \rho_0; \sigma) d \ln \rho \tag{6.4}$$

That is (Wada & Norman 2007, Eq. 18 and 19):

$$f_{mc}(\vec{r}_i; \rho_{mc,thres}, \rho_0, \sigma) = 0.5(1 - Erf[z(\rho_{mc,thres}/\rho_0; \sigma)]) \tag{6.5}$$

where $z(\rho_{mc,thres}/\rho_0; \sigma) = (ln(\rho_{mc,thres}/\rho_0) - \sigma^2)/(\sigma\sqrt{2})$ and Erf is the error function. The dependence on the particle position $\vec{r}_i$ is through the parameters ρ_0 and σ. To this end, we make the identification

$$< \rho >_V = \rho_{gas}(\vec{r}_i) \tag{6.6}$$

where $< \rho >_V$ is the PDF gaseous volume-averaged density (see § 6.2.2) and $\rho_{gas}(\vec{r}_i)$ is the gas density of the i-th particle as returned by the simulation code. In this way, ρ_0 can be calculated separately for each particle by combining Eqs. 6.2 and 6.6. This provides a link between the two PDF (i.e., subresolution) parameters ρ_0 and σ (see Eq. 6.2) with the (resolved) simulation output.

Then the total mass in active MCs, M_{mc}, can be easily obtained through the following steps:

1. For each cold gas particle i, we calculate $f_{mc}(\vec{r}_i; \rho_{mc,thres}, \rho_0, \sigma) \equiv f_{mc,i}$.

2. The mass of the i-th cold gas particle m_i is split into $m_i^{NDG} = m_i f_{mc,i}$ for its non-diffuse gas content, and $m_i^{DG} = m_i(1 - f_{mc,i})$ for its diffuse gas content.

3. M_{mc} is the sum of the non-diffuse gas content of the constituent gas particles in the object.

$$M_{mc} = \sum_{i,object} m_i^{NDG} \tag{6.7}$$

[2]Note that particle positions carry a subscript ($\vec{r}_i$), while (central points of) cell positions do not ($\vec{r}$). Otherwise, cells carry subscripts meaning their position in the grid (k-th).

The MC grid-density

In order to ascribe all the MCs to recent star formation, we have shared out the total molecular cloud mass M_{mc} in such a way that it is proportional to the density of young stars. The steps are the following:

1. Charge $\rho_{y*}(\vec{r}_i)$ to the grid to obtain $\rho_{y*,k}$ at the k-th grid cell

2. Calculate the global MC to young star mass fraction in the object

$$\alpha = M_{mc}/M_{y*} \tag{6.8}$$

3. The molecular cloud density at the k-th grid cell has been taken to be

$$\rho_{mc,k} = \alpha \times \rho_{y*,k} \tag{6.9}$$

   As said above, the rationale behind this assignation is that active MCs are around young stars.

4. The MC mass at the k-th grid cell is:

$$M_{mc,k} = V_k \times \rho_{mc,k} \tag{6.10}$$

   where V_k is the k-th cell volume, and must be such that the following normalization condition holds:

$$\sum_{cells k} M_{mc,k} = M_{mc} \tag{6.11}$$

MCs at sub-resolution scales

MCs sizes ($\sim 10 - 50$ pc) are smaller than the space resolution reached in most current hydrodynamical simulations run in a cosmological context. Therefore, at each grid cell, a number of MCs must be placed as follows:

$$N_{mc,k} = M_{mc,k}/m_{mc} \tag{6.12}$$

Dust content of MCs

Once we have the MC space distribution, we have to assign to each MC a dust content. We recall that a GRASIL input parameter is the dust to gass mass ratio δ, that can be set proportional to the metallicity. We make the same assumption here. We have charged the grid with the metallicity of the gas particles, and then, once we know at the k-th cell the (cold) gas density or mass, and the gas metallicity, we can calculate its dust content:

$$\delta(Z_k) = \frac{Z_{gas,k}}{110 \times Z_\odot} \tag{6.13}$$

where $Z_{gas,k}$ is the gas metallicity at the k-th grid cell, calculated from the metallicities of cold gas particles.

Young star luminosities

The next step is to provide the luminosity of the young stellar populations placed inside each active molecular cloud.

As in GRASIL, we adopt the following parametrization for the fraction $f(t)$ of the stellar populations energy radiated inside MCs as a function of their age:

$$f(t) = \begin{cases} 1 & t \leq t_0 \\ 2 - t/t_0 & t_0 < t \leq 2t_0 \\ 0 & t > 2t_0 \end{cases} \tag{6.14}$$

where t_0 is a free parameter setting the fraction of light that can escape the starburst region and mimics MC destruction by young stars ($\sim 10^6 - 10^7$ yr).

We calculate the SED, $L_\nu^{y*}(t_i, \vec{Z}_i, \vec{r}_i)$, for each young stellar particle ($i = 1, ..., N_{young,*}$) placed at $\vec{r}_i$, of age t_i, metallicity $\vec{Z}_i$, mass m_i and given IMF. Bruzual & Charlot (2003) models were used to calculate stellar emissions. To be consistent with hydrodynamic simulation codes (see § 6.4.1), we used a Salpeter (1955) IMF for simulated galaxies identified in `P-DEVA` runs, and a Chabrier (2003) IMF for those identified in `GASOLINE` runs. Next, the luminosity at grid cell k is charged from these luminosities at particle positions.

6.2.3 Space distribution of the cirrus component

According to the previous section, the diffuse mass content of the i-th cold gas particle is given by

$$m_i^{DG} = m_i(1 - f_{mc,i}) \tag{6.15}$$

where $f_{mc,i} \equiv f_{mc}(\vec{r}_i; \rho_{mc,thres}, \rho_0, \sigma)$ is given by Eq. 6.3 above, and $\vec{r}_i$ is the i-th particle position.

Therefore, the diffuse gas density associated to the i-th gas particle is:

$$\rho_c(\vec{r}_i) = (1 - f_{mc,i}) \times \rho_{gas}(\vec{r}_i) \tag{6.16}$$

This density is used to charge the grid and obtain the diffuse gas density at the k-th grid cell, $\rho_{c,k}$

To go from diffuse gas density to diffuse dust density at the k-th grid cell, we use:

$$\rho_{dust,k} = \delta(Z_k) \times \rho_{c,k} \tag{6.17}$$

where $\delta(Z_k)$ is as in Eq. 6.13.

6.2.4 Dust model

The dust is assumed to consist of a mixture of carbonaceous and silicate spherical grains, and PAHs. We used the optical properties of the grains, i.e., the absorption and scattering efficiencies Q_{abs} and Q_{sca} of graphite and silicate grains of different size, computed by B.T. Draine for 81 grain sizes from 0.001 to 10μm in logarithmic steps $\Delta \log a = 0.05$, and made available via anonymous ftp at *astro.princeton.edu*. These have been computed using Mie theory, the Rayleigh-Jeans approximation and geometric optics as described in Laor & Draine (1993).

The dust mixture used for the diffuse ISM is that proposed by Weingartner & Draine (2001a). They provide a functional form for the size distribution, and assume that when the graphite grains are smaller than 0.01μm they take the form of PAH molecules. The PAHs in the diffuse cirrus consist of a mixture of neutral and ionized particles, the ionization fraction depending on the gas temperature, the electron density and the ultraviolet field (Weingartner & Draine 2001b). In this work the ionization fraction suggested by Li & Draine (2001) is followed which was estimated to be an average balance for the diffuse ISM of the Milky Way (see more details in Schurer 2009).

For the size distribution of the dust grains within the dense molecular clouds we have adopted the same composition as that used by the GRASIL code originally described in Silva et al. (1998).

The MCs within the GRASIL code have been shown to give good fits to large star forming regions (Silva et al. 1998), and it has been used successfully to fit actively star-forming galaxies and ultra-luminous infrared galaxies (ULIRGS), which are thought to be dominated by molecular clouds (see Silva et al. (1998) and in particular Vega et al. (2005, 2008); Lo Faro et al. (2013)). It is also important to note that the abundance of PAHs in molecular clouds have been specifically tuned by Vega et al. (2005) to agree with the MIR properties of a sample of local actively star-forming galaxies. Given the extensive testing done for molecular clouds within GRASIL, we considered its particular dust composition to be an excellent choice for this work.

We also recall that both dust distributions are calibrated on the same observables, i.e. the average extinction curve and cirrus emission in the Milky Way.

Once the size distribution and the optical properties for the dust mixture have been set, it is then possible to calculate its absorption, scattering and extinction optical depth (see Silva (1999) for a summary of the definitions).

6.2.5 SED determination with GRASIL-3D

The aim of the model is to calculate the radiant flux (luminosity) from a given object measured by an external observer in a given direction (θ, ϕ) and at wavelength λ, using the expression:

$$F_\lambda(\theta,\phi) = 4\pi \sum_k V_k j_{\lambda,k} \exp[-\tau_{eff,\lambda}(k;\theta,\phi)] \tag{6.18}$$

(with units erg s^{-1} $Å^{-1}$), and where the sum is over the different small volumes V_k (the grid) over which the object has been divided, and

$$j_{\lambda,k} = j^{mc}_{\lambda,k} + j^{*}_{\lambda,k} + j^{c}_{\lambda,k} \tag{6.19}$$

is the volume emissivity (erg $cm^{-3}s^{-1}$ $Å^{-1}$ sr^{-1}) of the k-th volume element at wavelength λ, with $mc, *$ and c corresponding to molecular cloud, free stellar and cirrus components, and $\tau_{eff,\lambda}(k;\theta,\phi)$ is the effective optical thickness for cirrus absorption from the k-th volume element to the outskirts of the galaxy along the (θ,ϕ) direction. We describe these terms in the following sections, separately for MCs and cirrus, for which we solve the radiative transfer with different methods. Details on the computation of the dust emissivity, both for grains in thermal equilibrium and fluctuating ones, can be found in Silva (1999).

Radiation transfer in MCs

The radiation transfer through the molecular clouds within GRASIL-3D is calculated using the same technique as in GRASIL, since MCs have the same characteristics as those considered by Silva et al. (1998), where the starlight emitted from within a MC is approximated as a central source and MCs are spherical. We summarize here only the main features which are most important to the implementation in the new code.

The radiative transfer is solved using the Granato & Danese (1994) code, with the λ-iteration method, i.e. at each successive iteration the local temperature of the dust grains is calculated from the radiation field of the previous iteration. In such a way the code converges to a value for the radiation field at all radii of the molecular cloud which will give the correct dust temperature.

This simplified geometry results in a considerable decrease in the computational time. However it is insufficient to match the complex system of randomly distributed hot spots and cooler regions observed in real star forming molecular clouds, and could lead to unrealistically hot dust spots in their center. A maximum inner edge temperature was introduced in Silva et al. (1998) to compensate for this potentially too hot temperature. This was shown to be sufficient for the modelling of molecular clouds, giving good fits to observed data.

Given the central stellar source, the SED emerging from MCs depends only on one parameter, their optical depth:

$$\tau_{mc} \propto \delta \frac{m_{mc}}{r_{mc}^2} \tag{6.20}$$

Since we set $\delta \propto Z$ (Eq. 6.13), and Z now is a local quantity, the value of τ_{mc} depends on the cell position. This means that we have to calculate the radiation transfer separately for the MCs in each grid cell, due to the different values of τ and the central stellar source (see 6.2.2), even if we set the same t_0 for all MCs.

Radiation transfer through the diffuse cirrus

The same two assumptions as in GRASIL have been introduced to simplify the radiative transfer through the diffuse dust, namely:

1. The effect of dust self-absorption is ignored.

2. The effect of UV-optical scattering is approximated by means of an effective optical depth,

given by the geometrical mean of the absorption and scattering efficiencies (Rybicki & Lightman 1979):

$$\tau^2_{eff,\lambda} = \tau_{abs,\lambda}(\tau_{abs,\lambda} + \tau_{sca,\lambda}). \tag{6.21}$$

These approximations have been shown to give similar results when compared to the more rigorous Monte Carlo techniques of Witt et al. (1992) and Ferrara et al. (1999) in the majority of cases tested (Silva 1999). Using the two assumptions stated above, the local (angle averaged) radiation field in the i-th grid cell $J_{\lambda,i}$ (units erg s^{-1} Å^{-1} sr^{-1} cm^{-2}) due to the extinguished emissions of the free stars and molecular clouds from all the other cells can be calculated using the same equations as in the original GRASIL code, namely:

$$J_{\lambda,i} = \sum_k V_k(j^{mc}_{\lambda,k} + j^{*}_{\lambda,k}) \times \exp[-\tau_{eff,\lambda}(i,k)] \times r(i,k)^{-2} \tag{6.22}$$

where the sum is over the different cells of volume V_k over which the simulated galaxy has been divided. $j^{mc}_{\lambda,k}$ and $j^{*}_{\lambda,k}$ are the volume emissivity of the k-th volume element at wavelength λ, with mc and $*$ corresponding to molecular cloud and free stellar components, respectively, and $\tau_{eff,\lambda}(i,k)$ and $r(i,k)$ are the effective optical thickness and distance from the i-th to the k-th grid cells. Once the radiation field $J_{\lambda,i}$ has been calculated at any cell i, the cirrus emissivity $j^{c}_{\lambda,k}$ is calculated following Silva et al. (1998), section 2.4.

Together with the MC and free stars emissivity, the cirrus emissivity is used to calculate the emerging SED, $F_\lambda(\theta,\phi)$ (Eqs. 6.18 and 6.19).

A concern is in order when calculating the radiation field within the i-th cell caused by the stellar and MCs emissions within the same cell. In this case a (apparent) singularity appears. To overcome this problem, the cell is split into N_p random points, P_n, each representing a small volume $V(P_n) = V_i/N_p$, instead of being represented by its center, and the radiation field in the i-th cell caused by its own emission, $J_{\lambda,i;i}$, is calculated as:

$$J_{\lambda,i;i} = \sum_{n=1}^{N_p} \frac{J_{\lambda,i}(P_n)}{N_p} \tag{6.23}$$

where $J_{\lambda,i}(P_n)$ is the radiation field at P_n caused by the emission from the small volumes $V(P_m)$ represented by the remaining $N_p - 1$ random points:

$$J_{\lambda,i}(P_n) = (\frac{V_i}{N_p})(j^{mc}_{\lambda,i} + j^*_{\lambda,i}) \sum_{m=1}^{N_p-1} \frac{\exp[-\tau_{eff,\lambda}(m,n)]}{d(m,n)^2} \tag{6.24}$$

where again $j^{mc}_{\lambda,i}$ and $j^*_{\lambda,i}$ are the volume emissivity at the i-th cell coming from molecular clouds and stars, respectively; $d(m,n)$ is the distance between the m-th and the n-th random points at cell i; and

$$\tau_{eff,\lambda}(m,n) = \sigma_\lambda \times n_{H,i} \times d(m,n) \tag{6.25}$$

is the effective optical thickness between these m-th and the n-th random points.

It is worth noting than when $\max_{ithcell}\ \tau_{eff,\lambda}(m,n)$ is $<< 1$, then the following approximation holds:

$$J_{\lambda,i;i} = V_i \times (j^{mc}_{\lambda,i} + j^*_{\lambda,i}) \sum_{n=1}^{N_p} \sum_{m=1}^{N_p-1} d(m,n)^{-2}/N_p^2 \tag{6.26}$$

where the average of the inverse squared distances $d(m,n)$ is 0.42 when P_n and P_m points cover the unit cube. When taking this average, a volume-like factor going as d^2 appears such that no singularity is present when $d \to 0$.

However, when the effective optical thickness within the i-th cell is not $<< 1$, then we have a double summation involving $\tau_{eff,\lambda}$ to be calculated through the Monte Carlo cell splitting. Furthermore, in these situations, determining the contribution of the 26 neighboring cells to $J_{\lambda,i}$ using just the central points of the 27 cells could lead to inaccuracies in the results too. Therefore, a similar treatment was also applied to these 26 cells by splitting them into random sub-volumes.

For the practical implementation, the calculations have been made in the unit cube (i.e., cell side L=1). As $n_{H,i}$ in the expression giving $\tau_{eff,\lambda}(m,n)$ in Eq. 6.25 above does not change in the cube, the results can be rescaled to the actual grid cell side $L \neq 1$. To this end, the L=1 results have been tabulated for different values of $\tau_{eff,\lambda}(m,n)$. This allows calculation of the splitting averages (see for example Eq. 6.24) to be performed only once, with the tabulated results then applied to all of the different cells. Therefore, cell splitting does not add CPU time to the calculations.

Radiant flux calculation

Also the practical computation of the radiant flux in Eq. 6.18 requires a correct implementation. At high optical thicknesses, when calculating the absorption of the radiation emitted at the k-th cell along a given direction within this same cell, representing the cell by its central point gives a

poor representation of the extinction. A better approximation is again obtained by splitting the cell into N_p random points, P_n, and then the extinction is calculated along rays emerging from P_n, along directions (θ, ϕ), and finally calculating the averages at fixed directions as P_n covers the cell. Specifically, the contribution of the k-th cell to the radiant flux can be written as (i.e., from emissions within the k-th cell):

$$F_{\lambda,k}(\theta,\phi) = \frac{1}{N_p}\sum_{n=1}^{N_p} F_{\lambda,k}(P_n;\theta,\phi) \tag{6.27}$$

where $F_{\lambda,k}(P_n;\theta,\phi)$ is the contribution to the emission $F_{\lambda,k}(\theta,\phi)$ of the small volume $V(P_n) = V_k/N_p$ around point P_n resulting from cell k splitting. To calculate the extinction at cell k of rays emerging at point P_n, one has to calculate the distances from P_n to the cell borders along the (θ,ϕ) directions, $d(n;\theta,\phi)$. Indeed, as the emissivity is the same at any $V(P_n)$, the averages in Eq. 6.27 just involve the partial optical depths:

$$\tau_{\lambda,k}(n;\theta,\phi) = \sigma_\lambda \times n_{H,k} \times d(n;\theta,\phi), \tag{6.28}$$

namely:

$$\frac{1}{N_p}\sum_{n=1}^{N_p} \exp[-\tau_{\lambda,k}(n;\theta,\phi)]. \tag{6.29}$$

In the practical implementation, as explained in §6.2.5, the calculations have been made just once and for all in the unit cell, and the resulting values normalized to the actual cell sizes. Therefore, here again cell splitting does not add CPU time to the calculations.

The emission $F_\lambda(\theta,\phi)$ is the key tool to calculate simulated galaxy SEDs and their derivatives, such as luminosities, colors and images in different bands from the UV to the sub-mm.

Calculating images with GRASIL-3D

GRASIL-3D allows us to calculate images of simulated objects in different filters and as viewed from different directions (θ,ϕ). To this end, the rectangular grid is oriented with the z-axis in the chosen direction, and then, to calculate the radiant flux at point (x,y) (i.e., in the plane normal to the line-of-sight), we sum:

$$F_{\lambda,x,y} = \sum_k F_{\lambda,k}(\theta,\phi) \tag{6.30}$$

where $F_{\lambda,k}(\theta,\phi)$ is the extinguished emission from the k-th cell, and the sum goes over all the cells in the line-of-sight. In §6.4.3 some examples of images of simulated objects calculated with GRASIL-3D are shown. The output of the code in this imaging mode are an array of SEDs, one for each cell. Therefore, in order to produce actual images we need to post-process these SEDs, as it is explained in Appendix 6.7.

6.2.6 Summary: GRASIL-3D parameters

The GRASIL-3D code contains several free parameters for transposing particle positions from the simulation outputs onto the grid. These are new relative to the GRASIL code. The meaning of these parameters will be summarized, and the possible range of values each can take will be discussed in turn.

1. The grid size: A rectangular grid has been used. The softening parameter of simulations ϵ sets the minimum grid size (for consistency sake).

2. Threshold density for molecular clouds: Gas with densities above $\rho_{mc,thres}$ are set to form molecular clouds. A threshold value is commonly used by numerical simulations of molecular clouds. This value is backed up by a large number of observations of molecular clouds both from our own galaxy and nearby galaxies. Values for this parameter used in simulations have a range of values depending on the authors. For example, $\rho_{mc,thres}$ = 100 H nuclei cm^{-3} ≈3.3 $M_\odot$ pc^{-3} in Tasker & Tan (2009) and = 35 H nuclei cm^{-3} ≈ $1 M_\odot pc^{-3}$ in Ballesteros-Paredes et al. (1999) and Ballesteros-Paredes et al. (1999). An adequate range for this parameter is therefore taken to be $\rho_{mc,thres}$ = 10 - 100 H nuclei cm^{-3}.

3. Parameters for the log-normal PDF: Two parameters ρ_0 and σ govern the log-normal PDF function, see § 6.2.2. They are linked to the density of gas by Eqs. 6.6 and 6.2, so it is convenient to fix one of the parameters and use the equations to calculate the other. We fix σ, treating it as a free parameter, and compute ρ_0 from the gas density. Values for σ have been calculated to range from 2.36 to 3.012 in Wada & Norman (2007), while Tasker & Tan (2009) give σ = 2.0.

   Between them, $\rho_{mc,thres}$ and σ, control the calculation of the cirrus field and the proportion of the total gas in the galaxy in the form of molecular gas, f_{mc}. A useful check for the choice of these parameters can be made by comparing the final calculated average value for the

galaxy with observations. For example Obreschkow & Rawlings (2009) give the ratio as a function of the galaxy morphological type and gas mass (Figures 4 & 5 in that paper), see also Leroy et al. (2008). More recently Saintonge et al. (2011, 2012) conducted COLD GASS, a legacy survey for molecular gas in nearby, massive ($M_{star} \geq 10^{10}\mathrm{M}_{\odot}$) galaxies. Data on the molecular gas content in normal star forming galaxies at $z \sim 1-3$ are being gathered and analyzed by the PHIBSS team (Tacconi et al. 2013), a considerable improvement compared to our current understanding.

Otherwise, the treatment of the dust properties and the MC model closely follow the GRASIL code. We summarize the corresponding parameters as well as their range of values.

1. Escape time-scale from MCs, t_0: This parameter represents the time taken for stars to escape the molecular clouds where they were born. t_0 is likely to be of the order of the lifetime of the most massive stars, with masses $\sim 100\ M_{\odot}$ to $10\ M_{\odot}$ and corresponding lifetimes of 3 to 100 Myrs. In practice the timescale is likely to vary with the density of the surrounding ISM. For low-density environments like spiral galaxies, with low star formation rates, the lifetime is likely to be nearer the lower end of the range, corresponding to that of the most massive supernovae. On the other hand, t_0 is likely to be much closer to the longest value for a high-density environment like the star-forming central regions of starburst galaxies.

   The escape timescale was found to be a very important parameter of the GRASIL model. Typical values were found by comparison to local observations in Silva et al. (1998), yielding ~ 2.5 to 8 Myrs for normal spiral galaxies, and between 18 and 50 Myrs for strong starburst galaxies.

2. Optical depth of MCs: As shown in Eq. 6.20, the optical depth of MC depends on a combination of r_{mc} and m_{mc}. Observational estimates from our Galaxy suggest typical values $m_{mc} \sim 10^5$ to $10^6 M_{\odot}$ and $r_{mc} \sim 10$ to 50 pc. In order to match observed SEDs of local galaxies, Silva et al. (1998) set $m_{mc} \sim 10^6 M_{\odot}$ and derived values of r_{mc} between 10.6 pc and 17 pc.

The parameters needed to characterize the grain size distribution have been fixed, and, therefore are not considered as free in this work (see §6.2.4). Otherwise, it is worthwhile to recall that the simulations provide and fix the geometry of each galaxy component, as well as its SFR, metal

enrichment and gas fraction histories in such a way that no further parameters are needed to describe them.

6.2.7 Numerical performance of GRASIL-3D

GRASIL-3D is a Fortran paralell (MPI) code. It has been run with up to 1024 CPUs at Red Española de Supercomputación (RES), with good scaling properties. The optimal number of CPUs depends on various factors, of which the number of cells containing baryonic particles is the most important. This number can be expressed as a covering factor multiplied by the total number of cells, $L^3_{\rm box}$. While $L_{\rm box}$ is given as input according to the spatial resolution, the covering factor depends on the particulars of each hydrodynamical simulation. Typical values for the runs involving HD-5103B galaxy-like object presented in this work, with 60^3 grid cells and a covering factor close to 1, are 7500 sec with 32 CPUs.

GRASIL-3D can be considered a kind of *software telescope*, that is, a software device performing similar tasks as a telecope does. Indeed, the device can be used in two main modes, either to obtain images of simulated galaxies, or to obtain their SEDs and associated photometric properties: fluxes in different bands and colors.

The memory requirements depend on the using mode. Using high resolution SSP spectra (8500 wavelengths between 91 angstrom and 10 μm), the code needs 25, 100 and 300 Mb of RAM/CPU for meshes of 60^3, 100^3, 150^3 cells, respectively, in the SED-only mode. In the current imaging mode, GRASIL-3D produces 3 images corresponding to 3 lines of sights perpendicular to each other. For images, no high resolution SSP spectra are generally needed. Therefore, using low resolution SSP spectra (for example, 200 wavelengths between 91 angstrom and 10 μm), the memory requirement would be 36 and 95 Mb of RAM/CPU for meshes of 60^3 and 110^3, respectively, with these requirements scaling linearly with the number of wavelenghts in the SSPs.

6.3 Testing GRASIL-3D

6.3.1 Energy balance

The total energy absorbed by the MC or cirrus dust component has to be equal to the total energy they separately emit. Therefore, energy balance in either component is a necessary condition to be met by GRASIL-3D. As mentioned, the radiative transfer in MCs is as in the GRASIL model. To check the energy balance in the diffuse ISM, we calculate its heating by stars and MC emissions,

and compare it with the total (integrated over directions and wavelengths) diffuse ISM emission.

The total energy absorbed by the cirrus component can be written as:

$$E_{abs} = \sum_k \int d\lambda \int d\Omega E_{abs,\lambda}(k;\theta,\phi) \tag{6.31}$$

where we have summed over the grid cells V_k, and integrated over wavelength and direction the components:

$$E_{abs,\lambda}(k;\theta,\phi) = V_k j_{\lambda,k}(1 - \exp[-\tau_{eff,\lambda}(k;\theta,\phi)]) \tag{6.32}$$

i.e., the absorption of energy emitted at cell k at wavelength λ along rays traveling in the (θ,ϕ) direction to the outskirts of the galaxy, where $j_{\lambda,k}$ is the volume emissivity of the k-th cell (i.e., from stellar and MC emissions), and $\tau_{eff,\lambda}(k;\theta,\phi)$ is the effective optical depth (Eq. 6.21) from the (central point of the) k-th cell to the outskirts of the galaxy along the (θ,ϕ) direction.

Within this scheme, calculating the energy absorbed at cell k from its own emission is not straightforward. It can be written:

$$\begin{aligned} E_{abs}(k,k) = V_k \int d\lambda j_{\lambda,k} \\ \times \int d\Omega (1 - \exp[-\tau_{eff,\lambda}(k,k;\theta,\phi)]) \end{aligned} \tag{6.33}$$

and involves $d(k,k;\theta,\phi)$, that is, the distance traveled by a ray from the central point of the cell to its border along the (θ,ϕ) direction. We note that when $\max_{ithcell}\ \tau_{eff,\lambda}(m,n)$ is $<< 1$, then

$$1 - \exp[-\tau_{eff,\lambda}(k,k;\theta,\phi)] \simeq \sigma_\lambda n_{H,k} d(k,k;\theta,\phi) \tag{6.34}$$

and therefore the integral over directions is the average distance from the central point of a cell to its borders, along random directions.

When this condition is not satisfied, representing the cell by its central point gives poor results. A better approximation is obtained by splitting the cell in N_p random small volumes represented by points P_n, and then taking averages as in the previous section. By doing so, the energy absorbed at cell k from its own emission (Eq. 6.33) can be written as:

$$E_{abs}(k,k) = \frac{V_k}{N_p} \int d\lambda j_{\lambda,k}$$

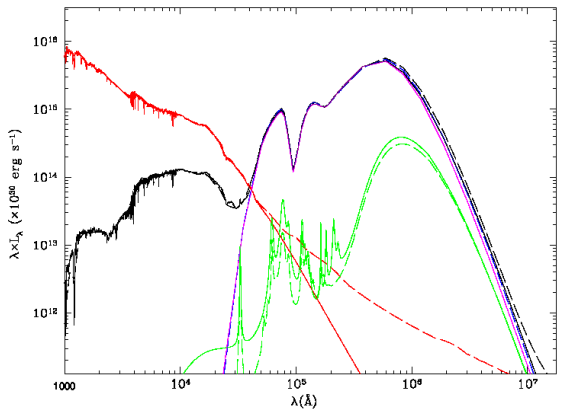

Figure 6.1: The SEDs of two models corresponding to ARP220 with a geometry of a King sphere. Dashed lines are for GRASIL, while continuous lines are for GRASIL-3D operating on a Monte Carlo realization of the same model, see text. The black lines are the final SEDs when dust effects are taken into account, the dashed blue and continuos magenta lines correspond to extinguished MCs emission (for GRASIL and GRASIL-3D, respectively), green to cirrus emission, and red to stellar emission when the dust effect is not taken into account.

$$\times \int d\Omega \sum_{n=1}^{N_p} (1 - \exp[-\tau_{eff,\lambda}(n;\theta,\phi)]) \tag{6.35}$$

involving the partial optical depths defined in Eq. 6.28. The angle average gives, in the limit of low optical thickness, the average distance from the central point of a cell to its borders along random directions, as expected. However, when this is not the case, cell splitting to calculate the heating by its own emissions leads to important differences. The practical implementation consists in calculating the splitting in the unit cell, and then rescale to the actual cell size.

The calculation of this heating allows us to test the energy balance within the cirrus. In Tables 6.3 and 6.5 we give some results for both the MC and the cirrus components, as well as for the overall bolometric luminosity. We see that the energy conservation is very good.

6.3.2 GRASIL-3D versus GRASIL results

As GRASIL-3D is based on the formulism of GRASIL (with slightly different dust model implementations), comparing the SEDs they produce when applied to the same galaxies is a necessary check for GRASIL-3D.

To this end, we have produced analytical galaxy models to be compared with GRASIL results. They are Monte Carlo realizations with N_{part} particles of King spheres (see Silva et al. 1998) and

Monte Carlo realizations of SFR histories. More specifically, following Silva et al. (1998), we have built a Monte Carlo model for ARP220 with a core radius $r_c = 0.5$ kpc, an age of 13 Gyr, where the SFRH $\phi(t)$ is constant in the interval of the age of the Universe 1 Gyr $< t_u <$ 12.95 Gyr, involving a stellar mass of $2.3 \times 10^{11} M_{\odot}$. Later on, for 12.95 Gyr $< t_u <$ 13 Gyr it undergoes an exponential burst with e-folding time $t_e = 0.05$ Gyr involving a gas mass of $2.5 \times 10^{10} M_{\odot}$. The gas mass fraction at $t_u = 13$ Gyr is $f_{gas} = 0.139$, the fraction of gas in molecular clouds is assumed constant at f_{mc}=0.5 and the parameter regulating the escape of young stars from MC is t_0 =50 Myr, with a solar metallicity and molecular cloud radii of $r_{mc} = 10.6$ pc.

In Figure 6.1 we show the SEDs for this model, calculated with both GRASIL-3D and GRASIL. Taking into account the differences of the dust model implementation, that mainly affect the cirrus and in particular their PAH emission (see discussion in Vega et al. 2005), the agreement can be considered very satisfactory. Note that the difference in the intrinsic stellar emission appears because the reported GRASIL computation (dashed red line) includes the emission from dust in the stellar envelopes directly into the stellar population models, following Bressan et al. (1998) and Bressan et al. (2002), while that of GRASIL-3D (full red line) does not.

6.4 Applications and Potentialities

GRASIL-3D has been interfaced with a variety of galaxies identified in cosmological hydrodynamic simulations. Here we show results of galaxies run with two different codes: `P-DEVA` and `GASOLINE`. We note that we are not able to make accurate statistical analyses yet, as we do not have a statistical number of high resolution galaxy simulations. Indeed, all we currently can achieve is to show that by interfacing GRASIL-3D with simulations (whose validity has been otherwise proved, see below), we obtain results consistent with observational data.

6.4.1 Hydrodynamic codes

P-DEVA

`P-DEVA` is an entropy-conserving AP^{3}M-SPH code, an OpenMP parallel version of the `DEVA` code (Serna et al. 2003), which includes the chemical feedback and cooling methods described in Martínez-Serrano et al. (2008). The primary concern when developing this code was that conservation laws (e.g. momentum, energy, angular momentum and entropy) hold accurately (see Serna et al. 2003, for details). The star formation recipe implemented in the `P-DEVA` code follows a Kennicutt – Schmidt-

like law with a given density threshold, ρ_*, and star formation efficiency c_*. In line with Agertz et al. (2011), inefficient SF parameters are implemented, which implicitly account for the regulation of star formation by feedback energy processes by mimicking their effects, which are assumed to work on sub-grid scales.

The chemical evolution implementation (Martínez-Serrano et al. 2008) accounts for the full dependence of the radiative cooling on the detailed composition of the gas, through a fast algorithm based on a metallicity parameter, $\zeta(T)$, which takes into account the weight of the different elements on the total cooling function. The code also tracks the full dependence of metal production on the detailed chemical composition of stellar particles (Talbot & Arnett 1973), through a Q_{ij} formalism implementation of the stellar yields, for the first time in a SPH code. A probabilistic approach for the delayed gas restitution from stars reduces the statistical noise and allows for a detailed study of the inner chemical structure of objects at an affordable computational cost. Moreover, the metals are diffused in such a way as to mimic the turbulent mixing in the interstellar medium, and the radiative cooling depends on the detailed gas particles metal composition.

Hydrodynamic evolution leads to gas particles being either cold or hot, as gas temperature distribution in simulated galaxies has two conspicuous maxima. Stars mostly form from the cold component. As we have said above, the star formation history is directly provided by the simulation. Stellar particles are considered as SSPs, with given age, metallicity and IMF $\Phi(M)$, specifically a Salpeter IMF (Salpeter 1955), with a mass range of $[M_l,M_u]=[0.1,100]M_\odot$. According to the chemical evolution scenario implemented in `P-DEVA`, stellar particles can be transformed into gaseous ones, according to a probabilistic rule.

Table 6.1: Data on the $z = 0$ sample of simulated disk-like galaxies

Name	$m_{\rm bar}$ [a]	$M_{\rm star}$	$M_{\rm gas}$	SFR [b]	$< Z_{\rm star} >$ [c]	$< Z_{\rm gas} >$ [d]	r_e [e]	r_s [f]	B/D [g]
	(10^5 $M_\odot$)	(10^{10} $M_\odot$)	(10^{10} $M_\odot$)	($M_\odot$/yr)	(10^{-2})	(10^{-2})	(kpc)	(kpc)	
g1536_L*	1.9	2.32	1.97	1.809	1.17	1.25	1.38	3.86	0.35
g21647	0.25	2.32	1.37	3.895	1.48	1.94	0.00	1.52	0.00
g7124	2.00	0.60	1.10	0.314	0.46	0.86	0.00	2.94	0.00
LD-5003A	3.82	1.66	0.39	0.550	1.77	2.47	0.28	2.72	0.39
HD-5004A	3.94	3.26	0.67	0.840	1.60	2.20	0.37	4.00	0.43
HD-5004B	3.94	3.05	0.86	0.986	1.52	1.96	0.26	3.29	0.30
HD-5103B	3.78	2.63	0.46	0.820	1.92	3.07	0.55	3.90	0.72
LD-5101A	3.79	1.29	0.33	0.622	1.65	1.99	0.32	3.83	0.19

[a] Baryonic particle mass. For `GASOLINE` runs, its initial value is given

[b] Integrated over the past 100 Myrs

[c] Average stellar metallicity (mass fraction)

[d] Average gas metallicity (mass fraction)

[e] Bulge scale length in the r band. A value 0 means pure exponential disk

[f] Disk scale length in the r band

[g] Bulge to disk luminosity ratio in the r band

GASOLINE

The GASOLINE galaxies are cosmological zoom simulations with initial conditions derived from the McMaster Unbiased Galaxy Simulations (MUGS, Stinson et al. 2010).

When gas becomes cool ($T < 15000$ K) and dense ($n_{th} > 9.3$ cm^{-3}), it is converted to stars according to a Kennincutt – Schmidt-like law with the star formation rate $\propto \rho^{1.5}$. Stars feed energy back into the surrounding gas. Supernova feedback is implemented using the blastwave formalism (Stinson et al. 2006) and deposits 10^{51} erg of energy into the surrounding medium at the end of the stellar lifetime of every star more massive than $8\,M_\odot$. Energy feedback from massive stars prior to their explosion as SNe has also been included (Stinson et al. 2013, as part of the MaGICC project). To mimic the weak coupling of this energy to the surrounding gas (Freyer et al. 2006), we inject pure thermal energy feedback, which is highly inefficient in these types of simulations (Katz 1992; Kay et al. 2002). We inject 10% of the available energy during this early stage of massive star evolution, but 90% is rapidly radiated away, making an effective coupling of the order of 1%.

Ejected mass and metals are calculated based on the Chabrier IMF (Chabrier 2003) and are distributed to the nearest neighbor gas particles using the smoothing kernel (Stinson et al. 2006). Literature yields for SNII (Woosley & Weaver 1995) and SNIa (Nomoto et al. 1997) are used. Metals are diffused by treating unresolved turbulent mixing as a shear-dependent diffusion term (Shen et al. 2010), allowing proximate gas particles to mix their metals. Metal cooling is calculated based on the diffused metals.

6.4.2 Disk galaxies

Simulated disk galaxies

In this case, simulations use the cosmological "zoom-in" technique, with high-resolution gas and dark matter in the region of the main object. The cosmological parameters of a ΛCDM model were assumed for P-DEVA (GASOLINE) runs ($\Omega_\Lambda = 0.723(0.760)$, $\Omega_m = 0.277(0.240)$, $\Omega_b = 0.04(0.04)$, and $h = 0.70(0.73)$), in a 10 Mpc (64 Mpc) per side periodic box.

As a first application, the SED of the HD-5103B galaxy, analyzed by Doménech-Moral et al. (2012), has been calculated and analyzed at $z = 0$. Moreover, the SEDs and colors of HD-5103B around one of its star-forming major mergers have been carefully studied and compared to the phase of milder SF activity at $z = 0$. To compare with currently available data on local, non-starbursting spiral galaxies, see §6.4.4 below, we have also analyzed 4 more galaxies run with P-DEVA (LD-

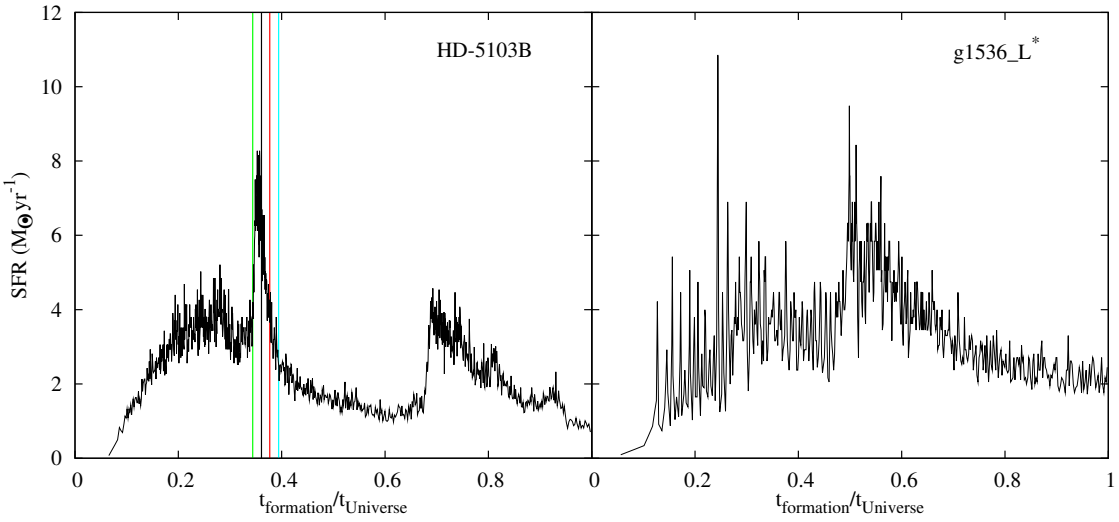

Figure 6.2: Left-hand panel: the stellar age distribution at $z = 0$ for the disk galaxy HD-5103B from Doménech-Moral et al. (2012), where color vertical lines mark the snapshots where this starbursting period will be analyzed in Section 4. Right-hand panel: the same for the g1536_L* galaxy from MaGICC runs (Brook et al. 2012).

5003A, HD-5004A, HD-5004B, LD-5101A, see Doménech-Moral et al. 2012), as well as 3 galaxies run with `GASOLINE` from the MaGICC project (g1536_L*, g21647, g7124, see Brook et al. 2012; Stinson et al. 2013). Except for g21647 and g7124 galaxies, first analyzed by Obreja et al. (2014), these galaxies have all previously appeared in the literature, where more details can be gathered. The choices of most of the relevant parameters to run the `P-DEVA` simulations, as well as many of those characterizing the galaxies properties, are summarized in Tables 1 and 2 of Doménech-Moral et al. (2012) and in Table 1 of Obreja et al. (2013).

An important parameter here is the softening, setting the grid cell size. The gravitational softening used in the five `P-DEVA` runs is $\epsilon_g = 400h^{-1}$ pc, while $\epsilon_g = 312,5$ pc for g1536_L* and g7124, and $\epsilon_g = 156,2$ pc for g21647 galaxies. Some properties of the $z = 0$ galaxies, provided by the simulations and some of them relevant to GRASIL-3D SED calculation, are given in Table 6.1. We see that both the SFR (averaged over the past 100 Myrs) and the specific SFR are low, that the disk and bulge scalelengths, and the bulge-to-disk luminosity ratios are consistent with observations, as other galaxy properties previously analyzed (see, for example Doménech-Moral et al. 2012; Stinson et al. 2013). The images of these galaxies (see for example Figure 6.6 for g1536_L* or Figure 1 in Doménech-Moral et al. 2012) show that they are not interacting galaxies, as defined for example by Smith et al. (2007) or Lanz et al. (2013), see § 6.4.4 below. Therefore, these 8 galaxies can be

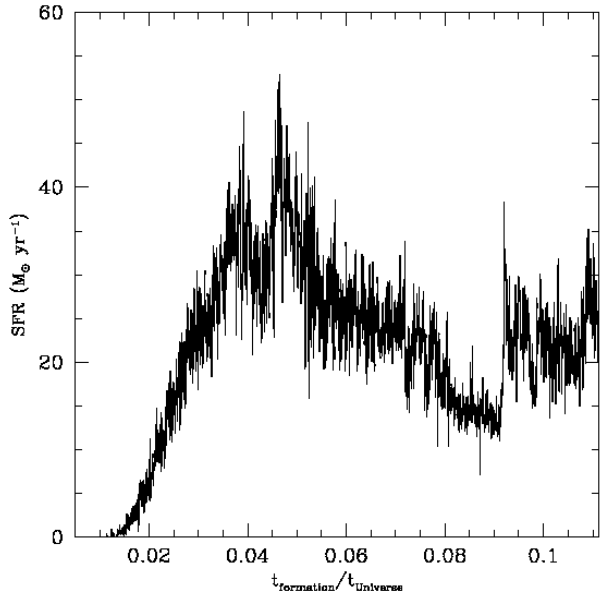

Figure 6.3: The stellar age distribution at $t_{\rm formation}/t_{\rm Universe} = 0.1113$ of the high z galaxy, D-6254, identified in the simulation #7629.

considered as local normal galaxies, with low or very low starbursting activity, and hereafter will be refereed to as the $z = 0$ sample of normal simulated disk-like galaxies.

More details on this $z = 0$ sample of simulated disk-like galaxies provided by GRASIL-3D can be found in Table 6.3, and on HD-5103B during its starbursting phase in Table 6.6. Results in both Tables will be discussed later on.

To calculate the SED of a galaxy, a crucial piece of information is its stellar age distribution. They are provided in Figure 6.2 for HD-5103B and g1536_L*, where we can see that HD-5103B has been involved in two major merger events during its assembly process, with starbursting activity. The first starbursting phase will be analyzed in detail in §6.4.4 as a model for a system with relatively high SF activity. [3].

Note that to transform from stellar age distribution to star formation rate, needed to calculate stellar luminosities, we corrected for gas restitution applying the Lia et al. (2002) formalism (see also Martínez-Serrano et al. 2008).

[3]This particular starburst phase has been chosen because it is the strongest one in our set of simulated spiral galaxies (see Doménech et al. 2012), however the results are shown transformed to zs typical of those of local galaxies.

Table 6.2: The parameter combinations used to test GRASIL-3D on simulated disk galaxies, either in starbursting phases (S) or in normal (N) ones

Set	Phase	t_0 (Myrs)	$\rho_{mc,thres}$ ($M_\odot kp^{-3}$)	σ
		r_{mc} =14 pc		
1	N	2.5	3.3×10^9	3
2	N	2.5	3.3×10^9	2
3	N	2.5	3.3×10^8	3
4	N	5	3.3×10^9	3
5	N	5	3.3×10^9	2
6	N	5	3.3×10^8	3
7	N, S	10	3.3×10^9	3
8	N, S	10	3.3×10^9	2
9	N, S	10	3.3×10^8	3
10	S	40	3.3×10^9	3
11	S	40	3.3×10^9	2
12	S	40	3.3×10^8	3
		r_{mc} =17 pc		
13	N, S	10	3.3×10^9	3
14	N, S	10	3.3×10^9	2
15	N, S	10	3.3×10^8	3

The parameter space and its validation

The allowed ranges of parameter values in GRASIL-3D have been discussed in Section 6.2.6. More specifically, in Table 6.2 we give the combinations of parameters we used for studying the $z = 0$ sample of normal simulated disk-like galaxies (those marked N in column 2), as well as the starbursting phases of HD-5103B (marked S in column 2). Each parameter set is identified by its name (first column) and a symbol in Figure 6.8.

To make identification easier, the table is divided by a double horizontal line, and each part is further divided by simple horizontal lines. The difference between the sets belonging to the upper and lower Table blocks are the parameters characterizing individual MCs, namely their radii

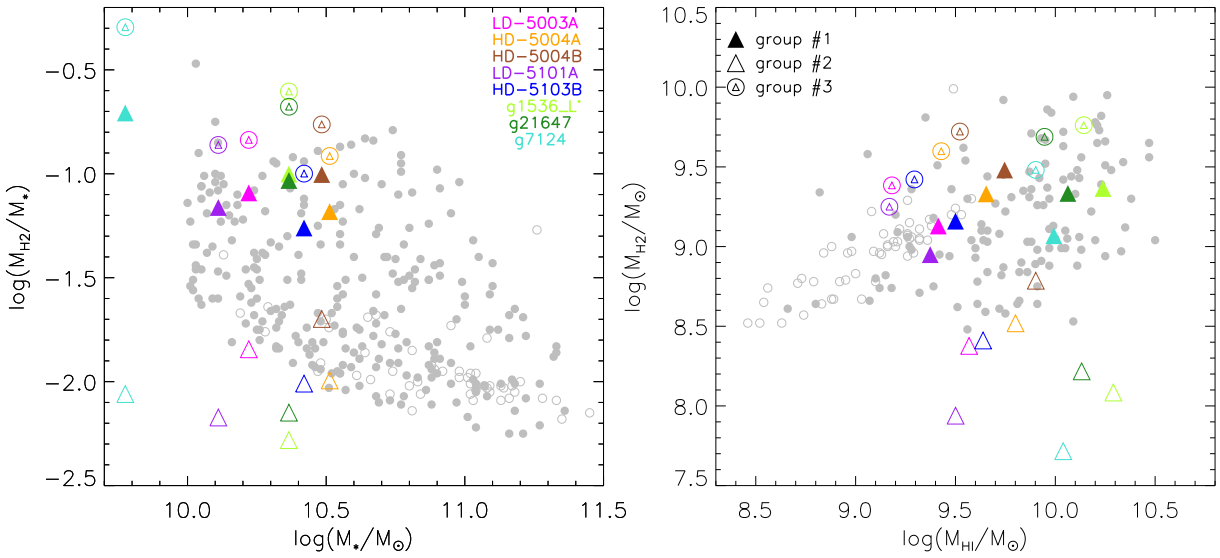

Figure 6.4: Comparison of molecular and atomic hydrogen content and stellar masses of the simulated sample of disk galaxies at $z = 0$ to those of galaxies in the COLD GASS survey (Saintonge et al. 2011). Different color symbols distinguish different objects according to the coding in the left-hand panel. Filled, open and composed symbols correspond to parameter Sets # (1,4,7,13), (2,5,8,14) and (3,6,9,15), respectively, these three groups giving degenerated results in these plots. Gray points are data, with open symbols corresponding to non-detections (upper limits). For details see Saintonge et al. (2012) and Figures 5 and 8 therein.

r_{mc}, entering in the calculation of their optical depth, now a local quantity (see Eqs. 6.20 and 6.13). Parameter sets separated by single horizontal lines have different t_0 values (we recall that this parameter sets the fraction of light that can escape the starburst regions, mimicking MC destruction by young stars, see Section 6.2.2).

Finally, the three parameter sets within each sub-block differ in the parameters setting the molecular mass (and cirrus) fraction at each grid cell, namely the threshold density for MC formation and the dispersion in the PDF, $\rho_{mc,thres}$ and σ respectively. They also set the global MC and cirrus mass, as well as the global MC fraction, f_{mc}, and through the cirrus mass, the total amount of dust in cirrus.

The models in Table 6.2 explore the entire range of allowed values for the t_0 parameter ($t_0 \sim 2.5$ - 8 Myrs for normal spiral galaxies, and $t_0 \sim 18 - 50$ Myrs for starbursting ones, according to Silva et al. (1998)), as well as the range for the $\rho_{mc,thres}$ and σ parameters. Regarding these last two: i) the extreme values of $\rho_{mc,thres}$ are 10 - 100 H nuclei cm^{-3} $\approx 3.3{\times}10^9 - 3.3{\times}10^8 M_\odot \times kpc^{-3}$ taking a H

nuclei-to-gas mass ratio of 0.75, and ii) for the dispersion of the log-normal PDF we have also taken its extreme values found in literature, $\sigma = 3$ and $\sigma = 2$. This would give 4 combinations describing extreme range values for the parameters governing the calculation of f_{mc}. It turns out that the combinations ($\rho_{mc,thres} = 3.3 \times 10^9 M_\odot kpc^{-3}, \sigma = 3$) and ($\rho_{mc,thres} = 3.3 \times 10^8 M_\odot kpc^{-3}, \sigma = 2$) give similar results, and therefore we have not shown the last.

As discussed in §6.2.4, only the $\rho_{mc,thres}$ and σ parameters affect the MC content of a given galaxy. Indeed, in Tables 6.6 and 6.7 the degeneracies among parameter Sets relative to masses of molecular and atomic hydrogen of simulated galaxies are clearly shown. In fact, using parameter Sets belonging to each of the following three groups # (1,4,7,13), # (2,5,8,14) and # (3,6,9,15), gives the same MC and cirrus content. Hereafter they will be named groups #1, #2 and #3 of parameter Sets, respectively.

An important and necessary consistency test for these choices is to compare the resulting masses of molecular and atomic hydrogen of simulated galaxies to observational data. This has been done in Figure 6.4 for local galaxies, where gray symbols are data on local galaxies taken from Saintonge et al. (2012), and color symbols correspond to the sample of 8 $z = 0$ simulated disk-like galaxies described above, see also Table 6.3 for parameter Set 4. More information on the MC content of some of the simulated galaxies can be found in Tables 6.6 and 6.7 for the different parameter Sets, where we see that the mass in their MC content increases when σ increases, from group #2 of parameter Sets to group #1, and increases more again when $\rho_{mc,thres}$ is reduced from 3.3 $\times 10^9$ $M_\odot kp^{-3}$ in group #1 to 3.3 $\times 10^8$ $M_\odot kp^{-3}$ in group #3.

Then, in Figure 6.4, we see that group #2 of parameter Sets results in too little molecular gas for the three galaxies run with `GASOLINE` (open green and turquoise triangles outside the data cloud), as well as for the LD-5101A one run with `P-DEVA`. Therefore group #2 of parameter Sets will not be further used in this work for these galaxies. However, the extreme f_{mc} values provided by group #2 and group #3 are within the range of observations for the other galaxies. Overall, of the 3 models in Figure 6.4 we see that the parameter Sets within group #1 give the best (and comfortably good) consistency with Saintonge et al. (2012) data of local galaxies. We also note that the stellar mass of g7124 is outside the rage of stellar masses in Saintonge et al. (2012).

As remarked in §6.2.6, PHIBSS survey on $z \sim 1 - 3$ massive galaxies ($M_* \geq 10^{10.4}$) by Tacconi et al. (2013), provides new data on their molecular content. An extrapolation to lower masses is provided by their Figure 12, to be compared to our results in Table 6.6 for the merging phase of

HD-5103B. The consistency is good for starburst galaxies[4]. We conclude that the values used for $\rho_{mc,thres}$ and σ adequately describe the molecular cloud content of simulated disk galaxies.

Regarding other parameters, we note that the values of both the time young stars remain enshrouded in MCs (t_0 = 2.5 Myrs, parameter Sets 1 - 3, t_0 = 5 Myrs, parameter Sets 4 - 6, and 10 Myrs, parameter Sets 7 - 9), and the masses and radii of molecular clouds ($m_{mc} = 10^6 M_\odot$ and r_{mc} = 14pc) we have used are typical of normal spiral galaxies according to the discussion in Section 6.2.6. We have also used a value of $t_0 = 40$ Myrs, more typical of starburst galaxies, to test the star-forming phases of these galaxies (parameter Sets 10, 11 and 12). Values of $t_0 = 10$ Myrs in combination with a molecular cloud radius $r_{mc} = 17$ pc (parameter Sets 13, 14 and 15) have been used to find out the effects of having a smaller optical depth in MCs (see Eq. (31)). The effects of GRASIL-3D parameter variations on the SEDs of simulated galaxies will be further discussed in Section 6.5.

[4]We note that starburst galaxies are likely to need a different conversion factor from the observed CO line flux to molecular gas mass ($\alpha \sim 1$ instead of 4.36).

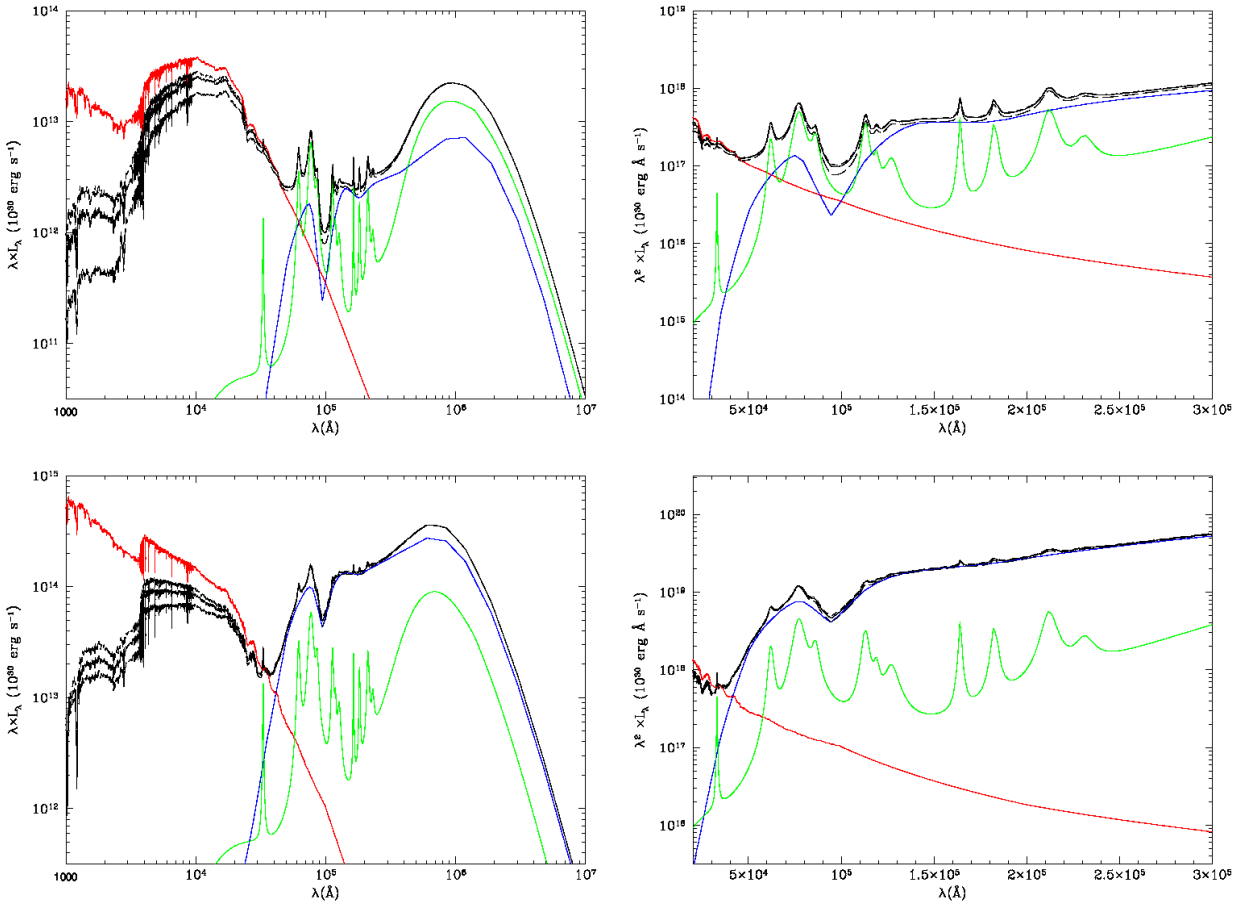

Figure 6.5: The rest-frame SEDs of disk galaxy HD-5103B at $z = 0$ calculated with parameter Set 4 (top left) and of starburst D-6254 with parameter set SB7 (bottom left), and the zooms in the PAH band region of the rest-frame emitted fluxes of HD-5103B (top right) and D-6254 (bottom right). The color code for the lines is the same as in Figure 1, with the upper (lower) black line corresponds to the face-on (edge-on) view of the galaxies, while the middle black line is the angle-averaged emission.

Table 6.3: Masses, luminosities and energy balances (in parentheses) for the sample of $z = 0$ disk-like galaxies calculated with parameter Set # 4

Name	Young Stars ($10^6 M_\odot$)	Free Stars ($10^{10} M_\odot$)	MCs ($10^{10} M_\odot$)	Dust in Cirrus ($10^7 M_\odot$)	L_{bol} (10^{44} erg sec^{-1})	L_c (10^{44} erg sec^{-1})	L_{mc} (10^{44} erg sec^{-1})
g1536_L*	18.269	2.3188	0.2312	9.5034	1.7857 (97.9)	0.4948 (98.4)	0.5506 (92.2)
g21647	46.906	2.3171	0.2155	9.5589	3.2408 (99.4)	1.2932 (96.9)	1.2597 (96.5)
g7124	7.4456	0.5959	0.1169	3.8345	0.5922 (94.6)	0.0715 (99.3)	0.2448 (87.1)
LD-5003A	6.4977	1.6624	0.1346	2.8819	0.4676 (99.9)	0.1197 (98.2)	0.1019 (94.2)
HD-5004A	8.2845	3.2545	0.2140	4.2582	0.8334 (99.2)	0.2413 (98.4)	0.1629 (95.0)
HD-5004B	10.651	3.0469	0.3023	4.5436	0.8426 (99.6)	0.2561 (99.4)	0.1761 (94.2)
HD-5103B	4.9310	1.2906	0.0889	2.1182	0.4090 (100)	0.0739 (96.7)	0.0681 (93.6)
LD-5101A	6.0475	2.5362	0.1433	4.0385	0.7864 (98.8)	0.2303 (98.7)	0.1471 (97.8)

The SEDs and luminosities of simulated disk galaxies

To demostrate how the SEDs of simulated galaxies look, in Figure 6.5 we show the SED of HD-5103B disk galaxy (top left) and a zoom of the corresponding emitted flux in the MIR region (top right), where the PAH band emission stands out. This SED has been calculated using the fiducial dust model described in Section 2.4 and the parameter Set 4 given in Table 6.2. Their color code is similar to that in Figure 1, with the upper (lower) black lines corresponding to the face-on (edge-on) view of the galaxies, while the middle black line is the angle-averaged emission. We can see in Figure 6.5 that, as expected, the difference between the face-on and edge-on views is remarkable in the UV and at optical wavelengths, while it is unimportant at longer ones. The comparison of these SEDs to observations will be analyzed in §6.4.4.

Other important data on simulated galaxies returned by GRASIL-3D, appart from those shown in Figure 6.4, are the total bolometric luminosity, L_{bol}, and the total cirrus and molecular cloud emmitted energy, L_c and L_{mc}, respectively. These can be found in Table 6.3 for the $z = 0$ sample of normal simulated disk-like galaxies, along with their respective energy balances. We see that the luminosities are consistent with observations (see §6.4.4 below), and that the balances are generally very good.

6.4.3 Simulated disk and merger images

In Figure 6.6 we show face-on and edge-on images of the g1536_L* galaxy at redshift $z = 0$ in 8 bands going from far-UV to FIR. From left to right and from top to bottom, they correspond to GALEX (FUV), Johnson (B and V), 2MASS (Ks), IRAC (4.5 μm), MIPS (24 μm), PACS (100 μm) and SPIRE (350 μm) bands. The physical size of each panel is 50 kpc per side. Note the clumpy appearence in the UV and IR bands, as compared with the other bands. The effects of dust obscuration are clear in the edge-on images, and particularly so in the B and V bands where dust lanes can be appreciated accross the disk. Bright spots are star formation regions, nicely visible on the spiral arms.

GRASIL-3D is very useful to study mergers of simulated galaxies, where geometries can be very complex. As an illustration, in Figure 6.7 we show two orthogonal views of a triple merger of disk galaxies at $z = 0.28$, giving rise to the HD-5103B spiral at $z = 0$. The bands are the same as in the previous Figure (rest-frame emission). In this case the panels correspond to 45 kpc per side. Again, the UV and IR emission are more clumpy than the other bands. Note that in one of the

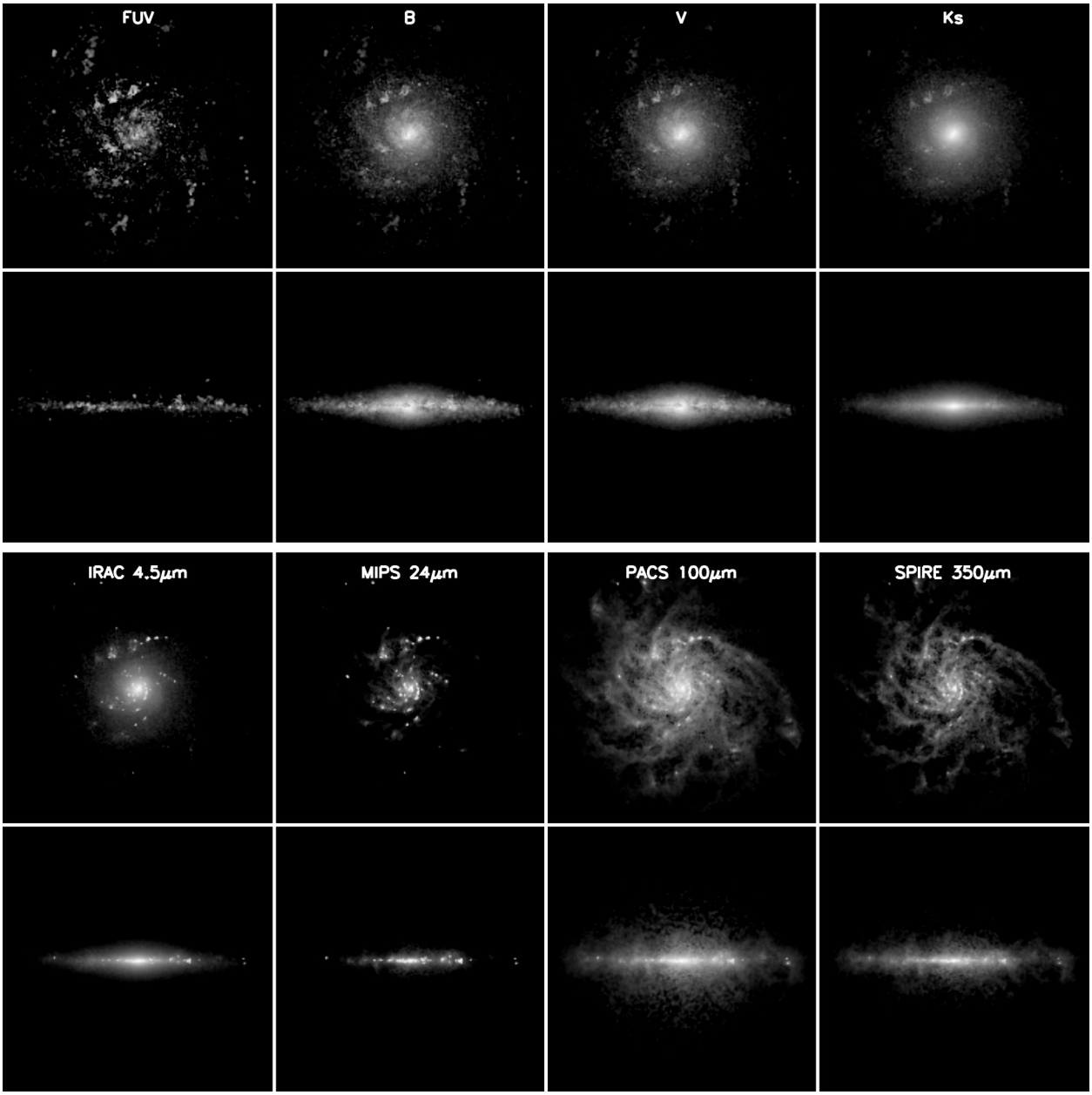

Figure 6.6: Face-on and edge-on images of the g1536_L* galaxy at redshift $z = 0$ in the 8 bands specfied in each panel. The physical size of each panel is 50 kpc per side. No telescope effects (like point-spread functions, pixel sizes, etc) have been taken into account.

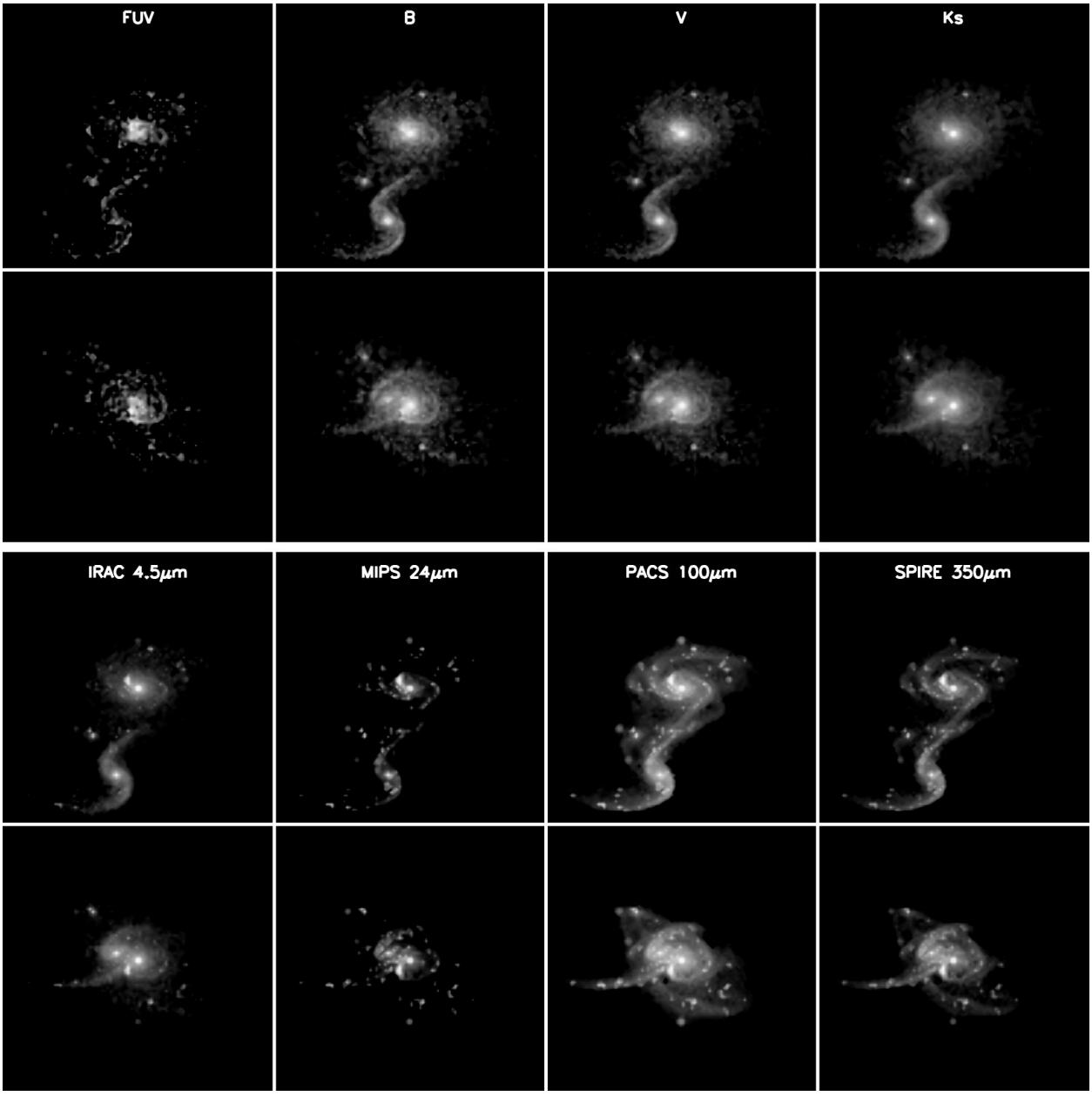

Figure 6.7: Two orthogonal views of a triple merger at $z = 0.28$ involving disk galaxies giving rise to HD-5103B spiral at $z = 0$. The 8 bands specfied in each panel are the same of the previous Figure. The physical size of each panel is 45 kpc per side. No telescope effects (like point-spread functions, pixel sizes, etc) have been taken into account.

perspectives, tidal tails (where IR emission concentrated in knots corresponds to star formation bursts) look very similar to those observed in the local Antennae merger, while in the other the spiral structure of one of the galaxies is still visible.

6.4.4 Comparing GRASIL-3D SEDs of disk galaxies to observations

It is important to know how well the SEDs of simulated galaxies behave as compared to observational data. We are particularly interested in the rest-frame near-IR region up to the far-IR, where the effects of cirrus and MC emission dominate. Comparisons with data coming from different projects are discussed in turn, taking into consideration the starbursting/quiescent SF phase and/or the interacting/non-interacting situation of simulated and real galaxies.

Observational data to compare with

The following observational samples and projects are used as reference:

1. ISO Key Project on the ISM of Normal Galaxies (Helou et al. 1996). Dale et al. (2000) provide ISO and IRAS broad-band fluxes. Based on the Lu et al. (2003) definition of stellar activity, Vega et al. (2005) classify these galaxies into FIR-active (i.e., starbursting, with $\log[L_{FIR}/L_B] \geq 0$ and $\log[f_\nu(60\mu m)/f_\nu(100\mu m)] \geq -0.24$, 43% of the sample), FIR-quiescent (with no or very low SF, $\log[L_{FIR}/L_B] < 0$ and $\log[f_\nu(60\mu m)/f_\nu(100\mu m)] < -0.24$, 31% of the sample) and FIR-intermediate (mild SB phases, 26% of the sample), see their Figure 3.

2. Lu et al. (2003) sample: a subsample of Dale et al. (2000) where the aromatic features in emission (hereafter AFEs) at 6.2, 7.7, 8.6, and 11.3 μm dominating the mid-infrared (MIR) are analyzed in detail. In addition, Lu et al. provide their ISOPHOT spectra.

3. The Spitzer IR Normal Galaxy Survey (SINGS), see Kennicutt et al. (2003) and Dale et al. (2005): 75 local galaxies with different morphologies with Spitzer data. By removing SINGS galaxies with close companions, Smith et al. (2007) have selected a sample of 42 non-tidally perturbed galaxies (their non-interacting sample; 26 spirals, 4 E+SO, 12 Irr/Sm galaxies). A subsample of these galaxies using a more conservative definition for being non-interactive is listed in Table 10 of Lanz et al. (2013) (as part of the KINGFISH project).

4. The Herschel project on Key Insights on Nearby Galaxies: Far Infrared Survey with Herschel (KINGFISH, Kennicutt et al. 2011), which consists of 61 galaxies where 57 are SINGS galax-

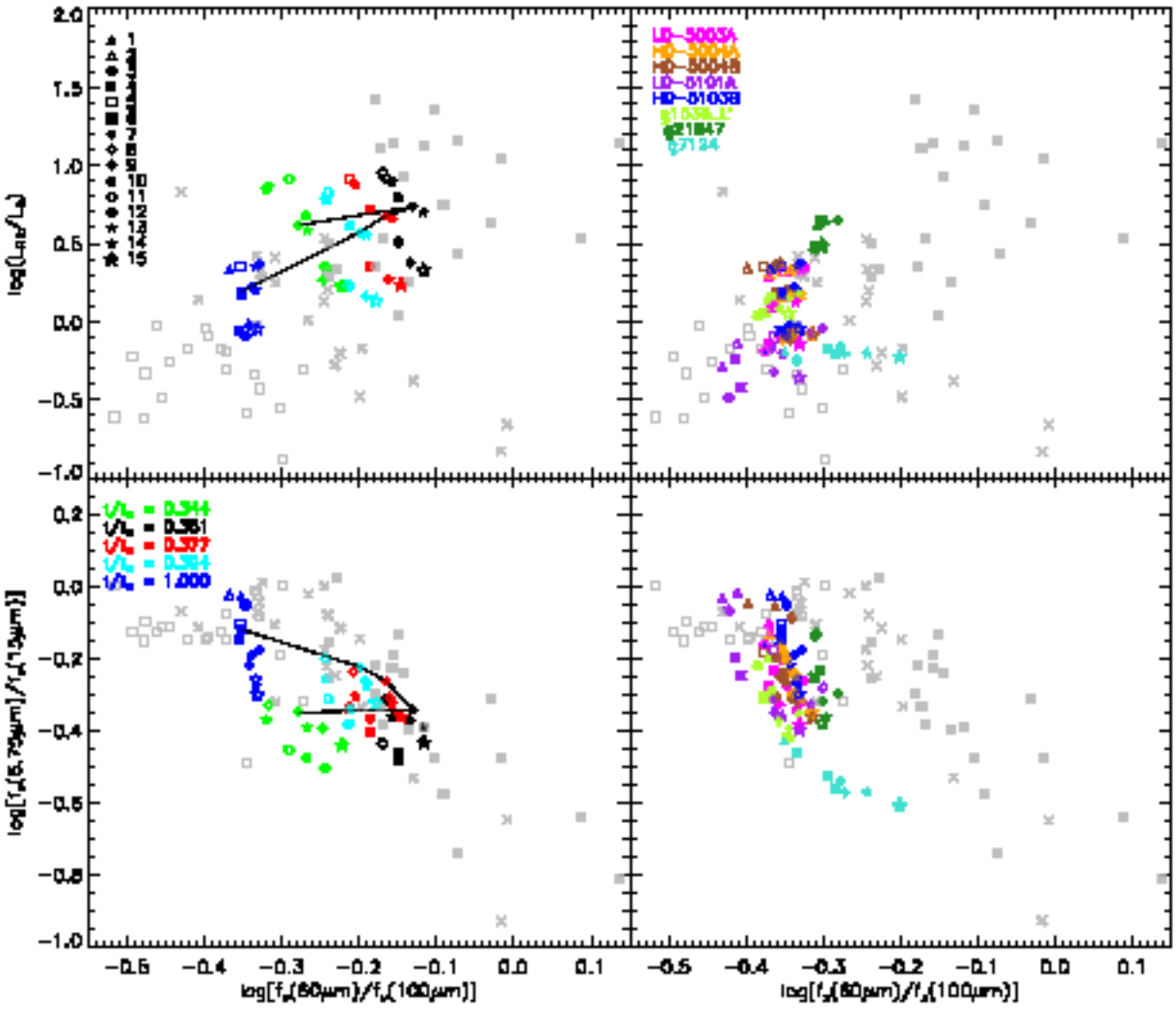

Figure 6.8: Upper-left panel: The rest-frame FIR/blue luminosity ratio $L_{\rm FIR}/L_{\rm B}$ versus the rest-frame IRAS flux density ratios $f_\nu(60\mu{\rm m})/f_\nu(100\mu{\rm m})$ for the HD-5103B galaxy at $z = 0$ (blue) and at different times around one of its major mergers, according to the color code in the lower left-hand panel. Different symbol shapes distinguish different parameter sets (see Table 6.2) as encoded on the left of this panel. Gray points are the same ratios for the Dale et al. 2000 sample shown for comparison, where the filled and empty squares represent FIR-active (i.e., starbursting galaxies) and FIR-quiescent objects, while crosses are intermediate systems (mild starbursts), according to the classification of Vega et al. 2005. Lower-left panel: Same as in the upper panel for the $f_\nu(6.7\mu{\rm m})/f_\nu(15\mu{\rm m})$ vs the $f_\nu(60\mu{\rm m})/f_\nu(100\mu{\rm m})$ flux ratios. Black lines in these two panels join consecutive parameter Set 7 results for the HD-5103B galaxy at its starburst phases and the Set 4 result for the quiescent phase at $z = 0$. The right-hand panels are similar to those at their left for the whole sample of 8 $z = 0$ simulated normal disk-like galaxies, whose identity is encoded by the colors at the left of this panel. Face-on emissions have been used to draw this Figure.

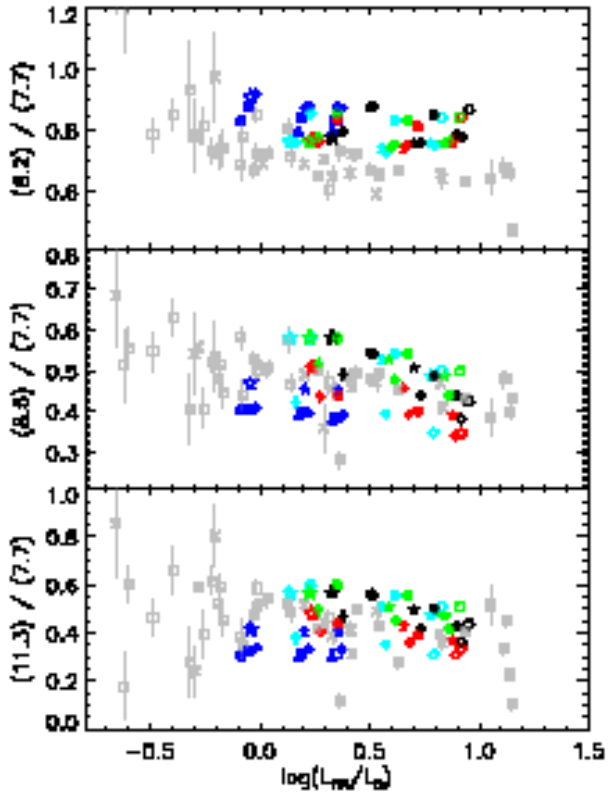

Figure 6.9: The relative strengths of the AFEs as a function of the FIR/blue luminosity ratio for the HD-5103B galaxy at $z = 0$ (blue) and at different times around one of its major mergres. The color and shape codes are the same as in Figure 6.8 (left-hand panels), with the gray points (filled and empty squares, and crosses) representing the observational sample of Lu et al. 2003, according to their nature (FIR-active, FIR-quiescent and intermediate, respectively).

ies. They are subluminous IR galaxies and all normal galaxy types are represented. All were imaged with Herschel PACS and SPIRE (Dale et al. 2012), including those listed by Lanz et al. (2013) as non-interactive.

Results

As most of these projects provide us just with photometric data (i.e., no spectra), rather than a direct comparison of SEDs, an appropriate method to compare calculated SEDs with observed ones comes from fluxes, colors or flux ratio comparisons. As a first exercise, we have made comparison to IRAS and ISOCAM results on normal local galaxies, i.e., the Dale et al. 2000 sample, classified by Vega et al. (2005) according to their SFR activity, see (i) in §6.4.4 above. In Figure 6.8 we

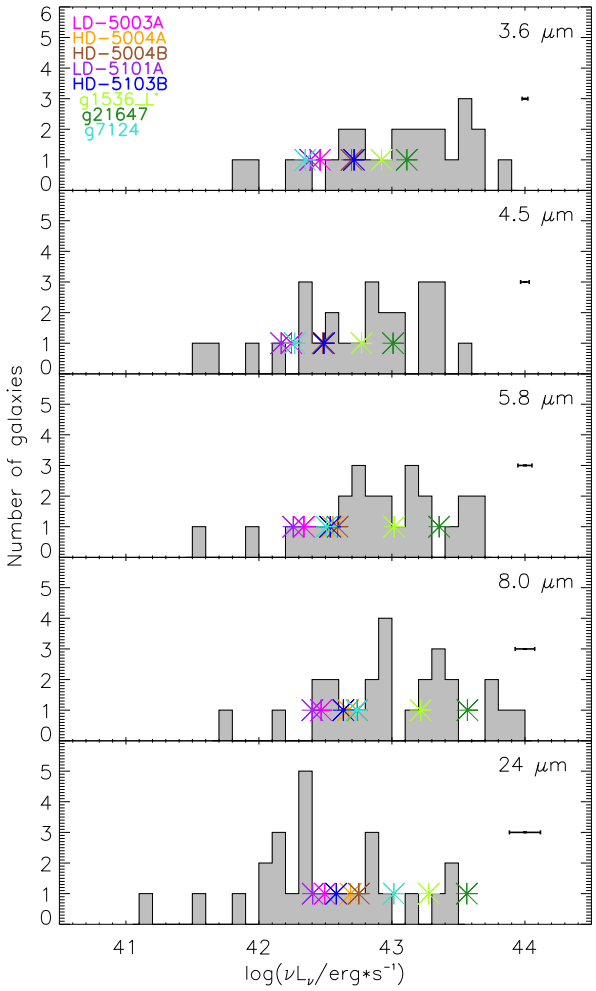

Figure 6.10: Comparison of fluxes in different Spitzer IRAC and MIPS bands for non-interacting normal disk-like galaxies. The histograms have been drawn with data for the sample of 26 non-interacting galaxies from Smith et al. (2007), Tables 2 and 6, selected from SINGS galaxies, see text. Points stand for the sample of 8 disk-like simulated $z = 0$ galaxies, their identity is encoded by colors as in previous Figures. Plotted are averages over results as model parameters take their allowed values (Table 2 for N phase). The error bars at the right of each panel give the maximum dispersions over the 8 simulated galaxies.

plot the FIR/blue luminosity ratio $L_{\rm FIR}/L_{\rm B}$ versus the IRAS 60 μm/ 100 μm flux density ratio, for the Dale sample (in gray) with different symbols standing for starbursting/FIR-active, mildy starbursting/FIR-intermediate and FIR-quiescent galaxies.

To test the ability of GRASIL-3D to return observational results for starbursting galaxies, the HD-5103B starbust period around $t/t_U \sim 0.35$ has been analyzed in detail by plotting its different phases in Figure 6.8, upper panel at the left, and comparing them with the situation at $z = 0$, where the SF activity is milder. The different colors distinguish different starburst phases. More specifically, green, black, red, and cyan correspond to $t/t_U = 0.344$, 0.361, 0.377, and 0.394, respectively. In Figure 6.2 we see that they correspond to the beginning of the starburst phase, two snapshots along the active phase (in black and red), and its end, respectively. We also plot these ratios for the HD-5103B at $z = 0$ (blue). Different symbols in the simulated galaxies stand for different parameter Sets, according to the code in the panel and to Table 6.2. Results for the different models in this Table have been drawn in Figure 6.8 to illustrate their dispersion due to parameter variation within their allowed ranges (note that parameter Sets with $t_0 = 40$ Myrs are excluded for $z = 0$ galaxies). To highlight the time evolution, in Figure 6.8 those points corresponding to parameter Set #7 (#4) in the starburst (quiescent) phases have been connected by a black line.

We see that these results are consistent with observational results. When compared to Figure 3 in Vega et al. (2005), for example, the black, red and cyan points correspond to FIR-active (starbursting) galaxies, irrespective of the GRASIL-3D parameter set we use, while the green points fall in the observational range for FIR-intermediate (mild starbursts) galaxies, and the blue points in that of either FIR-intermediate or quiescent galaxies. It is worth noting that, as expected, the most FIR-active galaxy phases among those analyzed correspond to the black symbols, that is, just at the time when the starburst in Figure 6.2 is at the top of its star formation activity. Moreover, as the black line highlights, the time evolution is also as expected. It causes a correlation between the $L_{\rm FIR}/L_{\rm B}$ and the IRAS 60 μm/ 100 μm flux density ratios as Figure 6.8 clearly shows.

To emphasize the correctness of GRASIL-3D results regarding the location of normal non-starbursting disk galaxies in this plot, results for the whole sample of simulated $z = 0$ disk galaxies described in Section 6.4.2 are shown in Figure 6.8 upper right-hand panel. In this case, colors distinguish galaxy identities, as specified in the left of the panel, while symbol shapes mean different parameter Sets, as above. We see that these non-starbursting disk-like galaxies show flux density ratios characteristic of FIR-quiescent or intermediate galaxies, according to Vega et al. (2005)

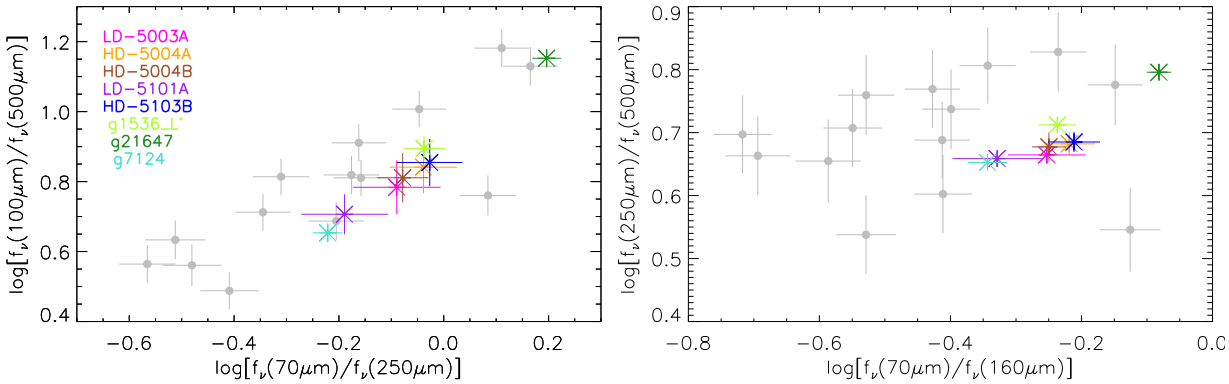

Figure 6.11: Comparison of some flux density ratios in Herschel bands for the $z = 0$ sample of simulated disk-like galaxies (colors) to the corresponding ratios for the non-interacting local spiral galaxies selected by Lanz et al. 2013 (gray symbols). Simulated points are averages over results as model parameters take their allowed values (Table 2 for N phase), and error bars stand for their dispersions.

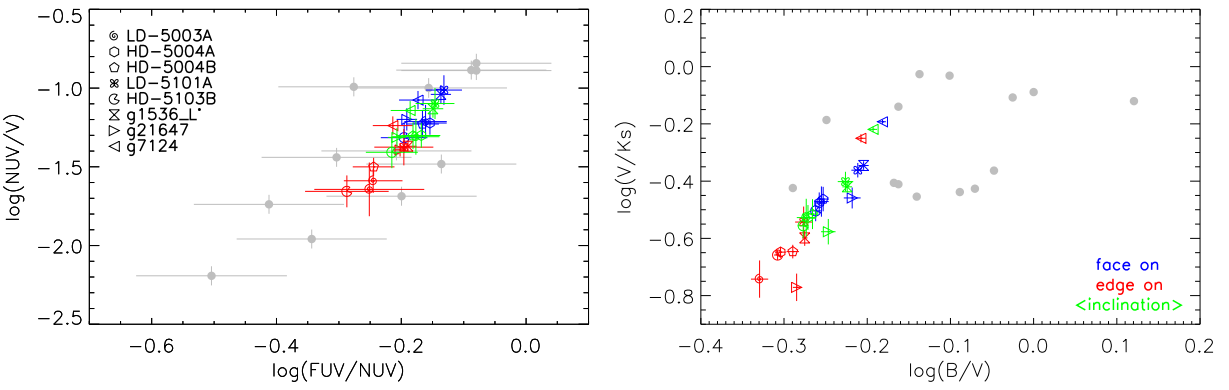

Figure 6.12: UV and optical flux density ratios plots for the sample of $z = 0$ simulated normal disk-like galaxies averaged over parameter sets, with their corresponding dispersions, in comparison to the sample of non-interacting galaxies from Lanz et al. (2013, grey points). Data are from Dale et al. (2007), where no error bars are provided for the flux density ratios shown in the right-hand panel. Colors stand for different disk orientations: face-on (blue), edge-on (red) and angle-averaged (green).

classification.

To further probe the capability of GRASIL-3D to describe starbursting against more quiescent galaxies, in Figure 6.8, lower panel on the left, the $f_\nu(6.75\mu m)/f_\nu(15\mu m)$ flux ratios are plotted against $f_\nu(60\mu m)/f_\nu(100\mu m)$. Symbol shapes or colors have the same meaning as in the upper left-hand panel. This plot can be directly compared with Figure 4 of Vega et al. (2005). A good consistency of simulations with the observational data can be appreciated regarding the location of the quiescent $z = 0$ phase and the starbursting ones relative to observational points. Moreover, when the different snapshots around the HD-5103B galaxy merger are considered, the motion of the color-color representative points in the plane follows trajectories (i.e., the black line) consistent with those shown in Figure 4 of Vega et al. (2005), once we take into account the much higher complexity of the merger for simulated galaxies as compared to the models plotted in Vega et al. (2005) [5].

Figure 6.8, lower panel on the right, shows the same flux ratios as shown in the left, in this case for the entire sample of simulated $z = 0$ disk-like galaxies. We see that the consistency is mostly good relative to non-starbursting galaxies in Dale (2000) sample.

Summing up, the four panels in Figures 6.8 demostrate that GRASIL-3D is a good tool to calculate the SED of galaxies in different phases of their SF activity, including the wet merger sequence causing the starbursts. Indeed, its capability in these tasks is comparable to GRASIL.

As mentioned above (§6.4.4 point (ii)), Lu et al. (2003) provide ISOPHOT spectra for a sample of 45 disk galaxies from the same ISO Key Project on Normal Galaxies, providing their average stacked spectra. They analyze the AFEs at 6.2, 7.7, 8.6, and 11.3 μm dominating the mid-infrared (MIR). Note the remarkable similarity between their average rest-frame spectra (Lu et al. 2003, Figure 3) and those shown in Figure 6.5 upper panel on the left and its F_ν zoomed version.

Therefore, another possible interesting comparison with observational results is provided by the relative strengths of the rest-frame AFEs for this same sample (Lu et al. 2003, Figure 8 and Table 6). For the five snapshots analyzed in the HD-5103B galaxy they are shown in Figure 6.9. The agreement is good and it supports these authors' main claim, namely that the dispersion in the AFE ratios is low for their sample (in the case of simulated results, this is particularly true when GRASIL-3D parameter sets are individually followed), and that little correlation is

[5] For example, in the case of simulated galaxies, the merger causes different SF mixed episodes, the gas and molecular cloud content are local and variable along the merger, and the optical depth for MCs is also local and variable in time.

seen between their variations and either the IRAS $f_\nu(60\mu m)/f_\nu(100\mu m)$ flux density ratios or the FIR/blue luminosity ratios (i.e., galaxy SF phase activity). Not shown in the Figure are the relative strengths of the AFEs corresponding to the entire z=0 sample of normal simulated disk-like galaxies, these relative strengths are compatible with those corresponding to FIR-quiescent and intermediate observed galaxies.

The galaxies in the *Spitzer* Infrared Nearby Galaxies Survey (SINGS, see Dale et al. 2005, 2007, and point (iii) in §6.4.4) constitute an essential reference sample to compare with the IR emission of any calculated SEDs. In this case, a subsample of non-interacting galaxies is available (Smith et al. 2007), allowing us to make comparisons separately.

We have therefore calculated the IRAC and MIPS flux ratios at 3.6, 4.5, 5.8, 8.0, 24, 70 and 160 μm for our sample of $z = 0$ disk-like galaxies. In calculating magnitudes at 3.6, 4.5, 5.8, 8.0 and 24 μm, we used zero points of 280.9, 179.7, 115.0, 64.1 and 7.14 Jy, respectively (IRAC Data Manual; MIPS Data Manual). In Figure 6.10 we show the fluxes in these 5 bands. Points are averages over results with different parameter Sets in Table 6.2 marked (N), and the flux histograms correspond to the sample of 26 non-interacting local galaxies analyzed in Smith et al. (2007). No color corrections were applied in calculating these fluxes. The agreement is good, proving that GRASIL-3D correctly returns fluxes in Spitzer filters for spiral galaxies.

A more restrictive selection of non-interacting galaxies from the normal galaxy sample of Smith et al. (2007) is provided by Lanz et al. (2013), see (iii) and (iv) in § 6.4.4. Figure 6.11 shows some FIR flux density ratio diagrams for our sample of 8 disk-like galaxies at $z = 0$ and the corresponding flux density ratios for the observed ones. Again we see that the consistency is satisfactory, showing that GRASIL-3D gives sound results in Herschel bands.

Apart from the IR analysis, colors in the UV and optical wavelengths have also been analyzed, see Figure 6.12 where face-on, edge-on and angle-averaged disk orientations are shown separately for simulated galaxies. As shown by these plots, the comparison to non-interacting local spiral galaxies (Lanz et al. 2013) is satisfactory for the sample of $z = 0$ disk-like galaxies.

As already mentioned, parameter changes within their allowed ranges have effects on the galaxy SEDs as well as on IRAS-ISO colors and AFE relative strengths. This will discussed in §6.5.

6.4.5 A starburst galaxy at high z

A second very interesting potentiality of GRASIL-3D is its application to high-z massive (multiple)-merging systems, picked in the fast phase of their assembly process (Domínguez-Tenreiro et al.

2006; Oser et al. 2010; Cook et al. 2009; Domínguez-Tenreiro et al. 2011). The timeliness of this application is reinforced by the fact that new observational facilities, such as Herschel and ALMA, observe at wavelengths where the IR emission maxima of these objects are shifted to, providing us with observational data to compare with, see for example Dowell et al. (2014), Hodge et al. (2013) and Decarli et al. (2014), among others.

One example of such systems is provided by the #7629 `P-DEVA` simulation, specifically designed to check GRASIL-3D when applied to such systems. In this simulation a box of 10 Mpc side has been sampled with $N_{DM} = 256^3$ DM and $N_{bar} = 256^3$ gas particles, and evolved using a spatial resolution of $\epsilon = 400/h$ pc. The cosmological model corresponds to a flat ΛCDM with $\Omega_\Lambda = 0.72$, $\Omega_M = 0.28$, $\Omega_{bar} = 0.046$ and $h = 0.7$ (very similar to the cosmological parameters used in the disk runs). To have massive enough systems at high zs, a normalization of the initial perturbation field higher than usual has been used ($\sigma_{pert} = 1.2$), therefore representing a dense subvolume of the universe, and the SF parameters have been taken as $\rho_* = 3 \times 10^{-25}$ g cm^{-3} and $c_* = 0.1$.

Different massive objects at high zs have been identified in the #7629 simulation. Here we focus on one of them labeled as D-6254. Its age distribution is given in Figure 6.3, showing that the object is a strong starburst. In Table 6.4 we give the GRASIL-3D parameter sets used in the SED analysis. Note that, again, those governing the molecular gas mass fraction f_{mc} explore the entire range of their possible values, while t_0 and parameters setting the properties of individual MCs take values consistent with those Silva et al. (1998) found for local starbursting galaxies (ARP220).

The corresponding gas mass and baryon fractions, f_{mc} and $f_{mc,star}$ respectively, can be found in Tables 6.6 and 6.7 where we see that, again, the mass in molecular clouds increases from parameter Sets SB5, SB8 and SB18 to Sets SB4, SB7 and SB17, as σ increases from 2 to 3, and increases further for Sets SB6, SB9 and SB19, where $\rho_{mc,thres}$ decreases from $3.3{\times}10^9$ M$_\odot$kp^{-3} to $3.3{\times}10^8$ M$_\odot$kp^{-3}. Moreover, if the conversion factor from the observed CO line flux to molecular gas mass is taken $\alpha \sim 1$ instead of 4.36, as likely needed for starburst galaxies (Tacconi et al. 2013), then the values we found for the parameter Sets SB4 (SB7 and SB17) and SB6 (SB9 and SB19) are consistent with those found by these authors for massive galaxies between redshifts $z \sim 2.0 - 2.5$, the most distant where such analysis has been made so far. The molecular gas content corresponding to the parameter Set SB5 (as well as Sets SB8 and SB18) are too low.

The rest-frame SED of this object calculated with parameter Set SB7, as well as its zoom in the AFE region, are shown in Figures 6.5, bottom left- and right-hand panels, respectively. These two Figures illustrate that, as expected in a strong starburst object, the dust emission is

Table 6.4: Different parameter sets used to analyze the effects of parameter variation on the D-6254 galaxy SEDs

Set	t_0 (Myrs)	$\rho_{mc,thres}$ ($M_\odot kp^{-3}$)	σ
		r_{mc} =10.6 pc	
SB4	20	3.3×10^9	3
SB5	20	3.3×10^9	2
SB6	20	3.3×10^8	3
SB7	40	3.3×10^9	3
SB8	40	3.3×10^9	2
SB9	40	3.3×10^8	3
		r_{mc} =17 pc	
SB17	40	3.3×10^9	3
SB18	40	3.3×10^9	2
SB19	40	3.3×10^8	3

dominated by MCs at any IR wavelength, and that, moreover, dust emission clearly dominates over the extinguished stellar emission at shorter wavelengths.

6.5 The effects of model parameters on the SEDs of simulated objects

An important question is how the change of parameters in the model affects the SEDs of the different simulated objects we consider. To analyze this point, for each object different SEDs have been calculated by changing these parameters within their allowed ranges, see §6.2.6 and Tables 6.2 and 6.4.

Table 6.5: Stellar masses, luminosities and energy balances (in parenthesis) of the HD-5103B galaxy at $z = 0$ according to the different parameter sets in Table 2

Set code	Young Stellar ($10^6 M_\odot$)	Free Stellar ($10^{10} M_\odot$)	L_{bol} (10^{44} erg sec^{-1})	L_c (10^{44} erg sec^{-1})	L_{mc} (10^{44} erg sec^{-1})
1	4.9136	2.5363	0.7871 (98.9)	0.2524 (99.56)	0.1164 (96.7)
2	4.9136	2.5363	0.7783 (97.8)	0.3172 (99.8)	0.1140 (98.8)
3	4.9136	2.5363	0.7934 (99.7)	0.1629 (99.0)	0.1165 (96.6)
4	6.0475	2.5362	0.7729 (99.5)	0.2334 (99.3)	0.1276 (96.9)
5	6.0475	2.5362	0.7665 (98.7)	0.3003 (98.4)	0.1252 (98.8)
6	6.0475	2.5362	0.7777 (99.9)	0.1462 (99.6)	0.1285 (96.3)
7	14.741	2.5353	0.7723 (99.5)	0.2094 (100.0)	0.1649 (97.9)
8	14.741	2.5353	0.7644 (98.4)	0.2740 (98.7)	0.1602 (99.2)
9	14.741	2.5353	0.7767 (99.9)	0.1270 (98.6)	0.1655 (97.6)
13	14.741	2.5353	0.7780 (99.8)	0.2103 (99.9)	0.1703 (94.8)
14	14.741	2.5353	0.7730 (99.6)	0.2759 (98.6)	0.1686 (95.8)
15	14.741	2.5353	0.7826 (99.2)	0.1274 (98.7)	0.1713 (94.2)

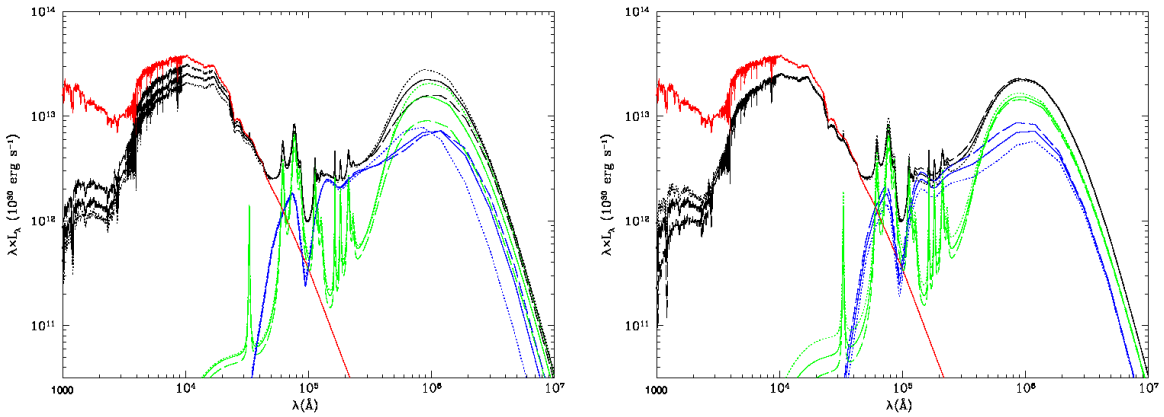

Figure 6.13: Comparison of the SEDs of the simulated galaxy HD-5103B at $z = 0$ obtained under different parameter sets. Left-hand panel compares the effects of changing $\rho_{mc,thres}$ and σ, with full, point and dashed lines corresponding to code 4, 5 and 6 parameter Sets. Right-hand panel compares the effects of changing the t_0 parameter, with full, point and dashed lines corresponding to code 4, 1 and 7 parameter Sets. See Table 2 for parameter set values. Color line codes are as usual and only angle-averaged emissions are plotted.

To properly interpret the results shown in Table 6.5, we recall that the total gas or stellar mass of a simulated galaxy, as well as its total bolometric luminosity in the absence of dust, are fixed by the simulation itself. Therefore, the sum of MC and cirrus total masses is fixed to the total gas mass, and the sum of the young and free stars is also fixed to the galaxy total stellar mass.

6.5.1 The SEDs

As an illustration of the effects of parameter variations on the SED, in Figures 6.13 we show the SED of HD-5103B galaxy at $z = 0$, calculated using parameter Sets 4, 5 and 6 (i.e., different $\rho_{mc,thres}$ and σ values, left-hand panel) and parameter Sets 4, 1 and 7 (i.e., different t_0 values, right-hand panel). On the left-hand panel we see that increasing f_{mc} (i.e., decreasing the cirrus fraction 5-4-6 parameter Sets), the dust absorption by cirrus in the UV and optical decreases, thereby decreasing the cirrus emission at longer wavelengths. The right-hand panel illustrates the consequences of increasing the time young stars remain within MCs: as t_0 increases from parameter Sets 1, 4, 7, the UV emission decreases, but the MC cloud emission increases, at the same time that the cirrus emission in the PAH region decreases.

6.5.2 The global masses and luminosities of the different galaxy components

As expected, Tables 6.6, 6.7 and 6.5 show that the global masses of the different galaxy components are insensitive to m_{mc} and r_{mc} variations, and the global luminosities L_{bol}[6] and L_c do not change. There is a tendency towards slightly higher values of L_{mc} as τ_{mc} decreases.

[6]Note that the values of the bolometric luminosity, L_{bol}, given in the the fourth column of Table 6.5 are constant and equal to the intrinsic stellar bolometric luminosity of HD-5103B, within the accuracy of the calculation (shown by the number in parenthesis at their right).

Table 6.6: Molecular Cloud and Cirrus Dust Content according to $\rho_{mc,thres}$ and σ for the galaxy HD-5103B at different zs

Group	Set	M_{MC}^{dust} (10^{10} $M_\odot$)	f_{mc} [a]	$f_{mc,star}$ [b]	M_{cirrus}^{dust} (10^{7} $M_\odot$)
		$t/t_U = 1$	$M_{\rm tot}$ [c]=2.97 10^{10} $M_\odot$	$M_{\rm gas} = 4.36\ 10^{9}$ $M_\odot$	
1	1, 4, 7, 13	0.1433	0.3286	0.0460	4.0385
2	2, 5, 8, 14	0.0257	0.0590	0.0100	5.8017
3	3, 6, 9, 15	0.2598	0.5956	0.0929	2.3493
		$t/t_U = 0.394$	$M_{\rm tot} = 1.40\ 10^{10}$ $M_\odot$	$M_{\rm gas} = 3.76\ 10^{9}$ $M_\odot$	
1	7, 10, 13	0.1674	0.4449	0.1409	1.1386
2	8, 11, 14	0.0855	0.2273	0.0773	1.9336
3	9, 12, 15	0.2423	0.6440	0.1918	0.5516
		$t/t_U = 0.377$	$M_{\rm tot} = 1.36\ 10^{10}$ $M_\odot$	$M_{\rm gas} = 3.77\ 10^{9}$ $M_\odot$	
1	7, 10, 13	0.1981	0.5253	0.1682	1.1156
2	8, 11, 14	0.1297	0.3439	0.1169	1.8727
3	9, 12, 15	0.2596	0.6886	0.2095	0.5573
		$t/t_U = 0.361$	$M_{\rm tot} = 1.30\ 10^{10}$ $M_\odot$	$M_{\rm gas} = 4.37\ 10^{9}$ $M_\odot$	
1	7, 10, 13	0.2773	0.6346	0.2441	0.9128
2	8, 11, 14	0.2127	0.4868	0.1986	1.5082
3	9, 12, 15	0.3328	0.7617	0.2794	0.4631
		$t/t_U = 0.344$	$M_{\rm tot} = 1.26\ 10^{10}$ $M_\odot$	$M_{\rm gas} = 5.59\ 10^{9}$ $M_\odot$	
1	7, 10, 13	0.3351	0.5998	0.3252	1.3797
2	8, 11, 14	0.1761	0.3153	0.2009	2.6681
3	9, 12, 15	0.4363	0.7811	0.3834	0.5958

[a] $f_{mc} = M_{mc}/M_{\rm gas}$

[b] $f_{mc,star} = M_{mc}/(M_{mc} + M_{star})$ as in Tacconi et al. 2013

[c] $M_{\rm tot} = M_{\rm star} + M_{\rm gas}$

Table 6.7: Molecular Cloud and Cirrus Dust Content according to $\rho_{mc,thres}$ and σ for the galaxies g1536_L* at $z = 0$ and D-6254 at $z = 4$.

Group	Set	M_{MC}^{dust} (10^{10} $M_\odot$)	f_{mc} [a]	$f_{mc,star}$ [b]	M_{cirrus}^{dust} (10^{7} $M_\odot$)
			g1536_L*		
		$t/t_U = 1$	$M_{\rm tot} = 3.32\ 10^{10}$ $M_\odot$	$M_{\rm gas} = 1.08\ 10^{10}$ $M_\odot$	
1	1, 4, 7, 13	0.1750	0.1617	0.0726	6.1449
2	2, 5, 8, 14	0.0109	0.0101	0.0049	7.3175
3	3, 6, 9, 15	0.4039	0.3731	0.1530	4.5585
			D-6254		
		$t/t_U = 0.110$	$M_{\rm tot} = 3.30\ 10^{10}$ $M_\odot$	$M_{\rm gas} = 7.29\ 10^{9}$ $M_\odot$	
1	SB4, SB7, SB17	0.3286	0.4506	0.1134	1.2033
2	SB5, SB8, SB18	0.1228	0.1684	0.0456	2.2805
3	SB6, SB9, SB19	0.4856	0.6656	0.1590	0.5395

[a] $f_{mc} = M_{mc}/M_{\rm gas}$

[b] $f_{mc,star} = M_{mc}/(M_{mc} + M_{star})$ as in Tacconi et al. 2013

The Tables also show that when t_0 increases, the global mass of young stars suffers an important increment in relative terms. The global mass of free stars decreases, but the effect is relatively less important. As a consequence, the total stellar energy to be processed by MCs increases, and, at the same time, the amount of stellar energy that directly heats the cirrus component becomes relatively less important. The resulting effect is that L_{mc} increases, while L_c decreases.

Regarding changes in $\rho_{mc,thres}$ and σ, we treat them in turn. When $\rho_{mc,thres}$ decreases, the global mass in MCs (and f_{mc}) increases, causing a decrement to the global gaseous mass in cirrus and to their dust content. A direct effect is that L_c decreases. L_{mc} keeps roughly constant, which can be understood as a consequence of the constant amount of energy from young stars heating the MC component.

The effects of σ variations on the global masses and L_c and L_{mc} luminosities are in the opposite direction of those caused by $\rho_{mc,thres}$ changes, as can be seen in Tables 6.6, 6.7 and 6.5. When both parameters vary, the effects can be somewhat compensated.

6.5.3 Flux density ratios

In this case, the major effects come from f_{mc} value changes due to $\rho_{mc,thres}$ and σ modifications, as illustrated by Figure 6.13. These effects are more apparent in the FIR/blue luminosity ratios shown in Figure 6.8, upper panels. Indeed, results corresponding to parameter sets bringing about degenerated f_{mc} values, namely # (2, 5, 8, 11, 14; open symbols), # (1, 4, 7, 10, 13; filled symbols), and # (3, 6, 9, 12, 15; composed symbols), show up grouped together in FIR/blue luminosity ratios. According to Tables 6.6 and 6.7, these groups of parameter sets correspond to increasing molecular gas content, and hence, to increasing L_B and decreasing cirrus emission in the FIR region. Indeed, in Figure 6.8 (top panels) we see that parameter Sets 2, 5, 8, 11 and 14 (not considered for `GASOLINE` galaxies) have the highest FIR/blue luminosity ratios. The effects are more important for FIR-active galaxies than for FIR-quiet phases, and they are within the data dispersion at given $f_\nu(60\mu m)/f_\nu(100\mu m)$ ratios, that are much less affected by f_{mc} variations.

The effects of changing the timescale for MC destruction, t_0, are not important on the FIR/blue luminosity ratios, L_{FIR}/L_B, and only modest on the IRAS 60 μm/ 100 μm flux density ratios, see Figure 6.8. Finally, changing the size of individual MCs corresponding to a 50% variation in their optical depth (Sets 13, 14 and 15 versus 7, 8 and 9), has no appreciable effects in Figure 6.8.

Other flux density ratios affected by changes in f_{mc} are the IRAS-ISO 6.75 μm/ 14 μm flux ratios (Figure 6.8 lower panel) as well as the FUV/NUV and V/Ks flux density ratios, effects shown

as error bars in Figure 6.12. Note however that the effects are consistent with the corresponding data dispersion. In this respect, we remind that f_{mc} changes due to parameter variations are generally consistent with observational data on f_{mc}. In the case of parameter Set 5 (and 2, 8, and 14) the corresponding points in Figures 6.4 are at the limits of the data cloud of points or outside it.

Finally, it is remarkable to note that, as shown by Figures 6.8 and 6.9, the effects of modifying the t_0 or r_{mc} parameters within their allowed ranges has insignificant effects in the disk flux density ratios.

These detailed analyses have been repeated for the D-6254 high-z merger galaxy by comparing results obtained under parameter sets in Table 6.4, and the conclusions are similar to those reached for disk galaxies.

6.6 Summary and conclusions

We have introduced a new photometric SED code, GRASIL-3D, which includes a careful modelling of the radiative transfer through the dust component of the ISM. GRASIL-3D is a new model based on the formulism of an existing and widely applied model, GRASIL, but specifically designed to be applied to systems with any arbitrarily given geometry, where radiative transfer through dust plays an important role, such as galaxies calculated by hydrodynamical galaxy formation codes.

A few codes exist that, by interfacing the outputs of hydrodynamic simulations, can Monte Carlo solve the radiative transfer through dust and therefore predict a multi-wavelength SED for simulated galaxies (SUNRISE, RADISHE, ART^2, see §6.1). Following GRASIL, some GRASIL-3D particular strengths relative to these codes can be summarized as: i) the radiative transfer is not solved through Monte Carlo methods, but in a grid; ii) it is designed to separately treat radiative transfer in molecular clouds and in diffuse cirrus component, whose dust composition are different (for example, lower PAH fraction in MC dust); iii) correspondingly, it takes into account the age-dependent dust reprocessing of stellar populations (note that GRASIL has been the first model to do so), arising from the fact that younger stars are associated with denser ISM environments, mimicking through the t_0 parameter the time young stars are enshrouded within molecular clouds before their destruction; iv) it includes a detailed non-equilibrium calculation for dust grains with diameter smaller than $a_{flu} \sim 250$ Å, which allows for a proper treatment of PAH features showing up in MIR.

Current cosmological hydrodynamical codes that follow galaxy formation cannot resolve molecular clouds, therefore some further modelling is required. A sub-resolution model to calculate the local mass in the form of molecular clouds has been implemented in GRASIL-3D, based on a theoretical log-normal PDF for the gas densities, as suggested by small scale (~ 1 kpc) simulations, and on the assumption that MCs are defined by a threshold, $\rho_{mc,thres}$. In this model, the mass of MC relative to the total mass gas, $f_{mc} = M_{mc}/M_{gas}$, as well as the cirrus density field, is set by two parameters, $\rho_{mc,thres}$ and σ, the PDF dispersion. The entire range of values for these parameters given by the literature has been explored in GRASIL-3D, with the result that f_{mc} is consistent with observations, with the exception of three galaxy models and a set of extreme parameter values producing a value of f_{mc} which is too low. This is a very important consistency check for GRASIL-3D.

When solving the radiative transfer for cirrus, a concern is in order when implementing the calculation of the radiation field in a grid cell due to the emissions of this same cell (where an apparent singularity appears), or the absorption of radiation emitted at the k-th cell along a given direction within this same cell. In these cases, at high optical thicknesses, representing the cell by its central point gives a poor representation of the physical processes resulting in inaccurate energy balances. An elegant improvement has been implemented in GRASIL-3D, where the cells are Monte Carlo split into N_p points representing sub-volumes, and the calculations made based on these decompositions. As a result, energy balances improve considerably, being $\sim 98\%$ or higher in most cases.

The code has a general applicability to the outputs of simulated galaxies, either using Lagrangian or Eulerian hydrodynamic codes. As an application, the new model has been interfaced with the `P-DEVA` and `GASOLINE` SPH codes. As first applications, and to show the code potentialities, GRASIL-3D has been used to calculate the SEDs for a variety of simulated galaxies: a sample of 8 normal non-interacting disk-like galaxies at $z = 0$, a merger event between disks, and a high-z massive galaxy in the phase of its fast mass assembly.

A detailed analysis of the calculated SEDs has been performed, putting particular emphasis in the rest-frame mid to far-IR region, where the effects of cirrus and MC emission dominate. Comparisons with data coming from different projects have been discussed for the disks, finding very encouraging results. Particularly remarkable are the agreements related to the PAH features, a very important SF discriminator, thereby opening interesting possibilities for applications of the code. In particular, GRASIL-3D allows the creation of 2D images of such galaxies, at several angles

and at different bands from UV to sub-mm.

The consequences of GRASIL-3D parameter variations on the SEDs of galaxies has been analyzed in detail, and the results point to no remarkable effects when parameter variations are kept within their allowed ranges. The main effects come from f_{mc} variations due to $\rho_{mc,thres}$ and σ modifications. In this case, the effects are not particularly relevant when compared to data dispersion, as long as f_{mc} values are compatible with recent data on molecular gas content of galaxies (Saintonge et al. 2011, 2012; Tacconi et al. 2013).

6.7 Appendix

6.7.1 The post-processing pipeline

Observational data comes in the form of fluxes in various spectral ranges or bands. Therefore, in order to compare the results of GRASIL-3D applied on simulations with observations we have to post–process the SEDs. For this reason we developed a code, *bandflux*, that does just that. It takes as input a GRASIL-3D SED and it computes the fluxes in various bands that can be selected from a total of 150, covering most of the widely used instruments.

We describe here the main flow of *bandflux*. The SED input of the code is the SED output of GRASIL-3D. Therefore, we will describe all the formulas we used to compute the fluxes starting from the variables $F_\lambda(\theta)$ and λ which are returned by GRASIL-3D (see Equation 6.18). In the current version, GRASIL-3D computes the radiant flux at eight different inclinations ($\theta \in \{0°,15°,30°,45°,60°,75°,90°\}$), by integrating $F_\lambda(\theta,\phi)$ over ϕ.

Since here we will be integrating over frequency ranges, we make the following notation conventions:

- $F_\lambda(\theta) = \int F_\lambda(\theta,\phi)d\phi \rightarrow F^\theta(\lambda)$.
- λ is the wavelength in the rest frame of the emitter.
- $\lambda_{obs} = (1+z)\lambda$ is the wavelength in the rest frame of the observer, where z is the redshift.
- $T(\lambda_{obs})$ is the filter response (transmission) as given in the online documentation of each particular instrument.
- c is the speed of light.

- $D_L = D_L(z)$ is the luminosity distance. For $z = 0$ objects the distance is assumed to be that to Andromeda, 740 kpc.

- The observed radiant flux (units $erg/s/cm^2/\mathring{A}$) is

$$F^{\theta}_{obs}(\lambda_{obs}) = \frac{1}{4\pi D_L^2} \frac{F^{\theta}(\lambda_{obs}/(1+z))}{(1+z)^3} \tag{6.36}$$

The redshift factor of $(1+z)^{-3}$ comes from i) photon energy at observer is (1+z) lower than at emission, ii) timespan at observer is (1+z) larger than at emission, and iii) wavelength at observer is (1+z) larger than at emission.

Each magnitude (flux) system now in use comes with its own peculiarities, but they all do have in common that the observed flux is a convolution of the incident flux on the detector with the response of the instrument and that they assume a certain normalization. The current version of *bandflux* computes three different fluxes: $flux_{AB}$, $flux_{blackbody}$ and $flux_{Herschel}$. All three fluxes are given in $Jy = 10^{23} erg/s/cm^2/Hz$. These particular three systems were chosen as to permit an easy and direct comparison with observations from far–ultraviolet to far–infrared.

The first one, $flux_{AB}$, is the flux in the AB magnitude system (Oke 1974). In this system, an object with constant flux per unit frequency interval has zero color. The normalization assumed in this case is a flat spectrum, hence $f_\nu d\nu = f_\lambda d\lambda$, where f_ν is measured in $erg/s/cm^2/Hz$ and f_λ in $erg/s/cm^2/\mathring{A}$. Therefore, the flux in the AB system is computed according to:

$$flux_{AB}(\theta) = \frac{1}{c} \frac{\int \lambda_{obs} F^{\theta}_{obs}(\lambda_{obs}) T(\lambda_{obs}) d\lambda_{obs}}{\int \lambda_{obs}^{-1} T(\lambda_{obs}) d\lambda_{obs}}, \tag{6.37}$$

where the c^{-1} factor comes from the fact that AB fluxes are quoted as per unit frequency not wavelength.

The second flux measure, $flux_{blackbody}$, is appropriate if we want to compare simulations with Spitzer MIPS data. In this case, the normalization is a black body spectrum of temperature 10000 K and the flux is reported at particular wavelengths, λ_{MIPS}, given by:

$$\lambda_{MIPS} \equiv \frac{\int \lambda_{obs} T(\lambda_{obs}) d\lambda_{obs}}{\int T(\lambda_{obs}) d\lambda_{obs}} \tag{6.38}$$

Thus, $flux_{blackbody}$ is given by the following formula:

$$flux_{blackbody}(\theta) = \frac{1}{c} \frac{1}{\lambda^3_{MIPS}(e^{\lambda_{bb}/\lambda_{MIPS}} - 1)} \frac{\int F^{\theta}_{obs}(\lambda_{obs}) T(\lambda_{obs}) d\lambda_{obs}}{\int \frac{T(\lambda_{obs})}{\lambda^5_{obs}(e^{\lambda_{bb}/\lambda_{obs}} - 1)} d\lambda_{obs}}, \tag{6.39}$$

where $\lambda_{bb} \equiv \frac{hc}{k_B T_{10000K}}$ is the wavelength at 10000 K. For deriving the formula above, we have used the resources available on the Spitzer web page `http://irsa.ipac.caltech.edu/data/SPITZER/docs/`.

Last but not least we have the Herschel fluxes for the PACS and SPIRE bands, with $\lambda_{Herschel} \in \{70, 100, 160, 250, 350, 500\}\ \mu m$. In this case we have used the information available on the instruments web pages, `http://herschel.esac.esa.int/twiki/bin/view/Public/PacsCalibrationWeb` and `http://herschel.esac.esa.int/twiki/bin/view/Public/SpireCalibrationWeb`. The resulting formula for computing fluxes is given below:

$$flux_{Herschel}(\theta) = \frac{\lambda_{Herschel}}{c} \frac{\int \lambda_{obs}^2 F_{obs}^{\theta}(\lambda_{obs}) T(\lambda_{obs}) d\lambda_{obs}}{\int \lambda_{obs} T(\lambda_{obs}) d\lambda_{obs}} \tag{6.40}$$

As explained above, the user can select as many filters as wanted and pass them to *bandflux* together with a SED. In the present version, the code first charges all the desired filters in a matrix, as well as the input SED. After that, it starts iterating, first over the filters and second over the eight lines of sight, to compute in each case the three fluxes described above, $flux_{AB}$, $flux_{blackbody}$ and $flux_{Herschel}$. Once all the computations are done, the results are saved in separate files for each line of sight. One such file contains a table in which each row refers to a filter (as given in the input) and gives the filter index, filter effective wavelength, observed fluxes and the luminosity distance assumed.

The code *bandflux* can also be used with GRASIL-3D in imaging mode. In this case, it will perform an extra loop over the SEDs of all the pixels, and the result is returned as one file per filter containing the 2D coordinates in the image and the associated fluxes.

Both the images presented in this chapter (see Figure 6.4.3), as well as the simulated galaxies fluxes that are compared with observational data in Section 6.4 have been derived using *bandflux*. We have not included point spread function effects as these are fairly easy to incorporate in the final step of actually making the images files, and also because in this way they can be changed according to the downgrading degree desired.

6.7.2 Projects involving GRASIL-3D

Testing observational tracers

In Obreja et al. (2014) (see Chapter 7), we study the evolution of the stellar masses, star formation rates and gas phase abundances of star forming galaxies in cosmological galaxy simulations

from the MaGICC project. We derive the stellar masses and star formation rates using observational relations based on spectral energy distributions by applying the new radiative transfer code GRASIL-3D to our simulated galaxies. The simulations match well the evolution of the stellar mass-halo mass relation, have a star forming main sequence that maintains a constant slope out to redshift z $\sim$ 2, and populate projections of the stellar mass - star formation - metallicity plane, similar to observed star forming disc galaxies. We discuss small differences between these projections in observational data and in simulations, and the possible causes for the discrepancies. The light-weighted stellar masses are in good agreement with the simulation values, the differences between the two varying between 0.06 dex and 0.20 dex. We also find a good agreement between the star formation rate tracer and the true (time-averaged) simulation star formation rates. Regardless if we use mass- or light-weighted quantities, our simulations indicate that bursty star formation cycles can account for the scatter in the star forming main sequence.

The early phases of galaxy clusters formation in IR

In Granato et al. (2014) we compute and study the infrared and sub-mm properties of high redshift ($z \gtrsim 1$) simulated clusters and proto-clusters. The results of a large set of hydro-dynamical zoom-in simulations including active galactic nuclei feedback, have been treated with the recently developed radiative transfer code GRASIL-3D, which accounts for the effect of dust reprocessing in an arbitrary geometry. Here, we have slightly generalized the code to adapt it to the present purpose. Then we have post-processed boxes of physical size 2 Mpc encompassing each of the 24 most massive clusters identified at z=0, at several redshift between 0.5 and 3, producing IR and sub-mm mock images of these regions and SEDs of the radiation coming out from them. While this field is in its infancy from the observational point of view, rapid development is expected in the near future thanks to observations performed in the far IR and sub-mm bands. Notably, we find that in this spectral regime our prediction are little affected by the assumption required by this post-processing, and the emission is mostly powered by star formation rather than accretion onto super massive black hole. The comparison with the little observational information currently available, highlights that the simulated cluster regions never attain the impressive star formation rates suggested by these observations. This problem becomes more intriguing taking into account that the brightest cluster galaxies in the same simulations turn out to be too massive (Ragone-Figueroa et al. 2013). It seems that the interplay be- tween the feedback schemes and the star formation model should be revised, possibly incorporating a positive feedback mode.

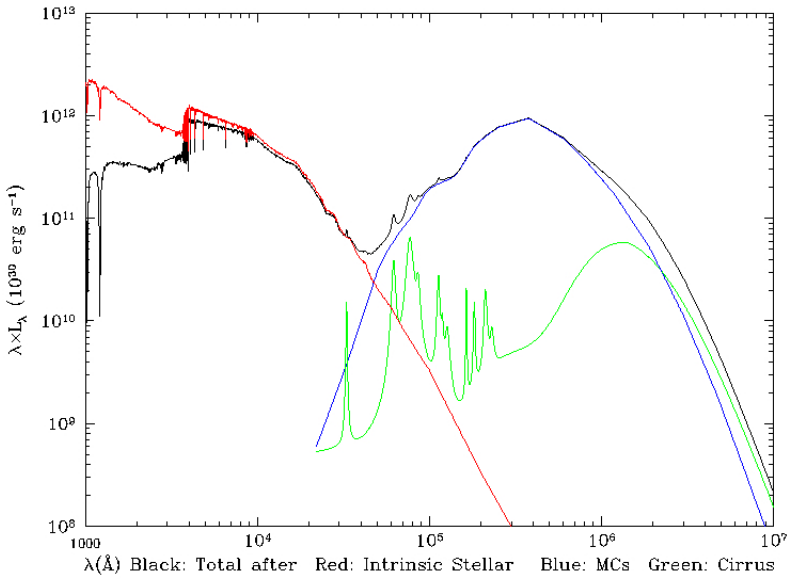

Figure 6.14: SED of a simulated Local Group dwarf. Credit: Isabel Santos, Master Thesis, UAM, July 2014.

SEDs of dwarf galaxies in the CLUES Local Group

This work is based on the so-called constrained initial conditions, in particular for the local Universe (CLUES project, `http://www.clues-project.org`, Gottloeber, Hoffman, & Yepes. (2010)). In this case, the local structures at scales larger than ∼5 Mpc have been fixed according to observational data on the density field and velocity flows, with random fluctuations seeding smaller structures. This enables us to analyze in detail our Local Universe formation, including the Local Group, its intra-group gas, its constituent galaxies of different masses, with an even increasing resolution (some 100 pcs to date). A Local Group type initial conditions have been run with `GASOLINE`. A sample of dwarf galaxies within this Local Group-like simulated structure have been identified and analyzed by Isabel Santos in her Master Thesis (UAM, July 2014; I. Santos et al. 2015, in preparation). We have used GRASIL-3D to compute the SEDs for some of the star forming dwarfs, finding two distinguishable dust components (one cold and one warm), a naturally occurring results given that the code solves the radiative transfer separately for cirrus and molecular clouds (see Figure 6.14). These simulated dwarfs have an observational counterpart in the dwarf sample (see Figure 6.15) whose FIR emission has been studied by Galametz et al. (2009).

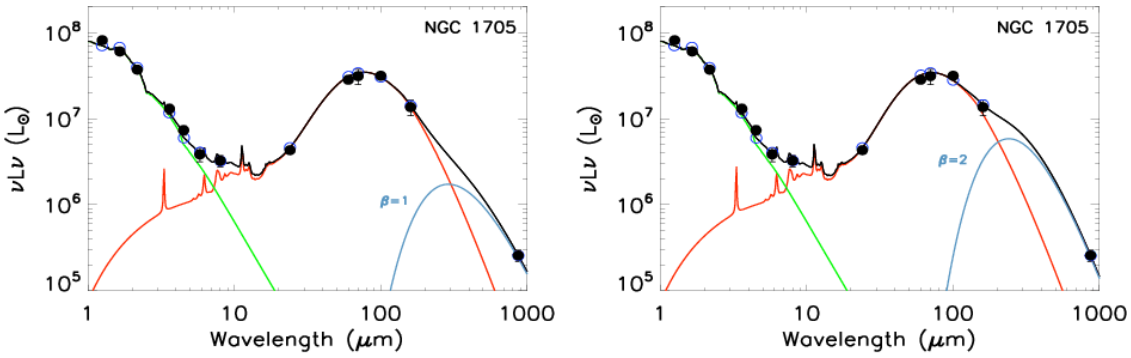

Figure 6.15: SEDs of two low metallicity local dwarfs. Credit: Galametz et al. 2009.

The luminosity function

A fourth application is in progress as a part of David Goz's PhD thesis at Osservatorio Astronomico di Trieste, Italy. Murante et al. 2015 and Goz et al. 2015 have recently presented results of cosmological simulations of disk galaxies carried out with the GADGET-3 code (Springel 2005), where star formation and stellar feedback are described using their MUlti Phase Particle Integrator (MUPPI) model. The description is based on a multi-phase model of the interstellar medium at unresolved scales, where mass and energy flows among the components are explicitly followed by solving a system of ordinary differential equations. This model also treats thermal energy from SNe and uses a kinetic feedback prescription that generates the massive outflows needed to avoid the over-production of stars (e.g. Monaco et al. 2012). Spiral galaxies with small bulge-to-total stellar mass ratios (B/T∼0.2) are obtained, extended stellar and gas disks, flat rotation curves and realistic values of stellar masses.

Currently the authors are working with GRASIL-3D to process large box-size simulations and make direct comparison with observations. Figure 6.16 shows, as a preliminary result, the correlation between the star formation rate and the bolometric IR luminosity (8-1000 μm) of simulated galaxies at $z = 0$. The red line is taken from Kennicutt (1998) and adjusted for a Chabrier IMF and the color of each point shows the total stellar mass of the galaxy. This particular simulation has box-size of 25 comoving Mpc and uses $2{\times}256^3$ dark matter and gas particles in the initial conditions. The gas particle mass is $5.36{\times}10^6 M_\odot$. The Plummer-equivalent softening length for gravitational forces is set to $L_{soft} = 2.08$ kpc comoving for the evolution up to $z = 2$. The softening is then held fixed at $L_{soft} = 0.69$ kpc in physical units from $z = 2$ to $z = 0$. The simulation employs MUPPI model for feedback and star formation, chemical evolution and tracking of 11 elements is

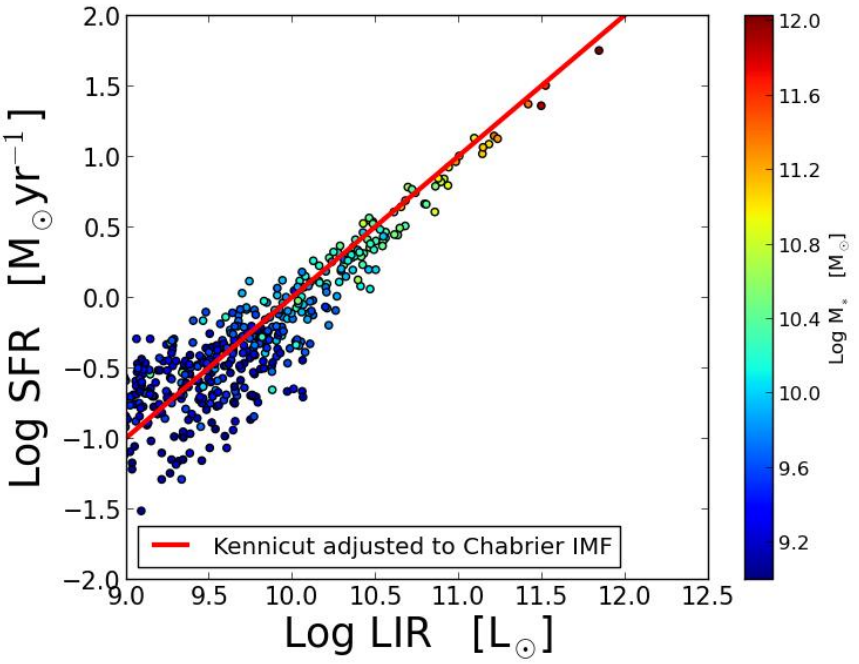

Figure 6.16: Correlation between the star formation rate and infrared luminosity. Credit: David Goz.

performed with the code of Tornatore et al. (2007), while metal-dependent cooling is performed following Wiersma et al. (2009).

References

Agertz O., Teyssier R., Moore B., 2011, MNRAS, 410, 1391

Ballesteros-Paredes J., Hartmann L., Vázquez-Semadeni E., 1999, ApJ, 527, 285

Ballesteros-Paredes J., Vázquez-Semadeni E., Scalo J., 1999, ApJ, 515, 286

Baugh C. M., Lacey C. G., Frenk C. S., Granato G. L., Silva L., Bressan A., Benson A. J., Cole S., 2005, MNRAS, 356, 1191

Bjorkman J. E., Wood K., 2001, ApJ, 554, 615

Bressan A., Granato G. L., Silva L., 1998, A&A, 332, 135

Bressan A., Silva L., Granato G. L., 2002, A&A, 392, 377

Brook C. B., Stinson G., Gibson B. K., Wadsley J., Quinn T., 2012, MNRAS, 424, 1275

Bruzual G., Charlot S., 2003, MNRAS, 344, 1000

Calura F., Pipino A., Matteucci F., 2008, A&A, 479, 669

Chabrier G., 2003, PASP, 115, 763

Chakrabarti S., Fenner Y., Cox T. J., Hernquist L., Whitney B. A., 2008, ApJ, 688, 972

Chakrabarti S., Whitney B. A., 2009, ApJ, 690, 1432

Cole S., Lacey C. G., Baugh C. M., Frenk C. S., 2000, MNRAS, 319, 168

Cook M., Lapi A., Granato G. L., 2009, MNRAS, 397, 534

Dale D. A., Aniano G., Engelbracht C. W., Hinz J. L., et al. 2012, ApJ, 745, 95

Dale D. A., Bendo G. J., Engelbracht C. W., et al. 2005, ApJ, 633, 857

Dale D. A., Gil de Paz A., Gordon K. D., et al. 2007, ApJ, 655, 863

Dale D. A., Silbermann N. A., Helou G., et al. 2000, AJ, 120, 583

Decarli R., Smail I., Walter F., Swinbank A. M., et al. 2014, ApJ, 780, 115

Doménech-Moral M., Martínez-Serrano F. J., Domínguez-Tenreiro R., Serna A., 2012, MNRAS, 421, 2510

Domínguez-Tenreiro R., Oñorbe J., Martínez-Serrano F., Serna A., 2011, MNRAS, 413, 3022

Domínguez-Tenreiro R., Oñorbe J., Sáiz A., Artal H., Serna A., 2006, ApJ, 636, L77

Dowell C. D., Darren C., Conley A., Glenn J., Arumugam V., et al. 2014, ApJ, 780, 75

Elmegreen B. G., 2002, ApJ, 577, 206

Ferrara A., Bianchi S., Cimatti A., Giovanardi C., 1999, ApJS, 123, 437

Fontanot F., De Lucia G., Monaco P., Somerville R. S., Santini P., 2009, MNRAS, 397, 1776

Fontanot F., Monaco P., Cristiani S., Tozzi P., 2008, in Lanteri L., Raiteri C. M., Capetti A., Rossi P., eds, 8th National Conference on AGN The Evolution of the AGN population in the MORGANA model

Freyer T., Hensler G., Yorke H. W., 2006, ApJ, 638, 262

Galametz, M., Madden, S., Galliano, F., Hony, et al. 2009, A&A, 508, 645

Granato G. L., Danese L., 1994, MNRAS, 268, 235

Granato G. L., De Zotti G., Silva L., Bressan A., Danese L., 2004, ApJ, 600, 580

Granato G. L., Lacey C. G., Silva L., Bressan A., Baugh C. M., Cole S., Frenk C. S., 2000, ApJ, 542, 710

Granato G. L., Ragone-Figueroa C., Dominguez-Tenreiro, R., Obreja A., Borgani S., De Lucia G., Murante G., 2014, ArXiv:1412.6105

Gottloeber, S., Hoffman, Y., & Yepes, G., 2010, ArXiv:1005.2687

Goz, D., Monaco, P., Murante, G., Curir, A., 2015, MNRAS, 447, 1774

Greenberg J. M., 1968, Interstellar Grains. the University of Chicago Press, p. 221

Groves B., Dopita M. A., Sutherland R. S., Kewley L. J., Fischera J., Leitherer C., Brandl B., van Breugel W., 2008, ApJS, 176, 438

Guhathakurta P., Draine B. T., 1989, ApJ, 345, 230

Helou G., Beichman C. A., Dinerstein H. L., Hollenbach D. J., Hunter D. A., Lo K. Y., Lord S., Lu N. Y., Malhotra S., Rubin R. H., Silbermann N., Stacey G., Thronson H., Werner M. W., 1996, in American Astronomical Society Meeting Abstracts Vol. 28 of Bulletin of the American Astronomical Society, The ISO Key Project on the ISM of Normal Galaxies. p. 1356

Hodge J. A., Karim A., Smail I., Swinbank A. M., et al. 2013, ApJ, 768, 91

Iglesias-Páramo J., Buat V., Hernández-Fernández J., et al. 2007, ApJ, 670, 279

Jonsson P., 2004, PhD thesis, University of California, nta Cruz, California, USA

Jonsson P., 2006, MNRAS, 372, 2

Jonsson P., Groves B., Cox T. J., 2010, MNRAS, 403, 17

Katz N., 1992, ApJ, 391, 502

Kay S. T., Pearce F. R., Frenk C. S., Jenkins A., 2002, MNRAS, 330, 113

Kennicutt, Jr., R. C., 1998, ApJ, 498, 541

Kennicutt R. C., Bendo G., Engelbracht C., Gordon K., et al. 2003, in American Astronomical Society Meeting Abstracts Vol. 35 of Bulletin of the American Astronomical Society, SINGS: The SIRTF Nearby Galaxies Survey. p. 1351

Kennicutt R. C., Calzetti D., Aniano G., Appleton P., et al. 2011, PASP, 123, 1347

Lacey C. G., Baugh C. M., Frenk C. S., Silva L., Granato G. L., Bressan A., 2008, MNRAS, 385, 1155

Lanz L., Zezas A., Brassington N., Smith H. A., Ashby M. L. N., da Cunha E., Fazio G. G., Hayward C. C., Hernquist L., Jonsson P., 2013, ApJ, 768, 90

Laor A., Draine B. T., 1993, ApJ, 402, 441

Lapi A., Shankar F., Mao J., Granato G. L., Silva L., De Zotti G., Danese L., 2006, ApJ, 650, 42

Leroy A. K., Walter F., Brinks E., Bigiel F., de Blok W. J. G., Madore B., Thornley M. D., 2008, AJ, 136, 2782

Li A., Draine B. T., 2001, ApJ, 554, 778

Li Y., Hernquist L., Robertson B., Cox T. J., Hopkins P. F., Springel V., Gao L., Di Matteo T., Zentner A. R., Jenkins A., Yoshida N., 2007, ApJ, 665, 187

Li Y., Hopkins P. F., Hernquist L., Finkbeiner D. P., Cox T. J., Springel V., Jiang L., Fan X., Yoshida N., 2008, ApJ, 678, 41

Lia C., Portinari L., Carraro G., 2002, MNRAS, 330, 821

Lo Faro B., Franceschini A., Vaccari M., Silva L., et al. 2013, ApJ, 762, 108

Lu N., Helou G., Werner M. W., Dinerstein H. L., Dale D. A., Silbermann N. A., Malhotra S., Beichman C. A., Jarrett T. H., 2003, ApJ, 588, 199

Lucy L. B., 1999, A&A, 344, 282

Martínez-Serrano F. J., Serna A., Domínguez-Tenreiro R., Mollá M., 2008, MNRAS, 388, 39

Monaco P., Fontanot F., Taffoni G., 2007, MNRAS, 375, 1189

Monaco, P., Murante, G., Borgani, S., Dolag, K., 2012, MNRAS, 421, 2485

Murante, G., Monaco, P., Borgani, S., Tornatore, L., Dolag, K., Goz, D., 2015, MNRAS, 447, 178

Nomoto K., Hashimoto M., Tsujimoto T., Thielemann F.-K., Kishimoto N., Kubo Y., Nakasato N., 1997, Nuclear Physics A, 616, 79

Obreja A., Domínguez-Tenreiro R., Brook C., Martínez-Serrano F. J., Doménech-Moral M., Serna A., Mollá M., Stinson G., 2013, ApJ, 763, 26

Obreja, A., Brook, C. B., Stinson, G., et al. 2014, MNRAS, 442, 1794

Obreschkow D., Rawlings S., 2009, MNRAS, 394, 1857

Oke J.B., 1974, ApJS, 27, 21

Oser L., Ostriker J. P., Naab T., Johansson P. H., Burkert A., 2010, ApJ, 725, 2312

Panuzzo P., Granato G. L., Buat V., Inoue A. K., Silva L., Iglesias-Páramo J., Bressan A., 2007, MNRAS, 375, 640

Ragone-Figueroa, C., Granato, G. L., Murante, G., Borgani, S., & Cui, W. 2013, MNRAS, 436, 1750

Rocca-Volmerange B., Drouart G., De Breuck C., Vernet J., et al. 2013, MNRAS, 429, 2780

Rybicki G. B., Lightman A. P., 1979, Radiative processes in astrophysics

Saintonge A., Kauffmann G., Kramer C., Tacconi L. J., et al. 2011, MNRAS, 415, 32

Saintonge A., Kauffmann G., Kramer C., Tacconi L. J., et al. 2012, VizieR Online Data Catalog, 741, 50032

Salpeter E. E., 1955, ApJ, 121, 161

Scannapieco C., Wadepuhl M., Parry O. H., et al. 2012, MNRAS, 423, 1726

Schurer A., 2009, PhD thesis, INTERNATIONAL SCHOOL FOR ADVANCED STUDIES, Via Beirut 4, I-34014 Trieste ITALY

Schurer A., Calura F., Silva L., Pipino A., Granato G. L., Matteucci F., Maiolino R., 2009, MNRAS, 394, 2001

Serna A., Domínguez-Tenreiro R., Sáiz A., 2003, ApJ, 597, 878

Shen S., Wadsley J., Stinson G., 2010, MNRAS, 407, 1581

Silva L., 1999, PhD thesis, SISSA - Trieste, Italy

Silva L., De Zotti G., Granato G. L., Maiolino R., Danese L., 2005, MNRAS, 357, 1295

Silva L., Fontanot F., Granato G. L., 2012, MNRAS, 423, 746

Silva L., Granato G. L., Bressan A., Danese L., 1998, ApJ, 509, 103

Silva L., Schurer A., Granato G. L., Almeida C., Baugh C. M., Frenk C. S., Lacey C. G., Paoletti L., Petrella A., Selvestrel D., 2011, MNRAS, 410, 2043

Smith B. J., Struck C., Hancock M., Appleton P. N., Charmandaris V., Reach W. T., 2007, AJ,

133, 791

Springel, V., 2005, MNRAS, 364, 1105

Stinson G., Seth A., Katz N., Wadsley J., Governato F., Quinn T., 2006, MNRAS, 373, 1074

Stinson G. S., Bailin J., Couchman H., Wadsley J., Shen S., Nickerson S., Brook C., Quinn T., 2010, MNRAS, 408, 812

Stinson G. S., Brook C., Macciò A. V., Wadsley J., Quinn T. R., Couchman H. M. P., 2013, MNRAS, 428, 129

Tacconi L. J., Neri R., Genzel R., Combes F., et al. 2013, ApJ, 768, 74

Talbot Jr. R. J., Arnett W. D., 1973, ApJ, 186, 51

Tasker E. J., Tan J. C., 2009, ApJ, 700, 358

Tornatore, L., Borgani, S., Dolag, K., Matteucci, F., 2007, MNRAS, 382, 1050

Vega O., Clemens M. S., Bressan A., Granato G. L., Silva L., Panuzzo P., 2008, A&A, 484, 631

Vega O., Silva L., Panuzzo P., Bressan A., Granato G. L., Chavez M., 2005, MNRAS, 364, 1286

Wada K., Norman C. A., 2007, ApJ, 660, 276

Weingartner J. C., Draine B. T., 2001a, ApJ, 548, 296

Weingartner J. C., Draine B. T., 2001b, ApJS, 134, 263

Wiersma, R. P. C., Schaye, J., Theuns, T., Dalla Vecchia, C., & Tornatore, L., 2009, MNRAS, 399, 574

Witt A. N., Thronson Jr. H. A., Capuano Jr. J. M., 1992, ApJ, 393, 611

Woosley S. E., Weaver T. A., 1995, ApJS, 101, 181

Yajima H., Li Y., Zhu Q., Abel T., 2012, MNRAS, 424, 884

Chapter 7

The Main Sequence and the Fundamental Metallicity Relation

This chapter is a copy of
"The main sequence and the fundamental metallicity relation in MaGICC Galaxies: evolution and scatter"
by Obreja, Brook, Stinson, Domínguez-Tenreiro, Gibson, Silva & Granato,
published in MNRAS 442, 1794, 2014

7.1 Introduction

The manner in which galaxies evolve and grow over their lifetime is reflected in the observed correlation between their star formation rate (SFR) and their assembled stellar mass, dubbed the *main sequence* (MS) *of star formation*. In the local Universe, the SFRs and stellar masses of star forming galaxies correlate tightly (Brinchmann et al. 2004; Elbaz et al. 2007; Noeske et al. 2007, e.g.), and the relation has also been shown to hold at higher redshifts (Daddi et al. 2007; Karim et al. 2011; Bouwens et al. 2011; Wuyts et al. 2011; Whitaker et al. 2012, among others). The slope of the main sequence remains relatively constant with redshift, with the zero point evolving in the sense that high-redshift galaxies form stars at a higher rate than local galaxies of similar stellar mass (Wuyts et al. 2011; Whitaker et al. 2012). The scatter around the main sequence shows little dependence on mass, nor on redshift. There is a hint of increased scatter with decreasing stellar mass (e.g. Whitaker et al. 2012).

Complementary to the locus of star forming galaxies on the main sequence, the relation between

the mass and metallicity of galaxies provides further insights and constraints on the history and evolution of galaxies. The mass-metallicity (M-Z) relation connects stellar masses to both the gas phase (e.g. Garnett 2002; Tremonti et al. 2004) and stellar metallicities (Cowie & Barger 2008; Pérez-Montero et al. 2009), and it has been observed over a range of redshifts (Tremonti et al. 2004; Erb et al. 2006; Kewley & Ellison 2008; Maiolino et al. 2008; Zahid, Kewley & Bresolin 2011; Henry et al. 2013a,b; Lara-López et al. 2013). At all zs the lower mass systems have lower metallicities. Care must be taken in interpreting and reconciling these results, as the evolution of the relation is subject to differences in the observational techniques used at different redshifts and to calibrations of their abundances based on observed rest-optical line ratios (e.g. Zahid, Kewley & Bresolin 2011).

The star forming main sequence and mass metallicity relation have been combined in the fundamental metallicity relation (FMR), relating the stellar mass, gas-phase metallicity and the SFR of galaxies (Mannucci et al. 2010; Lara-López et al. 2010). The FMR reflects the cycle of inflows that feed star formation, the production of metals and enrichment of the interstellar medium (ISM), and the subsequent ouflows that are driven by the energy released by the forming stellar populations (see Davé, Finlator & Oppenheimer 2012; Dayal, Ferrara & Dunlop 2013; Lilly et al. 2013).

These indicators of galaxy formation and growth provide important constraints on galaxy formation models. Perhaps the most ambitious of these models are those that include baryonic physics, employing hydrodynamics to follow the evolution of gas and star formation within a fully cosmological context, and allowing a detailed description of the structural, chemical and dynamical properties within the galaxies (Katz 1992; Steinmetz & Mueller 1994; Katz, Weinberg & Hernquist 1996).

Certainly, significant progress has been made with such models in recent years. In particular, simulations that regulate star formation in order to be more consistent with the empirical relation between stellar mass and halo mass (Moster et al. 2010; Guo et al. 2010) are having success in forming more realistic galaxies (Brook et al. 2011; Guedes et al. 2011; Brook et al. 2012; McCarthy et al. 2012; Munshi et al. 2013; Aumer et al. 2013; Marinacci, Pakmor & Springel 2013). A range of different feedback schemes have been used in these studies, and in particular many augment feedback from supernovae with feedback from massive stars prior to their explosion as supernovae (Stinson et al. 2013). Suffice to say that the recent simulations all input significantly more energy than was generally used in previous generations, which generally suffered from severe loss of angular momentum, and too much mass in the central regions (e.g. Navarro & Steinmetz 2000; Piontek &

Steinmetz 2011).

High resolution MaGICC 'zoom' simulations have been shown to match the stellar-halo mass relation over a wide range in mass, as well as a variety of scaling relations at z = 0, including those between luminosity, rotation velocity, size, HI gas content and metallicity (Brook et al. 2012; Stinson et al. 2013). No scaling with mass for the outflows, no mass-loading nor direction of outflows is input by hand in our simulations, so any scalings with galaxy mass arises naturally from the energy feedback implementation. These simulations also have slowly rising rotation curves and appropriately large disc-to-total ratios.

For redshifts z > 2, using relatively low resolution simulations where hydrodynamics was used throughout a volume of 114 Mpc^3, the simulated galaxies have also been shown to match the observed slope and scatter in the stellar mass - halo mass relation and galaxy stellar mass function for galaxies with stellar mass $M_* > 5 \times 10^{10} M_\odot$ (Kannan et al. 2013).

We further test our suite of high resolution 'zoom' MaGICC simulated galaxies by studying their evolution in the parameter space of halo mass, stellar mass, star formation rate and gas phase metal abundance, and we discuss our results in comparison with observational data. In a recent paper (Brook et al. 2013) studying these galaxies we have characterized the baryon cycle by quantifying the inflows, outflows and recycling rates of gas and metals into, and out of, the virial radius and star forming regions of our simulations. The evolution of the properties of stellar mass, star formation rates and metallicity that we follow in this study are a direct reflection of this baryon cycle.

7.2 The simulations

We analyze eight cosmological zoom simulations from the MaCICC project (Brook et al. 2012; Stinson et al. 2013), run with GASOLINE (Wadsley, Stadel & Quinn 2004), a parallel SPH tree-code. Initial conditions are derived from the McMaster Unbiased Galaxy Simulations (Stinson et al. 2010). The simulations include metal line cooling (Shen, Wadsley & Stinson 2010), the effect of a ultraviolet ionizing background, supernova and early stellar feedback. We describe here the most important implementations and refer the reader for details of the code to Wadsley, Stadel & Quinn (2004), and of the feedback implementation to (Stinson et al. 2010).

Stars are produced with a star formation rate $\propto \rho^{1.5}$ from cool (T<15000 K) and dense (n_{th}>9.3 cm^{-3}) gas, with a star formation efficiency parameter of 0.017. The blastwave formalism (Stinson et al.

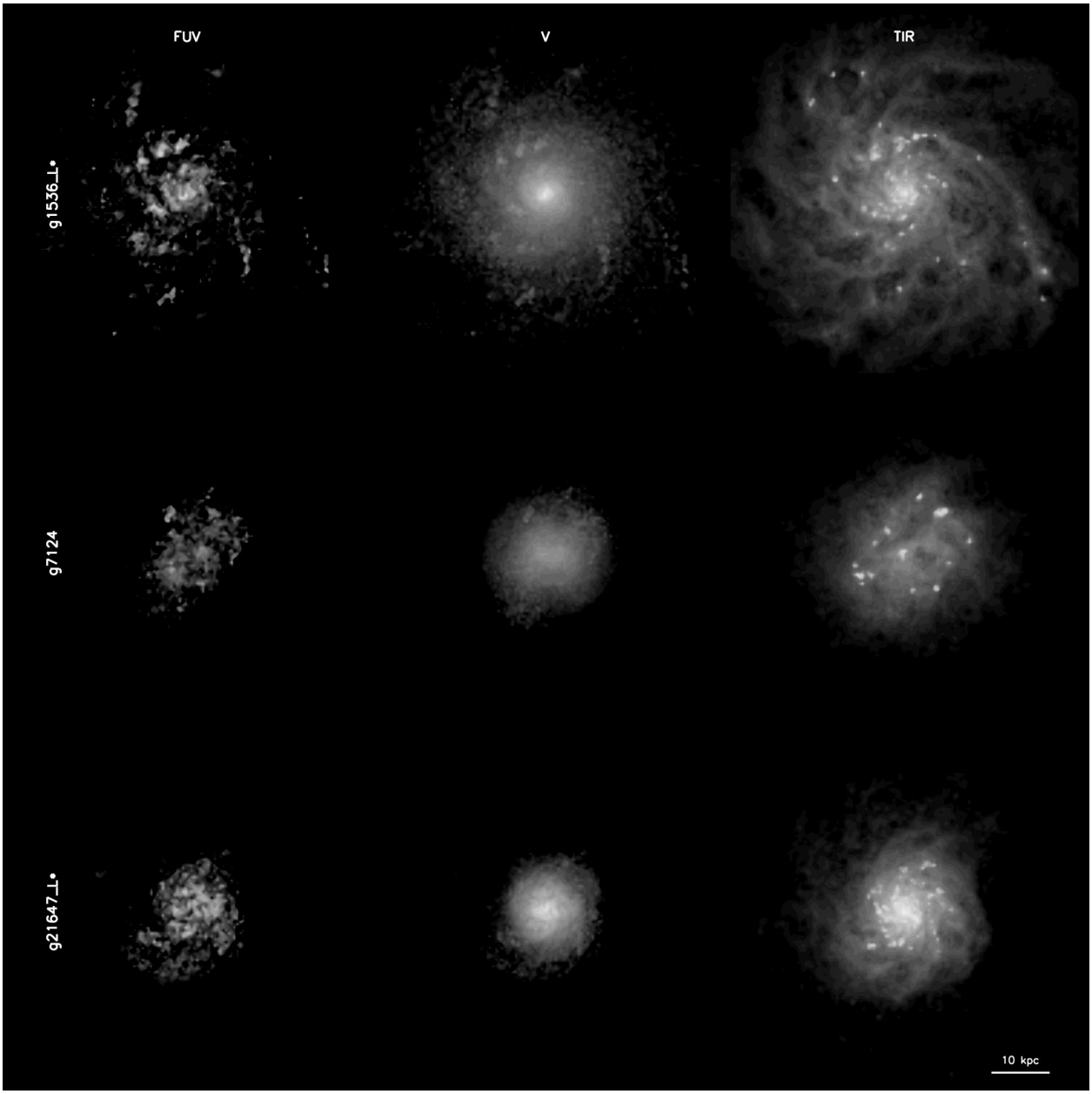

Figure 7.1: Example of GRASIL-3D images in the spectral ranges of far-UV, visible and total-IR (from left to right) for three of the more massive simulated galaxies at $z = 0$.

Name	m_{gas} ($10^4 M_\odot$)	h_{soft} (kpc)	M_{vir} ($10^{10} M_\odot$)	M_{star} ($10^9 M_\odot$)
g21647_L*	6.3		79.18	25.11
g1536_L*	6.3		67.95	23.61
g7124	6.3		41.80	6.29
g15784	2.5		16.42	4.26
g15807	2.5		27.81	1.47
g1536-Irr	2.5		7.71	0.45
g5664	2.5		5.92	0.24
g21647-Irr	2.5		9.18	0.20

Table 7.1: Simulation data where m_{gas} is the initial mass of gas particles, h_{soft} the minimum SPH smoothing length, and M_{vir} and M_{star} the total and stellar masses within the virial radius (Bryan & Norman 1998) at $z = 0$.

2006) is used to implement supernova feedback, at the end of massive stars ($8\,M_\odot$) lifetime, 10^{51} erg of energy being deposited into the surrounding medium. Prior to their explosion as SNe, massive stars inject energy into the surrounding gas. This feedback mechanism has also been included (Stinson et al. 2013) as pure thermal energy feedback in order mimic the weak coupling to the surrounding gas (Freyer, Hensler & Yorke 2006). Thermal energy feedback is highly inefficient in these types of simulations (Katz 1992; Kay et al. 2002), 90% of the injected energy being rapidly radiated away.

A Chabrier IMF (Chabrier 2003) is used to compute the ejected mass and metals, which are distributed among the nearest neighbor gas particles according to the smoothing kernel (Stinson et al. 2006). Metal abundances are based on the SNII yields of Woosley & Weaver (1995) and SNIa yields of Nomoto et al. (1997). The turbulent metal mixing is mimicked using a shear-dependent diffusion term (Shen, Wadsley & Stinson 2010). Cooling rates are computed by taking into account the diffused metals.

In Table 7.1 we give the stellar and virial mass at $z = 0$, the SPH smoothing lengths and the inital mass of gas particles for the simulated galaxies analysed in this study.

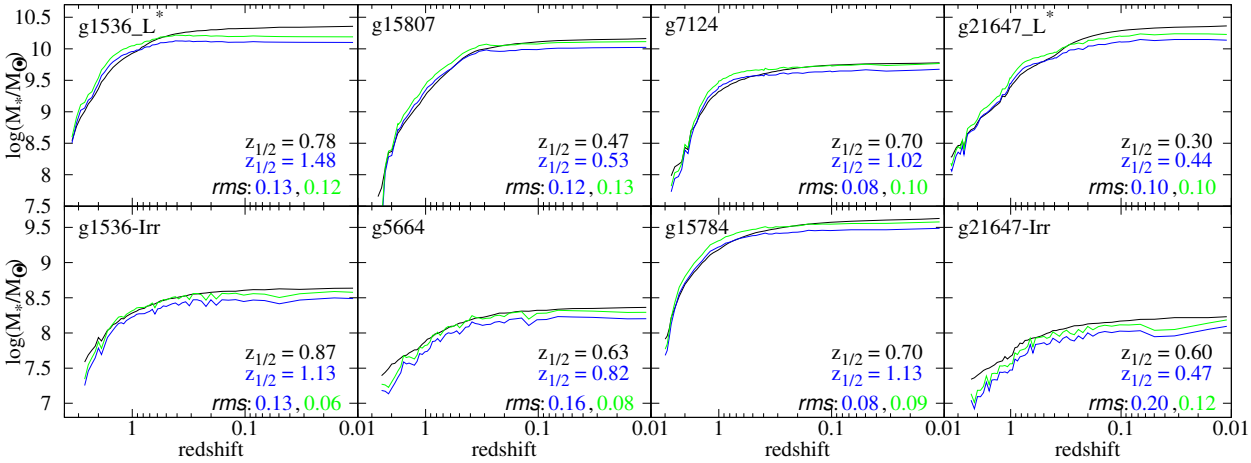

Figure 7.2: Stellar mass assembly for the simulated galaxies as predicted by simulations (black curves), and as derived using the B-V colors and mass-to-light ratios in the B-band (blue curves) and V-band (green curves) respectively. The half mass redshift, $z_{1/2}$ is given in each case for the black and blue curves. The *rms* scatter of the stellar mass derived using the B-V colors and the mass-to-light ratios in the B- and V-bands with respect to the *real* mass are also shown.

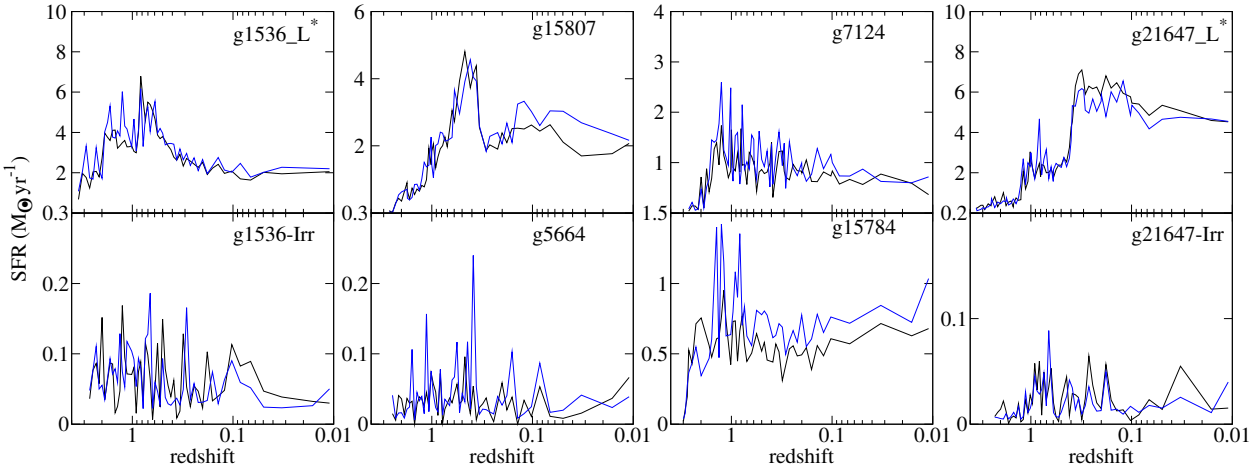

Figure 7.3: SFR histories for the simulated galaxies as predicted by simulations (black curves), and as derived using the infrared-corrected FUV luminosities (blue curves). The *observational* SFRs are fairly consistent with the *real* ones.

7.3 Post-processing with GRASIL-3D

In order to make a more meaningful comparison with observational data, we model the light-weighted quantities for stellar masses and star formation rates. For this purpose, we used the radiative transfer code, GRASIL-3D (Domínguez-Tenreiro et al. 2014), which is capable of generating Spectral Energy Distributions (SEDs) for simulated galaxies of arbitrary geometries, taking into account the dust processed light from stellar populations. These calculations assumed the same Chabrier IMF as used in the simulations, and the stellar library from Bruzual & Charlot (2003). We use a parameter set that governs the destruction of molecular clouds by the embedded stars which leads to fluxes from visible to IR in the ranges spanned by observational data samples. This parameter set has escape time-scale from molecular clouds of $t_0 = 10 Myrs$, radius for the clouds of $r_{mc} = 14 pc$, a cloud threshold density of $\rho_{mc,thres} = 3.3 \times 10^9 M_\odot kpc^{-3}$ and a log-normal probability distribution function with $\sigma = 3.0$, while the mass of a single cloud is assumed to be $m_{mc} = 10^6 M_\odot$.

We construct GRASIL-3D inputs for all the snapshots with $z < 3.5$ of the eight simulated galaxies, and obtained the face-on surface brightness profiles in the r-band. We then derive the Petrosian radii, R_P (Blanton et al. 2001), which we use to define the radial limits of our simulated galaxies (R_{lim}=$2R_P$). GRASIL-3D calculations have been done in the rest frame of the objects. Luminosities, fluxes and colors have been computed from the integrated face-on SEDs within R_{lim}. Therefore, our sample consists in eight galaxies 'observed'at various times in their evolution. In Figure 7.1 we show an example of GRASIL-3D images, in relevant bands for this study for three of the more massive simulated galaxies at $z = 0$.

It is important to stress that all post-processing with GRASIL-3D has been done using fixed parameters, which are nevertheless suitable for both starburst and quiescent galaxies (Domínguez-Tenreiro et al. 2014). Also, all observables have been computed in the rest-frame of the objects, and no detector properties apart from the transmissions in each band have been taken into account. Since we use broad band fluxes from far-UV to far-IR to estimate stellar masses and SFR, over a wide range of mass, these limitations are important. Technically, at high redshift, our smallest galaxies could not be observed in all bands we employ. Therefore, our comparison of light and mass weighted quantities is an idealized one. Nevertheless, the process of viewing the simulations in a manner analogous to observers helps to build confidence in the comparisons we make between observations and simulations.

There are various ways in which intrinsic properties like mass and SFR are inferred from observables. In the case of stellar masses, the current most widely used method is SED fitting, which became feasible with the recent advance in accurate multi-wavelength data and the refinement of stellar population synthesis models to include effects like post-main sequence stellar evolution. We decided to use simple color dependent mass-to-light relations, which nevertheless have been tested against other methods, like the Tully-Fisher one. The recent work of McGaugh & Schombert (2013) provides color dependent mass-to-light relations in four different bands (B, V, Ks and IRAC 3.6μm). We use the B- and V-bands mass-to-light ratios, which return masses closer to the simulations values than the ones in the Ks and IRAC 3.6μm bands.

Global SFRs can be inferred using emission lines or broad band fluxes (see Kennicutt & Evans 2012, for a review on SFR tracers). In our study we employ the far-UV tracer of Hao et al. (2011), where the FUV flux is corrected for dust obscuration using the total IR emission (TIR). These tracers reflect the SFR over timescales of $\sim$100 Myrs, which are well resolved by our simulations. However, one thing to keep in mind is that a good estimation of the TIR flux is, observationally difficult, if not impossible, especially for dwarf galaxies.

We firstly checked whether our galaxies fall within the $B-V$ and M_V ranges spanned by the data sample used by McGaugh & Schombert (2013). We also checked the ranges spanned by our objects in the $IRX = log(L_{TIR}/L_{FUV,obs})$ vs. $FUV - NUV$ diagram (Figure 3 of Hao et al. (2011)), finding that the majority of our objects have IRX within $[0.19, 2.39]$ and $FUV - NUV$ within $[0.07, 1.06]$, and moreover fall close the curve defined by the observational sample employed by Hao et al. (2011), albeit with a large dispersion (0.46 dex). While the observational sample contains only local normal star forming galaxies, some of the simulations snapshots correspond to peaks of star formation and some of the objects are dwarfs, cases outside of the sample used for the calibration. The error in the IRX-based attenuation correction for starburst is, in any case, < 0.3 mag (Hao et al. 2011). On the other hand, this prescription when applied to dwarfs might suffer from problems. Indeed, the highest rate of discrepancy in the IRX vs. $FUV - NUV$ occurs for the two lowest mass simulations (g5664 and g21647-Irr), which have a significant number of snapshots with $IRX < 0.19$ (35% and 56%, respectively). However, even in these two cases, the synthetic SFR closely follows the real one.

We shall be calling the whole sample *complete*, and the corresponding restriction to the observational ranges of Hao et al. (2011) and McGaugh & Schombert (2013), *limited*. There is no significant difference in our results between these two samples, as can be seen in consistency between

the light- and mass-weighted stellar mass and SFR in Figures 7.2 and 7.3.

In Figure 7.2 we give the stellar mass assembly tracks for the simulated galaxies. The black lines are obtained by summing the stellar mass within R_{lim}; the colored lines are obtained by applying the mass tracers from McGaugh & Schombert (2013), with blue (green) based on the M/L ratio in the B-band (V-band). The two light-weighted stellar masses follow quite closely the true simulation stellar mass, the difference being no larger than 0.20 dex. Figure 7.2 indicates that the most massive galaxies at low redshifts are better traced by the V-band derived masses, while at higher z the B-based stellar mass gives slightly better results. On the other hand, for the lower mass systems (g1536-Irr, g5664 and g21647-Irr), the V-band is a better tracer than the B-band at all zs.

The differences between the light-weighted (blue) and mass-weighted (black) SFRs is shown in Figure 7.3, where light-weighted SFRs are derived from IR-corrected FUV luminosities (Hao et al. 2011). This SFR tracer is based on the correlation between the IR/UV luminosity ratio and UV color, which is used to estimate the dust attenuation. The mass-weighted SFRs were computed by counting all the stellar particles that formed in the last 100 Myrs of each simulation snapshot. This time interval for averaging has been used in order to be consistent with the SFR tracer. The observational tracer follows closely the simulation bursty SFR. The differences between the 'observed'and 'true' SFRs are linked to the assumptions used when constructing the tracer. For example, the attenuation-corrected FUV luminosities of Hao et al. (2011) are consistent with evolutionary synthesis models which assume a constant solar metallicity. The mean fraction of SFR coming out in IR (averaging over all the snapshots of a galaxy) increases linearly with $\log(M_*)$ at $z = 0$. At the low mass end ($\sim 10^8 M_\odot$), the IR flux contributes 25% to the global SFR, while at $\sim 10^{10} M_\odot$ makes about 80% of the total SFR. Also, while for the three most massive galaxies (g1536_L*, g15807 and g21647_L*), this fraction increases quite smoothly with decreasing z, for the less massive ones it is highly variable.

Computing light-weighted quantities from face-on images means we are minimizing the effect of dust obscuration. Therefore, we checked the ranges of our observables when different inclinations are considered (face-on to edge-on). In the case of the mass tracers, the inclination affects more the high mass systems, an expected result given their higher degree of asymmetry as compared to the less massive ones. For the same reason, the effect generally grows as the redshift decreses, the exceptions to this tendency appearing in the particular cases where the galaxies appear as trasient disc-like structures. Thus, while for g7124, g1536-Irr, g5664, g15784 and g21647-Irr the higher mass

decrement with respect to the face-on values is 15%, for the massive galaxies, g1536_L*, g15807 and g21647_L* it can be as high as 25%, 25% and 50%, respectively. The extreme value of 50% decrease in the case of g21647_L* corresponds only to $z < 0.4$. For larger redshifts, the typical decrement for the three massive galaxies is ∼20%. The SFR tracer follows the same trend with redshift as the mass ones, but no clear trend with mass. Thus, typical values of the SFR decrease are ∼10%.

7.4 Results

The effect of different star formation and feedback parameters and implementations applied to a single Milky Way like galaxy, g1536_L*, has been studied by Stinson et al. (2013). The variation found in the evolution of star formation pointed to the need for feedback from massive stars prior to their explosion as supernovae. Using the same feedback scheme, a large sample of high mass simulated galaxies was also shown to match the relation at high redshift (Kannan et al. 2013). Here we test the effectiveness of the implemented feedback by exploring the evolution of our suite of high resolution zoom simulations that span a wide range in stellar mass.

7.4.1 Evolution of the stellar-halo mass relation

In Figure 7.4, we show the stellar mass - halo mass relation of our simulated galaxies over plotted on the empirical results from Moster, Naab & White (2013), along with their 1σ scatter, at four redshifts. The galaxies follow the same evolutionary path of stellar mass assembly as those inferred by the abundance matching techniques used in Moster, Naab & White (2013). The stellar masses in this figure are those computed directly from the simulations, but as seen above there is little difference if light-weighted stellar masses are used.

Our suite of simulated galaxies that include early stellar feedback from massive stars, as well as feedback from supernovae, not only resemble observations in the Local Universe, but also have stellar masses that evolve with redshift in a manner that resembles real galaxies.

7.4.2 Evolution of the M_* - SFR relation

The correlation between stellar mass and SFR in galaxies across the cosmic time provides a powerful constraint on the star formation implementations used in simulations. This correlation reflects the mass build-up of galaxies and their morphological diversity. Observationally, the star forming

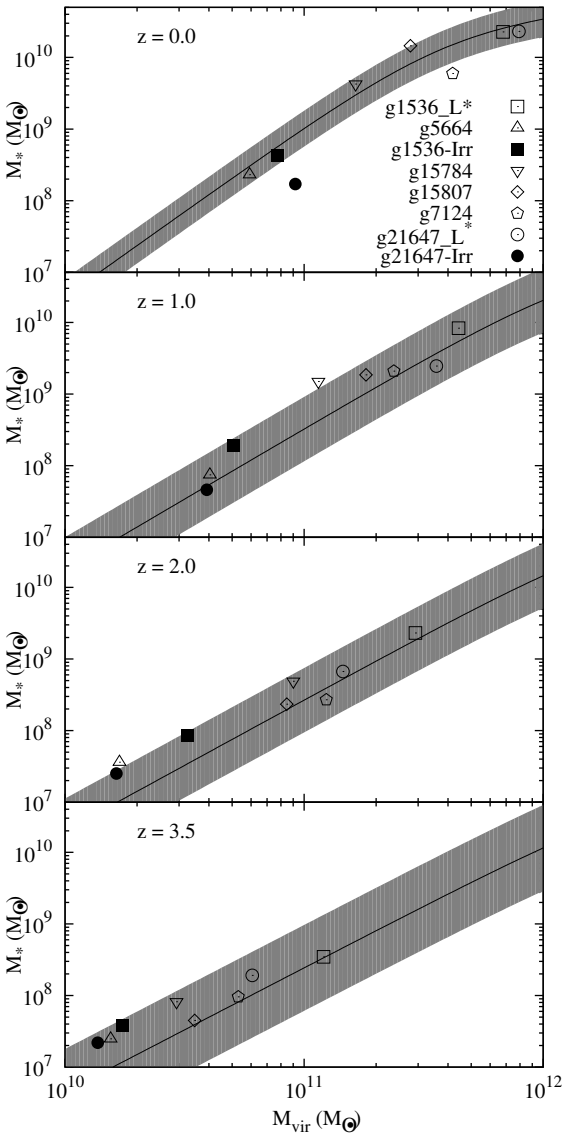

Figure 7.4: Stellar mass versus halo mass for the simulated galaxies, at four redshifts. The black curves are the abundance matching functions derived by Moster, Naab & White 2013, with their corresponding 1σ deviations (grey areas).

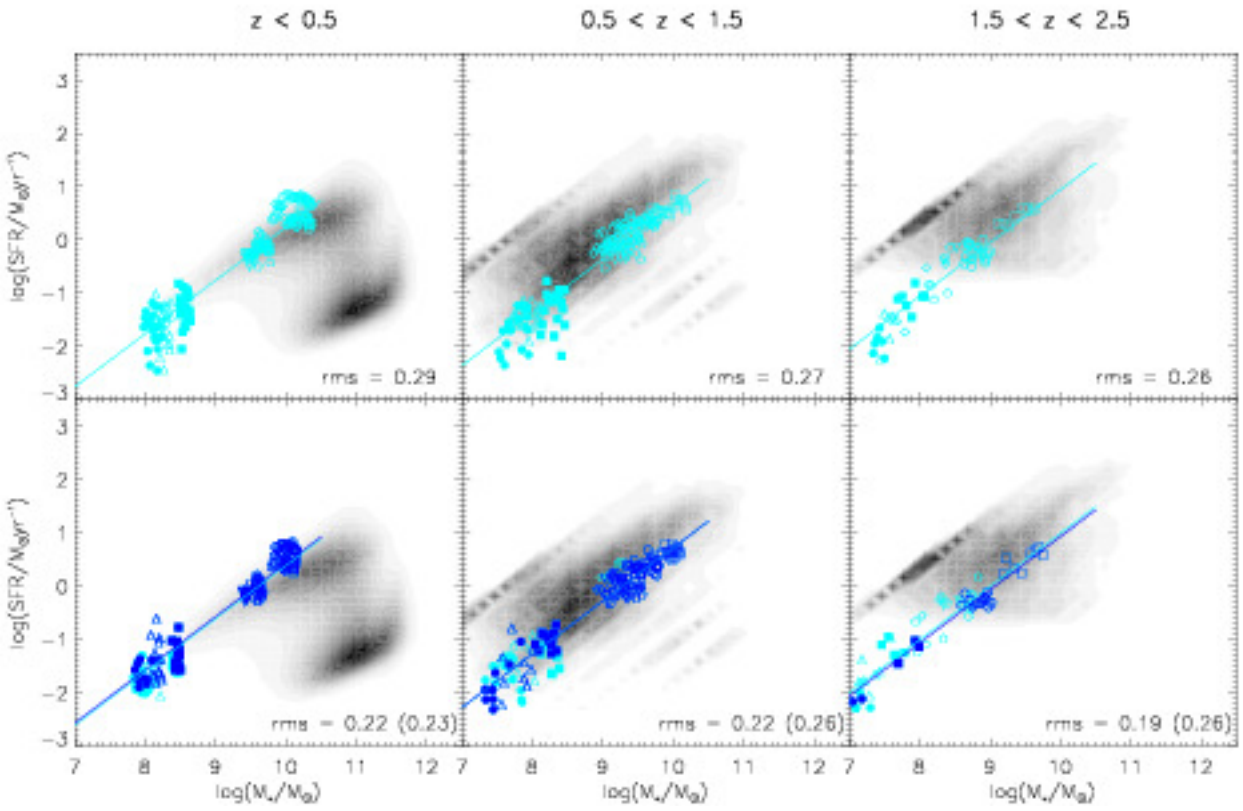

Figure 7.5: The evolution of M_* - SFR. Top panel: the SFR and M_* values derived from simulations directly. Bottom panels: the stellar masses were computed using the B-band mass-to-light ratios, and the SFR using the TIR-corrected FUV luminosities. The cyan points correspond to the *complete* sample, while the blue ones represent the *limited* one, including only the objects with observational properties within the ranges used to define the stellar mass and SFR tracers (Hao et al. 2011; McGaugh & Schombert 2013). The lines are the linear fits of constant slope 1 which minimize the scatter. The dispersions around each line are also shown in each corresponding panel. In the bottom panels, the two values of dispersion correspond to the *limited* and *complete* samples, respectively. The grey scale contours beneath the simulation data are the normalized 2D histograms of the observational sample studied by Wuyts et al. 2011. In the lowest redshift bin (left panels), the upper overdensity along which our simulations fall corresponds to the locus of star forming galaxies having low Sérsic indices (see Figure 1 of Wuyts et al. 2011).

galaxies have been shown to cluster along the so-called *star formation main sequence* (Brinchmann et al. 2004; Elbaz et al. 2007; Noeske et al. 2007; Daddi et al. 2007; Karim et al. 2011; Bouwens et al. 2011; Wuyts et al. 2011; Whitaker et al. 2012, among others). This sequence is usually parametrized with a power law ($SFR = \alpha M_*^{\beta}$), where both α and β can be taken to vary with the redshift. Typical values of the slope range from ∼0.4 to 1 (e.g. Karim et al. 2011; Wuyts et al. 2011; Whitaker et al. 2012; Zahid et al. 2012).

Some studies indicate that the slope remains constant, while the zero point varies with redshift. For example, Zahid et al. (2012) found that a constant slope $\beta = 0.7$ with $\alpha \sim exp(1.33z)$ reproduces the observational data up to z∼2.2. Based on one of the largest mass-complete sample of galaxies up to z=2.5, Whitaker et al. (2012) conclude that the slope of the MS does vary with z, but much less than the normalization. Most relevant to this present study of simulated star forming galaxies, they find a difference when restricting the sample to the blue star forming galaxies, for which they find that the slope is approximately 1. Similarly, Wuyts et al. (2011) use a large multi wavelength dataset, based on FIREWORKS (Wuyts et al. 2008), and find that a unitary slope reproduces well the observations of (star forming) disc galaxies, where such galaxies are selected as those having low (n<2) Sérsic indices. When fitting a slope of 1, they find that the *rms* scatter of the MS is only slightly larger than when both slope and normalizations are left to vary.

Studying the tightness of the MS, Salmi et al. (2012) also found an intrinsic slope close to unity, taking into account the effects of mass measurement errors, larger ranges for the SFR at fixed stellar mass and sample completeness. Recent studies have proven that large variations in the MS slope are, to a great extent, an effect of sample selection (Salmi et al. 2012; Whitaker et al. 2012; Guo, Zheng & Fu 2013).

In Figure 7.5 we show star formation rate as a function of stellar mass for three redshift ranges in the simulated galaxies. The upper panels give these quantities as derived directly from the simulations (total stellar mass within R_{lim} and SFR computed with the stellar particles in the same region that formed in a time range of 100 Myrs). The lower panels show the SFR based on the tracer of Hao et al. (2011) vs M_*, calculated using the M/L ratios in the B-band. The blue points represent only the data that fall within the observational ranges of both Hao et al. (2011) and McGaugh & Schombert (2013), while the cyan ones give the whole simulation sample. The blue and cyan lines are the linear regressions through the corresponding data points. When letting both parameters of the MS vary we obtain slopes in the range $1.0 - 1.1$. In the plot we fixed the slope to 1, and explore the scatter. The MS scatter in this case (the *rms* values shown in each panel) is very

similar to the one obtained when both slope and normalization are free. In all panels, simulation data has been super-imposed on the data of Wuyts et al. (2011) (Figure 1 of their paper).

As shown in Figure 7.2, there are small differences between the mass derived using a tracer based on the SED and the real stellar mass. Also the light weighted SFR (blue curves in Figure 7.3) slightly overestimates the 'true' SFR at higher z, the effect being larger for the least massive systems. This translates into a smaller dispersion of SFR at fixed M , as can be seen in Figure 7.5 by comparing the lower with the upper panels. As a consequence, the MS scatter is slightly smaller in the 'observed' trends than the 'true' simulation values.

Comparing SFR vs M_* with the observations of Wuyts et al. (2011) (Figure 1 of their paper), we see that at low redshift ($z < 0.50$) simulated galaxies populate a MS very close to the extrapolation of the observational sequence. However, at higher redshift the SFRs of simulated galaxies are *below* the extrapolations of the observational relations by $\sim\ 0.4\ -\ 0.5$ *dex*. It is important to keep in mind that observational samples are only complete at high stellar masses (e.g. $M_* > 10^{9.7} M_\odot$). If we compare the ranges spanned by the simulations with their data set, we see that the simulations fall well within the range occupied by observed disc galaxies with Sérsic indices $n < 2.0$ (bottom panels of Figure 7.5). Our simulations indicate that low mass star forming galaxies should lie below a simple extrapolation of the relation as derived from high mass galaxies at high redshift. On the other hand, if we compare our data with the MS derived by Guo, Zheng & Fu (2013) in the redshift range 0.6 - 0.8, the relation in simulations for $0.5 < z < 1.5$ is ~ 0.5 dex *above* the observational one.

Due to their shallow potential well, low mass galaxies are affected to a greater extent by stellar winds. Consequently they could provide tighter constraints on feedback mechanisms than more massive ones. However, detection of such systems is not trivial, more so farther than the local universe. In recent years, various observations managed to push the mass limit to systems with $M_* < 10^9 M_\odot$. For example, Henry et al. (2013a,b) presented a sample of 18 galaxies with stellar masses smaller than this limit at intermediate redshift ($z \sim 0.6 - 0.7$), for which they have reliably measured emission line fluxes. They estimated stellar masses and SFR from SED fitting. These galaxies have a scatter with respect to the linear regression (blue line) in the bottom central panel of Figure 7.5 of 0.6 dex, most of them having higher SFR values than the simulations.

At even higher zs, the only available detection method is lensing (Richard et al. 2011; Wuyts et al. 2012; Christensen et al. 2012; Belli et al. 2013). This method allows to observe distant low mass, relatively low SFR galaxies. However, these lensed galaxies at $z > 1.5$ have systematically

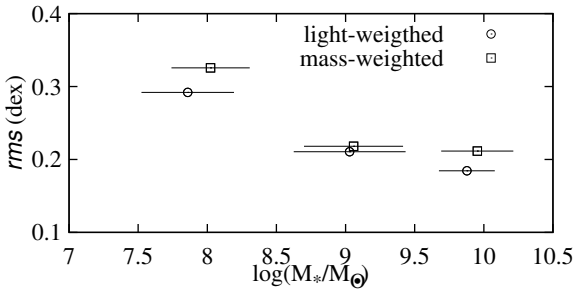

Figure 7.6: The scatter of the M_* - SFR relation for the simulated galaxies. The x-error bars represent the stellar mass dispersions. Open squares and circles correspond to the mass-weighted sample (cyan points in the top panels of Figure 7.5) and to the light-weighted one (cyan points in the bottom panels of the same figure). Since the scatter values have been computed taking into account the evolution of the MS zero point, the data has not been binned in redshift. For the two samples, a clear trend of decreasing scatter with increasing mass can be appreciated.

higher SFR than our simulations, tipically an order of magnitude higher. In this context our results for the least massive galaxies are perhaps best taken as a prediction of our model on how the MS will extend to lower masses.

7.4.3 Scatter in the M_* - SFR relation

The evolution of the star formation main sequence strongly constrains galaxy mass assembly. However, it is not only the relation in itself that is important, but also its scatter which reflects the intrinsic variability in the SFR of the star forming galaxy population.

The star formation rate history is anything but smooth, the variability increasing with decreasing stellar mass and increasing redshift (see Figure 7.3). The high SFR variability of the lower mass systems is a direct consequence of the shallow potential well of these objects: supernovae can eject large quantities of gas from the galaxies, with star formation cyclically quenched due to the depletion of the cold gas reservoir (Stinson et al. 2007). As the mass of simulated galaxies increases, the triggering and quenching of star formation due to gas outflows becomes less pronounced.

The model of galaxy formation implemented in the `GASOLINE` code relies on SN feedback to generate galactic outflows which enrich the environment and regulate the star formation. One of the consequences of this feedback model is that it naturally increases the variablity of the SFR. However, the burstiness of the SFR is a combined effect of stochastic gas accretion and feedback.

We do not have enough simulated galaxies to derive a statistically robust scatter in the M_*-SFR

relation at a given redshift. However, we can test how much scatter comes from the variation in SFR of individual galaxies, as they undergo bursts of star formation and relatively quiescent periods in their evolution. In order to derive such scatter, we have to include data from different time steps within the same z-bin, meaning that we must be mindful that the scatter that we measure is not simply the result of the evolution of the relation itself. The regular evolution of the relation (the zero point varies linearly with the expansion factor) allows us to find an expected SFR at any z for a given mass, and this can be used to derive the scatter in the MS. In Figure 7.6 we show the scatter derived using the expected SFR, as explained above, using the mass- and light-weighted stellar masses and star formation rates (open squares and open circles) plotted in the top and bottom panels of Figure 7.5, respectively. In order to get an estimate of the scatter variation with mass, we divided the two samples into three equally populated stellar mass bins.

We are able to compute the scatter irrespective of redshift precisely because the reference values for SFR are computed by interpolating the MSs in the three redshift bins. A clear trend of the MS scatter with stellar mass can be appreciated, less massive galaxies having a higher SFR variability. There is a difference between the scatter computed directly from the simulation outputs (mass-weighted M_* and SFR) and from the 'observed 'fluxes (light-weighted M_* and SFR). This difference was expected in light of Figure 7.3, where we saw that the SFR tracer better follows the *true* simulation values at high stellar masses than at the low end.

For the light-weighted sample, the scatter goes from $\sim$0.30 dex for $M_* < 10^8 M_\odot$ to $\sim$0.20 dex for $M_* > 10^9 M_\odot$ For the more massive simulated galaxies which have M_* in the range where observational samples are complete, the scatter of $\lesssim 0.3$ is similar to the one found by observers (e.g. Daddi et al. 2007; Noeske et al. 2007; Elbaz et al. 2007; Zahid et al. 2012). Therefore, from our small sample of simulated galaxies, it appears that most and perhaps all of the dispersion in the MS could be explained by the intrinsic scatter in the SFR, which is a direct consequence of the bursty star formation history of individual galaxies.

7.4.4 The mass-metallicity relation

Star formation is primarily governed by the cold gas reservoir available. The stellar mass of galaxies correlates with gas metallicity (Lequeux et al. 1979). While the stellar mass reflects the baryon mass locked into stars, the gas metallicity traces the material reprocessed by stars and the coupling of the galaxy to its environment, in terms of inflows of fresh or pre-enriched gas and the outflows of metals in galactic winds. This correlation provides one of the means by which the feedback

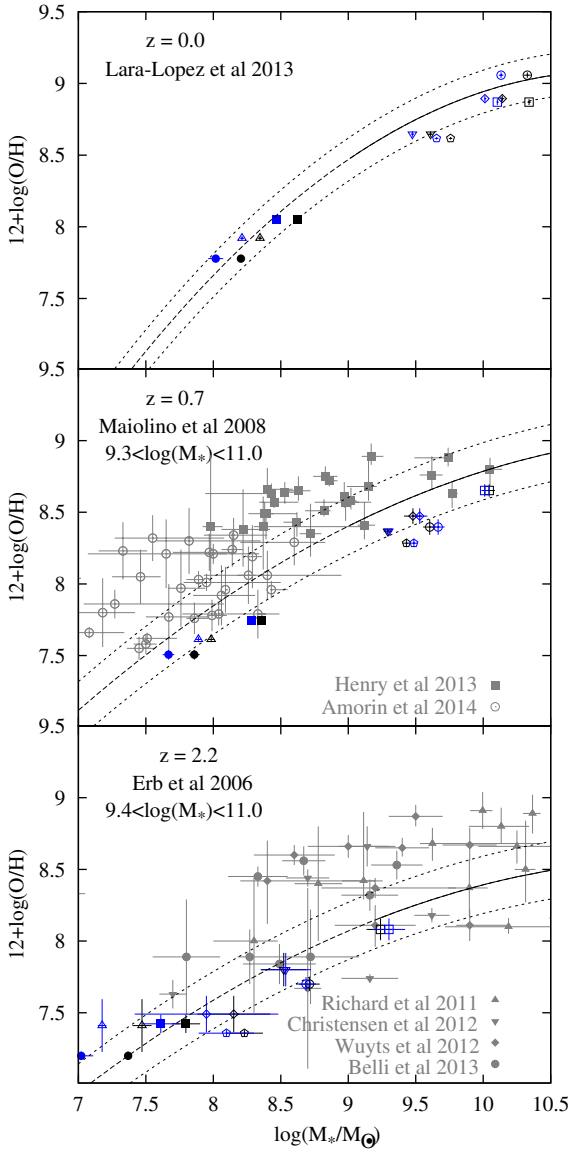

Figure 7.7: Oxygen abundance as function of stellar mass at three different redshifts. The black solid curves are the observational M-Z relations obtained by Lara-López et al. 2013 (top panel), Maiolino et al. 2008 (center panel) and Erb et al. 2006 (bottom panel). The dashed black lines give the low mass extrapolation of these relations, while the dotted black ones give the scatter of 0.15, 0.20 and 0.20 dex, respectively. The limits in the center and bottom panels indicate the corresponding stellar mass ranges for the samples of Maiolino et al. 2008 and Erb et al. 2006. The blue and black points correspond to masses derived using the mass-to-light ratio in the B band and to *true* simulation values, respectively. The shape coding is the same as in Figure 7.4. In the center and bottom panels we overplotted in grey some of the observational samples (indicated in the corresponding legends) which have the lowest mass system detected at high-z.

processes affecting this baryon cycle can be tested against observations (Brooks et al. 2007).

In Figure 7.7 we show the Oxygen abundance versus M_* at three redshifts, chosen to make a comparison with the observational samples in Erb et al. (2006), Maiolino et al. (2008) and Lara-López et al. (2013) at high, intermediate and low z, respectively. The M-Z relation of Maiolino et al. (2008) has been rescaled to a Chabrier IMF. We use the mean[1] $12 + log(O/H)$ of the cold gas ($T < 10^4 K$) within R_{lim}.

The simulated galaxies follow well the observation at high and low redshift (top and bottom panels), being roughly within the observed scatter from the extrapolations of the M-Z relations (Lara-López et al. 2013; Erb et al. 2006). For the $z = 0$ we use the scatter from Lara-López et al. (2013), while for Maiolino et al. (2008) and Erb et al. (2006) curves we assumed a value 0.20 dex. At intermediate z there is less agreement in absolute values of simulations and observations, with the former being $\sim$ 0.2 *dex* smaller than the latter in the entire mass range. Yet the trend of metallicity with mass is very well reproduced by the simulations even at this intermediate mass range. In simulations, the metallicity evolution between z$\sim$2.2 and z$\sim$0.7 varies from $\sim$0.25 dex for the lowest mass systems up to $\sim$0.50 dex for the massive ones. A similar trend can be appreciated in observations, by comparing the extrapolations of the relations in Erb et al. (2006) and Maiolino et al. (2008). Thus, the difference in metallicity given by the two curves grows from 0.2 dex for $M_* \sim 10^{7.5} M_\odot$ to 0.5 dex for $M_* \sim 10^{9.5} M_\odot$. On the other hand, the observational local M-Z relation is steeper than the intermediate and high z ones, when considering the extrapolation at lower stellar masses.

In the same figure, we overplotted the data provided by some of the recent observations which get to stellar masses as low as $M_* \sim 10^{7.6} M_\odot$ at high redshift (Richard et al. 2011; Wuyts et al. 2012; Christensen et al. 2012; Belli et al. 2013). We also show the sample of Henry et al. (2013a) at z$\sim$0.65. At z$\sim$2.2, in the region of mass overlap between simulations and observations, a good agreement can be appreciated. The observational samples at high zs have large errors, and roughly higher abundances ($\sim$0.2 dex) than the empirical curve found by Erb et al. (2006). In any case, a good agreement between observations and simulations can be appreciated. At intermediate redshifts, however, the data of Henry et al. (2013a) is above the Maiolino et al. (2008) curve in most cases, and shows much less evolution with stellar mass. Therefore, the tension between observations and simulations is increased, especially at low stellar masses.

It is important to note that different methods are used to measure the metallicities in the

[1]Using the median had minimal impact on the results.

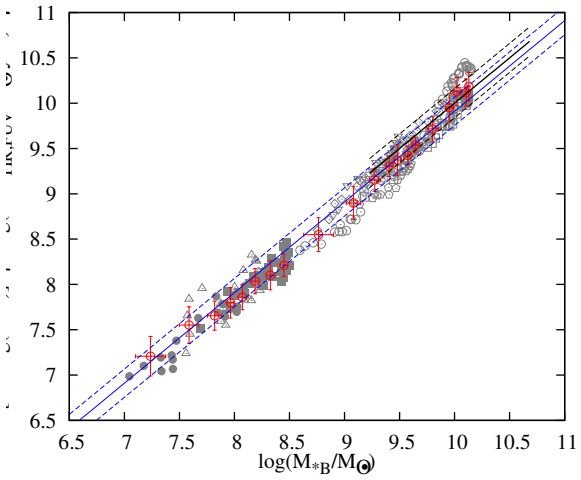

Figure 7.8: The FMR of star forming galaxies. The stellar mass is given as a linear combination of $12 + log(O/H)$ and $log(SFR)$, following Lara-López et al. 2010, with: $\alpha = 1.122$, $\beta = 0.474$ and $\gamma = -0.097$. The grey points are the simulated galaxies in the redshift range $z < 3.5$, plotted with the same symbols as in Figure 7.4. The solid blue line is the linear fit of constant slope 1 which minimize the scatter, while the dashed blue lines give the corresponding 1σ of 0.16 *dex*. The open red circles represent the simulations in equally populated stellar mass bins. The solid and dashed black lines are the one to one correspondence of Lara-López et al. 2010 and its 1 σ deviation (0.16 *dex*). The solid blue line is 0.09 *dex* below the solid black one.

different studies, meaning that the absolute values are subject to having different calibrations (e.g. Zahid et al. 2012), with different metallicities calibrations resulting in abundances that can vary as much as $\sim$ 0.3 dex. We also note that the shape of the M-Z relation remains a matter of debate.

7.4.5 The mass-SFR-metallicity relation

The correlations found between the stellar mass and SFR (Brinchmann et al. 2004) on one hand, and stellar mass and gas metallicity (Lequeux et al. 1979), on the other, raised the question whether they are not just projections of a fundamental relation. In this respect, Ellison et al. (2008) found that indeed the mass - metallicity relation depends on the SFR. Consequently, in two parallel studies, Mannucci et al. (2010) and Lara-López et al. (2010) proposed combinations of these observables (stellar mass, star formation rate and metallicity) which hold across a wide redshift range (up to $z \sim 3.5$).

In order to minimize the scatter of the so called *Fundamental Metallicity Relation* (FMR),

Mannucci et al. (2010) introduced a new variable, $\mu_\alpha = log(M_*) - \alpha \cdot log(SFR)$. A value of $\alpha = 0.32$ minimizes the scatter of median metallicities of SDSS galaxies, while high z galaxies show the same range of $\mu_{0.32}$ as low redshift galaxies. In an equivalent way, Lara-López et al. (2010) found that using a linear combination of $12 + log(O/H)$ and $log(SFR)$, the stellar mass can be recovered with an accuracy of 0.2 *dex*. Therefore, they proposed that $log(M_*/M_\odot) = \alpha[12 + log(O/H)] + \beta\ log(SFR/M_\odot yr^{-1}) + \gamma$ with a standard deviation of 0.16 *dex*, if no errors are considered in metallicity and star formation rate. They showed that it holds up to redshift$\sim$3.5.

In Figure 7.8 we give the FMR of our simulated galaxies showing a total of 324 snapshots of our suite of simulations between $z = 3.5$ and $z = 0$ (grey points), and find that they lie on a linear sequence. We fitted a line through the points allowing both normalization and slope to vary obtaining a scatter only 0.01 *dex* smaller than when fixing the slope to 1. Thus, we show in solid blue the FMR obtained by setting the slope to 1 and leaving the zero point as only free parameter. The dashed blue line is the corresponding 1σ scatter of 0.16 *dex*. The FMR of simulated galaxies is ~ 0.1 *dex* below the extrapolation of the observational relation to low mass and low metallicity galaxies (solid black line, Lara-López et al. 2010). Within the mass range where the simulations overlap with the Lara-López et al. (2010) sample, the simulations fall within the 1 σ scatter of the observations.

While both metallicity and SFR correlate tightly with stellar mass, they do so much losely, if at all, with each other, in simulations and observations alike. In simulations, stellar mass and cold gas metallicity evolve smoothly and in a quite similar manner with redshift, leading to a small scatter in the M-Z relation, while the SFR shows large variations, especially for less massive systems. However, combining the three in the FMR, no redshift evolution is observed and the scatter is reduced, even with respect to the M-Z relation. We stress, though, that the large dynamical range in this study is obtained by combining snapshots of a small number of galaxies 'observed' at different zs. From this perspective, the simulated galaxies evolve along the FMR.

7.5 Conclusions

Using cosmological galaxy simulations from the MaGICC project, we study the evolution of the stellar masses, star formation rates and gas phase abundances of star forming galaxies. We derive the stellar masses and star formation rates using observational relations based on spectral energy distributions by applying the new radiative transfer code GRASIL-3D to our simulated galaxies.

We compare light-weighted masses and star formation rates with the their mass-weighted counterparts from simulations. We find that the simple stellar mass tracers from McGaugh & Schombert (2013), based on integrated colors and mass-to-light ratios are in good agreement with the simulation values, the difference between them being less than ∼0.20 dex. Also, the Hao et al. (2011) star formation rate tracer based on IR-corrected FUV luminosity follows closely the simulation.

Although the MaGICC simulations have the stellar feedback fixed in order match the stellar mass-halo mass relation at a given mass and at $z = 0$, all our eight galaxies, spanning two orders of magnitude in mass, actually are within one σ of the abundance matching curves up to redshift $z \sim 3.5$.

We show that the simulated galaxies populate projections of the stellar mass - star formation rate - metallicity plane, similar to observed star forming disc galaxies. Thus, in the $log(M_*)$-$log(SFR)$ plane, simulated galaxies fall along a line of slope 1, up to redshift 2.5, the normalization increasing with z. Both the slope as well as the scatter around these relations are in agreement with observational data. However, the normalizations for the simulated galaxies at higher zs are lower than in observations by as much as ~ 0.5 *dex*. This may be a problem for the simulations, yet we emphasize that the simulations are generally of lower mass than complete galaxy surveys, albeit with overlap. A close comparison with Wuyts et al. (2011) data shows that our suite of simulations fall well within the range of observed data. Indeed, there is a hint that the low mass end of observed data has a lower normalization than the high mass end. It will be intriguing to see whether this prediction of our model matches future observational samples that are able to probe to lower stellar masses. On our end, a larger sample of simulated galaxies will also allow a more comprehensive comparison of our theoretical model with observations.

Similar to observations, the scatter in the MS seems to be independent of z, and decreasing with increasing stellar mass. By analyzing this sample of eight galaxies, 'observed' at different times, we conclude that most of the *Main Sequence* scatter can be explained by the intrinsically bursty history of star formation.

In the stellar mass - gas phase abundance plane, the simulated discs follow the observations roughly within 2σ up to redshift $z \sim 2.2$. Finally, our sample of simulated star forming galaxies also show a tight correlation among stellar mass, star formation rate and metallicity, with the same coefficients as in Lara-López et al. (2010) apart from a difference of 0.09 *dex* in normalization. The scatter around this FMR is the same as in the observational sample (0.16 *dex*).

References

Aumer M., White S., Naab T., Scannapieco C., 2013, ArXiv:1304.1559

Belli S., Jones T., Ellis R. S., Richard J., 2013, ApJ, 772, 141

Blanton M. R. et al., 2001, AJ, 121, 2358

Bouwens R. J. et al., 2011, ApJ, 737, 90

Brinchmann J., Charlot S., White S. D. M., Tremonti C., Kauffmann G., Heckman T., Brinkmann J., 2004, MNRAS, 351, 1151

Brook C. B. et al., 2011, MNRAS, 415, 1051

Brook C. B., Stinson G., Gibson B. K., Shen S., Macciò A. V., Wadsley J., Quinn T., 2013, ArXiv:1306.5766

Brook C. B., Stinson G., Gibson B. K., Wadsley J., Quinn T., 2012, MNRAS, 424, 1275

Brooks A. M., Governato F., Booth C. M., Willman B., Gardner J. P., Wadsley J., Stinson G., Quinn T., 2007, ApJ, 655, L17

Bruzual G., Charlot S., 2003, MNRAS, 344, 1000

Bryan G. L., Norman M. L., 1998, ApJ, 495, 80

Chabrier G., 2003, PASP, 115, 763

Christensen L. et al., 2012, MNRAS, 427, 1953

Cowie L. L., Barger A. J., 2008, ApJ, 686, 72

Daddi E. et al., 2007, ApJ, 670, 156

Davé R., Finlator K., Oppenheimer B. D., 2012, MNRAS, 421, 98

Dayal P., Ferrara A., Dunlop J. S., 2013, MNRAS, 430, 2891

Domínguez-Tenreiro, R., Obreja, A., Granato, G. L., et al. 2014, MNRAS, 439, 3868

Elbaz D. et al., 2007, A&A, 468, 33

Ellison S. L., Patton D. R., Simard L., McConnachie A. W., 2008, ApJ, 672, L107

Erb D. K., Shapley A. E., Pettini M., Steidel C. C., Reddy N. A., Adelberger K. L., 2006, ApJ, 644, 813

Freyer T., Hensler G., Yorke H. W., 2006, ApJ, 638, 262

Garnett D. R., 2002, ApJ, 581, 1019

Guedes J., Callegari S., Madau P., Mayer L., 2011, ApJ, 742, 76

Guo K., Zheng X. Z., Fu H., 2013, ArXiv:1309.4093

Guo Q., White S., Li C., Boylan-Kolchin M., 2010, MNRAS, 404, 1111

Hao C.-N., Kennicutt R. C., Johnson B. D., Calzetti D., Dale D. A., Moustakas J., 2011, ApJ, 741, 124

Henry A., Martin C. L., Finlator K., Dressler A., 2013a, ApJ, 769, 148

Henry A. et al., 2013b, ArXiv:1309.4458

Kannan R., Stinson G. S., Macciò A. V., Brook C., Weinmann S. M., Wadsley J., Couchman H. M. P., 2013, ArXiv:1302.2618

Karim A. et al., 2011, ApJ, 730, 61

Katz N., 1992, ApJ, 391, 502

Katz N., Weinberg D. H., Hernquist L., 1996, ApJs, 105, 19

Kay S. T., Pearce F. R., Frenk C. S., Jenkins A., 2002, MNRAS, 330, 113

Kennicutt R. C., Evans N. J., 2012, ARA&A, 50, 531

Kewley L. J., Ellison S. L., 2008, ApJ, 681, 1183

Lara-López M. A. et al., 2010, A&A, 521, L53

Lara-López M. A. et al., 2013, MNRAS, 434, 451

Lequeux J., Peimbert M., Rayo J. F., Serrano A., Torres-Peimbert S., 1979, A&A, 80, 155

Lilly S. J., Carollo C. M., Pipino A., Renzini A., Peng Y., 2013, ApJ, 772, 119

Maiolino R. et al., 2008, A&A, 488, 463

Mannucci F., Cresci G., Maiolino R., Marconi A., Gnerucci A., 2010, MNRAS, 408, 2115

Marinacci F., Pakmor R., Springel V., 2013, ArXiv:1305.5360

McCarthy I. G., Schaye J., Font A. S., Theuns T., Frenk C. S., Crain R. A., Dalla Vecchia C., 2012, MNRAS, 427, 379

McGaugh S., Schombert J., 2013, ArXiv:1303.0320

Moster B. P., Naab T., White S. D. M., 2013, MNRAS, 428, 3121

Moster B. P., Somerville R. S., Maulbetsch C., van den Bosch F. C., Macciò A. V., Naab T., Oser L., 2010, ApJ, 710, 903

Munshi F. et al., 2013, ApJ, 766, 56

Navarro J. F., Steinmetz M., 2000, ApJ, 538, 477

Noeske K. G. et al., 2007, ApJ, 660, L43

Nomoto K., Hashimoto M., Tsujimoto T., Thielemann F.-K., Kishimoto N., Kubo Y., Nakasato N., 1997, Nuclear Physics A, 616, 79

Pérez-Montero E. et al., 2009, A&A, 495, 73

Piontek F., Steinmetz M., 2011, MNRAS, 410, 2625

Richard J., Jones T., Ellis R., Stark D. P., Livermore R., Swinbank M., 2011, MNRAS, 413, 643

Salmi F., Daddi E., Elbaz D., Sargent M. T., Dickinson M., Renzini A., Bethermin M., Le Borgne D., 2012, ApJ, 754, L14

Shen S., Wadsley J., Stinson G., 2010, MNRAS, 407, 1581

Steinmetz M., Mueller E., 1994, A&A, 281, L97

Stinson G., Seth A., Katz N., Wadsley J., Governato F., Quinn T., 2006, MNRAS, 373, 1074

Stinson G. S., Bailin J., Couchman H., Wadsley J., Shen S., Nickerson S., Brook C., Quinn T., 2010, MNRAS, 408, 812

Stinson G. S., Brook C., Macciò A. V., Wadsley J., Quinn T. R., Couchman H. M. P., 2013, MNRAS, 428, 129

Stinson G. S., Dalcanton J. J., Quinn T., Kaufmann T., Wadsley J., 2007, ApJ, 667, 170

Tremonti C. A. et al., 2004, ApJ, 613, 898

Wadsley J. W., Stadel J., Quinn T., 2004, New Astronomy, 9, 137

Whitaker K. E., van Dokkum P. G., Brammer G., Franx M., 2012, ApJ, 754, L29

Woosley S. E., Weaver T. A., 1995, ApJS, 101, 181

Wuyts E., Rigby J. R., Sharon K., Gladders M. D., 2012, ApJ, 755, 73

Wuyts S. et al., 2011, ApJ, 742, 96

Wuyts S., Labbé I., Schreiber N. M. F., Franx M., Rudnick G., Brammer G. B., van Dokkum P. G., 2008, ApJ, 682, 985

Zahid H. J., Dima G. I., Kewley L. J., Erb D. K., Davé R., 2012, ApJ, 757, 54

Zahid H. J., Kewley L. J., Bresolin F., 2011, ApJ, 730, 137

Chapter 8

Summary and conclusions

In this work we have studied the formation patterns of galaxies in SPH cosmological zoom-in simulations from both and intrinsic perspective as well as an observational one. We have employed two different SPH codes, `P-DEVA` and `GASOLINE` that mainly differ in the way star formation is implemented. `P-DEVA` uses implicit feedback by means of low star formation efficiency, while `GASOLINE` assumes explicit feedback which drives large scale outflows. Another difference lies in the chemical evolution. In `P-DEVA` the full Q_{ij} matrix formalism (Talbot & Arnett 1973) has been implemented, helping to improve the [α/Fe] enhancement determination.

The aim of this work is, on one hand, to describe the link between the emergence of structures at galactic scales (bulges, thin/thick disks, stellar halos) and the Cosmic Web dynamics, and on the other to develop robust ways in which simulations can be compared to observational data.

First we have analyzed and compared the bulges of a sample of L_* disk galaxies from cosmological hydrodynamical simulations run with `P-DEVA` and `GASOLINE`. In all simulations, we found a marked knee-shape in the bulge mass aggregation tracks, corresponding to the transition from an early phase of rapid assembly to a later slower one. This feature has been used to separate simulated bulges into two populations. We found that that our bulges show an important early starburst resulting from the collapse-like fast phase of mass assembly, followed by a second phase with lower star formation, driven by a variety of processes such as disk instabilities and/or mergers. Classifying bulge stellar particles identified at $z = 0$ into old and young according to these two phases, we found bulge stellar sub-populations with distinct kinematics, shapes, stellar ages and metal contents. The young components are more oblate, generally smaller, more rotationally supported, with higher metallicity and less alpha-element enhanced than the old ones. These re-

sults are consistent with the current observational status of bulges, and provide an explanation for some apparently paradoxical observations, such as bulge rejuvenation and metal-content gradients observed. Our results suggest that bulges of L_* galaxies will generically have two bulge populations that can be interpreted in terms of classical and pseudo-bulges. The relative proportions of the two varies with the galaxy mass and specific mass accretion and merger histories.

Next, we have studied the progenitors of spheroids (bulges and stellar halos) and disk from the point of view of the Cosmic Web dynamics. We have separately traced back to high zs the stellar populations of the spheroid and disk components of simulated late type galaxies and look at how their properties evolve. We found that progenitors of both spheroids and disk form Cosmic Web–like structures at high z, with the later being more evolved than the former. This confirms the predictions of models for advanced stages of gravitational instability. The distinction between the corresponding stellar populations is driven by their specific angular momentum content j, which, at its turn, can be partially explained in terms of the Cosmic Web evolution, and partially in terms of two low z processes. Firstly, the spheroid progenitors suffer strong j-loss at collapse, which contrasts to the insignificant loss of disk progenitors. Secondly, proto–disk–gas infall is initially aligned or it gets effectively aligned with the disk by disk-induced gravitational torques acting in the circumgalactic region. The proto–spheroid–gas, on the other hand follows more ballistic trajectories. These low z processes have their origins in the different initial conditions driven imprinted at high z by the Cosmic Web dynamics.

In order to close the circle, we further divided the kinematically selected disks into thin and thick ones based on their behavior in the age–α-enhancement plane, where two different tracks can be clearly distinguished. We choose this classification in order to be able to compare our simulations with very recent observational samples for the solar neighborhood. By doing this selection, we found a good agreement with observations of the solar neighborhood in metallicities, ages, velocities and velocity dispersion trends of both thin and thick disks. The main discrepancy with observational data comes from the α-enhancement in g1536 galaxy.

Following the assembly patterns of the age selected thin and thick disks, we find similar web-like structuring at high z for both components, which first disappear for the later and then for the former. In the context of the disk–spheroid build up, we conclude that spheroids, thick and thin disks display a web–like structure initially, which disappears as the gas collapses sequentially to form the first, second and third component. All three gain angular momentum as predicted by the Tidal Torque Theory, but due to their different gas collapse regimes lose it to various degrees. The

spheroids form through rapid collapse at high z, losing angular momentum catastrophically, while thick and thin disk form later on losing angular momentum to a much lesser degree, if any. The final outcome is a sequence of later assembly times, increasing angular momenta, higher metallicities and younger ages as we go from thin to thick disks to spheroids.

The second part of this work is concerned with how exactly simulations should be analyzed in order to make reliable comparisons with observations. For this purpose, our group, in close collaboration with Prof. G.L. Granato and L. Silva at Osservatorio Astronomico di Trieste, Italy, has recently developed a radiative transfer code, GRASIL-3D, that computes spectral energy distributions for simulated galaxies, as well as the relevant post–processing pipeline. This further processing of the simulations is a necessary step since all observable properties of galaxies are light-weighted. Up to this point GRASIL-3D has been interfaced with the SPH codes `P-DEVA`, `GASOLINE` and `GADGET`. It does not use Monte Carlo methods to solve the radiative transfer equations, but a grid. The code is based on a previous 1–D model, GRASIL, that has been successfully used in semi-analytical studies. The most notable strengths of the code are the following: i) it solves the radiative transfer equations separately for molecular clouds and diffuse gas, which are known to have different dust compositions, ii) it accounts for the age-dependent dust reprocessing by stars, and iii) it includes a detailed non-equilibrium calculation for dust grains with diameter smaller than $a_{flu} \sim 250$ Å. The code introduces a few extra parameters, which are however necessary since the resolution of most current cosmological simulations does not yet reach molecular clouds scales. Nevertheless, we have tested the code with parameters covering the full ranges allowed by observations with very satisfactory results.

For a one–to–one comparison with observations, we have developed a post-processing pipeline that convolves the GRASIL-3D spectral energy distributions with various detector responses. In this way we can compute fluxes and flux maps (images) that mimic how simulated galaxies would be *observed* with various telescopes. To test the code against observations, we have looked at a sample of eight normal, non-interacting disk-like galaxies at $z = 0$, a merger event between two disks, and a high-z massive galaxy. We have compared the fluxes of these simulated galaxies from far–ultraviolet to far–infrared to observational data compiled from the literature finding very good agreement.

The first application of the code has been to a sample of `GASOLINE` galaxies spanning four magnitudes in stellar mass. We have looked at how this galaxies evolve in the stellar mass – star formation rate – Oxygen abundance space, using *light weighted* masses and star formation rates.

We have estimated these two quantities using observational tracers that combine fluxes in visible bands for the mass, and fluxes in far–ultraviolet and the total flux in infrared for the star formation rates. Doing all calculations in the rest frame of the galaxies we found these observational tracers to follow closely the *true* simulation values. This is a very encouraging result specially for the star formation rate that can be very bursty for lower mass systems. In this 3D parameter space, our simulated galaxies show a tight correlation with the same coefficients as observational samples, with a slight mismatch in the normalization. Similar to observational samples, the correlation for the simulated galaxies does not evolve with redshift.

Chapter 9

Resumen y conclusiones

En este trabajo hemos estudiado los patrones de formación de galaxias en simulaciones SPH cosmológicas de zoom-in desde una perspectiva intrínseca, así como desde una perspectiva observacional. Hemos empleado dos códigos SPH diferentes, `P-DEVA` y `GASOLINE`, que difieren principalmente en la forma de modelizar la formación estelar. `P-DEVA` utiliza un modelo de retroalimentación implícito por medio de una baja eficiencia de formación estelar, mientras que `GASOLINE` asume un modelo explícito que produce eflujos de gas a gran escala. Otra diferencia radica en la evolución química. En `P-DEVA` se ha implementado el formalismo completo de la matriz Q_{ij} (Talbot & Arnett 1973), que ayuda a mejorar la estimación de [α/Fe].

El objetivo de este trabajo es, por un lado, describir la relación entre la aparición de estructuras a escalas galácticas (bulbos, discos finos/gruesos, halos estelares) y la dinámica de la red cósmica, y por otro, desarrollar formas robustas de comparar simulaciones con datos observacionales.

En primer lugar hemos analizado y comparado los bulbos de una muestra de galaxias L_* de disco, simuladas en un contexto cosmológico con `P-DEVA` y `GASOLINE`. En todas las simulaciones, encontramos una transición marcada en forma de codo en las secuencias de agregación de masas de los bulbos, correspondiente a la transición desde una fase temprana de ensamblaje rápido a una posterior más lenta. Esta característica se ha utilizado para separar las poblaciones estelares de los bulbos simulados en dos poblaciones. Hemos encontrado que nuestros bulbos muestran un importante brote estelar temprano, resultante de la fase rápida de agregación de masa, seguido por una segunda fase con formación estelar más baja, impulsada por una variedad de procesos tales como la inestabilidad y/o fusiones de discos. Clasificando las partículas estelares de los bulbos identificados a $z = 0$ en viejas y jóvenes según su pertenencia a una de estas dos fases, encontramos

subpoblaciones estelares con propriedades cinemáticas, de formas, de edades estelares y contenidos metálicos distintas. Las componentes jóvenes son más achatadas, generalmente más pequeñas, sostenidas en una mayor proporción por rotación, con mayor contenido de elementos pesados y menos enriquecimiento de elementos α que los viejos. Estos resultados son consistentes con observaciones recientes de bulbos galácticos, y proporcionan una explicación para algunas observaciones aparentemente paradójicas, como el rejuvenecimiento de algunos bulbos y los gradientes de contenido de elementos pesados observados. Nuestros resultados sugieren que los bulbos de galaxias L_* genéricamente tendrán dos poblaciones estelares que pueden ser interpretadas en términos de bulbos clásicos y pseudo-bulbos. Las proporciones relativas de las dos componentes varían con la masa de las galaxias, sus tasas de acrecimiento de masa y sus historias de formación estelar.

A continuación, hemos estudiado los progenitores de esferoides (bulbos y halos estelares) y discos desde el punto de vista de la dinámica de la red cósmica. Hemos seguido por separado, a altos zs, las poblaciones estelares de los componentes esferoidales y de disco de las galaxias simuladas de tipo tardío y hemos estudiado cómo evolucionan sus propiedades. Encontramos que los progenitores de ambos forman a alto zs estructuras parecidas a la red cósmica, la de los esferoides siendo más evolucionada que la de los discos. Esto confirma las predicciones de los modelos que describen las etapas avanzadas de la inestabilidad gravitatoria. La distinción entre las poblaciones estelares correspondientes es causada por sus contenidos de momento angular específico, j, que, a su vez, se puede explicar en parte en términos de la evolución de la red cósmica, complementado por dos procesos a bajo z. En primer lugar, los progenitores de los esferoides sufren una fuerte pérdida de j durante el colapso, que contrasta con la pérdida insignificante que sufren los progenitores de discos. En segundo lugar, la caída de gas del proto-disco está inicialmente alineada con el disco viejo ya formado, por el efecto de pares gravitacionales, pares inducidos por el mismo disco viejo en las regiones circumgálacticas. El gas del proto-esferoide, por otra parte, sigue trayectorias más balísticas. Estos procesos a bajo z tienen su origen en las diferentes condiciones iniciales grabadas a alto z por la dinámica de la red cósmica.

Para cerrar el círculo, hemos dividido los discos seleccionados cinemáticamente en finos y gruesos en base a su comportamiento en el plano edad - α-enhancement, donde se pueden distinguir claramente dos secuencias. Elegimos esta clasificación con el fin de poder comparar nuestras simulaciones con muestras observacionales muy recientes para la vecindad solar. Al hacer esta selección, encontramos un buen acuerdo con los datos observacionales de la vecindad solar en las tendencias de las metalicidades, edades, velocidades y dispersión de velocidades de ambos discos, finos y grue-

sos. La única discrepancia con los datos observacionales está en el α-enhancement en una galaxia concreta, la galaxia g1536.

Siguiendo los patrones de ensamblaje de los discos delgados y gruesos seleccionados por edad, encontramos unas estructuras similares a las de la red cósmica a alto z para ambas componentes, estructuras que primero desaparecen por los discos gruesos y después para los delgados. En el contexto de los resultados anteriores para discos y esferoides, concluimos que los esferoides, discos gruesos y delgados muestran inicialmente una estructura tipo red, que desaparece a medida que el gas colapsa secuencialmente para formar los primeros, los segundos, y los terceros, respectivamente. Las tres componentes ganan momento angular según lo predicho por la Tidal Torque Theory, pero debido a las diferencias entre los regímenes de colapso del gas, pierden j en grados diferentes. Los esferoides se forman por colapso rápido a alto z, perdiendo gran parte de su momento angular, mientras que los discos gruesos y finos se forman más tarde y más lentamente, perdiendo mucho menos de sus momentos angulares iniciales. El resultado final es una secuencia de tiempos de ensamblajes más tardíos, momentos angulares más grandes, mayores metalicidades y edades más jóvenes, al ir desde discos delgados a discos gruesos a esferoides.

La segunda parte de este trabajo está relacionado con las maneras de analizar simulaciones con el fin de hacer comparaciones fiables con datos observacionales. Para este propósito, nuestro grupo, en colaboración con el Prof. G.L. Granato y L. Silva del Osservatorio Astronomico di Trieste, en Italia, ha desarrollado recientemente un código de transporte radiativo, GRASIL-3D, que calcula las distribuciones espectrales de energía para galaxias simuladas, así como los códigos pertinente de postprocesamiento. Este tratamiento posterior de las simulaciones es un paso necesario, dado que todas las propiedades observables de galaxias son pesadas en luz. Hasta este momento, GRASIL-3D se ha interconectado con los códigos SPH `P-DEVA`, `GASOLINE` y `GADGET`. Nótese que GRASIL-3D no utiliza el método de Monte Carlo para resolver las ecuaciones de transporte radiativo, sino una malla. El código se basa en un modelo anterior, GRASIL, que ha sido utilizado con éxito en estudios semianalíticos. Los puntos fuertes más notables del código son los siguientes: i) resuelve las ecuaciones de transporte radiativo por separado para las nubes moleculares y el gas difuso, que se sabe que tienen diferentes composiciones en polvo; ii) tiene en cuenta la dependencia del reprocesado de polvo con la edad de las estrellas; e iii) incluye un cálculo detallado de no equilibrio para los granos de polvo con diámetro menor que $a_{flu} \sim 250$Å. El código introduce algunos parámetros adicionales, paso necesario, dado que la resolución de la mayoría de las simulaciones cosmológicas actuales todavía no llega a escalas de nubes moleculares. Sin embargo, hemos testado el código

en un rango de parámetros que cubren los rangos completos permitidos por las observaciones, con resultados muy satisfactorios.

Para una comparación directa con observaciones, hemos desarrollado un código de postprocesamiento qur convoluciona las distribuciones espectrales de energía de GRASIL-3D con respuestas de diversos detectores. De esta manera, podemos calcular los flujos y mapas de flujo (imágenes) de las galaxias simuladas tal y como serían *observadas* con varios telescopios. Para comparar los resultados de GRASIL-3D con observaciones, hemos analizado una muestra de ocho galaxias normales, sin interacciones, a $z = 0$, un evento de fusión entre dos galaxias disco y una galaxia masiva a alto z. Hemos comparado los flujos de estas galaxias simuladas desde el rango del ultravioleta lejano hasta el infrarrojo lejano con datos observacionales recopilados de la literatura, encontrando un muy buen acuerdo.

La primera aplicación del código ha sido a una muestra de galaxias `GASOLINE` que abarcan cuatro órdenes de magnitud en masa estelar. Hemos estudiado cómo evolucionan estas galaxias en el espacio de la masa estelar - tasa de formación de estelar - abundancia de oxígeno. Hemos estimado estas dos cantidades usando trazadores observacionales que combinan flujos en bandas visibles, para la masa, y flujos en el ultravioleta con el flujo total en el infrarrojo, para las tasas de formación estelar. Haciendo los cálculos en el sistema de referencia de las galaxias, encontramos que los trazadores observacionales siguen muy bien los valores *verdaderos* de las simulaciones. Este es un resultado muy alentador, especialmente para la tasa de formación estelar que puede ser altamente irregular y variable para sistemas de menor masa. En este espacio de parámetros tridimensional, nuestras galaxias simuladas muestran una estrecha correlación, exhibiendo los mismos coeficientes, que las muestras observacionales, excepto un ligero desajuste en la normalización. Lo mismo que en las observaciones, esta correlación en las galaxias simuladas no evoluciona con el desplazamiento al rojo.